Numerical multi-scale modelling of composite plates

Dissertation

zur Erlangung des Grades des

Doktors der Ingenieurwissenschaften (Dr.-Ing.)

der Naturwissenschaftlich-Technischen Fakultät III

Chemie, Pharmazie, Bio- und Werkstoffwissenschaften

der Universität des Saarlandes

von

Dipl.-Ing. Cécile Eliane Helfen

Saarbrücken

2012

Tag des Kolloquiums	14. Januar 2013
Dekan:	Univ.-Professor Dr. Volkhard Helms
Berichterstatter:	Prof. Dr.-Ing. Stefan Diebels
	Prof. Dr.-Ing. habil. Holm Altenbach
Vorsitz:	Prof. Dr. Hans-Georg Herrmann
Akad. Mitarbeiter:	Dr.-Ing. Frank Aubertin

À Thomas

Preface

This research work has been performed in the Chair of Applied Mechanics between September 2009 and October 2012. The financial support of the DFG (Deutsche Forschungsgemeinschaft) under the grant Di 430/11-1 is gratefully acknowledged.

Firstly, I would like to thank my advisor Prof. Dr.-Ing. Stefan Diebels, for his help and support during my time in the Chair of Applied Mechanics. I really appreciated the constructive discussions; his scientific knowledge in the field of material modelling and homogenisation contributed significantly to this work. Secondly, my thanks go to Prof. Dr.-Ing. habil. Holm Altenbach for being the co-referee of my Ph. D., and especially for the helpful remarks on plate theory.

I also want to thank my colleagues from the Chair of Applied Mechanics. Furthermore, I thank Michaela Reimringer for improving my English.

Finally, I would like to gratefully thank my family and friends for their support and understanding during my studies. Last but not least, I would like to thank my husband Thomas for his precious support, love and understanding. He provided the trust and courage I needed to achieve this work and succeeded in making me happy even in the most difficult moments.

Abstract

Composite plates, such as sandwich structures or hybrid laminates, are widely used in the field of transport industry, due to their outstanding mechanical properties for a relatively reduced weight. However, they show a complex material behaviour, which can not be properly described by using a simple mixture rule. Moreover, it can be necessary to model non-linear material behaviour -like for instance plasticity- if dealing with a forming process. Due to the restriction of most of the plate theories to linear material behaviour, the development of a numerical multi-scale modelling of composite plates is of interest.

In the presented work, the modelling of the mechanical behaviour of composite plates is based on a numerical homogenisation, or so-called FE^2, for composite plates. The principle is to split the problem into two characteristic scales: on the one hand, the macroscale, containing the kinematics of the plates, and on the other hand, a so-called mesoscale, discretizing the layers stacking order with their individual properties.

In this work, special attention is paid towards the definition of the analytical tangent using the Multi-Level Newton Algorithm (MLNA) and towards the resolution of the Poisson's thickness locking phenomenon, enabling the consideration of the thickness change by an improved projection strategy. The validity of the proposed method towards linear and non-linear material behaviour is verified using various numerical experiments.

Zusammenfasung

Verbundstrukturen finden heutzutage, aufgrund ihrer interessanten mechanischen Eigenschaften bei relativ niedrigem Gewicht, immer mehr Anwendung im Bereich der Transportindustrie. Allerdings weisen Verbundstrukturen auch ein komplexes mechanisches Verhalten auf. Zudem kann die Modellierung von nicht-linearem Materialverhalten notwendig werden, wie zum Beispiel von Plastizität, wenn ein Tiefziehen durchgeführt werden soll. Aufgrund der Begrenzung der meisten Plattentheorien zu linearem Materialverhalten, wird eine numerische Mehrskalensimulation für Kompositplatten entwickelt.

In dieser Arbeit wird die Modellierung des mechanischen Verhaltens von Kompositplatten mit einer numerischen Homogenisierung, auch FE^2 genannt, weiterentwickelt. Das Prinzip der FE^2 für Platten basiert auf der Teilung des Problems in zwei Skalen: einerseits wird die Makroskala, die die Plattenkinematik enthält, betrachtet und andererseits wird die sogenannte Mesoskala, die die Einzelschichten diskretiziert, berücksichtigt.

In der vorliegenden Arbeit soll der Definition der analytischen Tangente mit dem Multi-Level Newton Algorithm (MLNA) und der Lösung des Poissons Locking besondere Aufmerksamkeit geschenkt werden, welche die Dickenänderung mit einer verbesserte Projektionsmethode berücksichtigt. Anschließend wird die Verifizierung der Mehrskalenmethode für lineares und nicht-lineares Materialverhalten durchführt, die im Rahmen unterschiedlicher numerischer Experimente angewendet wird.

Résumé

Les matériaux composites, comme par exemple les structures sandwich ou les matériaux laminaires hybrides, trouvent de nos jours de plus en plus d'utilisations dans l'industrie du transport, en raison de leurs bonnes propriétés mécaniques pour un poids relativement réduit. Cependant, ce type de structures présente un comportement mécanique très complexe, qui ne peut être décrit qu'imparfaitement par une loi des mélanges. De plus, il peut être nécessaire de prendre en considération des lois de comportement non-linéaire -par exemple la plasticité- comme c'est dans le cas pour un emboutissage. La plupart des théories des plaques se limitant à des lois de matériaux linéaires, une méthode multi-échelles numérique est utilisée pour la modélisation du comportement mécanique de plaques composites.

Dans le cadre de ce travail, la modélisation du comportement mécanique des plaques composites est effectuée par une méthode d'homogénéisation numérique, ou autrement appelée FE^2, adaptée aux plaques. Le principe consiste en la séparation du problème en deux échelles: d'une part, l'échelle macroscopique, qui contient la cinématique d'une plaque, et d'autre part, l'échelle mésoscopique, qui décrit l'ordre des couches avec leurs différentes propriétés.

Dans le cadre de cette thèse, une attention particulière est donnée à la définition d'une tangente analytique par l'Algorithme Multi-Level de Newton (MLNA), ainsi qu'à la résolution du problème de locking de Poisson, grâce à une amélioration de la méthode de projection. Dans une dernière partie, la validité de la méthode pour des lois de matériaux linéaires et non-linéaires est verifiée dans le cadre d'expériences numériques.

Contents

Chapter 1

Introduction

1.1 Motivation

Nowadays, composite materials and especially composite plates represent a growing interest of many industries, like for instance the transport industry. This is because they enable the combination of good mechanical properties at a relatively low weight. However, they show a quite complex mechanical behaviour, which can not be properly described by a simple mixture rule. Due to the price and the complexity of the composites, the modelling of this kind of structures is an interesting issue, because it enables a better understanding of their behaviour and furthermore an optimisation of the layer staking order can take place.

In the scope of this work, the mechanical behaviour of composite plates, and especially of sandwich structures and hybrid laminates, as represented in Fig. 1.1, is investigated. The hybrid laminate is composed of several layers of different materials: at the top, bottom and in the middle, metal layers are set, which are made of an aluminium or a titan alloy and exhibit an elasto-plastic material behaviour. In between, some Carbon Fiber Reinforced Polymers (CFRPs) are embedded and present an anisotropic elastic behaviour.

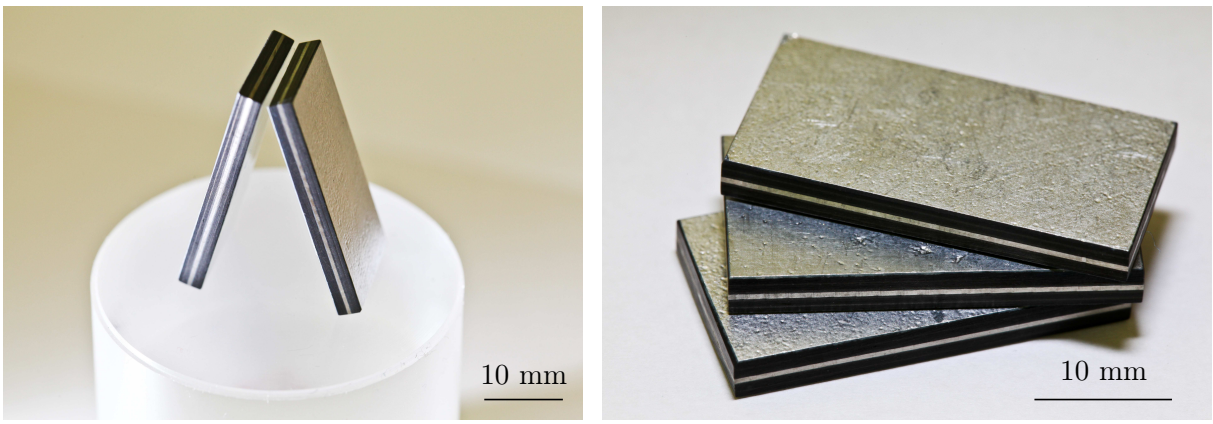

Figure 1.1: Hybrid laminates containing metal layers and CFRP (Carbon Fiber Reinforced Polymer) layers

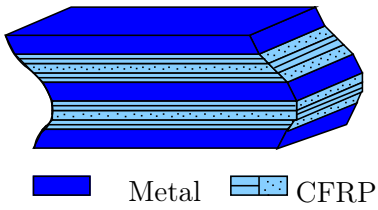

Figure 1.2: Structure of the hybrid laminate containing the layer organisation (metal/CFRP(0°/90°/0°)/metal/CFRP(0°/90°/0°)/metal)

In our case, the matrix material is made of PA 6.6, i. e. Polyamide 6.6 or generally known as nylon, or of PEEK (Polyether Ether Ketone). The fibers are long fibers and there is only one family of fibers per layer. Due to the high volume percentage of fibers -almost 50%-, the material behaviour of the CFRP is assumed to be elastic anisotropic and the viscoelastic part of the matrix material is neglected. The structure of the composite plate is represented in Fig. 1.2 and a picture of the CFRP layers, taken with a optical microscope, can be seen in Fig. 1.3. The structures represented in Fig. 1.1 are supplied by the DLR in Cologne (Prof. Dr.-Ing. Marion Bartsch, Dr.-Ing. Joachim Hausmann, Karola Schulze) and the structure in Fig. 1.3 by the professorship lightweight structures and polymer engineering (Univ.-Prof. Dr.-Ing. habil. Lothar Kroll, Sebastian Nendel), respectively.

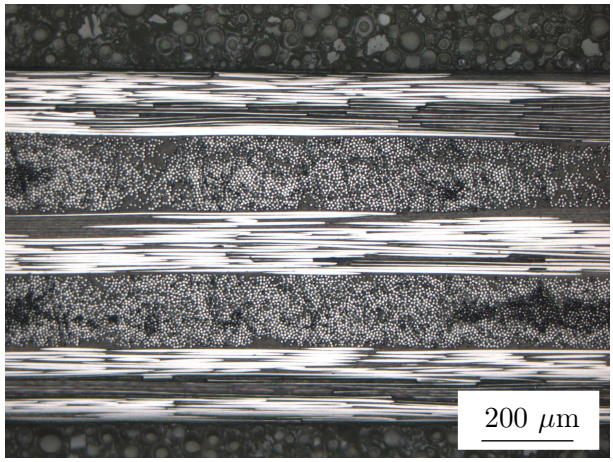

Figure 1.3: Optical microscopy picture of five CFRP (Carbon Fiber Reinforced Polymer) layers with orientation (0°/90°/0°/90°/0°)

This work aims at the modelling of the mechanical behaviour of composites plates. Because some layers are metallic, it is important to consider non-linear material behaviour and especially elasto-plasticity. Indeed, a deep drawing of composite plates is nowadays of interest of the transport industries, cf. [62, 146], and a simulation could enable an optimisation of the forming process. But which solutions exist, in order to model the mechanical behaviour of a composite plate containing layers with linear and non-linear material behaviour?

1.2 State of the Art

Basically, there are three types of methods for the modelling of the mechanical behaviour of composite plates: a three-dimensional FE (Finite Elements) modelling, a FE plate (or shell respectively) or a homogenisation strategy, as represented in Fig. 1.4. Firstly, the composite plate can be modelled using a three-dimensional FE modelling (on the left in Fig. 1.4). Regarding this solution, it is possible to consider a non-linear material behaviour like for instance elasto-plasticity. However, this solution shows high computational costs, especially for contact or for large deformation analysis like for instance for a forming process, cf. [22, 23]. Moreover, some instabilities can occur for very thin elements: this is the case for the hybrid laminate.

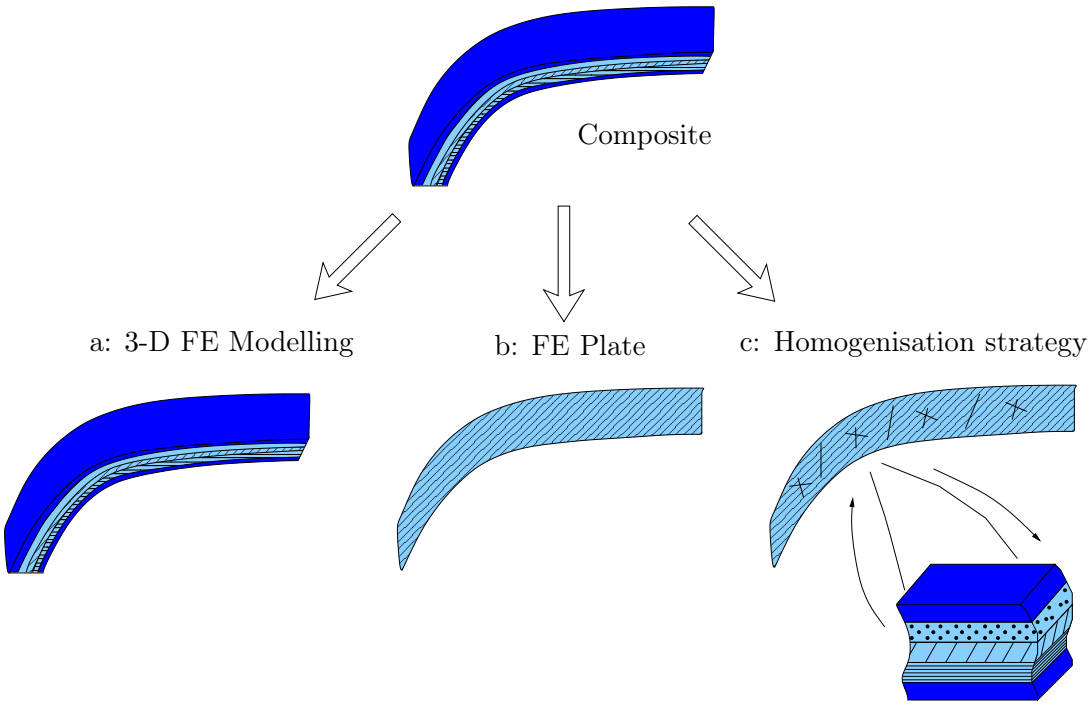

Figure 1.4: The different possibilities to model the behaviour of a composite plate: a: three-dimensional FE modelling, b: FE (Finite Element) Plate and c: Homogenisation method

The second possibility is to use a shell or a plate structure, as represented in the middle of Fig. 1.4. Because of the huge amount of work made in this field, it will not be tried to write a detailed review of the plate theories. In this case, one may refer to [9, 14, 24] among others. In the following, the main types of plate and shell theories are described with the focus on non-linear material behaviour and composite materials. As mentioned before, a non-linear material behaviour has to be considered, which excludes most of the "classical"[1] plate theories, due to their limitation to linear behaviour. So the **zig-zag**

[1]By "classical" plate theories I mean the first plate theories which were discovered and which are nowadays still often used, contrarily to one of their extensions made thereafter. Under this definition I

theories, which are widely used for studying the behaviour of sandwich and composite laminates (cf. [31, 54, 195]), are also excluded. To the knowledge of the author, the plate theories are mainly applied to linear material behaviour, cf. [24]. Indeed, most of the plate theories and most of the plate elements can only consider elastic material behaviour and encounter the problem of locking [13, 20]. In order to solve these issues, a degenerated shell or a solid-shell structure can be used.

The principle of a **degenerated shell** consists in the FE discretisation of a three-dimensional continuum "with linear shape function in thickness direction", cf. [14], leading to a shell. The degenerated shells, also called "continuum-based shell elements", cf. [14], were firstly developed by Ahmad et al. in 1968 [2]. They avoid many locking phenomena by using a three-dimensional discretisation and, after the discretisation, some assumptions in the shape functions lead to the shell formulation. Although the computational costs are high due to the three-dimensional mesh, the degenerated shells have the advantage of considering a three-dimensional constitutive law without further modifications. As a consequence, also non-linear material behaviour can be considered. However, the degenerated shells have also drawbacks. Some of them relate to the boundary conditions and in geometrically non-linear cases, to the "complicated update of the rotations", cf. Hauptmann & Schweizerhof [78]. These issues can be solved by using **solid-shell structures**, which are based on the combination of solid elements with shell elements. If using solid-shell elements, no rotational degrees of freedom are needed but the displacement degrees of freedom are applied to the upper and lower shell surfaces, cf. [77]. But finally, they show the problem of locking phenomena again, cf. [69, 136].

Another type of shell is issued from the so-called **direct approach** or **Cosserat shells**. The main idea was firstly described by the brothers Cosserat and Cosserat in 1909 [39] with the introduction of additional degrees of freedom to the classical theory. In the classical Cauchy continuum, a solid is composed of an infinite number of points which can only be submitted to translations. In contrast, in the Cosserat theory, a solid is not built of an infinite number of points but of small volumes, which can be submitted not only to translations but also to rotations, cf. [9]. The brothers Cosserat also developed an extension for shells based on a direct derivation of the classical continuum. This concept is also known as micropolar theory and was described by Ericksen & Truesdell in 1958 in [51]. The theory is geometrically exact and shows better results in case of very thin structures, where the length scale of the microstructure is of the same order of magnitude as the thickness of the plate, cf. [10]. Nevertheless, the theory encounters criticisms, cf. [14]. As a consequence, and due to the high level of complexity of these theories, they will not be studied in this work.

The last type of plates and shells are the so-called **plates and shells derivated from the three-dimensional continuum**. The plate theories derivated from the three-dimensional continuum were the first ones which appeared and their discovery spread over almost two centuries, as developed in chapter 3.1. The first correct attempt can be attributed to Love [120] and Kirchhoff [99], which developed the plate theory which now carries their names. This theory describes the behaviour of thin plates with the help of

mean the plate theories following the Kirchhoff ansatz and the plate theories following the Reissner or Mindlin ansatz; more information are given in chapter 3.

three translational degrees of freedom; the two rotations are obtained as the derivatives of the out-of-plane displacement. As a consequence, the transverse shear vanishes. Later on, Mindlin [131] and Reissner [156] developed an extension of this theory which solves its drawbacks. While the Love-Kirchhoff theories do not consider the transverse shear, and are consequently limited to very thin plates, the Reissner-Mindlin theories take the transverse shear into account with the introduction of the two more degrees of freedom accounting for the rotations. Consequently, the Reissner-Mindlin theories can be successfully used for thicker plates.

During the last 40 years, many works have been done using the "classical" plate theories or one of their extensions, cf. [5, 6, 24, 154]. The classical plate theories following the Reissner or Mindlin ansatz have proved to be nowadays frequently used because of their efficiency and stability: in the work of Kim & Reddy (2012) [98], the formulation of FE plate elements following the Kirchhoff and the Mindlin concept is proposed. In Vo & Lee (2011) [186], an extension of the First order Shear Deformation Theory (FSDT)[2] is applied to model the behaviour of fiber reinforced beams. In Hashemi et al. (2012) [72], an exact solution of a third order shear displacement theory -itself an extension of the first order shear deformation theory, containing cubic order for the displacement in the in-plane direction- is presented for thick laminated transversely isotropic plates under vibration. Maleki et al. (2012) [121] present an analytical solution of the FSDT theory under dynamic loading. And Janghorban (2012) [87] explains the static analysis of microbeams under thermomechanical loading.

Unfortunately, most classical plate or shell theories have numeric drawbacks; perhaps the most important ones are the problems of locking, as already mentioned above. Nowadays, most of the locking issues have found a solution with some improved element types, cf. [13, 20] and this is briedly described in Subsect. 3.4. However, the classical theories do not consider any deformation in the thickness direction and only an elastic behaviour can be used [154]. Some extensions to consider viscoelastic material behaviour have to be mentioned, cf. [3]. But to the knowledge of the author, the classical plate theories are mainly restricted to linear material behaviour, the constitutive laws are two-dimensional ones, cf. [3, 9] and the lack of consideration of the deformation in the thickness direction remains a concerning issue.

However, some extensions of the Mindlin concept were made in order to overcome this drawback. When considering the Mindlin concept, one or two degrees of freedom can be added to obtain an out-of-plane displacement of linear or quadratic order, respectively. The plate theory following the Mindlin concept is usually called the 5-parameters theory, due to the five degrees of freedom. Considering the Mindlin concept with one or two more degrees of freedom leads to the 6- or to the 7-parameters theories, respectively, referring to the number of degrees of freedom. The first idea of the improved Mindlin concept may be attributed to Hildebrand, Reissner and Thomas in 1949, cf. [13] and later refined by Kätzig [105]. In the Mindlin concept, the normal deformation in thickness direction is simply neglected in comparison to the normal strains in the in-plane direction and a plane stress assumption is followed. In contrast, the normal deformation in thickness

[2]First Order Shear Deformation Theory (FSDT) is one of the names of the plate theories with five degrees of freedom following the Mindlin concept adapted to consider the behaviour of laminates.

direction is constant for the 6-parameters theory. For the plate theory with seven degrees of freedom, a linear function is obtained for the out-of-plane normal deformation ε_{33} and a three-dimensional constitutive law is assumed. This concept can be found in different papers, among them [13, 162, 180, 181], which propose the so-called $(1, 1, 2)$-model, named after the order of the displacement in the three directions respectively and in [13, 122] with special attention to its numerical treatment.

Another treatment of the seventh degree of freedom is possible, namely with the EAS (Enhanced Assumed Strain) method, where the last degree of freedom is directly introduced in the out-of-plane normal strain, so that the out-of-plane normal deformation is described by a linear function, cf. [13, 21, 106, 161]. A FE shell containing a thickness change within the EAS method and the resolution of locking problems can be found in the dissertation of Bischoff in 1999 [13], or in the work of Schlebusch in 2005 [165]. In Bletzinger et al. (2000), another solution, the Discrete Shear Gap (DSG) method, is used to avoid shear locking, cf. [15]. Other solutions are possible, like for instance considering higher order elements, as proposed by Rank et. al. [151] or a non-linear strain for a six degrees of freedom model, cf. [34]. Lastly, it has to be mentioned that extensions including non-linear material behaviour, like for instance elasto-plasticity, have been proposed, e. g. in the work of Roehl & Ramm in 1996 [161] or to include viscoplasticity for the Timoshenko beam in the dissertation of Matthes [124]. Recently, some authors proposed other extensions of the method, resulting in a plate theory containing nine degrees of freedom, e. g. Polit et al. in 2012 [148]. In Carrera & Miglioretti in 2012 [25], a genetic algorithm is used to determine which plate theory is the most accurate for the description of a considered bending test, from a FSDT to an extension of it containing twelve degrees of freedom.

Due to drawbacks especially toward locking, a FE plate can lead to inaccuracy. For this reason, a homogenisation strategy is studied in this work. The principle of a multiscale solution, as represented on the right in Fig. 1.4, is to split the problem into two separate scales: the macroscale and the microscale. The macroscale contains the kinematics of the plate, but instead of using the constitutive law of the plate, which leads in most of the cases to a linear material behaviour, the macroscopic constitutive law is replaced by a direct consideration of the microstructure in the microscale. For the multiscale modelling, there are two possibilities: to use an "analytical" multiscale method or a "numerical" concurrent or computational multiscale strategy. With respect to the homogenisation, the modelling of three-dimensional structures is first described and in a second step, the special case of plates is examined.

In the **analytical homogenisation**, the microstructure is considered in a separate analytical computation of the microscale. This method was firstly proposed by Ponte Castañeda, cf. [26, 27] and Suquet [177] toward plasticity for composite materials. For the homogenisation procedure, another possibility is to take into account the effective properties of the microstructure. A Representative Volume Element (RVE) has to be found, which is big enough to be "representative" for the microstructure but small enough to enable computation in a maintainable time scale. By considering, separately to the macroscale,

several FE computations for the microscale which are proceeded under different loadings, the constitutive law can be identified. This method can be applied to heterogeneous materials, if the length scale of the heterogeneities is much smaller than the length scale of the macroscale, as applied in [184] for the Perzyna's elasto-viscoplastic model or by Zohdi & Wriggers for a matrix containing particles, cf. [200].

Later on, some developments have been proposed [115] to consider composite materials, with special attention to the history of loading in case of viscoelastic material behaviour. The numerical homogenisation method proved to be equally efficient for fiber reinforced materials, cf. [19, 197] and for composite structures including a random repartition of the fibers, cf. [118]. The multiscale method is very useful for composite materials and so far, many strategies exist as shown in the review by Kanouté et al. [94]. Recently, some extensions to include viscoplastic material behaviour were proposed, as made by Segurado et al. [172] or to consider the mechanical behaviour of solders, cf. Brandmair et al. [18].

The second possibility for a multiscale method is to use the numerical multiscale or the so-called **FE^2 method**, where the FE computations of the both scale are proceeded simultaneously. The principle of the FE^2 method is not to consider the two scales separately but to link them during the computation. From each integration point of the macroscale, the deformations are projected to the microscale, and within the microscale, a FE computation of the RVE is applied. Then, the macroscopic stresses are identified with the Hill-Mandel condition, as proposed by Feyel & Chaboche for fiber composites, cf. [56]. Under the supervision of Miehe, several works on FE^2 problems were written with consideration of a consistent tangent, cf. [127, 129, 130], also for composite materials. As for the computational homogenisation in practice with ABAQUS®, it can be referred to the paper of Yuan & Fish in 2008, cf. [196]. Later on, an adaptive homogenisation, combining the two types of homogenisation, analytical and numerical, is proposed for a reduction of the computing time, cf. [53].

However, it may be convenient to incorporate some second order terms for the macroscale, while the microscale follows a Cauchy theory. The higher order FE^2 method enables a consideration of size effects, as proposed by Feyel in 2003 in [55] for Cosserat media. A theory of micromorphic media can also be used, as proposed by Forest [58, 59], Forest & Sab [60], Kanit et al. [93], Neff & Forest [134] or a micropolar theory, as proposed by Larsson & Diebels [111] for materials with soft inclusions. Randomly distributed voids were studied by Kouznetsova et al. [103, 104] for elastic and elasto-plastic materials. Later on, the theory of micromorphic media was used to model the behaviour of cellular materials, cf. [91, 89, 90]. Further details about a second order numerical homogenisation can be found in Kouznetsova's [102] or in Jänicke's dissertation [88]. For an elasto-plastic composite, a recent development was introduced by Forest and Trinh in [61]. In 2010, Larsson and Runesson proposed a local numerical homogenisation, where it is needed, for elasto-plastic material behaviour with microscopic heterogeneities, cf. [110].

Concerning a multiscale method applied to plates, an analytical homogenisation was proposed in 1989 by Laschet et al. [112] and a numerical homogenisation in 1993 by Fish &

Wagiman for laminated plates, cf. [57]. The specific case of masonry was studied in [28] and Hohe [82] proposed a homogenisation scheme for sandwich panels. Recently, some work has been done on orthotropic sandwich plates, cf. [1] or for elastic thin structures with particles, cf. [119]. A numerical homogenisation made with ABAQUS® was proposed by Oskay & Pal in [139] for thin heterogeneous plates, including a damage model. Some works also consider the modeling of failure in adhesive layers within the framework of cohesive zones, cf. [123] or simulate the behaviour of cohesive zones for multiscale plates, cf. [193].

A computational homogenisation for plates was published later by Geers et al. in 2007, cf. [65], for a plate theory following the Mindlin concept. One year later, Landervik & Larsson proposed a first and a second order numerical homogenisation for shell materials, and especially for a porous layer, where a plate theory with thickness change was used for the shell kinematics, cf. [108, 109]. In the same year, Grytz & Meschke came up with a computational homogenisation for shell problems for a finite shell theory, cf. [68]. Coenen et al. proposed a computational homogenisation for both Kirchhoff and Reissner-Mindlin type plates in 2008 [35]. The computational homogenisation following the Kirchhoff kinematics was also developed in 2010 in a further paper, cf. [36].

1.3 Objectives of the Work

In the presented work, two solutions for modelling the behaviour of the composite plates are compared. On the one hand, a simple plate theory with thickness change is considered. On the other hand, the FE^2 method for plates is studied. There is naturally a link between the two methods, because the numerical homogenisation contains the kinematics of a plate theory for the macroscale. In this work, the smaller scale is not really a microstructure but rather a "mesostructure", because a different layer stacking order is considered and not a structure with a microscopic length scale. In the following, the plate is referred to as the macroscale and the three-dimensional RVE as "mesoscale".

The objective of this work is to propose a numerical concurrent homogenisation method for plates. In this framework, the homogenisation is only performed in the two directions parallel to the midplane, whereas a full discretisation is performed in the thickness direction. Accordingly, a plate theory is considered for the macroscale, while the mesoscale contains a three-dimensional boundary value problem. Consequently, the problems of locking related to the plate have to be solved. In this work, some classical solutions are used to avoid some of the locking effects, and a special attention is paid towards the resolution of the Poisson locking. The Poisson locking appears for a plate without consideration of the thickness change, i. e. for the plate theory following the Mindlin concept. The Poisson locking has an important consequence if the Poisson's ratio is going to 0.5, as encountered for plastic incompressibility. An innovative solution to avoid the Poisson locking in the framework of the numerical homogenisation of plates is investigated, which enables the consideration of thicker plates and incompressible material behaviour. Consequently, the proposed FE^2 method can be successfully applied for thick composite plates of different types, such as hybrid laminates and sandwich plates.

In the presented work, the numerical homogenisation for plates is compared to the performance of a plate theory with thickness change. Both methods enable to solve the Poisson locking issue. However, the numerical homogenisation shows high computational costs. Most of the works related to this method use a numerical tangent, which slows down the computation considerably. In the presented work, the Multi-Level Newton Algorithm, cf. [70], is used to find an accurate tangent for the FE^2 method.

1.4 Outline

The second chapter comprises a summary of continuum mechanics and the description of isotropic and anisotropic hyperelastic materials, describing the polymer alone and the fiber reinforced polymer material behaviour, respectively. Then, an elasto-plastic material, considered as a particular case of an elasto-viscoplastic material behaviour is described. Special attention is given towards the definition of the analytical tangent. After a short historical review of the plate theories, the third chapter comprises the description of the strong and weak formulations of the plate theories considered in this work. Then, a description of the locking effects and of some aspects related to the convergence of the plate theory is performed.

The fourth chapter explains the numerical homogenisation scheme. Firstly, a brief summary of the plate kinematics used for the FE^2 method is given, followed by the description of the projection strategy. In fact, the projection seems to have a critical influence on the results and an accurate choice of them enables better performances for the FE^2 method. Then, a complete description of the boundary value problem is presented. In a last part, the meso-macro transition is described. Here, special attention is paid to the definition of the analytical tangent, which enables a significant reduction of the computational cost. In the fifth chapter, the performance of the two methods, the plate theory with thickness change on the one side and the FE^2 on the other side, are compared. Finally, conclusions are drawn and possible improvements are explained in the sixth chapter.

1.5 Notations

In the presented work, the tensors of zero order, commonly known as scalars, are represented by italic letters like

$$\alpha, \beta, i, j...$$

The vectors or first order tensors are written in small bold letters

$$\mathbf{b}, \mathbf{r}, \mathbf{u}...,$$

and the second order tensors are represented by bold letters

$$\boldsymbol{\varepsilon}, \boldsymbol{\sigma}, \boldsymbol{\gamma}, \mathbf{P}...$$

For tensors of higher order than the second order, the order of the tensor is explicitly given for clarity, like for instance

$$^4\mathbb{C},\ \overset{4}{\mathbf{B}}\ ...$$

In the basis of space with three dimensions, a Cartesian coordinate system is defined with the basis vectors $\mathbf{e}_1$, $\mathbf{e}_2$ and $\mathbf{e}_3$. The Einstein convention is used, that means that the symbol "sum" is not written when an index is repeated two times

$$\sum_{i=1}^{3} a_i\,\mathbf{e}_i \;=\; a_i\,\mathbf{e}_i \;=\; a_1\,\mathbf{e}_1 + a_2\,\mathbf{e}_2 + a_3\,\mathbf{e}_3.$$

The tensor products are defined as

$$\mathbf{A}\cdot\mathbf{B} \;=\; A_{ik}B_{kl}\,\mathbf{e}_i\otimes\mathbf{e}_l,$$

and

$$\mathbf{A}:\mathbf{B} \;=\; A_{ij}\,B_{ij}.$$

The outer product between two vectors is defined as

$$\mathbf{u}\times\mathbf{v} \;=\overset{3}{\mathbf{E}}\!:(\mathbf{u}\otimes\mathbf{v}),$$

with the permutation tensor

$$\overset{3}{\mathbf{E}} = \;\varepsilon_{ijk}\,\mathbf{e}_i\otimes\mathbf{e}_j\otimes\mathbf{e}_k,$$

where

$$\varepsilon_{ijk} \;=\; \begin{cases} 1 & \text{for} \quad i,j,k = 1,2,3/2,3,1/3,1,2, \\ -1 & \text{for} \quad i,j,k = 1,3,2/3,2,1/2,1,3, \\ 0 & \text{else.} \end{cases}$$

The identity tensor is defined as

$$\mathbf{I} \;=\; \delta_{ij}\,\mathbf{e}_i\otimes\mathbf{e}_j,$$

and the Kronecker symbol as

$$\delta_{ij} \;=\; \begin{cases} 1 & \text{for} \quad i = j, \\ 0 & \text{for} \quad i \neq j. \end{cases}$$

Chapter 2

Continuum Mechanics

Continuum mechanics [73, 154] deals with the description of the motion and deformation of a material body exposed to forces and torques. It is a phenomenological theory, which uses mathematical models (in the macroscopic scale) in order to describe the mechanical behaviour. The macroscopic scale is considered, that means that the discrete structure of the material (atoms, molecules...) is not considered and continuum mechanics deals with a macroscopic description of the material behaviour.

At the end of the 18^{th} century, Euler worked on the mechanics of rigid and deformable bodies and his work can be considered as important for the future continuum mechanics, cf [4]. Later on, Cauchy worked on the elasticity of a deformable body and laid the foundations for the continuum mechanics by proposing the use of the stress tensor, cf. [178]. Later in the 20^{th} century and especially in its second part, Rivlin [158, 159, 160] showed that "illuminating problems for incompressible non-linearly elastic solids and for incompressible non-Newtonian fluids could be solved for arbitrary non-linear constitutive equations", cf. Truesdell [182]. Truesdell proposed a synthesis and clarification for the theory of elasticity and it led to the modern theory of continuum mechanics. In the famous "Handbuch der Physik" [182], the basis of elasticity, thermodynamics, kinetics and fluids dynamics was given. Later on, further interpretations were made, among them by Altenbach & Altenbach [4], Holzapfel [84] and Haupt [73] which were particularly used to achieve this work and to write this part.

The description of the phenomenological behaviour of a material can be separated in three parts:

- the kinematics focus on the geometric aspects and describe the relations between positions, displacements and deformations;
- the balance equations represent the conservation of mass, momentum and moment of momentum. Also balance relations for energy and entropy are postulated, following the thermodynamics;
- the constitutive laws, which describe the material behaviour of materials, i. e. the relation between stress and deformations. In the context of this work and because of the considered material behaviour, the description of isotropic and also anisotropic hyperelastic material behaviour, as well as viscoplastic behaviour, is presented.

The topic of this work is limited to the description of the mechanical behaviour of composites plates; therefore the behaviour of shells will be excluded. As a consequence, the con-

sidered system of coordinates is Cartesian, and the co- and contravariant vectors [100, 157] are supposed to be identical.

2.1 Kinematics

In continuum mechanics, a deformable solid, composed of a set of material particles, is named $\mathcal{B}$ and it is placed in a three-dimensional space with an Euclidien geometry. In this case, it is assumed that the solid is composed of an infinite number of material points continuously distributed in space and that each material point is subjected to only three translations. This theory forms the classical or Cauchy-type continuum mechanics. It is to differentiate from the Cosserat theory [39], which assumes that a body is composed of an infinite set of rigid bodies, which are subjected to translations and rotations and therefore presents six degrees of freedom, cf. Eringen [52], Altenbach et al. [9].

In order to describe finite deformations, a reference configuration or undeformed configuration, specified as the configuration at an initial time (or for $t = 0$) is defined. Similarly, a current or deformed configuration, defined at a time t, is set. A material point X occupies a unique position $\mathbf{X}$ in the reference configuration and a unique position $\mathbf{x}$ in the current configuration, as represented in Fig. 2.1. Therefore, the path $\boldsymbol{\chi}$, describing the function of motion of the point X during the time t, is also unique and can be written as

$$\mathbf{x} = \boldsymbol{\chi}(\mathbf{X}, t). \tag{2.1}$$

The function of motion is uniquely invertible and its inverse with respect to the space coordinates is the Euler representation as

$$\mathbf{X} = \boldsymbol{\chi}^{-1}(\mathbf{x}, t). \tag{2.2}$$

The displacement is defined as the difference between the position of the considered point X at the current configuration with the position of the point in the reference configuration as

$$\mathbf{u} = \mathbf{x} - \mathbf{X}. \tag{2.3}$$

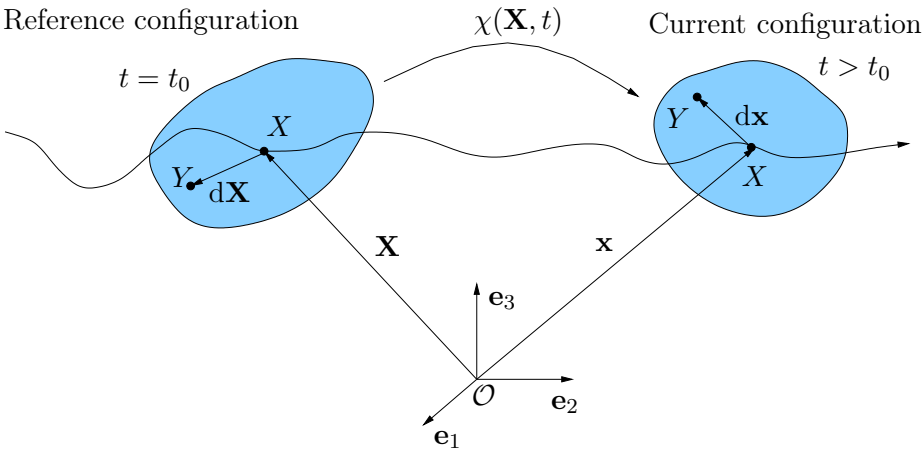

Figure 2.1: Reference and current configurations

Two neighbouring points X and Y can be connected by a material line element defined as $\mathrm{d}\mathbf{X}$ in the reference configuration and $\mathrm{d}\mathbf{x}$ in the current configuration. The transport of a material line element from the undeformed to the deformed configuration is defined as $\mathbf{F}$, cf. [107, 113]

$$\mathrm{d}\mathbf{x} \;=\; \mathrm{Grad}\,\boldsymbol{\chi}(\mathbf{X},t)\cdot\mathrm{d}\mathbf{X} \;=\; \mathbf{F}\cdot\mathrm{d}\mathbf{X}, \tag{2.4}$$

or the so-called deformation gradient

$$\mathbf{F} \;=\; \mathrm{Grad}\,\boldsymbol{\chi}(\mathbf{X},t) \;=\; \frac{\partial\mathbf{x}}{\partial\mathbf{X}}. \tag{2.5}$$

It is to mention that the deformation gradient is in general an unsymmetric tensor. For an undeformed configuration, the deformation gradient becomes the identity tensor

$$\mathrm{Grad}\,\mathbf{X} \;=\; \frac{\partial\mathbf{X}}{\partial\mathbf{X}} \;=\; \mathbf{I}. \tag{2.6}$$

With the definition of the displacement given in Eq. (2.3), the deformation tensor can be computed as

$$\mathbf{F} \;=\; \frac{\partial\mathbf{x}}{\partial\mathbf{X}} \;=\; \frac{\partial(\mathbf{X}+\mathbf{u})}{\partial\mathbf{X}} \;=\; \mathbf{I}+\mathrm{Grad}\,\mathbf{u} \tag{2.7}$$

and its inverse $\mathbf{F}^{-1}$ as

$$\mathbf{F}^{-1} \;=\; \frac{\partial(\mathbf{x}-\mathbf{u})}{\partial\mathbf{x}} \;=\; \mathbf{I}-\mathrm{grad}\,\mathbf{u}, \tag{2.8}$$

with the gradient

$$\mathrm{grad}\,\mathbf{X} \;=\; \frac{\partial\mathbf{X}}{\partial\mathbf{x}}. \tag{2.9}$$

The Jacobi-determinant is defined as the determinant of the deformation tensor $\mathbf{F}$

$$J \;=\; \det\frac{\partial\mathbf{x}}{\partial\mathbf{X}}; \tag{2.10}$$

the Jacobi-determinant describes about the volume change with $J=\rho_0/\rho$; for an incompressible material for instance, the Jacobi-determinant is equal to 1.

The first derivative of the position of the point X in the current configuration with respect to the time gives the velocity $\mathbf{v}$

$$\dot{\mathbf{x}}(\mathbf{X},t) \;=\; \frac{\mathrm{d}\boldsymbol{\chi}(\mathbf{X},t)}{\mathrm{d}t} \;=\; \mathbf{v}(\mathbf{X},t), \tag{2.11}$$

and the second derivative the acceleration $\mathbf{a}$

$$\ddot{\mathbf{x}}(\mathbf{X},t) \;=\; \frac{\mathrm{d}^2\boldsymbol{\chi}(\mathbf{X},t)}{\mathrm{d}t^2} \;=\; \mathbf{a}(\mathbf{X},t). \tag{2.12}$$

Both derivatives are described as material derivatives, because they are defined for a single fixed material point X. In continuum mechanics, two possible description exist: the first

one is the material or Lagrangean description, where the position of one point will be followed during the time, cf. [41], with

$$\mathbf{a} = \tilde{\mathbf{a}}(\mathbf{X}, t). \tag{2.13}$$

The symbol $\tilde{\cdot}$ is used to differentiate the function $\tilde{\mathbf{a}}$ from the acceleration itself. The second possible description is the spatial or Eulerian description, where the focus is made on the observation of a spatial area and the passing of particles going through the area, cf. [42]

$$\mathbf{a} = \tilde{\tilde{\mathbf{a}}}(\mathbf{x}, t). \tag{2.14}$$

The material description is used for the description of a solid body; on the contrary, the spatial description finds application in fluid mechanics. In order to describe the behaviour of an hybrid laminate, the material or Lagrangean description is followed.

A surface element is described by the outer product of two non parallel line elements $\mathrm{d}\mathbf{X}_1$ and $\mathrm{d}\mathbf{X}_2$ in the undeformed configuration and, respectively, $\mathrm{d}\mathbf{x}_1$ and $\mathrm{d}\mathbf{x}_2$ in the deformed configuration with

$$\begin{aligned} \mathrm{d}\mathbf{A} &= \mathrm{d}\mathbf{X}_1 \times \mathrm{d}\mathbf{X}_2, \\ \mathrm{d}\mathbf{a} &= \mathrm{d}\mathbf{x}_1 \times \mathrm{d}\mathbf{x}_2. \end{aligned} \tag{2.15}$$

The definition of the deformation gradient (2.5) can be used to draw the relation between the surface element in the reference configuration and the surface element in the current configuration with

$$\mathrm{d}\mathbf{a} = (\mathbf{F} \cdot \mathrm{d}\mathbf{X}_1) \times (\mathbf{F} \cdot \mathrm{d}\mathbf{X}_2) = (\det \mathbf{F})\, \mathbf{F}^{T-1} \cdot \mathrm{d}\mathbf{A}. \tag{2.16}$$

In a similar way, the mixed product of three material line elements defines the volume element in both configuration

$$\begin{aligned} \mathrm{d}V &= (\mathrm{d}\mathbf{X}_1 \times \mathrm{d}\mathbf{X}_2) \cdot \mathrm{d}\mathbf{X}_3, \\ \mathrm{d}v &= (\mathrm{d}\mathbf{x}_1 \times \mathrm{d}\mathbf{x}_2) \cdot \mathrm{d}\mathbf{x}_3. \end{aligned} \tag{2.17}$$

As for the areas, the deformation gradient can be introduced

$$\mathrm{d}v = ((\mathbf{F} \cdot \mathrm{d}\mathbf{x}_1) \times (\mathbf{F} \cdot \mathrm{d}\mathbf{x}_2)) \cdot (\mathbf{F} \cdot \mathrm{d}\mathbf{x}_3), \tag{2.18}$$

and with the definition of its determinant as

$$\det \mathbf{F} = \frac{((\mathbf{F} \cdot \mathrm{d}\mathbf{x}_1) \times (\mathbf{F} \cdot \mathrm{d}\mathbf{x}_2)) \cdot (\mathbf{F} \cdot \mathrm{d}\mathbf{x}_3)}{(\mathrm{d}\mathbf{X}_1 \times \mathrm{d}\mathbf{X}_2) \cdot \mathrm{d}\mathbf{X}_3}, \tag{2.19}$$

the relation for a volume element between undeformed and deformed configuration becomes

$$\mathrm{d}v = (\det \mathbf{F})\, \mathrm{d}V. \tag{2.20}$$

As a matter of fact, the deformation gradient is not convenient to illustrate the deformations applied to a body, because it contains both deformation and rotation, cf. [4, 41].

For this reason, it can be useful to decompose it in an unique way in an orthogonal and in a symmetric positive definite tensor

$$\mathbf{F} = \mathbf{R} \cdot \mathbf{U} = \mathbf{V} \cdot \mathbf{R}. \tag{2.21}$$

$\mathbf{R}$ describes the rotation and is a proper orthogonal tensor, defined as

$$\mathbf{R} \cdot \mathbf{R}^T = \mathbf{I}, \quad \det \mathbf{R} = +1. \tag{2.22}$$

$\mathbf{U}$ and respectively $\mathbf{V}$ describes the translation and are symmetric positive definite tensors

$$\mathbf{U} = \mathbf{U}^T, \quad \mathbf{V} = \mathbf{V}^T. \tag{2.23}$$

$\mathbf{U}$ is called the right stretch tensor and $\mathbf{V}$ the left stretch tensor, respectively. $\mathbf{U}$ and $\mathbf{V}$ have the same eigen vectors and the same eigen values. However, the computation of $\mathbf{U}$ and $\mathbf{V}$ is extremely expensive, because it requires the computation of an eigen problem. For these reasons, the square value of a material line is introduced as

$$\mathrm{d}S^2 = \mathrm{d}\mathbf{X} \cdot \mathrm{d}\mathbf{X}, \tag{2.24}$$

for the reference configuration and

$$\mathrm{d}s^2 = \mathrm{d}\mathbf{x} \cdot \mathrm{d}\mathbf{x} = (\mathbf{F} \cdot \mathrm{d}\mathbf{X}) \cdot (\mathbf{F} \cdot \mathrm{d}\mathbf{X}) = \mathrm{d}\mathbf{X} \cdot \mathbf{C} \cdot \mathrm{d}\mathbf{X}, \tag{2.25}$$

for the current configuration. It defines then the right Cauchy-Green deformation tensor $\mathbf{C}$ as

$$\mathbf{C} = \mathbf{F}^T \cdot \mathbf{F}. \tag{2.26}$$

Further transformation of the right Cauchy-Green tensor leads to a relation with the stretch tensor $\mathbf{U}$ as

$$\begin{aligned} \mathbf{C} &= \mathbf{F}^T \cdot \mathbf{F} = (\mathbf{R} \cdot \mathbf{U})^T \cdot (\mathbf{R} \cdot \mathbf{U}) \\ &= \mathbf{U}^T \cdot \mathbf{R}^T \cdot \mathbf{R} \cdot \mathbf{U} = \mathbf{U} \cdot \mathbf{U} = \mathbf{U}^2. \end{aligned} \tag{2.27}$$

In a similar way, the left Cauchy-Green deformation tensor $\mathbf{B}$ can be introduced as

$$\mathrm{d}S^2 = \mathrm{d}\mathbf{X} \cdot \mathrm{d}\mathbf{X} = (\mathbf{F}^{-1} \cdot \mathrm{d}\mathbf{x}) \cdot (\mathbf{F}^{-1} \cdot \mathrm{d}\mathbf{x}) = \mathrm{d}\mathbf{x} \cdot \mathbf{B}^{-1} \cdot \mathrm{d}\mathbf{x}. \tag{2.28}$$

It follows that

$$\mathbf{B}^{-1} = \mathbf{F}^{T-1} \cdot \mathbf{F}^{-1} \Leftrightarrow \mathbf{B} = \mathbf{F} \cdot \mathbf{F}^T. \tag{2.29}$$

Further transformations of $\mathbf{B}$ lead to

$$\mathbf{B} = \mathbf{F} \cdot \mathbf{F}^T = \mathbf{V} \cdot \mathbf{R} \cdot \mathbf{R}^T \cdot \mathbf{V} = \mathbf{V}^2. \tag{2.30}$$

It is to notice that in the undeformed state, the deformation tensor, the right and left Cauchy-Green tensor are equal to the tensor identity

$$\mathbf{F} = \mathbf{I} \Leftrightarrow \mathbf{C} = \mathbf{B} = \mathbf{I}. \tag{2.31}$$

It is convenient to define the strain by the difference between the deformed and undeformed deformation state

$$\mathrm{d}s^2 - \mathrm{d}S^2 \;=\; \mathrm{d}\mathbf{x}\cdot\mathrm{d}\mathbf{x} - \mathrm{d}\mathbf{X}\cdot\mathrm{d}\mathbf{X}. \tag{2.32}$$

Further transformations of Eq. (2.32) lead to the definition of the Green-Lagrangean strain tensor $\mathbf{E}$ in the reference configuration

$$\mathrm{d}s^2 - \mathrm{d}S^2 \;=\; \mathrm{d}\mathbf{X}\cdot\mathbf{C}\cdot\mathrm{d}\mathbf{X} - \mathrm{d}\mathbf{X}\cdot\mathrm{d}\mathbf{X} \;=\; \mathrm{d}\mathbf{X}\cdot(\mathbf{C}-\mathbf{I})\cdot\mathrm{d}\mathbf{X}, \tag{2.33}$$

with

$$\mathbf{E} \;=\; \frac{1}{2}(\mathbf{C}-\mathbf{I}). \tag{2.34}$$

In the expression of a constitutive law, it can be useful to use $\mathbf{E}$ and not $\mathbf{F}$, because in the undeformed configuration, the Green-Lagrangean strain tensor $\mathbf{E}$ is equal to $\mathbf{0}$ whereas $\mathbf{F}$ is equal to the identity tensor $\mathbf{I}$. In a similar way, the Euler-Almansi strain tensor can be defined, if the definition of the line element in the current reference is given as a function of the line element in the reference configuration

$$\mathrm{d}s^2 - \mathrm{d}S^2 \;=\; \mathrm{d}\mathbf{x}\cdot(\mathbf{I}-\mathbf{B}^{-1})\cdot\mathrm{d}\mathbf{x} \;=\; \mathrm{d}\mathbf{x}\cdot 2\,\mathbf{A}\cdot\mathrm{d}\mathbf{x}. \tag{2.35}$$

The Almansi tensor is then written as

$$\mathbf{A} \;=\; \frac{1}{2}(\mathbf{I}-\mathbf{B}^{-1}). \tag{2.36}$$

Due to further transformations of the Green-Lagrangean strain tensor $\mathbf{E}$

$$\begin{aligned}\mathbf{E} \;&=\; \frac{1}{2}(\mathbf{F}^T\cdot\mathbf{F}-\mathbf{I}) \;=\; \frac{1}{2}((\mathbf{I}+\mathrm{Grad}\,\mathbf{u})^T\cdot(\mathbf{I}+\mathrm{Grad}\,\mathbf{u})-\mathbf{I}),\\ \mathbf{E} \;&=\; \frac{1}{2}(\mathrm{Grad}^T\,\mathbf{u}+\mathrm{Grad}\,\mathbf{u}+\mathrm{Grad}^T\,\mathbf{u}\cdot\mathrm{Grad}\,\mathbf{u})\end{aligned} \tag{2.37}$$

and in a similar way for the Euler-Almansi strain tensor $\mathbf{A}$

$$\mathbf{A} \;=\; \frac{1}{2}(\mathbf{I}-\mathbf{F}^{T-1}\cdot\mathbf{F}^{-1}) \;=\; \frac{1}{2}(\mathrm{grad}\,\mathbf{u}+\mathrm{grad}^T\,\mathbf{u}+\mathrm{grad}^T\,\mathbf{u}\cdot\mathrm{grad}\,\mathbf{u}), \tag{2.38}$$

the linearisation of both Green-Lagrangean and Euler-Almansi strain tensors for small deformation gives the value of the engineering strain in the linear case

$$\boldsymbol{\varepsilon} \;=\; \frac{1}{2}(\mathrm{Grad}\,\mathbf{u}+\mathrm{Grad}^T\,\mathbf{u}). \tag{2.39}$$

The linear deformation theory can be interpreted as a particular case of the continuum mechanics, because for small displacements, small displacement gradients and small rotations, we have $\boldsymbol{\varepsilon}\approx\mathbf{E}\approx\mathbf{A}$ and $\mathrm{Grad}\,\mathbf{u}\approx\mathrm{grad}\,\mathbf{u}$.

The rate of change of a material line element defines the relative velocity of two neighbouring material points X and Y

$$(\mathrm{d}\mathbf{x})^{\cdot} \;=\; (\mathbf{F}\cdot\mathrm{d}\mathbf{X})^{\cdot} \;=\; \dot{\mathbf{F}}\cdot\mathrm{d}\mathbf{X}, \tag{2.40}$$

because the time change of the line element in the reference configuration vanishes. The material velocity gradient is defined as

$$\operatorname{Grad} \mathbf{v} \;=\; \dot{\mathbf{F}}(\mathbf{X}, t). \tag{2.41}$$

Using the definition of the deformation gradient (2.5), Eq. (2.40) becomes

$$(\mathrm{d}\mathbf{x})^{\cdot} \;=\; \dot{\mathbf{F}} \cdot \mathbf{F}^{-1} \cdot \mathrm{d}\mathbf{x} \;=\; \mathbf{L} \cdot \mathrm{d}\mathbf{x}, \tag{2.42}$$

and the spatial velocity gradient is defined as

$$\mathbf{L} \;=\; \dot{\mathbf{F}} \cdot \mathbf{F}^{-1}. \tag{2.43}$$

The spatial deformation gradient can be split in a symmetric part and in a skew part

$$\mathbf{L} \;=\; \mathbf{D} + \mathbf{W}, \tag{2.44}$$

where $\mathbf{D} = \mathbf{D}^T$ is the symmetric part and it is called the deformation velocity

$$\mathbf{D} \;=\; \frac{1}{2}(\mathbf{L} + \mathbf{L}^T) \;=\; \mathbf{D}^T. \tag{2.45}$$

$\mathbf{W} = -\mathbf{W}^T$ is the skew part or called the spin tensor

$$\mathbf{W} \;=\; \frac{1}{2}(\mathbf{L} - \mathbf{L}^T) \;=\; -\mathbf{W}^T. \tag{2.46}$$

$\mathbf{W}$ describes the rotation velocity of the deformation tensor's principal axis, cf. [73].

2.2 Balance Relations

The kinematics describe the deformations and the geometry of motion and can be considered independently from the material behaviour or from the applied loading. The influence of the "outside world", cf. [73], is taken into account in the balance relations, which are described in this part. Because of the considered issue, the balance relations are firstly developed in the thermo-mechanical case, and the section is restricted afterwards to thermo-mechanical problems and does not include any magnetic or electric properties.

2.2.1 Balance of Mass

The mass is basically defined as the integration of the density over the volume of the body $\mathcal{B}$ with

$$m \;=\; \int_{\mathcal{V}} \rho \, \mathrm{d}v, \tag{2.47}$$

where the volume of the body is defined as $\mathcal{V}$ and its surface as $\mathcal{A}$. The time change of the mass must be zero, because the mass stays constant during the time. This axiom leads to the formulation

$$\frac{\mathrm{d}}{\mathrm{d}t} \int_{\mathcal{V}} \rho \, \mathrm{d}v \;=\; 0. \tag{2.48}$$

In order to obtain the local balance, the order of the time derivative and the integral has to be changed. To do so, the integral over the initial volume is introduced. This is not influenced by any temporal change, as illustrated in [41]

$$\frac{\mathrm{d}}{\mathrm{d}t}\left(\int_{\mathcal{V}_0} \rho \, \det \mathbf{F} \, \mathrm{d}V\right) \;=\; \int_{\mathcal{V}_0} \frac{\mathrm{d}}{\mathrm{d}t}\left(\rho \, \det \mathbf{F}\right) \mathrm{d}V \;=\; 0, \tag{2.49}$$

and $\mathcal{V}_0$ describes the initial volume of the body or its volume at a time $t = t_0$. Further transformations lead to

$$\int_{\mathcal{V}_0} \left(\dot{\rho} \, \det \mathbf{F} + \rho \, \frac{\mathrm{d}}{\mathrm{d}t}[\det \mathbf{F}]\right) \mathrm{d}V \;=\; \int_{\mathcal{V}} \left(\dot{\rho} + \rho \, \operatorname{div} \mathbf{v}\right) \mathrm{d}v \;=\; 0. \tag{2.50}$$

Within further transformations using the material time derivative of the density

$$\dot{\rho} \;=\; \frac{\mathrm{d}\rho}{\mathrm{d}t} \;=\; \frac{\partial \rho}{\partial t} + \operatorname{grad} \rho \cdot \mathbf{v}, \tag{2.51}$$

and the product rule, the Eq. (2.50) can be written in its local form as

$$\frac{\partial \rho}{\partial t} + \operatorname{div}(\rho \mathbf{v}) \;=\; 0. \tag{2.52}$$

Integration in time yields to the relation between the current density and its initial value

$$\rho \;=\; \rho_0 \left(\det \mathbf{F}\right)^{-1}. \tag{2.53}$$

2.2.2 Balance of Momentum

Basically, the balance of momentum describes the time change of the momentum as set by the third axiom of Newton. It says that the resulting forces applied to a body cause a change of the momentum

$$\dot{\mathbf{l}} \;=\; \mathbf{f}. \tag{2.54}$$

The momentum $\mathbf{l}$ of a material body $\mathcal{V}$ is defined with its velocity and density

$$\mathbf{l} \;=\; \mathbf{l}(\mathcal{V}, t) \;=\; \int_{\mathcal{V}} \dot{\mathbf{x}} \, \mathrm{d}m \;=\; \int_{\mathcal{V}} \rho \, \dot{\mathbf{x}} \, \mathrm{d}v. \tag{2.55}$$

The applied forces are defined as the sum of the forces applied to its surface ($\mathbf{t}$) and the force density ($\rho \, \mathbf{b}$), like for instance the gravity

$$\mathbf{f} \;=\; \int_{\mathcal{A}} \mathbf{t} \, \mathrm{d}a + \int_{\mathcal{V}} \rho \, \mathbf{b} \, \mathrm{d}v. \tag{2.56}$$

After transformation using the Cauchy theorem $\mathbf{t} = \mathbf{T} \cdot \mathbf{n}$, the balance of momentum becomes

$$\frac{\mathrm{d}}{\mathrm{d}t} \int_{\mathcal{V}} \rho \, \dot{\mathbf{x}} \, \mathrm{d}v \;=\; \int_{\mathcal{A}} \mathbf{T} \cdot \mathbf{n} \, \mathrm{d}a + \int_{\mathcal{V}} \rho \, \mathbf{b} \, \mathrm{d}v, \tag{2.57}$$

with $\mathbf{T}$ defined as the Cauchy stress. A further transformation of the time derivative of the velocity can be applied as

$$\frac{\mathrm{d}}{\mathrm{d}t}\int_{\mathcal{V}} \rho\,\dot{\mathbf{x}}\,\mathrm{d}v \;=\; \int_{\mathcal{V}} \rho\,\ddot{\mathbf{x}}\,\mathrm{d}v. \tag{2.58}$$

With the use of the divergence theorem in the current configuration and excluding the problem of shock waves, the local form of the balance of momentum can be written as

$$\rho\,\ddot{\mathbf{x}} \;=\; \operatorname{div}\mathbf{T} + \rho\,\mathbf{b}. \tag{2.59}$$

Further transformations, as explained in [41], lead to the local form of the balance of momentum in the reference configuration

$$\rho_0\,\frac{\mathrm{d}^2\mathbf{x}}{\mathrm{d}t^2} \;=\; \operatorname{Div}\mathbf{P} + \rho_0\,\mathbf{b}, \tag{2.60}$$

with $\mathbf{x}$ the position of a point in the actual configuration. $\mathbf{P}$ is the first Piola-Kirchhoff stress tensor and it is defined as

$$\mathbf{P} \;=\; (\det\mathbf{F})\,\mathbf{T}\cdot\mathbf{F}^{T-1}. \tag{2.61}$$

Whereas the Cauchy stress $\mathbf{T}$ is related to the applied forces in a surface element $\mathrm{d}\mathbf{a}$ in the current configuration, the first Piola-Kirchhoff stress is related to the same applied forces, but in relation with a surface element $\mathrm{d}\mathbf{A}$ in the reference configuration. The Cauchy stress $\mathbf{T}$ is symmetric, whereas the first Piola-Kirchhoff is generally non-symmetric.

In the linear deformation theory, the stress is also not depending on a specific configuration (because they are approximately similar), and only the Cauchy stress is generally used. In this work, the Cauchy stress for the linear deformation theory is also written as $\boldsymbol{\sigma}$, in order to differentiate it from the Cauchy stress $\mathbf{T}$ for finite deformations.

2.2.3 Balance of Moment of Momentum

If no body torque and no surface torque are applied, the moment of momentum is defined as

$$\mathbf{h}_p \;=\; \int_{\mathcal{V}} \mathbf{x}\times\rho\,\mathbf{v}\,\mathrm{d}v \tag{2.62}$$

and its change is caused by the moment applied to the body as

$$\dot{\mathbf{h}}_p \;=\; \mathbf{m}_p. \tag{2.63}$$

Similarly as for the balance of momentum, we get the balance of moment of momentum

$$\frac{\mathrm{d}}{\mathrm{d}t}\int_{\mathcal{V}} (\rho\,\mathbf{x}\times\dot{\mathbf{x}})\,\mathrm{d}v \;=\; \int_{\mathcal{A}} (\mathbf{x}\times\mathbf{t})\,\mathrm{d}a + \int_{\mathcal{V}} (\mathbf{x}\times\rho\,\mathbf{b})\,\mathrm{d}v. \tag{2.64}$$

Further transformation of Eq. (2.64) leads to

$$\int_{\mathcal{V}} [\mathbf{x} \times (\rho\, \ddot{\mathbf{x}} - \operatorname{div} \mathbf{T} - \rho\, \mathbf{b}) + \mathbf{I} \times \mathbf{T}]\, \mathrm{d}v \;=\; \mathbf{0} \tag{2.65}$$

Because of the balance of momentum, given in Eq. (2.59), the former Eq. (2.65) can be reduced to

$$\mathbf{I} \times \mathbf{T} \;=\; \mathbf{0}. \tag{2.66}$$

Consequently, the Cauchy stress tensor is symmetric

$$\mathbf{T} \;=\; \mathbf{T}^T. \tag{2.67}$$

2.2.4 Balance of Energy or First Law of Thermodynamics

The balance of energy, also called the first law of thermodynamics, describes the energetic state for any volume of the body. The energy density is defined as the sum of the kinetic and the internal energy, cf. [4, 41, 43, 73]

$$e \;=\; \int_{\mathcal{V}} (\rho\, \varepsilon + \frac{1}{2}\, \rho\, \dot{\mathbf{x}} \cdot \dot{\mathbf{x}})\, \mathrm{d}v \;=\; U + K, \tag{2.68}$$

with the kinetic energy K

$$K \;=\; \frac{1}{2} \int_{\mathcal{V}} (\rho\, \dot{\mathbf{x}} \cdot \dot{\mathbf{x}})\, \mathrm{d}v, \tag{2.69}$$

and the internal energy U

$$U \;=\; \int_{\mathcal{V}} \rho\, \varepsilon\, \mathrm{d}v. \tag{2.70}$$

ε is the specific internal energy. The first law of thermodynamics describes the temporal change of the energy e, which can be caused by a heat or a mechanical power

$$\frac{\mathrm{d}}{\mathrm{d}t}(U + K) \;=\; P + Q. \tag{2.71}$$

The mechanical power P is defined as

$$P \;=\; \int_{\mathcal{A}} \dot{\mathbf{x}} \cdot \mathbf{t}\, \mathrm{d}a + \int_{\mathcal{V}} \dot{\mathbf{x}} \cdot \rho\, \mathbf{b}\, \mathrm{d}v, \tag{2.72}$$

and the heat power Q as

$$Q \;=\; \int_{\mathcal{A}} -\mathbf{q} \cdot \mathbf{n}\, \mathrm{d}a + \int_{\mathcal{V}} \rho\, r\, \mathrm{d}v, \tag{2.73}$$

where $\mathbf{q}$ is the heat flux and r the heat supply. The balance of energy can be written as

$$\frac{\mathrm{d}}{\mathrm{d}t}\int_{\mathcal{V}}(\rho\,\varepsilon+\frac{1}{2}\rho\,\dot{\mathbf{x}}\cdot\dot{\mathbf{x}})\,\mathrm{d}v\;=\;\int_{\mathcal{A}}(\dot{\mathbf{x}}\cdot\mathbf{t}-\mathbf{q}\cdot\mathbf{n})\,\mathrm{d}a+\int_{\mathcal{V}}(\dot{\mathbf{x}}\cdot\rho\,\mathbf{b}+\rho\,r)\,\mathrm{d}v. \tag{2.74}$$

By further transformation with the divergence theorem, the balance of energy becomes

$$\rho\,\dot{\varepsilon}+\rho\,\ddot{\mathbf{x}}\cdot\dot{\mathbf{x}}\;=\;\mathrm{div}(\dot{\mathbf{x}}\cdot\mathbf{T}-\mathbf{q})+\dot{\mathbf{x}}\cdot\rho\,\mathbf{b}+\rho\,r. \tag{2.75}$$

By multiplication of the balance of momentum (2.59) with $\dot{\mathbf{x}}$ and introduction in the former Eq. (2.75), we can get the balance of internal energy as

$$\rho\,\dot{\varepsilon}\;=\;\mathbf{T}:\mathbf{D}-\mathrm{div}\,\mathbf{q}+\rho\,r, \tag{2.76}$$

cf. [107, 113].

2.2.5 Balance of Entropy or Second Law of Thermodynamics

The second law of thermodynamics states the principle of irreversibly, that means that the "entropy production is never negative", cf. [73]

$$\rho\,\dot{\eta}+\mathrm{div}\left(\frac{\mathbf{q}}{\theta}\right)-\frac{\rho\,r}{\theta}\;=\;\hat{\eta}\geq 0, \tag{2.77}$$

where η is the specific entropy, $\hat{\eta}$ the entropy production and θ the absolute temperature. With the introduction of the Legendre transformation ($\psi=\varepsilon-\theta\,\eta$) and the balance of internal energy (2.76), the balance of entropy gets

$$-\rho\,\dot{\psi}+\rho\,\eta\,\dot{\theta}-\frac{\mathbf{q}}{\theta}\cdot\mathrm{grad}\,\theta+\mathbf{D}:\mathbf{T}\geq 0. \tag{2.78}$$

Eq. (2.78) is known in continuum mechanics as the Clausius-Duhem inequality. In isothermal case, the balance of entropy becomes, for the current configuration

$$-\rho\,\dot{\psi}+\mathbf{D}:\mathbf{T}\geq 0, \tag{2.79}$$

and it is called the Clausius-Planck inequality. The Clausius-Planck inequality can be written in the reference configuration as

$$-\rho_0\,\dot{\psi}+\dot{\mathbf{E}}:\mathbf{S}\geq 0, \tag{2.80}$$

with $\mathbf{S}$ the second Piola-Kirchhoff stress.

In order to describe the behaviour of a material, it can be convenient to know the deformations or stress in both reference and current configuration. To do so, we can use the concept of dual variables, developed by Haupt & Tsakmakis [76], which states that the stress power in the reference configuration must be equal to the stress power in the current configuration

$$\frac{1}{\rho_0}\,\mathbf{S}:\dot{\mathbf{E}}\;=\;\frac{1}{\rho}\,\mathbf{T}:\mathbf{D}. \tag{2.81}$$

With further transformations of Eqs (2.81), a direct relation between the Cauchy stress in the current configuration and the second Piola-Kirchhoff stress in the reference configuration is obtained

$$\mathbf{S} = (\det \mathbf{F})\, \mathbf{F}^{-1} \cdot \mathbf{T} \cdot \mathbf{F}^{-T}. \tag{2.82}$$

It is to mention that both Cauchy stress and second Piola-Kirchhoff stress are symmetric. On the contrary to the Cauchy stress, the second Piola-Kirchhoff stress has no physical interpretation in terms of forces but it is the power conjugated quantity to $\dot{\mathbf{E}}$.

2.3 Constitutive Equations

The equations set before are independent from the considered material. However, a relation between the stress and the deformation is needed and it is defined with the constitutive equations.

2.3.1 General Considerations

The last part of the chapter "continuum mechanics" is devoted to the description of the material behaviour of materials, firstly developed by Noll in the nineteen sixties and improved in [138]. Any constitutive equations have to follow some general principle, among them the principle of determinism, which states that the current stress state of the material body depends only on the past history of the body's motion, cf. [73]. The principle of local action explains that a state of stress is only determined by the history of motion of the point's environment and not by all body particles. The material objectivity or so-called principle of material frame indifference states that every representation of material properties have to be independent of the frame of reference. Moreover, the constitutive law must not violate the balance equations.

As represented in Fig. 2.2, there are basically four types of material behaviour, defined as material with or without equilibrium hysteresis and as rate dependent or rate independent material, cf. [73]:

- the simplest material law is the one which is rate independent and without equilibrium hysteresis; it is declared as a hyperelastic material;
- a material which is rate independent but has an equilibrium hysteresis is an elasto-plastic material behaviour;
- a rate dependent material without equilibrium hysteresis is a viscoelastic material;
- the latter type is a rate dependent material with hysteresis; it is called an elasto-viscoplastic material or abbreviated as a viscoplastic material.

In Fig. 2.2, the plain lines are characteristics for a material behaviour for an arbitrary rate and the dash lines represent the equilibrium curve, that means that for a slow process, the material behaviour will follow the dash lines. For instance, a viscoelastic material at a slow process shows no hysteresis.

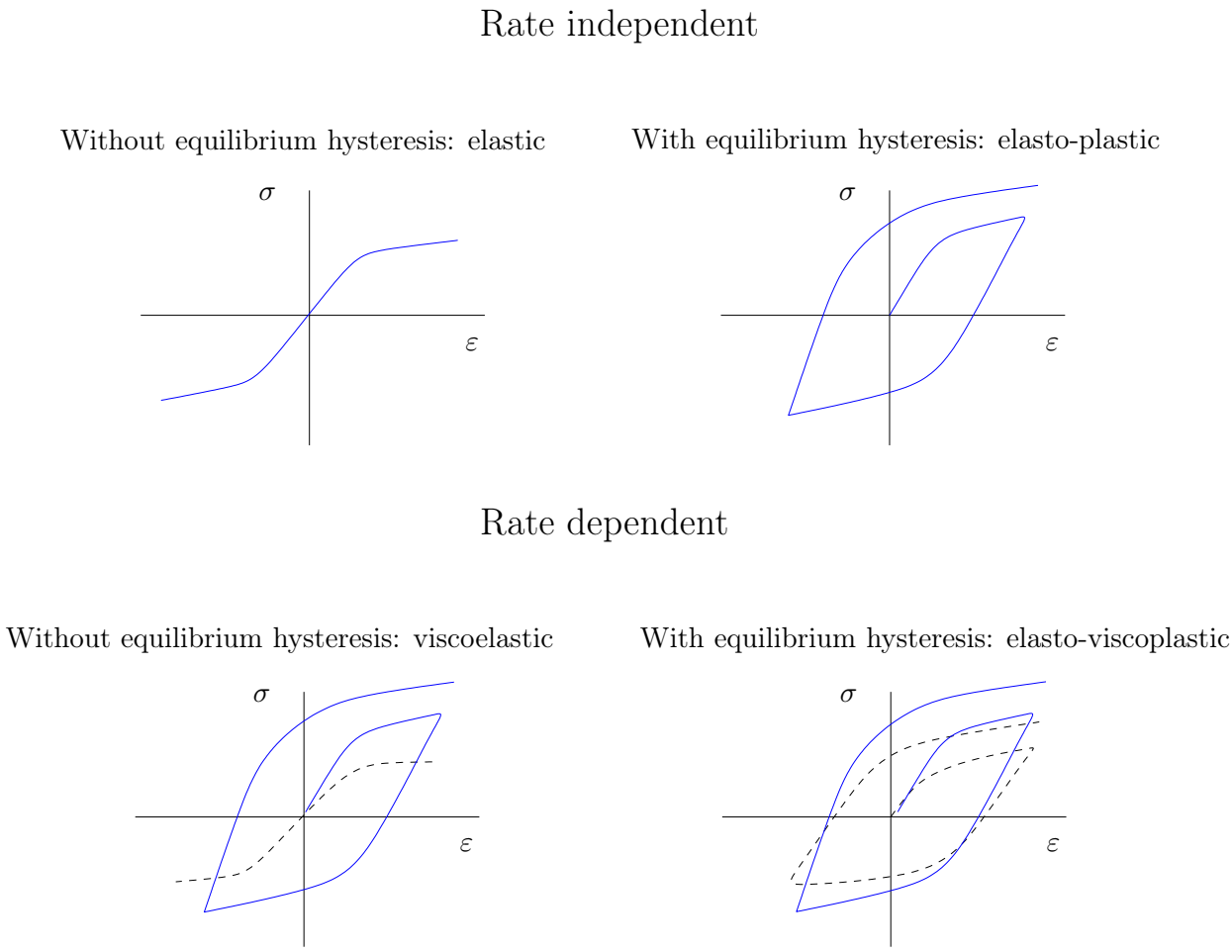

Figure 2.2: Four categories of material behaviour, adapted from Haupt, Continuum Mechanics and Theory of Materials, Springer-Verlag, 2000 [73]

In the present work, the composite material is made of carbon fibers reinforced polymers (CFRP), where the considered polymer is a thermoplastic like Nylon (Polyamide 6.6) or PEEK (Polyether Ether Ketone). Although the thermoplastic can present a viscoelastic behaviour, especially at high temperature, the influence of the viscoelastic part is too small in comparison with the stiffness of the fibers to be considered. For these reasons, the material behaviour corresponding to the carbon fibers reinforced thermoplastic is an anisotropic hyperelastic material, as developed in the subsection 2.3.2.

The composite plates are also made of metal layers which are aluminium or titan alloys. Both show a classical elasto-plastic material behaviour. However, the description of a viscoplastic material behaviour will be explained and implemented; and the elasto-plasticity is considered as a particular case of the viscoplasticity, as developed in subsection 2.3.3.

For both categories of materials, a general description is presented, followed by the detailed description of the chosen model.

2.3.2 Hyperelasticity

Isotropic Hyperelasticity

A hyperelastic material assumes that a free energy function ψ in a form of potential exists [73, 84]

$$\rho_0 \, \psi \; = \; \Psi \; = \; \Psi(\mathbf{C}). \tag{2.83}$$

Because the principle of material objectivity has to be respected, neither the right nor the left Cauchy-Green Deformation tensor are accurate, because the free energy function would be linked to a configuration in this case. To avoid this problem, the invariants are used, because they are independent from the configurations and identical for $\mathbf{B}$ and $\mathbf{C}$. They were first introduced by Rivlin [158] and are defined for a tensor $\mathbf{C}$ as

$$\begin{aligned} \mathrm{I}_{\mathbf{C}} \; &= \; \mathrm{I}_1 \; = \; \mathrm{tr}(\mathbf{C}), \\ \mathrm{II}_{\mathbf{C}} \; &= \; \mathrm{I}_2 \; = \; \frac{1}{2}\left[(\mathrm{tr}\,\mathbf{C})^2 - \mathrm{tr}\,\mathbf{C}^2\right], \\ \mathrm{III}_{\mathbf{C}} \; &= \; \mathrm{I}_3 \; = \; \det \mathbf{C}. \end{aligned} \tag{2.84}$$

Because further invariants are needed in case of anisotropy, we use the notation $\mathrm{I}_1, \mathrm{I}_2, \mathrm{I}_3$ to refer as the first, second and third principal invariant of a tensor. The free energy function depends further on the three first invariants of $\mathbf{C}$, in case of isotropy

$$\Psi \; = \; \Psi(\mathrm{I}_1, \mathrm{I}_2, \mathrm{I}_3). \tag{2.85}$$

By introducing the derivative of the free energy function

$$\dot{\Psi} \; = \; \frac{\partial \Psi(\mathrm{I}_1, \mathrm{I}_2, \mathrm{I}_3)}{\partial \mathbf{C}} : \dot{\mathbf{C}} \tag{2.86}$$

in the Clausius-Planck inequality with respect to the reference configuration (2.80), it leads to

$$\mathbf{S} \; = \; 2 \, \frac{\partial \Psi(\mathrm{I}_1, \mathrm{I}_2, \mathrm{I}_3)}{\partial \mathbf{C}}. \tag{2.87}$$

Using the chain rule of differentiation

$$\mathbf{S} \; = \; 2 \left[\frac{\partial \Psi}{\partial \mathrm{I}_1} \frac{\partial \mathrm{I}_1}{\partial \mathbf{C}} + \frac{\partial \Psi}{\partial \mathrm{I}_2} \frac{\partial \mathrm{I}_2}{\partial \mathbf{C}} + \frac{\partial \Psi}{\partial \mathrm{I}_3} \frac{\partial \mathrm{I}_3}{\partial \mathbf{C}} \right] \tag{2.88}$$

leads to the following expression for the second Piola-Kirchhoff stress

$$\mathbf{S} \; = \; 2 \left[\left(\frac{\partial \Psi}{\partial \mathrm{I}_1} + \mathrm{I}_1 \frac{\partial \Psi}{\partial \mathrm{I}_2} \right) \mathbf{I} - \frac{\partial \Psi}{\partial \mathrm{I}_2} \mathbf{C} + \mathrm{I}_3 \frac{\partial \Psi}{\partial \mathrm{I}_3} \mathbf{C}^{-1} \right]. \tag{2.89}$$

By applying the concept of dual variables (2.81) or by using an similar development from the Clausius-Planck inequality with respect to the current configuration (2.79), the expression of the Cauchy stress can be defined as

$$\mathbf{T} \; = \; 2 \, J^{-1} \left[\left(\frac{\partial \Psi}{\partial \mathrm{I}_1} + \mathrm{I}_1 \frac{\partial \Psi}{\partial \mathrm{I}_2} \right) \mathbf{B} - \frac{\partial \Psi}{\partial \mathrm{I}_2} \mathbf{B}^2 + \mathrm{I}_3 \frac{\partial \Psi}{\partial \mathrm{I}_3} \mathbf{I} \right], \tag{2.90}$$

or similar expressions by using the theorem of Cayley-Hamilton, cf. [84]. In this case, the invariants implicitly refer to $\mathbf{B}$ -although the invariants of $\mathbf{B}$ or $\mathbf{C}$ are the same.

For incompressible materials ($\det \mathbf{C} = \mathrm{I}_3 = 1$), it can be demonstrate that the balance of mass (2.52) leads to a further constraint

$$\operatorname{div} \mathbf{v} \;=\; \mathbf{L} : \mathbf{I} \;=\; \mathbf{D} : \mathbf{I} \;=\; 0, \tag{2.91}$$

which will be introduced in the Clausius-Planck inequality, cf. [41] driving to the Cauchy stress

$$\mathbf{T} \;=\; -p\,\mathbf{I} + 2J^{-1}\,\mathbf{B} \cdot \frac{\partial \rho_0\,\psi(\mathrm{I}_1, \mathrm{I}_2)}{\partial \mathbf{B}}. \tag{2.92}$$

The Lagrangean multiplicator p is identified as the pressure. In order to implement a material behaviour, the stiffness or Jacobian is needed, as explained in [126, 175] for the user subroutine UMAT in ABAQUS®. In order to avoid a slow down of the computations, a numerical tangent should not be used but attempts are made to find an analytical one. In case of hyperelasticity, the stiffness tensor is also the elasticity tensor, and it can be obtain as

$${}^4\mathbb{C} \;=\; 4\,\frac{\partial^2 \Psi}{\partial \mathbf{C}\,\partial \mathbf{C}}, \tag{2.93}$$

cf. [166, 194]. For a free energy function defined as

$$\Psi \;=\; \Psi_1(\mathrm{I}_1) + \Psi_2(\mathrm{I}_2) + \Psi_3(\mathrm{I}_3), \tag{2.94}$$

as it is encountered in most cases, the mixed derivatives[1] of Ψ vanishes and it leads to the reduced expression of ${}^4\mathbb{C}$ as

$$\begin{aligned} {}^4\mathbb{C} \;&=\; 4\left[\left(\frac{\partial^2 \Psi}{\partial \mathbf{I}_1^2} + \mathrm{I}_1^2\,\frac{\partial^2 \Psi}{\partial \mathbf{I}_2^2} + \frac{\partial \Psi}{\partial \mathbf{I}_2}\right)\mathbf{I}\otimes\mathbf{I} - \frac{\partial^2 \Psi}{\partial \mathbf{I}_2^2}\,(\mathbf{C}\otimes\mathbf{I} + \mathbf{I}\otimes\mathbf{C})\right. \\ &+\; \left.\frac{\partial^2 \Psi}{\partial \mathbf{I}_2^2}\,\mathbf{C}\otimes\mathbf{C} + \mathrm{I}_3\left(\mathrm{I}_3\frac{\partial^2 \Psi}{\partial \mathbf{I}_3^2} + \frac{\partial \Psi}{\partial \mathbf{I}_3}\right)\mathbf{C}^{-1}\otimes\mathbf{C}^{-1} - \frac{\partial \Psi}{\partial \mathbf{I}_2}\,\overset{4}{\mathbf{I}} - \frac{\partial \Psi}{\partial \mathbf{I}_3}\mathbf{I}_{\mathbf{C}-1}\right], \end{aligned} \tag{2.95}$$

where $\overset{4}{\mathbf{I}}$ is the fourth order identity tensor defined as $\dfrac{\partial \mathbf{C}}{\partial \mathbf{C}}$ and $\mathbf{I}_{\mathbf{C}-1}$ is defined as $-\dfrac{\partial \mathbf{C}^{-1}}{\partial \mathbf{C}}$; it can be proved by using the theorem of Cayley-Hamilton that is is equal to $\mathbf{C}^{-1}\otimes\mathbf{C}^{-1}$.

Anisotropic Hyperelasticity

In order to describe the carbon fibers reinforced polymer, an anisotropic constitutive law is needed. Lots of biological tissues show a transverse isotropic behaviour; as a result, many researches have been made in this field, cf. [11, 64, 85, 147, 191, 192] or sometimes for composite materials [114]. Because in each layer, the fibers are -at least theoretically- continuously distributed in the matrix and because each fiber is oriented in the same direction and has the same length and properties within one layer, a transverse isotropic

[1] I mean the form $\dfrac{\partial^2 \Psi}{\partial \mathrm{I}_i \partial \mathrm{I}_j} = 0$, for $i \neq j$.

material law, as a specific case of the anisotropy, can be used, cf. [84]. Within this assumption, the bonding of the fibers in the matrix is assumed to be perfect.

In case of anisotropy, the stress depends equally from the fibers orientation; consequently, we introduce preferred directions. For a transverse isotropic material, which contains only one family of fibers, there is only one preferred direction called the fiber direction $\mathbf{a}_0$ in the reference configuration, cf. [84]. In the current configuration, the preferred direction becomes $\mathbf{a}$; the fiber direction vectors in both configuration are normalized

$$|\mathbf{a}_0| \;=\; 1, \qquad |\mathbf{a}| \;=\; 1. \tag{2.96}$$

Because of the possibility for the fibers to elongate, we define the stretch λ along the direction $\mathbf{a}_0$ as

$$\lambda\, \mathbf{a}(\mathbf{x},t) \;=\; \mathbf{F}(\mathbf{x},t)\cdot \mathbf{a}_0(\mathbf{X}), \tag{2.97}$$

which means that the stretch defines the ratio between the fibers length in the undeformed and deformed configuration. The square value of the stretch is given as the following expression,

$$\lambda^2 \;=\; \mathbf{a}_0\cdot\mathbf{F}^T\cdot\mathbf{F}\cdot\mathbf{a}_0 \;=\; \mathbf{a}_0\cdot\mathbf{C}\cdot\mathbf{a}_0, \tag{2.98}$$

because the fiber direction vectors are normalized. Similarly as for an isotropic hyperelastic material, a transverse isotropic material assumes the existence of a free energy function depending of the invariants. The extra invariants, needed for the description of the anisotropy, are introduced by an arbitrary product of the fiber direction and the Cauchy-Green tensor and are called "mixed invariants", cf. [16], in order to differentiate them from the "classical" principal invariants $\mathrm{I}_1, \mathrm{I}_2, \mathrm{I}_3$. Because of the normalization of the fiber direction, the invariants only involving the fiber direction cannot be differentiated and the following mixed invariants using the fibers direction and the Cauchy-Green tensor are built

$$\mathrm{I}_4 \;=\; \mathbf{a}_0\cdot\mathbf{C}\cdot\mathbf{a}_0, \qquad \mathrm{I}_5 \;=\; \mathbf{a}_0\cdot\mathbf{C}\cdot\mathbf{C}\cdot\mathbf{a}_0, \tag{2.99}$$

and the condition of polyconvexity is verified if $\mathrm{I}_4 > 0$, cf. [149, 169, 170]. For further discussion about mixed invariants and polyconvexity, the reader is referred to [169, 170, 174, 187, 188, 189, 190]. The constitutive equation is expressed similarly as for the isotropic hyperelastic material as

$$\mathbf{S} \;=\; 2\,\frac{\partial \Psi(\mathrm{I}_1,\mathrm{I}_2,\mathrm{I}_3,\mathrm{I}_4,\mathrm{I}_5)}{\partial \mathbf{C}}. \tag{2.100}$$

With the derivatives of the mixed invariant

$$\frac{\partial \mathrm{I}_4}{\partial \mathbf{C}} \;=\; \mathbf{a}_0\otimes\mathbf{a}_0; \qquad \frac{\partial \mathrm{I}_5}{\partial \mathbf{C}} \;=\; \mathbf{a}_0\otimes\mathbf{C}\cdot\mathbf{a}_0 + \mathbf{a}_0\cdot\mathbf{C}\otimes\mathbf{a}_0, \tag{2.101}$$

the constitutive law in the reference configuration for a transverse isotropic material becomes

$$\begin{aligned}\mathbf{S} \;&=\; 2\left[\left(\frac{\partial\Psi}{\partial \mathrm{I}_1} + \mathrm{I}_1\,\frac{\partial\Psi}{\partial \mathrm{I}_2}\right)\mathbf{I} - \frac{\partial\Psi}{\partial \mathrm{I}_2}\,\mathbf{C} + \mathrm{I}_3\frac{\partial\Psi}{\partial \mathrm{I}_3}\,\mathbf{C}^{-1}\right.\\ &+\; \left.\mathrm{I}_4\,\frac{\partial\Psi}{\partial \mathrm{I}_4}\,\mathbf{a}_0\otimes\mathbf{a}_0 + \frac{\partial\Psi}{\partial \mathrm{I}_5}\,(\mathbf{a}_0\otimes\mathbf{C}\cdot\mathbf{a}_0 + \mathbf{a}_0\cdot\mathbf{C}\otimes\mathbf{a}_0)\right].\end{aligned} \tag{2.102}$$

The constitutive law in the current configuration can be obtained with the concept of dual variables

$$\begin{aligned}\mathbf{T} &= 2\left[\left(\frac{\partial\Psi}{\partial \mathrm{I}_1}+\mathrm{I}_1\frac{\partial\Psi}{\partial \mathrm{I}_2}\right)\mathbf{B}-\frac{\partial\Psi}{\partial \mathrm{I}_2}\mathbf{B}^2+\mathrm{I}_3\frac{\partial\Psi}{\partial \mathrm{I}_3}\mathbf{I}\right.\\ &+ \left.\mathrm{I}_4\frac{\partial\Psi}{\partial \mathrm{I}_4}\mathbf{a}\otimes\mathbf{a}+\frac{\partial\Psi}{\partial \mathrm{I}_5}\left(\mathbf{a}\otimes\mathbf{B}\cdot\mathbf{a}+\mathbf{a}\cdot\mathbf{B}\otimes\mathbf{a}\right)\right]. \end{aligned} \tag{2.103}$$

It is to notice that a volumetric deviatoric split is also possible, in the scope of anisotropic hyperelasticity [46, 85] or anisotropic thin shells [45]. Further development to incorporate orthotropy are possible, among them [125, 166, 185]. In the scope of this work, we are restrained to hyperelasticity; the reader can refer to further work for isotropic viscoelasticity [37, 38, 75, 83, 155, 171], for anisotropic viscoelasticity [141] or for damage [167].

In case of a numerical homogenisation, the deformations are projected to a three-dimensional FE problem. The numerical homogenisation method for composite plates can be successfully employed for finite deformations. However, in the scope of the presented work, this method is applied to small deformations. Therefore, a practical example of an anisotropic constitutive law for small deformations is given. For small strains, the first and second Piola-Kirchhoff stresses are approximately equal to the Cauchy stress and the stress tensor can be written as $\boldsymbol{\sigma}\approx\mathbf{T}\approx\mathbf{S}$, as for the strains $\boldsymbol{\varepsilon}\approx\mathbf{E}\approx\mathbf{A}$.

The free energy function has the form

$$\begin{aligned}\Psi(\boldsymbol{\varepsilon},\mathbf{a}) &= \frac{1}{2}\lambda\left(\operatorname{tr}\boldsymbol{\varepsilon}\right)^2+\mu_T\,\operatorname{tr}\boldsymbol{\varepsilon}^2+\alpha\left(\mathbf{a}\cdot\boldsymbol{\varepsilon}\cdot\mathbf{a}\right)\operatorname{tr}\boldsymbol{\varepsilon}\\ &+ 2\left(\mu_L-\mu_T\right)\left(\mathbf{a}\cdot\boldsymbol{\varepsilon}^2\cdot\mathbf{a}\right)+\frac{1}{2}\beta\left(\mathbf{a}\cdot\boldsymbol{\varepsilon}\cdot\mathbf{a}\right)^2 \end{aligned} \tag{2.104}$$

cf. [166]. The stress is obtained by the derivative of the free energy function as

$$\begin{aligned}\boldsymbol{\sigma} &= \frac{\partial\Psi(\boldsymbol{\varepsilon},\mathbf{a})}{\partial\boldsymbol{\varepsilon}}=\lambda\,\operatorname{tr}(\boldsymbol{\varepsilon})\mathbf{I}+2\,\mu_T\,\boldsymbol{\varepsilon}+\alpha\left[\operatorname{tr}\boldsymbol{\varepsilon}\,\mathbf{a}\otimes\mathbf{a}+\left(\mathbf{a}\cdot\boldsymbol{\varepsilon}\cdot\mathbf{a}\right)\mathbf{I}\right]\\ &+ 2\left(\mu_L-\mu_T\right)\left(\mathbf{a}\otimes\boldsymbol{\varepsilon}\cdot\mathbf{a}+\mathbf{a}\cdot\boldsymbol{\varepsilon}\otimes\mathbf{a}\right)+\beta\left(\mathbf{a}\cdot\boldsymbol{\varepsilon}\cdot\mathbf{a}\right)\mathbf{a}\otimes\mathbf{a}. \end{aligned} \tag{2.105}$$

The model contains five parameters, namely λ, μ_T, μ_L, α and β.

In continuum mechanics[2], the fourth-order elasticity tensor contains $3\times3\times3\times3=81$ items. However, it can be convenient to use the Voigt notation (appendix 7.1), in order to enable an easiest representation of the elasticity tensor. Using the Voigt notation, the stresses and strains, which are tensors of second order for the continuum mechanics and contains each $3\times3=9$ items, are reduced to vectors containing six items, due to symmetry. Consequently, the elasticity tensor can be expressed as a tensor of second order containing 6×6 items, due to minor symmetries $\mathbb{C}_{ijkl}=\mathbb{C}_{jikl}=\mathbb{C}_{ijlk}$ and to major symmetries $\mathbb{C}_{ijkl}=\mathbb{C}_{klij}$, cf. [84]. It is to mention that in the Voigt notation, the elasticity tensor is normally defined with the bold letter $\mathbf{C}$; however, in order to avoid confusion with the right Cauchy-Green deformation tensor, the letter $\mathbb{C}$ is used instead. For clarity, when dealing with stress or strain written in the Voigt notation, an index $(.)^1$

[2] Although a similar development can be performed for a Cosserat continuum.

is introduced, as for instance ${}^1\boldsymbol{\sigma}$.

For a transverse isotropic material, where the fiber direction is $\mathbf{a}_0 = \mathbf{e}_3$, the elasticity tensor, developed in Voigt notation is

$$
{}^2\mathbb{C} = \begin{bmatrix} \mathbb{C}_{11} & \mathbb{C}_{12} & \mathbb{C}_{12} & 0 & 0 & 0 \\ \mathbb{C}_{12} & \mathbb{C}_{22} & \mathbb{C}_{23} & 0 & 0 & 0 \\ \mathbb{C}_{12} & \mathbb{C}_{23} & \mathbb{C}_{22} & 0 & 0 & 0 \\ 0 & 0 & 0 & \mathbb{C}_{44} & 0 & 0 \\ 0 & 0 & 0 & 0 & \mathbb{C}_{55} & 0 \\ 0 & 0 & 0 & 0 & 0 & \mathbb{C}_{55} \end{bmatrix} = \begin{bmatrix} \gamma & \lambda+\alpha & \lambda+\alpha & 0 & 0 & 0 \\ \lambda+\alpha & \lambda+2\,\mu_T & \lambda & 0 & 0 & 0 \\ \lambda+\alpha & \lambda & \lambda+2\,\mu_T & 0 & 0 & 0 \\ 0 & 0 & 0 & \mu_T & 0 & 0 \\ 0 & 0 & 0 & 0 & \mu_L & 0 \\ 0 & 0 & 0 & 0 & 0 & \mu_L \end{bmatrix}
$$

with $\gamma = \lambda + 2\,\alpha + \beta + 4\,\mu_L - 2\,\mu_T$. The Voigt convention is here employed with ${}^2\mathbb{C}_{44} \equiv {}^4\mathbb{C}_{2323}$, ${}^2\mathbb{C}_{55} \equiv {}^4\mathbb{C}_{1313}$ and ${}^2\mathbb{C}_{66} \equiv {}^4\mathbb{C}_{1212}$. As consequence, we get the following correspondence with the constitutive law and the elasticity constants

$$
\mathbb{C}_{11} = \lambda + 2\,\alpha + \beta + 4\,\mu_L - 2\,\mu_T; \qquad \mathbb{C}_{22} = \mathbb{C}_{33} = \lambda + 2\,\mu_T; \qquad \mathbb{C}_{12} = \mathbb{C}_{13} = \lambda + \alpha;
$$
$$
\mathbb{C}_{23} = \lambda; \qquad \mathbb{C}_{44} = \frac{1}{2}\left(\mathbb{C}_{22} - \mathbb{C}_{23}\right) = \mu_T; \qquad \mathbb{C}_{55} = \mathbb{C}_{66} = \mu_L.
$$

The constitutive law is applied for a carbon fiber reinforced PEEK[3] with the material constants expressed in the Table 5.1.

$E_1 = 138$ GPa	$E_2 = 10.2$ GPa	$G_{23} = 5.7$ GPa	$\nu_{12} = 0.3$	$\nu_{23} = 0.275$

Table 2.1: Material constants for the transverse isotropic material

The fiber reinforced polymer is subjected to a tension test, with the boundary conditions expressed in Fig. 2.3. The same tension test is performed for a transverse isotropic material with an angle orientation from $-90°$ to $+90°$.

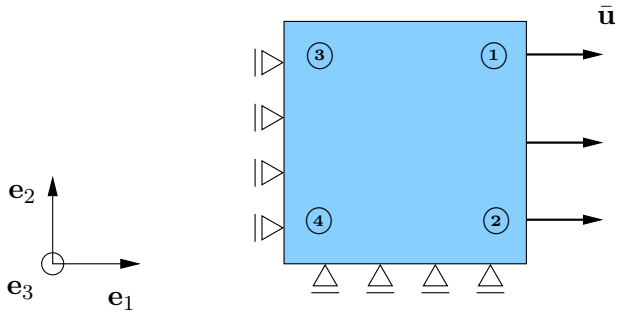

Figure 2.3: Schematic representation of the tension test

The normal stress and the vertical displacement in the points ① to ④ are represented in Figs 2.4 and 2.5. It is to mention that the normal stress shows a symmetric distribution

[3]Polyether Ether Ketone, a thermoplastic polymer

for the upper points ① and ④, as well as for the lower points ② and ③, respectively. For a fiber orientation angle of 0°, the stress σ_{11} reaches the maximal value $E_1/10$ for the tension test of 10%; the stress σ_{22} reaches the minimal value $E_2/10$ when the fiber orientation angle is 90°. The vertical displacement of the bottom points is 0, and it can be observed that the displacement of the upper points are symmetric to each other.

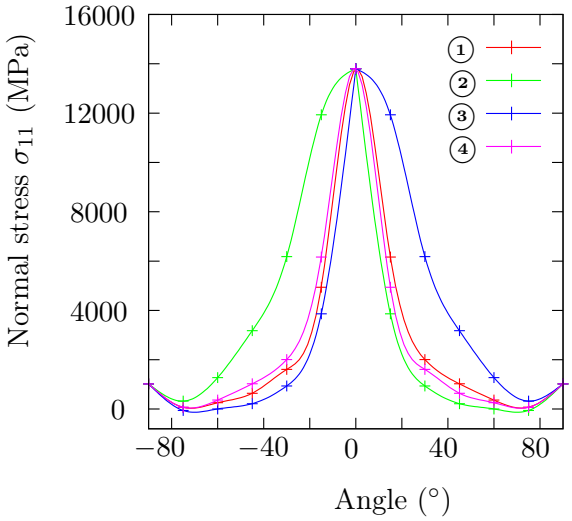

Figure 2.4: Nodes's normal stress as a function of the angle and of the position of the points ①...④

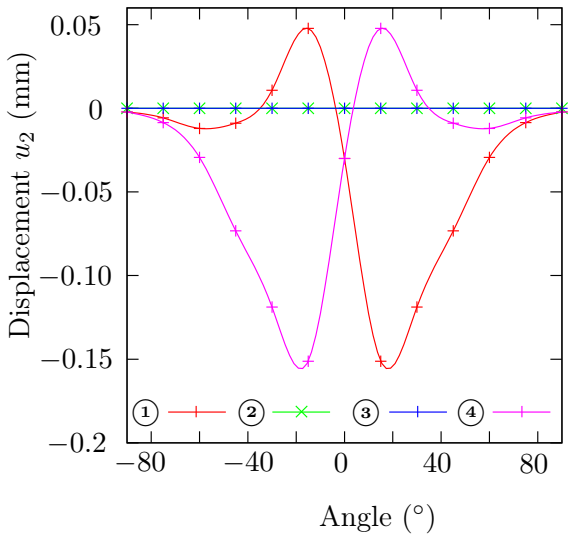

Figure 2.5: Nodes's vertical displacement as a function of the angle and of the position of the points ①...④

2.3.3 Viscoplasticity

Lots of metals present an elasto-plastic material behaviour; however, we choose to implement an elasto-viscoplastic model. Indeed, an elasto-plastic model can be taken as a particular case of a viscoplastic model if the viscosity is very small. Moreover, the resolution of the consistency condition is avoided, as explained later in this part.

In the first instance, a general model for finite deformations is described. The numerical concurrent homogenisation for plates can be applied for finite deformations. However, in the scope of the presented work, where the numerical homogenisation is applied for composite plates, the method is performed in the small deformation domain. Therefore in the second instance, a small strain model is explicitly described. Finally, a method to find the consistent tangent, the Multi-Level Newton Algorithm (MLNA), is developed.

General Model for Finite Deformations

In this part, a plasticity theory with elastic range is presented, as developed for by Haupt in case of plasticity or viscoplasticity [73] and by Perzyna for viscoplasticity [143, 144, 145]. An elasto-plastic or an elasto-viscoplastic material shows irreversible deformations and its behaviour depends on the load history. An elasto-plastic material possesses basically an elastic part and an inelastic part; for the case of finite deformations, the deformations are split in a multiplicative way in an elastic part and an inelastic part

$$\mathbf{F} \;=\; \mathbf{F}_{\mathrm{e}} \cdot \mathbf{F}_{\mathrm{p}}, \tag{2.106}$$

where $\mathbf{F}_{\mathrm{e}}$ represents the elastic deformation tensor and $\mathbf{F}_{\mathrm{p}}$ is the plastic part of the deformation tensor, also defined with an index $(.)_{\mathrm{i}}$ by some authors in reference to the inelastic deformations. For plasticity, a full discharge is not possible, because of the inhomogeneous eigen deformation which stays in the body. For this reason, the body could be divided in small parts, until these parts are fully discharged. But in this state, the unloaded pieces of the body don't match, since they have suffered different deformations; this deformation state is "locally stress free", cf. [73]. In case of plasticity, an intermediate deformation is defined, which is locally stress free, as represented in figure 2.6. Within this framework, the transport of a material line element between the reference ($\mathrm{d}\mathbf{X}$), intermediate ($\mathrm{d}\hat{\mathbf{x}}$) and current ($\mathrm{d}\mathbf{x}$) configuration are defined as

$$\begin{aligned} \mathrm{d}\mathbf{x} &= \mathbf{F} \cdot \mathrm{d}\mathbf{X}, \\ \mathrm{d}\hat{\mathbf{x}} &= \mathbf{F}_{\mathrm{p}} \cdot \mathrm{d}\mathbf{X}, \\ \mathrm{d}\mathbf{x} &= \mathbf{F}_{\mathrm{e}} \cdot \mathrm{d}\hat{\mathbf{x}}. \end{aligned} \tag{2.107}$$

Similarly as for an hyperelastic material, a plastic right Cauchy-Green deformation tensor can be introduced as

$$\mathbf{C}_{\mathrm{p}} \;=\; \mathbf{F}_{\mathrm{p}}^{T} \cdot \mathbf{F}_{\mathrm{p}}, \tag{2.108}$$

as well as a plastic Green-Lagrange strain tensor

$$\mathbf{E}_{\mathrm{p}} \;=\; \frac{1}{2}(\mathbf{F}_{\mathrm{p}}^{T} \cdot \mathbf{F}_{\mathrm{p}} - \mathbf{I}). \tag{2.109}$$

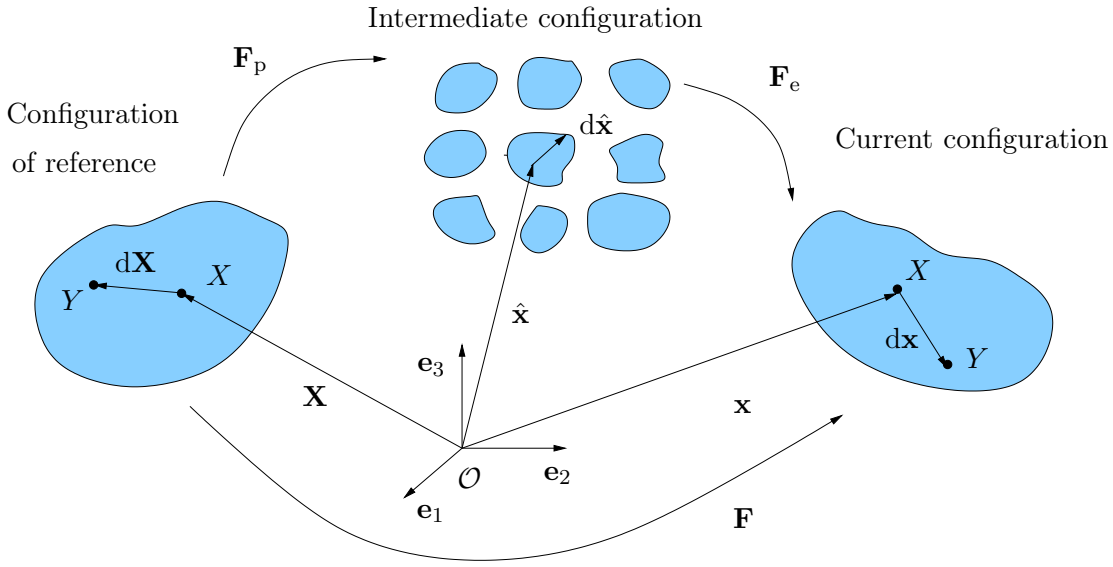

Figure 2.6: Schematic representation of the configuration of reference, of the current configuration and of the intermediate configuration

The Green-Lagrange strain tensor of the total deformations is defined as

$$\mathbf{E} = \frac{1}{2}(\mathbf{F}_\mathrm{p}^T \cdot \mathbf{F}_\mathrm{e}^T \cdot \mathbf{F}_\mathrm{e} \cdot \mathbf{F}_\mathrm{p} - \mathbf{I}), \tag{2.110}$$

which introduces the deformation tensor of the intermediate configuration as

$$\hat{\mathbf{\Gamma}} = \mathbf{F}_\mathrm{p}^{T-1} \cdot \mathbf{E} \cdot \mathbf{F}_\mathrm{p}^{-1} \tag{2.111}$$

as the push forward from the reference configuration to the intermediate configuration. It is to notice that in the intermediate configuration, the strains are divided in a additive way as

$$\hat{\mathbf{\Gamma}} = \hat{\mathbf{\Gamma}}_\mathrm{e} + \hat{\mathbf{\Gamma}}_\mathrm{p}, \tag{2.112}$$

the $\hat{(.)}$ describes the quantities of the intermediate configuration. Therefore, it defines a purely elastic Green-Lagrange strain tensor

$$\hat{\mathbf{\Gamma}}_\mathrm{e} = \frac{1}{2}(\mathbf{F}_\mathrm{e}^T \cdot \mathbf{F}_\mathrm{e} - \mathbf{I}), \tag{2.113}$$

and a purely plastic Euler-Almansi strain tensor as

$$\hat{\mathbf{\Gamma}}_\mathrm{p} = \frac{1}{2}(\mathbf{I} - \mathbf{F}_\mathrm{p}^{T-1} \cdot \mathbf{F}_\mathrm{p}^{-1}). \tag{2.114}$$

According to the concept of dual variables, the dual stress of $\hat{\mathbf{\Gamma}}$ is the second Piola-Kirchhoff stress of the intermediate configuration, cf. Haupt (2008) [73] as

$$\hat{\mathbf{S}} = J_\mathrm{p}\, \mathbf{F}_\mathrm{p} \cdot \mathbf{T} \cdot \mathbf{F}_\mathrm{p}^T = J\, \mathbf{F}_\mathrm{e}^{-1} \cdot \mathbf{S} \cdot \mathbf{F}_\mathrm{e}^{T-1}, \tag{2.115}$$

where in the case of plastic incompressibility, the Jacobian of the plastic domain reduced to $J_\mathrm{p} = 1$. A plastic velocity gradient is defined as

$$\hat{\mathbf{L}}_\mathrm{p} \;=\; \dot{\hat{\mathbf{F}}}_\mathrm{p} \cdot \hat{\mathbf{F}}_\mathrm{p}^{-1}. \tag{2.116}$$

By applying the same transformation as for $\hat{\mathbf{\Gamma}}$ and $\hat{\mathbf{S}}$, we define the covariant or lower-convected Oldroyd rate[4]

$$\overset{\triangle}{\hat{\mathbf{\Gamma}}} = \hat{\mathbf{F}}_\mathrm{p}^{T-1} \cdot \dot{\mathbf{E}} \cdot \hat{\mathbf{F}}_\mathrm{p}^{-1} \;=\; \dot{\hat{\mathbf{\Gamma}}} + \hat{\mathbf{L}}_\mathrm{p}^{T} \cdot \hat{\mathbf{\Gamma}} + \hat{\mathbf{\Gamma}} \cdot \hat{\mathbf{L}}_\mathrm{p}, \tag{2.117}$$

and the contravariant or upper-convected Oldroyd rate[5] as

$$\overset{\triangledown}{\hat{\mathbf{S}}} = \dot{\hat{\mathbf{S}}} - \hat{\mathbf{L}}_\mathrm{p}^{T} \cdot \hat{\mathbf{S}} - \hat{\mathbf{S}} \cdot \hat{\mathbf{L}}_\mathrm{p}. \tag{2.118}$$

Similarly as for the strain, the strain rate can be divided in a additive split as

$$\overset{\triangle}{\hat{\mathbf{\Gamma}}} = \overset{\triangle}{\hat{\mathbf{\Gamma}}}_\mathrm{e} + \overset{\triangle}{\hat{\mathbf{\Gamma}}}_\mathrm{p} = \hat{\mathbf{D}}_\mathrm{e} + \hat{\mathbf{D}}_\mathrm{p}, \tag{2.119}$$

with the elastic and plastic strain rates of the intermediate configuration as

$$\begin{aligned} \hat{\mathbf{D}}_\mathrm{e} \;&=\; \overset{\triangle}{\hat{\mathbf{\Gamma}}}_\mathrm{e} = \dot{\hat{\mathbf{\Gamma}}}_\mathrm{e} + \hat{\mathbf{L}}_\mathrm{p}^{T} \cdot \hat{\mathbf{\Gamma}}_\mathrm{e} + \hat{\mathbf{\Gamma}}_\mathrm{e} \cdot \hat{\mathbf{L}}_\mathrm{p}; \\ \hat{\mathbf{D}}_\mathrm{p} \;&=\; \overset{\triangle}{\hat{\mathbf{\Gamma}}}_\mathrm{p} = \dot{\hat{\mathbf{\Gamma}}}_\mathrm{p} + \hat{\mathbf{L}}_\mathrm{p}^{T} \cdot \hat{\mathbf{\Gamma}}_\mathrm{p} + \hat{\mathbf{\Gamma}}_\mathrm{p} \cdot \hat{\mathbf{L}}_\mathrm{p}. \end{aligned} \tag{2.120}$$

With further simplifications within the Eqs (2.114) and (2.116), the Eq. (2.120) becomes

$$\hat{\mathbf{D}}_\mathrm{p} \;=\; \frac{1}{2}\left[\hat{\mathbf{L}}_\mathrm{p} + \hat{\mathbf{L}}_\mathrm{p}^{T}\right]. \tag{2.121}$$

An elastic function is defined, which specifies the behaviour of the material in the elastic domain as

$$\hat{\mathbf{S}} \;=\; \mathbf{g}_1(\hat{\mathbf{\Gamma}}_\mathrm{e}), \tag{2.122}$$

where $\mathbf{g}_1$ is an isotropic tensor function. Then, a yield function is used; it gives the border of the elastic domain and plastic domain in the stress space

$$F \;=\; F(\hat{\mathbf{S}}, \hat{\mathbf{X}}, k) \;=\; f(\hat{\mathbf{S}} - \hat{\mathbf{X}}, k). \tag{2.123}$$

It is to mention that a major difference between elasto-plasticity and viscoplasticity lies in the yield function: for an elasto-plastic material, the yield function can be *only* negative or zero. On the contrary for viscoplasticity, the yield function can have a negative, zero *or* positive value and the consistency condition is not needed. For elasto-plasticity, the consistency condition forbids the yield function to have a value greater than zero, and enables in the same way a determination of the parameter λ. Instead of this, a further definition of the parameter λ is needed for viscoplasticity. Therefore, the flow rule can be

[4] known in German as the "obere Lie-Ableitung", cf. [73, 92]
[5] known in German as the "untere Lie-Ableitung", cf. [73, 92]

written for either elasto-plasticity or viscoplasticity as

$$\text{elasto-plasticity:} \qquad \hat{\mathbf{D}}_{\mathrm{p}} = \lambda \frac{\partial f}{\partial \mathbf{S}}, \quad \dot{f} = 0, \qquad \text{for } F = 0 \text{ and loading,}$$

$$\text{viscoplasticity:} \qquad \hat{\mathbf{D}}_{\mathrm{p}} = \lambda \frac{\partial f}{\partial \mathbf{S}}, \quad \lambda = \frac{1}{\eta} \langle f \rangle^m, \quad \text{for } F \geq 0 \text{ and loading.}$$

$\langle \cdot \rangle$ are the Macauley brackets[6], expressed as

$$\langle x \rangle = \begin{cases} x \text{ for } x \geq 0 \\ 0 \text{ for } x < 0. \end{cases} \tag{2.124}$$

There are two classical hardening: the isotropic hardening and the kinematic hardening, as represented in Fig. 2.7. The isotropic hardening, represented in the left hand side, assumes an increase of the radius of the yield surface, but with a conservation of the position of its center. On the contrary for a kinematic hardening, drawn on the middle, the radius of the yield surface stays unchanged, but it suffers a translation.

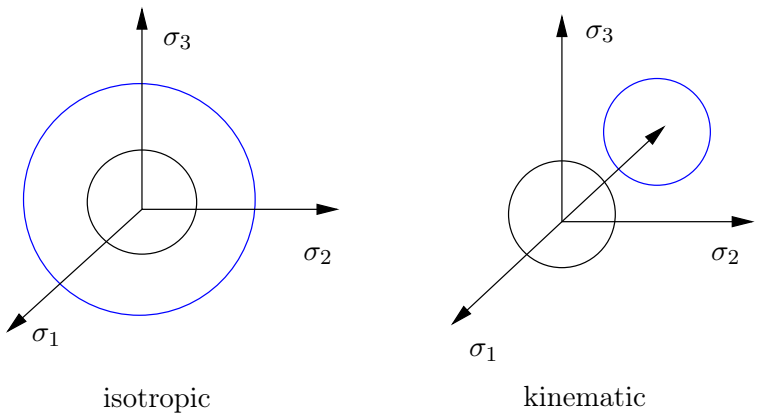

Figure 2.7: Representation of the yield surface as a function of the hardening in the principal stress space (black: initial yield surface, blue: yield surface after hardening)

For a kinematic hardening, the evolution equation is defined following the Armstrong-Frederick ansatz as

$$\overset{\triangledown}{\hat{\mathbf{X}}} = c\,\hat{\mathbf{D}}_{\mathrm{p}} - b\,\dot{s}_{\mathrm{p}}(t)\,\hat{\mathbf{X}}, \tag{2.125}$$

where $\overset{\triangledown}{\hat{\mathbf{X}}}$ is the upper-convected Oldroyd rate of the backstress tensor. c and b are material parameters: $+c\,\hat{\mathbf{D}}_{\mathrm{p}}$ illustrates the production and displacement of dislocations and $-b\,\dot{s}_{\mathrm{p}}(t)\,\hat{\mathbf{X}}$ represents the obstacles for the dislocations. The plastic arclength is defined as

$$\dot{s}_{\mathrm{p}}(t) = ||\hat{\mathbf{D}}_{\mathrm{p}}||. \tag{2.126}$$

[6]known in German as "Föppl Klammer"

The isotropic hardening is defined as a change in the radius of the yield surface as

$$k \;=\; k(s_{\mathrm{p}}). \tag{2.127}$$

The elasticity tensor is defined as the fourth-order tensor

$$\overset{4}{\mathbb{C}} = \overset{4}{\mathbb{C}}\,(\mathbf{E}) \;=\; \frac{\mathrm{d}}{\mathrm{d}\mathbf{E}}\mathbf{g}_1(\mathbf{E}) \tag{2.128}$$

For the model of elasto-plasticity at finite strains, see appendix 7.2. Many other models are available and in particular the reader can be referred to [74, 128, 117, 168, 12, 30]. It is to mention that some methods have also been developed to incorporate a fiber reinforced material behaviour for plasticity, cf. [63], or an orthotropic elasto-plastic material behaviour, cf. [168].

Small Strain Model

Previously, an elasto-viscoplastic model at finite deformations, considered as one of the most general case, has been explained. Indeed, the elasto-plastic material model can be considered as a special case of the viscoplastic material behaviour, if the viscosity η vanishes.

A numerical multi-scale modelling can be accurately used for finite strains. However, in the presented work, the numerical homogenisation is applied to a small deformations issue. Therefore, an explicit elasto-viscoplastic model, according to [49, 73], is given for small strains.

The description of the material behaviour at small strains and in one dimension can be motivated with rheological elements, as explained in [73] among others. A generalization of the constitutive laws given by the rheological elements in three dimensions can lead to the constitutive law for small deformations. In the scope of this work, we will use the viscoplasticity model developed by [70, 73]. For the geometrically[7] linear case, the deformations are split in an additive way for small deformations

$$\boldsymbol{\varepsilon} \;=\; \boldsymbol{\varepsilon}_{\mathrm{e}} + \boldsymbol{\varepsilon}_{\mathrm{p}}. \tag{2.129}$$

The stress is defined as

$$\boldsymbol{\sigma} \;=\; K\;\mathrm{tr}(\boldsymbol{\varepsilon})\,\mathbf{I} + 2\,G\,(\boldsymbol{\varepsilon} - \boldsymbol{\varepsilon}_p)^D, \tag{2.130}$$

where $(\diamond)^D$ is the deviatoric part of the tensor $(\diamond)$ defined as

$$(\diamond)^D \;=\; (\diamond) - \frac{1}{3}\;\mathrm{tr}(\diamond)\,\mathbf{I}. \tag{2.131}$$

K is the bulk modulus, defined as a function of the Young's modulus E and the Poisson's ratio ν as $K = \dfrac{E}{3(1-2\,\nu)}$ and G is the shear modulus defined as $G = \mu \;=\; \dfrac{E}{2(1+\nu)}$. The von Mises yield function can be written as

$$F(\boldsymbol{\sigma}, \mathbf{X}) \;=\; \frac{1}{2}(\boldsymbol{\sigma} - \mathbf{X})^D : (\boldsymbol{\sigma} - \mathbf{X})^D - \frac{1}{3}\,k^2, \tag{2.132}$$

[7] It is to differentiate with the physically linear case. Geometric linearity supposes small deformations, physical linearity is related to the material law: an elasto-plastic for small strains material is physically non-linear and geometrically linear.

with $\mathbf{X}$ the backstress tensor. Considering a small deformation model, it can be proved that the intermediate configuration coincides with the reference configuration. Consequently, the notations $\bar{(.)}$, which have been employed to denote the quantities referring to the intermediate configuration, can be neglected. The lower-convected Oldroyd rate becomes simply the material derivative.

For a negative yield function, $F(\boldsymbol{\varepsilon}, \boldsymbol{\varepsilon}_p) < 0$, the material is in the elastic state. For an elasto-plastic material, if the yield function is equal to zero, the plastic domain is reached. A yield function strictly superior to zero with $F > 0$ cannot exist for an elasto-plastic material (this is guaranteed with the consistency condition). On the contrary for an elasto-viscoplastic material, a positive value of the yield function is possible and defines the viscoplastic part.

The plastic deformations are written as a function of the normal $\mathbf{N}$

$$\dot{\boldsymbol{\varepsilon}}_p \,=\, \lambda\, \mathbf{N} \,=\, \lambda\, \frac{(\boldsymbol{\sigma} - \mathbf{X})^D}{||(\boldsymbol{\sigma} - \mathbf{X})^D||} \quad \text{for } F \geq 0 \text{ and loading} \tag{2.133}$$

with

$$\mathbf{N} \,=\, \frac{(\boldsymbol{\sigma} - \mathbf{X})^D}{||(\boldsymbol{\sigma} - \mathbf{X})^D||}. \tag{2.134}$$

Concerning the hardening, an isotropic hardening law can be written for small deformations as a function of the plastic strain rate deformations

$$\dot{k} \,=\, \dot{k}(\dot{s}), \tag{2.135}$$

with k the radius of the yield surface in the principal stress space. The accumulated plastic strain rate $\dot{s}$ is defined as

$$\dot{s} \,=\, \left(\frac{2}{3}\, \dot{\boldsymbol{\varepsilon}}_p : \dot{\boldsymbol{\varepsilon}}_p \right)^{1/2}, \tag{2.136}$$

cf. [73]. A kinematic hardening can also be considered as

$$\dot{\mathbf{X}} \,=\, c\, \dot{\boldsymbol{\varepsilon}}_p - b\, \dot{s}\, \mathbf{X} \,=\, \lambda\, (c\, \mathbf{N} - b\sqrt{2/3}\, \mathbf{X}), \tag{2.137}$$

with the backstress tensor $\mathbf{X}$ representing the center of the yield surface in the principal stress space. In the framework of viscoplasticity with elastic range for small deformations, we use the formulation introduced in [49, 70] and define the material function λ as

$$\lambda(\boldsymbol{\sigma}, \mathbf{X}) \,=\, \frac{1}{\eta} \left\langle \frac{F(\boldsymbol{\sigma}, \mathbf{X})}{\sigma_0^2} \right\rangle^m. \tag{2.138}$$

Numerical Aspects

In order to solve the system of equations for the viscoplasticity model, a time discretisation is applied and the implicit Euler starting values are defined. For a given deformation $\boldsymbol{\varepsilon}$, a time discretisation of the evolution equation is applied with the plastic deformation ${}^S\boldsymbol{\varepsilon}_\mathrm{p}$ of

the last increment k. The starting value are the value computed during the last increment $(k-1)$. The trial stress ${}^{T}\boldsymbol{\sigma}$ has to be defined, and it depends on the total deformation and on the starting value of the plastic deformation

$$ {}^{T}\boldsymbol{\sigma} \;=\; K\;\mathrm{tr}(\boldsymbol{\varepsilon})\,\mathbf{I} + 2\,G\,(\boldsymbol{\varepsilon} - {}^{S}\boldsymbol{\varepsilon}_p)^{D} \tag{2.139} $$

with $\diamond^{S}$ defined as starting value of $\diamond$. The von Mises yield function is then computed as a function of the trial stress

$$ F({}^{T}\boldsymbol{\sigma},{}^{S}\mathbf{X}) \;=\; \frac{1}{2}({}^{T}\boldsymbol{\sigma} - {}^{S}\mathbf{X})^{D}\cdot({}^{T}\boldsymbol{\sigma} - {}^{S}\mathbf{X})^{D} - \frac{1}{3}\,k^2. \tag{2.140} $$

If the von Mises yield function is negative, the elastic domain is considered. However, if the von Mises yield function is positive or equal to zero, the viscoplastic domain is reached and both evolution equation and hardening have to be solved for the plastic deformation with a Newton (or Pegasus) iteration. The main difference with an elasto-plastic model leads in the resolution of the consistency condition for elasto-plasticity; on the contrary for viscoplasticity, the material function λ is resolved with

$$ \lambda(\boldsymbol{\sigma},\mathbf{X}) \;=\; \frac{1}{\eta}\left\langle \frac{F(\boldsymbol{\sigma},\mathbf{X})}{\sigma_0^2}\right\rangle^{r} \Leftrightarrow \zeta \;=\; \Delta t\,\lambda. \tag{2.141} $$

Further, the parameter ζ is used instead of λ. The Eq. (2.141) can be solved with a Newton iteration; however, for efficiency, a Pegasus method is chosen, cf. [49, 70]. The Pegasus method is a modified Regula Falsi method, and it seems to be more efficient than the classical Newton iteration in this case, cf. [70]. Its principle, developed by [44, 50], can be found in the appendix 7.3.

The plastic deformation is then updated using the implicit Euler time discretisation

$$ \boldsymbol{\varepsilon}_p \;=\; {}^{S}\boldsymbol{\varepsilon}_p + \Delta t\,\lambda\,\mathbf{N} \;=\; {}^{S}\boldsymbol{\varepsilon}_p + \zeta\,\mathbf{N}, \tag{2.142} $$

as well as the backstress tensor

$$ \mathbf{X} \;=\; {}^{S}\mathbf{X} + \Delta t\,\lambda\,(c\,\mathbf{N} - b\sqrt{2/3}\,\mathbf{X}) \Rightarrow \mathbf{X} \;=\; \mu_k\,({}^{S}\mathbf{X} + \zeta\,c\,\mathbf{N}). \tag{2.143} $$

Lastly, the stress are written as

$$ \boldsymbol{\sigma} \;=\; K\;\mathrm{tr}(\boldsymbol{\varepsilon})\,\mathbf{I} + 2\,G\,(\boldsymbol{\varepsilon} - \boldsymbol{\varepsilon}_p)^{D}, \tag{2.144} $$

cf. [49, 70]. The physical meaning of this algorithm can be represented in Fig. 2.8, cf. [40]. The circle represents the yield surface. In the first iteration, represented by the first cross along the blue curve, the material stays in the elastic domain. In the next iteration, the trial stress is computed, and can be found outside the yield surface. It means that the viscoplastic domain is reached. Then, the real stress state is computed and the new yield surface is equally computed (represented by the dot lines).

Consistent Tangent Operator

The consistent tangent operator shows to have a dramatic importance for the FE method. It is of course possible to try to overcome it with the help of a numerical tangent. However,

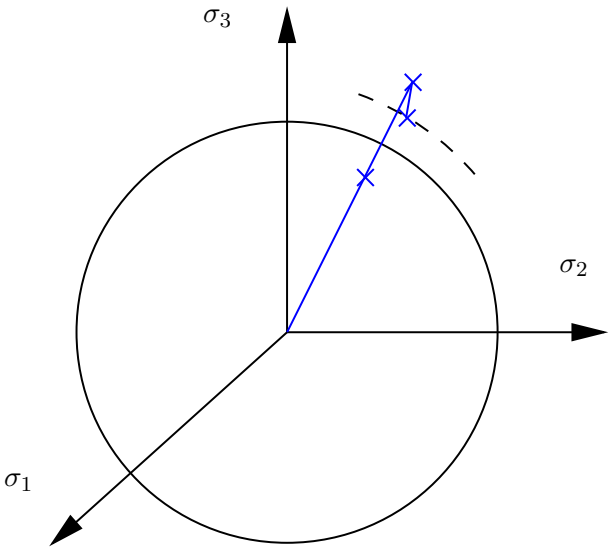

Figure 2.8: Schematic representation of the plasticity algorithm

this method has the drawback to radically slow down the computations. For this reason, the attempt is made to find an analytical tangent; this is relatively easy for linear elastic materials, but presents more difficulties for plasticity or viscoelasticity, due to the dependencies of the stress on the elastic and plastic deformations. In this work, we will use a Multi-Level Newton Algorithm (MLNA), firstly proposed by [150] for electrical issues and later on by [47, 48, 49, 71, 70] in mechanics for the resolution of viscoelastic, elasto-plastic or viscoplastic problems. The principle of it is to split the viscoplastic problem in a global and in a local level. The global level contains the global equilibrium equation, written for a strong formulation

$$\operatorname{div} \boldsymbol{\sigma} + \mathbf{f} \;=\; 0 \tag{2.145}$$

where the stress $\boldsymbol{\sigma}$ is defined with the elasticity relation

$$\boldsymbol{\sigma} \;=\; \mathbf{g}(\boldsymbol{\varepsilon}, \boldsymbol{\varepsilon}_p), \tag{2.146}$$

and $\boldsymbol{\varepsilon}_p$ is the plastic deformation, as defined in Eq. (2.133). A discretisation of the domain is made and the displacement can be expressed with the shape function $\mathbf{N}$

$$\mathbf{u} \;=\; \sum_{j=1}^{n} \mathbf{N}_j \, \mathbf{u}_j \;=\; \mathbf{N}_j \, \mathbf{u}_j, \tag{2.147}$$

as well as the virtual displacements

$$\delta\mathbf{u} \;=\; \sum_{j=1}^{n} \mathbf{N}_j \, \delta\mathbf{u}_j \;=\; \mathbf{N}_j \, \delta\mathbf{u}_j. \tag{2.148}$$

On the global level, the weak formulation of the global equilibrium condition is written as

$$\int_V \operatorname{grad} \delta\mathbf{u} : \boldsymbol{\sigma} \, \mathrm{d}V \;=\; \int_V \delta\mathbf{u} \cdot \mathbf{f} \, \mathrm{d}V \;=\; 0 \;\;\Leftrightarrow\;\; \mathbf{G} \;=\; 0. \tag{2.149}$$

The local level comprises the evolution equation, containing the vector of the internal variables $\mathbf{q} = (\boldsymbol{\varepsilon}_\mathrm{p}, \mathbf{k}, ...)$ as

$$\mathbf{A}\,\dot{\mathbf{q}} - \mathbf{l}(\mathbf{u}, \mathbf{q}) = 0 \tag{2.150}$$

The following system of non-linear equations has to be solved

$$\begin{cases} \mathbf{G}(\mathbf{u}, \mathbf{q}) = \mathbf{0} \\ \mathbf{l}(\mathbf{u}, \mathbf{q}) = \mathbf{0} \end{cases} \tag{2.151}$$

and this will be done using a Newton iteration

$$\left[\begin{array}{c|c} \frac{\partial \mathbf{G}}{\partial \mathbf{u}} & \frac{\partial \mathbf{G}}{\partial \mathbf{q}} \\ \hline \frac{\partial \mathbf{l}}{\partial \mathbf{u}} & \frac{\partial \mathbf{l}}{\partial \mathbf{q}} \end{array}\right] \cdot \left[\begin{array}{c} \mathrm{d}\mathbf{u} \\ \hline \mathrm{d}\mathbf{q} \end{array}\right] = - \left[\begin{array}{c} \mathbf{R_u} \\ \hline \mathbf{R_q} \end{array}\right], \tag{2.152}$$

with $\mathbf{R_u}$ the residuum of the global level and $\mathbf{R_q}$ the residuum of the local level. In the global level, the quantities are defined for each element, that means that there is a coupling. Consequently, the matrix $\partial\mathbf{G}/\partial\mathbf{u}$ is a sparse matrix. In contrast, in the local level, the quantities are related to the integration's points, and there is no coupling between the neighbouring elements for this quantity. As a consequence, the matrix $\partial\mathbf{l}/\partial\mathbf{q}$ is a block diagonal matrix. Therefore, it is more efficient to solve the system using the MLNA (Multi-Level Newton Algorithm) method, cf. [49, 70], as presented thereafter.

1. In the first step, the local residuum is considered, that means that the displacement is $\mathrm{d}\mathbf{u} = \mathbf{0}$ and the second line becomes

   $$\frac{\partial \mathbf{l}}{\partial \mathbf{q}} \cdot \mathrm{d}\mathbf{q} = -\mathbf{R_q} \tag{2.153}$$

   With the Eq. (2.153), the evolution of the internal variables $\mathbf{q}$ can be defined for a given state of the displacement.

2. In a second step, $\mathbf{R_q} = \mathbf{0}$ is considered. In this case, the Eq. (2.152) can be used to link the variations of the internal variables $\mathrm{d}\mathbf{q}$ and the global displacement $\mathrm{d}\mathbf{u}$.

   $$\frac{\partial \mathbf{l}}{\partial \mathbf{u}} \cdot \mathrm{d}\mathbf{u} + \frac{\partial \mathbf{l}}{\partial \mathbf{q}} \cdot \mathrm{d}\mathbf{q} = -\mathbf{R_q}. \tag{2.154}$$

   Because the global level is considered, the local residuum vanishes $\mathbf{R_q} = 0$ and it leads to a relation between $\mathrm{d}\mathbf{q}$ and $\mathrm{d}\mathbf{u}$

   $$\mathrm{d}\mathbf{q} = \left(\frac{\partial \mathbf{l}}{\partial \mathbf{q}}\right)^{-1} \cdot \left(-\frac{\partial \mathbf{l}}{\partial \mathbf{u}}\right) \cdot \mathrm{d}\mathbf{u}. \tag{2.155}$$

   The plastic internal variable is then known as a function of the displacement as $\mathbf{q} = \mathbf{q}(\mathbf{u})$.

3. In the third step, the global level is again considered, but the first line of the system is solved and the consistent tangent is identified

$$\frac{\partial \mathbf{G}}{\partial \mathbf{u}} \cdot \mathrm{d}\mathbf{u} + \frac{\partial \mathbf{G}}{\partial \mathbf{q}} \cdot \mathrm{d}\mathbf{q} \;=\; -\mathbf{R}_{\mathbf{u}}, \tag{2.156}$$

which can be modified with Eq. (2.155)

$$\left(\frac{\partial \mathbf{G}}{\partial \mathbf{u}} + \frac{\partial \mathbf{G}}{\partial \mathbf{q}} \cdot \frac{\mathrm{d}\mathbf{q}}{\mathrm{d}\mathbf{u}} \right) \cdot \mathrm{d}\mathbf{u} \;=\; -\mathbf{R}_{\mathbf{u}}. \tag{2.157}$$

Then, the analytical tangential stiffness can be identified as

$$\mathbf{K} \;=\; \frac{\partial \mathbf{G}}{\partial \mathbf{u}} + \frac{\partial \mathbf{G}}{\partial \mathbf{q}} \cdot \frac{\mathrm{d}\mathbf{q}}{\mathrm{d}\mathbf{u}} \tag{2.158}$$

cf. [49, 70]. In the scope of the before presented model, it can be proved that the analytical tangent stiffness is written as

$${}^{4}\mathbb{C} \;=\; \frac{\partial \mathbf{g}}{\partial \boldsymbol{\varepsilon}} + \frac{\partial \mathbf{g}}{\partial \boldsymbol{\varepsilon}_p} \cdot \frac{\mathrm{d}\boldsymbol{\varepsilon}_p}{\mathrm{d}\boldsymbol{\varepsilon}}, \tag{2.159}$$

with $\mathbf{g}$ defining the elasticity relation.

Further transformations for the considered small strain model leads to

$${}^{4}\mathbb{C} \;=\; \frac{\mathrm{d}}{\mathrm{d}\boldsymbol{\varepsilon}} \left(K \; \mathrm{tr}(\boldsymbol{\varepsilon})\, \mathbf{I} + 2\, G\, (\boldsymbol{\varepsilon} - {}^{S}\boldsymbol{\varepsilon}_p)^{D} - 2\, G\, \zeta\, \mathbf{N} \right), \tag{2.160}$$

cf. [49, 70]. With the computation of the derivative of the norm as function of the total deformation using $\mathbf{N} = \boldsymbol{\Xi}/||\boldsymbol{\Xi}||$, the analytical tangent can be written as

$${}^{4}\mathbb{C} \;=\; 2\, G \left(\frac{K}{2\, G}\, \mathbf{I} \otimes \mathbf{I} + \gamma_1 ({}^{4}\mathbf{I} - \frac{1}{3} \mathbf{I} \otimes \mathbf{I}) - \gamma_2 \mathbf{N} \otimes \mathbf{N} + \boldsymbol{\Gamma} \otimes \mathbf{N} \right) \tag{2.161}$$

with

$$\begin{aligned}
\gamma_1 \;&=\; 1 - \zeta\, \frac{2\, G}{||\boldsymbol{\Xi}||}; \\
\gamma_2 \;&=\; \frac{2\, G}{\beta} + \zeta\, \frac{2\, G}{||\boldsymbol{\Xi}||} \left(1 + \frac{1}{\beta} \sqrt{\frac{2}{3}}\, \left(b\, \mu^2\, {}^{S}\mathbf{X} \right) \cdot \mathbf{N} \right); \\
\boldsymbol{\Gamma} \;&=\; \zeta\, \frac{2\, G}{\beta\, ||\boldsymbol{\Xi}||} \sqrt{\frac{2}{3}}\, \left(b\, \mu^2\, {}^{S}\mathbf{X} \right), \\
\beta \;&=\; -\sqrt{\frac{2}{3}}\, b\, \mu^2\, ({}^{s}\mathbf{X} \cdot \mathbf{N}) + \left(2\, G + \mu\, c \left[1 - \zeta \sqrt{\frac{2}{3}}\, b\, \mu \right] \right) \\
&\quad + \frac{1}{\sqrt{2\, \sigma_0^2\, \left(\frac{\zeta\, \eta}{\Delta t} \right)^{1/m} + \frac{2}{3}\, k^2}}\, \frac{\sigma_0^2\, \eta}{m\, \Delta t}\, \left(\frac{\zeta\, \eta}{\Delta t} \right)^{1/m - 1}
\end{aligned} \tag{2.162}$$

cf. [70].

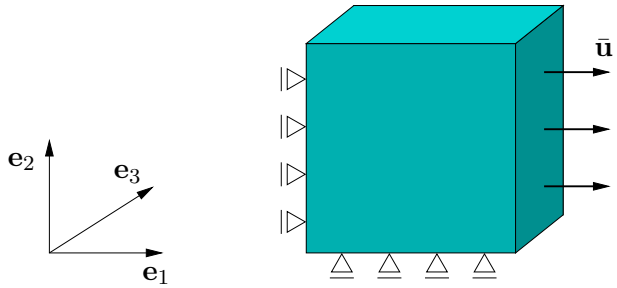

Figure 2.9: Schematic representation of the tension test in three dimensions: one of the faces with normal $\mathbf{e}_1$ is submitted to a tension and the other face is blocked in the $\mathbf{e}_1$-direction with $u_1 = 0$. One of the faces with normal $\mathbf{e}_2$ is blocked in the $\mathbf{e}_2$-direction with $u_2 = 0$ and one of the faces with normal $\mathbf{e}_3$ is blocked in the $\mathbf{e}_3$-direction with $u_3 = 0$ (not represented in the picture)

The model can be illustrated by a tension test of a three-dimensional element, with the boundary conditions drawn in Fig. 2.9. In a first instance, an elasto-plastic material is considered; that means that the viscosity is very small. In this case, the influence of the material parameters c and b is represented in Figs 2.10 and 2.11. In order to define the influence of c, the parameter b is firstly set to zero, as well as the viscosity. If the parameter c is equal to zero, the material has an ideal plastic material behaviour and the tangent of the curve is equal to zero. For a growing parameter c, the slope of the tangent increases and a larger stress is reached for the same deformation in the plastic domain. An opposite phenomenon can be observed for the parameter b: for a larger b, an ideal plastic behaviour is reached. When b is going to zero, the slope of the tangent increases: it can be explained with the Eq. (2.137), due to the negative sign of b. In a physical interpretation, the parameter c represents the production of dislocations and b the obstacles for them.

The influence of the strain rate and of the viscosity parameter can be seen in Figs 2.12 and 2.13. For a high strain rate, the normal stress reaches a higher value; a similar effect can be seen for a higher viscosity. For a larger viscosity, it can be shown that the plastic plateau is not instantaneously reached but with a delay, due to the viscoplastic effects. Indeed, for an ideal plastic material, as observed in the Figs 2.10 and 2.11 or for a viscosity equal to 1 s, the plastic plateau is reached directly. For a vanishing viscosity ($\eta = 1$ s), the elasto-plastic model can be considered as a specific case of viscoplasticity. In the following, an elasto-plastic material with hardening is considered.

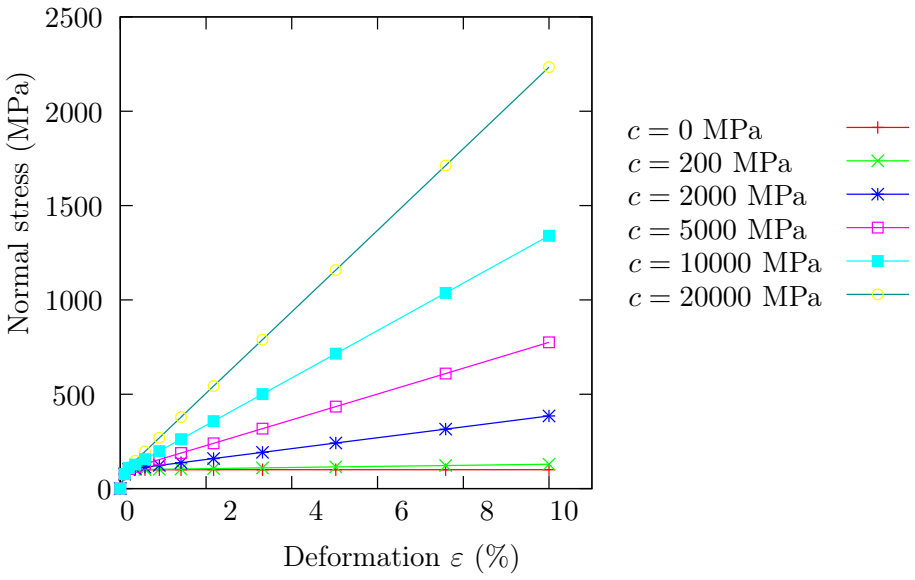

Figure 2.10: Normal stress vs. deformation: influence of the parameter c in the normal stress σ_{11}, for an elasto-plastic material (with $\eta = 1$ s, $b = 0$ [-])

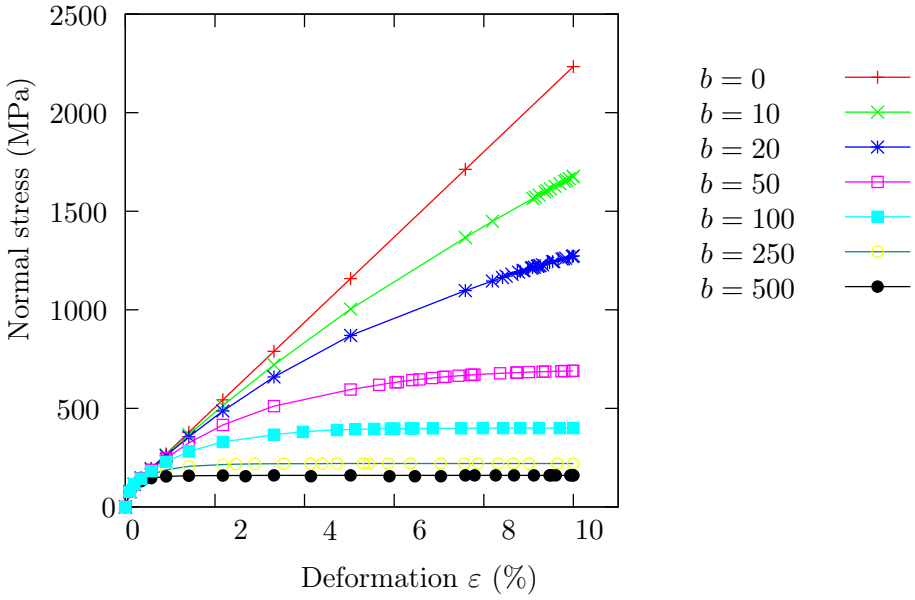

Figure 2.11: Normal stress vs. deformation: influence of the parameter b in the normal stress σ_{11}, for an elasto-plastic material (with $\eta = 1$ s, $c = 20000$ MPa)

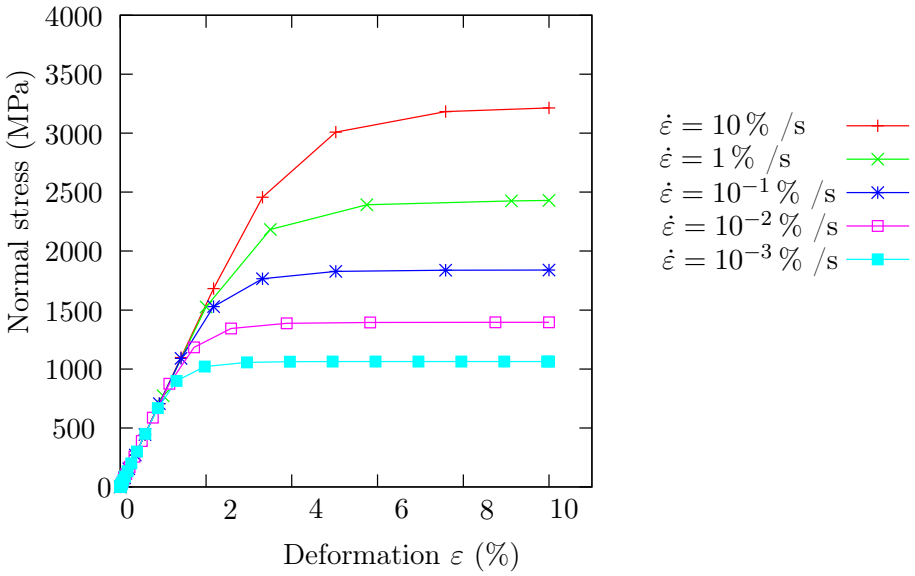

Figure 2.12: Normal stress vs. deformation: influence of the strain rate in the normal stress σ_{11}

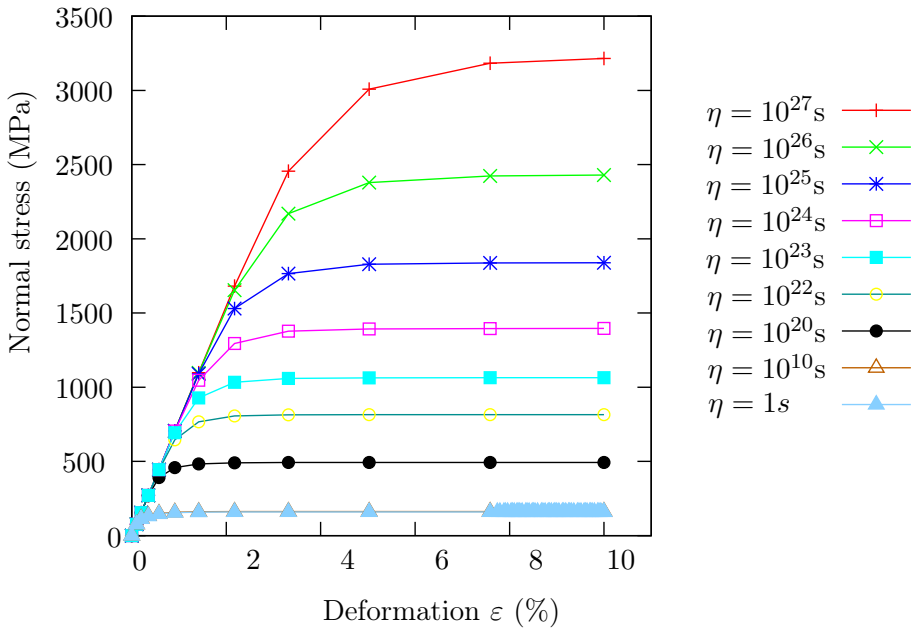

Figure 2.13: Normal stress vs. deformation: influence of the viscosity in the normal stress σ_{11}

Chapter 3

Macroscale: Plate Theory

For a numerical homogenisation for composite plates, a plate is defined as the macroscale and a three-dimensional FE computation is used for the mesoscale. In this part, the plate theory with seven degrees of freedom is explained: this theory is proposed for the further comparison of the results. Nevertheless, the plate theory with five degrees of freedom used for the numerical homogenisation can be considered as a particular case of the plate theory with seven degrees of freedom. Firstly, a short historical introduction is presented, followed by further comments concerning the choice of the plate theory. Then, the strong formulation of the model equations is described, as well as some aspects of the weak formulation. Lastly, we introduce a discussion about the convergence and the locking effects. In the present work, a special attention is given to the resolution of the Poisson locking, because this locking is of importance for an incompressible material behaviour, which is the case for plastic incompressibility.

3.1 Short Historic Introduction

When did the history of plate theories actually begin? In fact, the history of the plate theory cannot be totally different from the history of the beam theory and before this from the classical mechanics; therefore, we decided to arbitrary start our historical review with some elements related to the development of the beam theory, cf. [13, 178]. The background of the beam theory was given by the work of Galilei, followed by Jakob Bernoulli (I) and Leonhard Euler. However, the beam theory reached an achievement with Navier and Cauchy at the beginning of the 19^{th} century.

At the end of the 18^{th} century, the scientist and musician Chladni studied the acoustics of plates and their vibration modes. Later on, Jakob Bernoulli (II) tried to find a mathematical way to describe Chladni's experiments, but discrepancies arose. For this reason, the french academy gave a price to whom who find a suitable theory to the experiments; however the closing day had to be postponed twice, because no accurate theories were found at that time. But finally, the french mathematician Sophie Germain won the first price with her third work and her essay "Recherches sur la théorie des surfaces élastiques" was published in an improved version in 1821. She gave the hypothesis that the forces and work are proportional to the arithmetic average of the main curvature. Based on that she developed the partial equations for a plate submitted to an oscillation. It was later improved by Poisson and Navier; but their work suffered shortage, too. Finally, Kirchhoff's work, despite some shortage (in the demonstration of the first hypoth-

esis for example, cf. [178]), gave a certain improvement for the plate theory for thin plates.

Rayleigh (1877) and Love (1888) proposed improvements. For Naghdi, the method used by Love and Kirchhoff could be called a "derivation from the continuum theory", cf. [132]. The thin plates theory (also called sometimes Love-Kirchhoff plate theory) is based on the hypothesis that a cross section, straight and normal to the plate's midplane before deformations, stays straight and normal to the plate's midplane after deformations. In this theory, no consideration of the shear stress is encountered in case of a bending. This theory shows a good agreement with experiments for thin plates, where the ratio thickness/length is smaller than 1/20. This theory can be set as equivalent to the Bernoulli beam. An extension to consider the behaviour of laminates was further made and it is generally called the Classical Laminate Theory (CLT) in the English-speaking literature.

At the beginning of the 20^{th} century, the Ukrainian-American scientist Timoshenko proposed an improvement of the beam theory from Euler and Bernoulli with the insertion of the transverse shear. The improvement of the classical beam theory from Bernoulli enables the consideration of thicker beams. An equivalent theory for a thick plate can be found in the theories proposed independently by Reissner and Mindlin in the middle of the last century. In both theories, the cross section stays straight after deformations but can suffer a rotation in reference to the plate's midplane. The theories enable a consideration of the shear stresses, and can be applied with success to thicker plates, where the ratio thickness/length reaches 1/10. It was equally extended to incorporate the behaviour of laminates and this theory is nowadays called the First order Shear Deformation Theory (FSDT).

In his work in 1972, Naghdi proposed a reinforcement of the current theories with the consideration of the thermodynamics [132], followed by the work of Zhilin in 1976 [199]. Later on, Krätzig [105] proposed a shell theory with thickness change, although some authors [13, 24] propose the hypothesis that the first plate theory, in which the constitutive law is fully a three-dimensional one, and in which the out-of-plane displacement is of quadratic order, would probably have been treated by Hildebrand, Reissner and Thomas in 1949, cf. [81].

In the present work, two different plate theories are used: on the one hand, a plate theory with five degrees of freedom following the Mindlin concept is regarded for the numerical homogenisation of plates. On the other hand, a plate theory with seven degrees of freedom [13] is considered for comparison. These methods are issued from the derivation of the continuum theory. But why is a plate theory with five degrees of freedom used for the numerical homogenisation and a theory with seven degrees of freedom for the comparison using a plate theory?

Other methods to draw the behaviour of plates or shells are also available, like the Cosserat-type shell, as mentioned in the introduction. The Cosserat shells are mathematically more difficult because they result from a direct derivation from the three-dimensional equations. The direct derivation of the shell theory from the three-dimensional equations was proposed by the brother Cosserat in 1909, cf. [39], in the so-called "Cosserat surfaces" and later on improved by Ericksen & Truesdell [51]. A review of the Cosserat-types the-

ories for surfaces can be found in [9, 66, 133]. Although there are some criticisms about the Cosserat plates, cf. [14], they show to be more accurate for thin structures, especially if the thickness of the plate is approximately equal to the thickness of the microstructure, cf. [10].

Another possibility consists in the degenerated concept proposed by Ahmad et al. in 1968, cf. [13]. Its principle consists of a discretisation of a three-dimensional continuum, after that a two-dimensional shell problem is derivated from the three-dimensional model by considering a linear ansatz for the shape function in thickness direction, cf. [14]. The use of any degenerated shell theories, as mentioned before, is avoided because of two principal reasons. Firstly, the discretisation of a three-dimensional continuum [20] is computationally more expensive, and there is the necessity to consider several integration points through the thickness; this point is especially to avoid when a computationally expensive technique like the FE^2 method, is regarded. Secondly, some drawbacks arise for the boundary conditions and for finite strains in the "complicated update of the rotations", cf. [78]. As a consequence, the use of a degenerate shell theory is avoided, as well as a Cosserat-like shell because of its complexity. A shell theory "derivat[ed] from the continuum theory" [132] is used, because of its simplicity and effectiveness.

But there are further differentiations in these theories: the polynomial order of the approximation of the horizontal displacement can be used to set the order of these theories. The displacement in the three directions can be approximated with polynomial functions. In the plate theory derivated from the continuum theory, the both displacements parallel to the plate's midplane are approximated with a polynomial function, which gives the order of the plate theory considered (N), as represented in Fig. 3.2. The Love-Kirchhoff plate theory is considered as the "zero" order theory, because the displacement of the cross section (drawn in red) can be approximated by a constant function. Another possibility is to approximate the horizontal displacements with linear functions, as it is the case in the plate theory of Reissner or Mindlin, leading to the first order theory (the so-called First order Shear Deformation Theory). The displacement in direction parallel to the midplane can be approximated with a quadratic or cubic polynomial function, leading to a plate theory of second or third order, respectively.

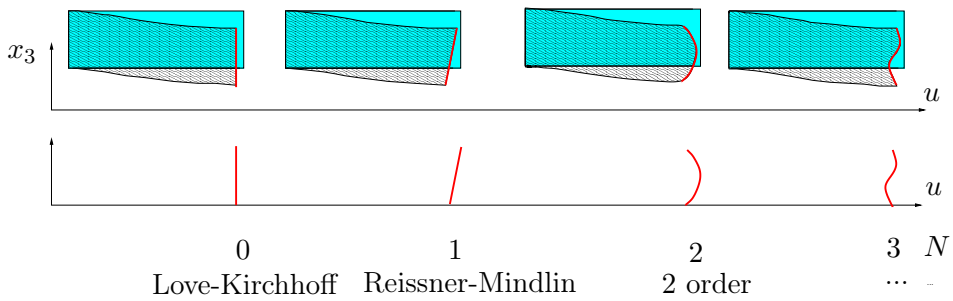

Figure 3.1: Schematic representation of the different plate theory, adapted from M. Bischoff, Theorie und Numerik einer dreidimensionalen Schalenformulierung, 1999, Ph.D.-thesis, Universität Stuttgart [13]

However, a homogenisation based on a Kirchhoff plate was already proposed, cf. [29], based on the plate theories proposed in [33]. In the scope of a numerical homogenisation, a FE^2 model for thin plates was studied by Coenen et al. (2008) [36]. Nevertheless, as pointed by Lillbacka et al. (2006) in [116], a numerical homogenisation using a plane stress assumption on the macroscale counts for drawbacks. Therefore, a higher order theory, as for instance a plate theory with seven degrees of freedom, should be used. Meanwhile, in the present work, a plate theory following the Mindlin concept is considered for the FE^2 method and the drawback related to the plane stress assumption are overcome by using a modified projection strategy.

In the Mindlin plate theory, the displacements of the cross section can be approximated with a linear function, as represented in Fig. 3.1. In contrast to the plate theory following the Kirchhoff concept, for the Mindlin concept, a cross section straight and normal to the plate's midplane before deformation stays straight after deformation but can afford a rotation. An approximation with a higher order polynomial function is also possible, as explained in [8, 152, 153, 154]. However, it can be shown that these theories are useful in the case of sandwich plates, and only if the materials composing the different layers present very different stiffnesses. Nevertheless, these theories do not bring a much better result for hybrid laminates. Due to the effectiveness and computing time, a plate theory with a linear displacement in the both directions parallel to the midplane is considered. It is to mention that other plate theories are also available for the modelling of composite plates, as described in the review by Carrera [24]. However, as mentioned in the introduction -in Chapt. 1- to the knowledge of the author, most of them are limited to linear material behaviour, as for instance the zig-zag theories or the layerwise theories. Due to this drawback, these theories are not considered in this work. Consequently, a numerical multi-scale modelling of the composite plates is performed.

3.2 Strong Formulation

In this section, a plate theory with seven degrees of freedom is developed, and the plate theory with five degree of freedom can be seen as one of its particular cases. After having described the basic assumption for the plate theory, the displacements and deformations are given. Then, the balance relations are considered, followed by the definition of the stress resultants. For this work, the mainly used literature are the works by Bischoff (1999) [13], Altenbach et al. [5, 6] and Reddy [154].

3.2.1 Assumptions Towards the Plate Theory

A plate is basically defined as a solid with one dimension much smaller than the other ones. A plate has a relatively limited thickness and the thickness coordinate is per definition defined as the $\mathbf{e}_3$ axis, as represented in Fig. 3.2. The plate presents the length l, the width L and the thickness h. The midplane is defined with $x_3 = 0$. The contact between the different layers or between the fibers or particles and the matrix is assumed to be perfect, which can be a limitation because of the delamination.

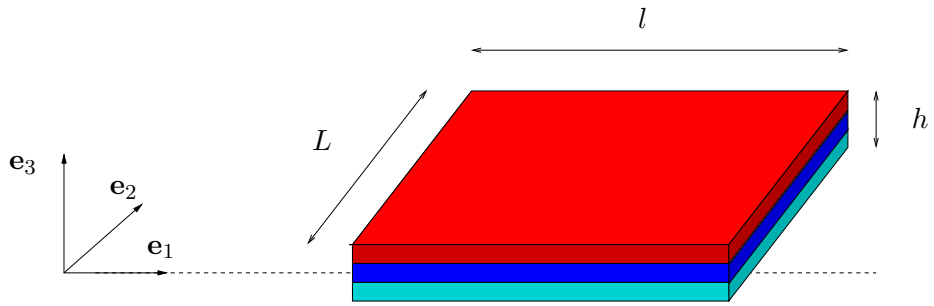

Figure 3.2: Basic definition of a plate, with l the length, L the width and h the thickness

Most of the plate theories are limited to small deformations, but this does not represent a too restrictive drawback, because in practice most of the composite plates cannot encounter a large deformation state. Moreover, the material behaviour is assumed to be linear for most of the plate theories; some exceptions were made for viscoelastic material behaviour [3] or for an elasto-plastic material law [161], but these extensions are not concerning the plate theory following the Mindlin concept.

In a plate theory following the Mindlin concept, no thickness change is considered and the deformation ε_{33} is assumed to be zero, cf. [6], and discrepancies towards the thickness change can occur. In contrast, a plate theory with seven degrees of freedom enables a consideration of the thickness change. In this case, two more degrees of freedom are added, in order to obtain a quadratic order for the out-of-plane displacement, resulting in a linear function for the deformation ε_{33}. It is to mention that other works are also available, with different treatment of the seventh degree of freedom. As developed by [21, 161, 165] for the Enhanced Assumed Strain (EAS) method, it is also possible to consider linear functions for the three displacements, and to add the seventh degree of freedom directly in the out-of-plane normal deformation ε_{33}.

3.2.2 Kinematics

The displacements parallel to the midplane follow a linear function and the displacement through the plate's thickness follows a quadratic function, cf. [13, 105, 162, 180, 181],

$$\begin{aligned} u(x_1, x_2, x_3) &= u_0(x_1, x_2) + x_3\, \varphi_1(x_1, x_2), \\ v(x_1, x_2, x_3) &= v_0(x_1, x_2) + x_3\, \varphi_2(x_1, x_2), \\ w(x_1, x_2, x_3) &= w_0(x_1, x_2) + x_3\, \theta_1(x_1, x_2) + x_3^2\, \theta_2(x_1, x_2), \end{aligned} \tag{3.1}$$

where u_0, v_0 and w_0 are the three translational degrees of freedom, defined at $x_3 = 0$. φ_1 and φ_2 are the two rotations along the in-plane axis. θ_1 and θ_2 are the two extra degrees of freedom, which give the plate theory the possibility to encounter a thickness change. The seven degrees of freedom are only depending on the two in-plane coordinates; the dependency in the thickness coordinate is written explicitly. As mentioned before, this theory is also called the $(1, 1, 2)$-model, cf. [13], due to the polynomial order of the three displacements u, v, w: linear for u and v, quadratic for w. In this work, Kienzler [96] defines a consistent plate theory if the polynomial order of the displacement in thickness

direction (w) is smaller than the polynomial order of the displacement in the longitudinal direction (u and v). This is not the case for the $(1,1,2)$-model. This fact could explain the convergence problem encountered for the FE^2 method based on a plate theory with seven degrees of freedom. Consequently, the FE^2 method employs a plate theory following the Mindlin ansatz, which is consistent, cf. Kienzler [96], and the consideration of the thickness change is performed with a modification of the projection. However, no convergence problems were met for the FE plate with thickness change for the computed examples. Because the plate theory with thickness change presents the advantage to consider a three-dimensional constitutive law, it is used in the following for the comparison using a plate theory.

The in-plane deformations are linear functions of the thickness coordinate x_3 and can be written as

$$\begin{aligned} \varepsilon_{11} &= \frac{\partial u_0}{\partial x_1} + x_3 \frac{\partial \varphi_1}{\partial x_1}, \\ \varepsilon_{22} &= \frac{\partial v_0}{\partial x_2} + x_3 \frac{\partial \varphi_2}{\partial x_2}. \end{aligned} \tag{3.2}$$

The in-plane shear deformation is given as

$$\gamma_{12} = \frac{\partial u_0}{\partial x_2} + \frac{\partial v_0}{\partial x_1} + x_3 \left(\frac{\partial \varphi_1}{\partial x_2} + \frac{\partial \varphi_2}{\partial x_1} \right). \tag{3.3}$$

These fields are the same for the five degrees of freedom plate theory following the Mindlin ansatz and for the present plate theory with thickness change. However, the deformation in the thickness direction vanishes for the Mindlin plate; in the plate theory with thickness change, it takes the value

$$\varepsilon_{33} = \theta_1 + 2\, x_3\, \theta_2. \tag{3.4}$$

The out-of-plane deformations are quadratic functions of the thickness coordinate and can be written as

$$\begin{aligned} \gamma_{13} &= \frac{\partial w_0}{\partial x_1} + \varphi_1 + x_3 \frac{\partial \theta_1}{\partial x_1} + x_3^2 \frac{\partial \theta_2}{\partial x_1}, \\ \gamma_{23} &= \frac{\partial w_0}{\partial x_2} + \varphi_2 + x_3 \frac{\partial \theta_1}{\partial x_2} + x_3^2 \frac{\partial \theta_2}{\partial x_2}. \end{aligned} \tag{3.5}$$

On the contrary for the Mindlin plate, the out-of-plane shear deformations are constants because the terms depending on the thickness coordinate vanish. A global representation of the deformation can be written as

$$\begin{aligned} \boldsymbol{\varepsilon} = & \begin{pmatrix} u_{0,1} & u_{0,2} + v_{0,1} & w_{0,1} + \varphi_1 \\ u_{0,2} + v_{0,1} & v_{0,2} & w_{0,2} + \varphi_2 \\ w_{0,1} + \varphi_1 & w_{0,2} + \varphi_2 & \theta_1 \end{pmatrix} + x_3 \begin{pmatrix} \varphi_{1,1} & \varphi_{1,2} + \varphi_{2,1} & \theta_{1,1} \\ \varphi_{1,2} + \varphi_{2,1} & \varphi_{2,2} & \theta_{1,2} \\ \theta_{1,1} & \theta_{1,2} & 2\,\theta_2 \end{pmatrix} \\ & + x_3^2 \begin{pmatrix} 0 & 0 & \theta_{2,1} \\ 0 & 0 & \theta_{2,2} \\ \theta_{2,1} & \theta_{2,2} & 0 \end{pmatrix}, \end{aligned} \tag{3.6}$$

and $(.)_{,i}$ is the partial derivative of $(.)$ defined as $\dfrac{\partial(.)}{\partial x_i}$. This can be sum up as

$$\boldsymbol{\varepsilon} \;=\; \boldsymbol{\varepsilon}_0 + x_3\,\boldsymbol{\kappa} + x_3\,\boldsymbol{\Theta}. \tag{3.7}$$

It is to mention that the plate theory following the Mindlin ansatz can be seen as a special case of the plate theory with thickness change, if the degrees of freedom θ_1 and θ_2 vanish.

The compatibility condition was previously strongly discussed: some authors states that this is a necessary condition for the element formulation for the convergence, cf. [176]. Other authors [101] point that the compatibility condition is not necessary for the convergence. The consistency condition

$$\frac{\partial^2 \gamma_{ij}}{\partial x_i\,\partial x_j} \;=\; \frac{\partial^2 \varepsilon_{ii}}{\partial x_j^2} + \frac{\partial^2 \varepsilon_{jj}}{\partial x_i^2}, \tag{3.8}$$

is verified for the considered plate theory with seven degrees of freedom, cf. [180], for $(i,j) = (1,2),(1,3),(2,3)$.

3.2.3 Stress, Moment and Higher Order Resultants

In the framework of a plate theory with thickness change, no further transformation of the constitutive law is needed. This point represents one of the advantages of this theory in comparison with the theories following the Mindlin or the Kirchhoff concept. The constitutive laws are three-dimensional ones, that means that the engineering stress resultant $\mathbf{N}$ is a tensor of second order

$$\mathbf{N} \;=\; \begin{bmatrix} N_{11} & N_{12} & N_{13} \\ N_{21} & N_{22} & N_{23} \\ N_{31} & N_{32} & N_{33} \end{bmatrix}, \tag{3.9}$$

as well as the moment resultants $\mathbf{M}$. The conjugated term to the quadratic deformation is called $\mathbf{H}$ and has the size of a vector

$$\mathbf{H}^T \;=\; [H_1, H_2]^T. \tag{3.10}$$

$\mathbf{H}$ can be called the "bimoment", cf. [13], because it results from the curvature of the plate or "hyperstress" following higher order theories. The confusion with the shear resultants from the First order Shear Deformation Theory has to be avoided.

In the plate theory, the relation between the stresses and the engineering stress resultants $\mathcal{N}_M$ can be written as

$$\mathcal{N}_M \;=\; [N_{ij}, M_{ij}, H_\alpha]^T \;=\; \int_{-h/2}^{h/2} [P_{ij}, P_{ij}\,x_3, P_{3\alpha}\,x_3^2]^T \,\mathrm{d}x_3, \tag{3.11}$$

with $\mathbf{P}$ the first Piola-Kirchhoff stress, $i,j = 1,2,3$ and $\alpha = 1,2$. The physical meaning of the hyperstress can be read from Eq. (3.11) as the integration over the thickness of the plate of the first Piola-Kirchhoff stress multiplied with the square value of the thickness coordinate.

In the following, the Voigt notation is employed, as explained in Sect. 2.3 and in Appendix 7.1. Because the deformation are symmetric, as observed in Eq. (3.6), the stress resultants and the moment resultants are also symmetric. Consequently, the Voigt notation can be used, and in this case, the deformations are written in a vector form with six items as

$$
{}^1\boldsymbol{\varepsilon} \;=\; \begin{pmatrix} u_{0,1} \\ v_{0,2} \\ \theta_1 \\ u_{0,2}+v_{0,1} \\ w_{0,1}+\varphi_1 \\ w_{0,2}+\varphi_2 \end{pmatrix} + x_3 \begin{pmatrix} \varphi_{1,1} \\ \varphi_{2,2} \\ 2\,\theta_2 \\ \varphi_{1,2}+\varphi_{2,1} \\ \theta_{1,1} \\ \theta_{1,2} \end{pmatrix} + x_3^3 \begin{pmatrix} 0 \\ 0 \\ 0 \\ 0 \\ \theta_{2,1} \\ \theta_{2,2} \end{pmatrix}, \tag{3.12}
$$

as well as the stress and moment resultants

$$
\begin{aligned}
{}^1\mathbf{N} &= [N_{11}, N_{22}, N_{33}, N_{12}, N_{13}, N_{23}]^T, \\
{}^1\mathbf{M} &= [M_{11}, M_{22}, M_{33}, M_{12}, M_{13}, M_{23}]^T.
\end{aligned} \tag{3.13}
$$

It is to mention that the higher order stress resultants $\mathbf{H}$ are not transformed.

The constitutive equation can be defined as

$$
\mathcal{N}_M \;=\; \mathbb{C} : \begin{bmatrix} {}^1\boldsymbol{\varepsilon}_0 \\ {}^1\boldsymbol{\kappa} \\ {}^1\boldsymbol{\Theta} \end{bmatrix} \;\Leftrightarrow\; \begin{bmatrix} {}^1\mathbf{N} \\ {}^1\mathbf{M} \\ {}^1\mathbf{H} \end{bmatrix} \;=\; \begin{bmatrix} \mathbb{C}^1 & \mathbb{C}^2 & \mathbb{C}^5 \\ \mathbb{C}^9 & \mathbb{C}^3 & \mathbb{C}^6 \\ \mathbb{C}^7 & \mathbb{C}^8 & \mathbb{C}^4 \end{bmatrix} : \begin{bmatrix} {}^1\boldsymbol{\varepsilon}_0 \\ {}^1\boldsymbol{\kappa} \\ {}^1\boldsymbol{\Theta} \end{bmatrix} \tag{3.14}
$$

with $\mathbb{C}^i$ the general stiffness coefficients. $\mathbb{C}^1, \mathbb{C}^2$ and $\mathbb{C}^3$ are tensor of second order containing 6×6 items; $\mathbb{C}^4$ is a tensor of second order containing 2×2 items; $\mathbb{C}^5, \mathbb{C}^6$ are tensor of second order containing 2×6 items and $\mathbb{C}^7, \mathbb{C}^8$ are tensor of second order containing 6×2 items. Some simplifications can be performed: in most of the cases the hyperstresses are only depending on the quadratic deformations $\boldsymbol{\Theta}$ and $\mathbb{C}^5$, $\mathbb{C}^6$, $\mathbb{C}^7$ and $\mathbb{C}^8$ are set to zero. Similarly as for the "classical theories" [154], in case of symmetric laminates, the stiffness coefficient $\mathbb{C}^2$ and $\mathbb{C}^9$ are set to zero. A constitutive law following the Voigt notation can be explicitly written for an isotropic elastic material for $\mathbb{C}^1$ as

$$
\mathbb{C}^1 \;=\; \begin{bmatrix} \frac{E}{1-\nu^2}\,h & \frac{E\,\nu}{1-\nu^2}\,h & \frac{E\,\nu}{1-\nu^2}\,h & 0 & 0 & 0 \\ \frac{E\,\nu}{1-\nu^2}\,h & \frac{E}{1-\nu^2}\,h & \frac{E\,\nu}{1-\nu^2}\,h & 0 & 0 & 0 \\ \frac{E\,\nu}{1-\nu^2}\,h & \frac{E\,\nu}{1-\nu^2}\,h & \frac{E}{1-\nu^2}\,h & 0 & 0 & 0 \\ 0 & 0 & 0 & G\,h & 0 & 0 \\ 0 & 0 & 0 & 0 & G\,h & 0 \\ 0 & 0 & 0 & 0 & 0 & G\,h \end{bmatrix}, \tag{3.15}
$$

for the stress resultants,

$$\mathbb{C}^3 = \begin{bmatrix} \frac{E}{1-\nu^2}\frac{h^3}{12} & \frac{E\,\nu}{1-\nu^2}\frac{h^3}{12} & \frac{E\,\nu}{1-\nu^2}\frac{h^3}{12} & 0 & 0 & 0 \\ \frac{E\,\nu}{1-\nu^2}\frac{h^3}{12} & \frac{E}{1-\nu^2}\frac{h^3}{12} & \frac{E\,\nu}{1-\nu^2}\frac{h^3}{12} & 0 & 0 & 0 \\ \frac{E\,\nu}{1-\nu^2}\frac{h^3}{12} & \frac{E\,\nu}{1-\nu^2}\frac{h^3}{12} & \frac{E}{1-\nu^2}\frac{h^3}{12} & 0 & 0 & 0 \\ 0 & 0 & 0 & G\frac{h^3}{12} & 0 & 0 \\ 0 & 0 & 0 & 0 & G\frac{h^3}{12} & 0 \\ 0 & 0 & 0 & 0 & 0 & G\frac{h^3}{12} \end{bmatrix}, \tag{3.16}$$

for the moment resultants and

$$\mathbb{C}^4 = \begin{bmatrix} G\frac{h^5}{60} & 0 \\ 0 & G\frac{h^5}{60} \end{bmatrix}, \tag{3.17}$$

for the hyperstress. These results are valid for a one layer material. For a composite plate containing several layers, the reader is referred to the Appendix 7.4. In Appendix 7.4, the constitutive law for a composite plate, according to the First order Shear Deformation Theory, is also developed. A further advantage of the plate theory with seven degrees of freedom -or of the numerical homogenisation- is that no correction factor is needed for the shear forces.

3.2.4 Balance Equations

By applying the principle of virtual displacements, it can be proved [154] that the following equations are obtained

$$\begin{bmatrix} N_{11,1} + N_{12,2} \\ N_{12,1} + N_{22,2} \\ N_{13,1} + N_{23,2} + \mathcal{N}(w_0) + q \\ M_{11,1} + M_{12,2} - N_{13} \\ M_{12,1} + M_{22,2} - N_{23} \\ -N_{33} + M_{13,1} + M_{23,2} \\ -2\,M_{33} + H_{13,1} + H_{23,2} \end{bmatrix} = \mathbf{0},$$

in case of a static problem without external forces. The first five equations are similar as for the plate theory following the Mindlin ansatz; the last two ones result from the formulation of the thickness change.

3.3 Weak Formulation

In this part, some details about the FE analysis of plates are explained. For a complete description, it can be referred to Wriggers [194], for two- and three-dimensional problems and for plate elements. Some literature specified to the formulation of a FE method for plates can be found in [97, 179] for a Kirchhoff plate or in [98, 154] for the classical plate theory and the First order Shear Deformation Theory.

After discretisation of the domain and creation of the mesh, the principle of virtual work can be applied. It states that the virtual power of the stresses in a volume V is equal to the virtual power of the forces acting on the boundary S of the volume

$$\begin{aligned}\int_{\mathcal{V}} \delta\mathbf{u} : \boldsymbol{\sigma}\, \mathrm{d}V &= \delta u_{0,1}\, N_{11} + \delta u_{0,2}\, N_{12} \\ &+ \delta v_{0,1}\, N_{12} + \delta v_{0,2}\, N_{22} \\ &+ \delta w_{0,1}\, N_{13} + \delta w_{0,2}\, N_{23} \\ &+ \delta\varphi_{1,1}\, M_{11} + \delta\varphi_{1,2}\, M_{12} + \delta\varphi_1\, N_{13} \\ &+ \delta\varphi_{2,1}\, M_{12} + \delta\varphi_{2,2}\, M_{22} + \delta\varphi_2\, N_{23} \\ &+ \delta\theta_1\, N_{33} + \delta\theta_{1,1}\, M_{13} + \delta\theta_{1,2}\, M_{23} \\ &+ 2\,\delta\theta_2\, M_{33} + \delta\theta_{2,1}\, H_1 + \delta\theta_{2,2}\, H_2. \end{aligned} \tag{3.18}$$

$\mathbf{N}, \mathbf{M}, \mathbf{H}$ are the resultants of the stress distribution in the surface area. Assuming that $\delta\theta_1 = \delta\theta_2 = 0$ leads to principle of virtual displacement for the plate theory following the Mindlin concept within the Finite Element Method. In addition to the definition of the weak form, a discretisation of the geometry in finite elements is needed, which defines elements and nodes. The field quantities, such as deformations and stresses, are approximated with ansatz functions, which are defined locally. The kinematic degrees of freedom can be approximated with an interpolation function, like for example a Lagrange function

$$\begin{aligned} u_0(x_1,x_2) &= \sum_{k=1}^{n} \psi^k(x_1,x_2)\, u_0^k, & \varphi_1(x_1,x_2) &= \sum_{k=1}^{n} \psi^k(x_1,x_2)\, \varphi_1^k, \\ v_0(x_1,x_2) &= \sum_{k=1}^{n} \psi^k(x_1,x_2)\, v_0^k, & \varphi_2(x_1,x_2) &= \sum_{k=1}^{n} \psi^k(x_1,x_2)\, \varphi_2^k, \\ w_0(x_1,x_2) &= \sum_{k=1}^{n} \psi^k(x_1,x_2)\, w_0^k, & \theta_1(x_1,x_2) &= \sum_{k=1}^{n} \psi^k(x_1,x_2)\, \theta_1^k, \\ & & \theta_2(x_1,x_2) &= \sum_{k=1}^{n} \psi^k(x_1,x_2)\, \theta_2^k, \end{aligned} \tag{3.19}$$

where n is the total number of nodes. The interpolations are chosen to be locally quadratic, in order to avoid locking effects. The vector containing the seven degrees of freedom is defined as

$$\begin{aligned} {}^1\mathbf{u} &= {}^1\mathbf{u}_0 + x_3\, {}^1\mathbf{u}_1 + x_3^2\, \theta_2\, \mathbf{e}_3 \\ &= \begin{pmatrix} u_0 \\ v_0 \\ w_0 \end{pmatrix} + x_3 \begin{pmatrix} \varphi_1 \\ \varphi_2 \\ \theta_1 \end{pmatrix} + x_3^2\, \theta_2\, \mathbf{e}_3 \end{aligned} \tag{3.20}$$

The displacements can be written in the form of vectors for the translational displacements ${}^1\mathbf{u}_0$ and the rotations ${}^1\mathbf{u}_1$ as

$$\begin{aligned} {}^1\mathbf{u}_0 &= \sum_{k=1}^{n} \boldsymbol{\psi}_0^k(x_1, x_2) \cdot {}^1\mathbf{u}_0^k, \\ {}^1\mathbf{u}_1 &= \sum_{k=1}^{n} \boldsymbol{\psi}_1^k(x_1, x_2) \cdot {}^1\mathbf{u}_1^k. \end{aligned} \tag{3.21}$$

The $\boldsymbol{\psi}_i^k$ are the matrices containing the shape functions. As for two or three-dimensional problems, an isoparametric concept has to be followed; as developed by [5, 154, 194]. Finally, the generalised strains can be written as

$$\begin{aligned} {}^1\boldsymbol{\varepsilon}_0 &= \sum_{k=1}^{n} \mathbf{D}_0^k \cdot {}^1\mathbf{u}_0^k, \\ {}^1\boldsymbol{\kappa} &= \sum_{k=1}^{n} \mathbf{D}_1^k \cdot {}^1\mathbf{u}_1^k, \\ {}^1\boldsymbol{\Theta} &= \sum_{k=1}^{n} \mathbf{D}_2^k \, {}^1\theta_2^k, \end{aligned} \tag{3.22}$$

with $\mathbf{D}_i^k$ are the matrices representation of the differential operator. It is to mention that, considering the Voigt notation, the deformations are defined as vectors containing six items. As a consequence, the matrices representation of the differential operators $\mathbf{D}_0^k$ and $\mathbf{D}_1^k$ are matrices containing each 6×6 items and $\mathbf{D}_2^k$ is a vector defining the differential operator for the seventh degree of freedom as $\left[\frac{\partial}{\partial x_1}, \frac{\partial}{\partial x_2}\right]^T$.

Using the principle of virtual work (3.18) with the generalized displacements (3.21) and strains (3.22) leads to the following linear system of equations

$$\mathbf{K} \cdot \begin{bmatrix} \mathbf{u}_0 \\ \mathbf{u}_1 \\ u_2 \end{bmatrix} = \mathbf{f}, \tag{3.23}$$

with $\mathbf{f}$ the vector of the volume forces and the surface forces. The symmetric stiffness matrix $\mathbf{K}$ is defined as

$$\mathbf{K} = \int_{\mathcal{B}} \mathbf{D}^T \cdot \mathbb{C} \cdot \mathbf{D} \, \mathrm{d}v, \tag{3.24}$$

for a two or three-dimensional problem. For the presented plate theory, the symmetric stiffness matrix $\mathbf{K}$ is developed in appendix 7.5.

3.4 Convergence and Locking

Unfortunately, many locking or hourglass stiffness effects occur for FE plates, cf. [13, 101, 122, 165]. There is not a single definition of locking [13], but different ways to define the locking. Bischoff [13] defines three different ways to describe the locking effect: the mathematical, the numerical and the mechanical point of view. The mathematical point of view describes the effect of one parameter on the convergence properties of the problem. However, it does not include all locking effects, as for instance the shear locking which does not exist according to this definition [101] and the "mathematical point of view describes more a bad conditioning problem than the locking"[1], cf. Braess [17]. The numerical point of view was shown by Hughes [86] and describes the tendency of one element to present a too stiff reaction with a parameter, which defines the ratio of the number of degrees of freedom related to the constraints upon the number of constraints. This parameter is then compared with the optimal constraint. The mechanical point of view is defined with the appearance of parasitic stresses, which do not exist in the exact solution. In the present work, the mechanical point of view is followed and the main types of locking, which appears for the FE plate, are described, cf. [13, 101].

The **shear locking** happens for linear elements under bending conditions, where some parasitic stresses occur, because the elements are too stiff. In our work, quadratic elements are used to avoid this effect. Furthermore, for FE plates, the **transverse shear locking** can take place, also under bending conditions. For a pure bending problem, there are parasitic shear stresses, which do not appear in a three-dimensional FE computation. In this work, a practical solution is obtained by quadratic elements, since this effect occurs for bilinear elements. Another solutions for the shear locking and the transverse shear locking consist by using a reduced integration or the ANS (Assumed Natural Strain) method, cf. [101].

For FE shells or for curved elements, some other locking effects can appear like the **membrane locking** or **the curvature thickness locking** . The membrane locking occurs for curved elements -but not for curved linear or bilinear elements- and for very thin structures, where some parasitic membrane stresses are observed. The curvature thickness locking happens for curved elements with thickness change, where some parasitic normal stresses in thickness direction are observed, due to the bad approximation of the normal deformation in thickness direction, cf. [165]. It can be solved with an ANS method or a DSG (Discrete Shear Gap) method. Because these locking effects occur only for shell or curved elements, they will not be treated in this work, but the reader is referred to the dissertations by Bischoff [13], Koschnick [101] and Schlebusch [165].

In this work, special attention is paid to the **Poisson or volume locking**, cf. [13]. It is to mention that no volume locking occurs for a Poisson ratio equal to 0 and that the volume locking is more important for a Poisson's ratio tending to 0.5. Because it is the case for an elasto-plastic material behaviour with plastic incompressibility, a special attention is given to the solution of the Poisson locking in the present work. The Poisson locking occurs for a plate theory with five or six degrees of freedom; however, it can be

[1] "Aus mathematischer Sicht würde man lieber von einem schlecht konditionnierten Problem sprechen als von Locking", cf. Braess [17], translated by myself

avoided for a plate theory with thickness change. In the present work, a displacement field of quadratic order for the displacement in thickness direction is considered for the comparison using the FE plate; nevertheless it is also possible to consider only a linear displacement field and to use the EAS (Enhanced Assumed Strain) method, as mentioned before.

There are mainly two types of solutions for the locking problems [13]: on the one hand, the parts which are responsible for the locking are remote, as it is the case for the selective integration, the ANS or the DSG methods. On the other hand, there is the possibility to equilibrate the behaviour between stress and strain with the insertion of other parts, as performed in the EAS method for instance. The principle of the ANS (Assumed Natural Strain) method is not to compute the transverse shear directly as the derivative of the displacements, because it leads to parasitic stresses in this case. Instead of that, the discrete deformations are computed from the so-called sampling points and an interpolation to the element is performed using specific ansatz functions. The sampling points are located in the middle of the edge. For a complete description of the ANS method, it can be referred to [13, 101, 165], among others. The Discrete Shear Gap (DSG) method, also defined as the Discrete Strain Gap method [101], was firstly proposed by Bletzinger et al. [15]. The principle is similar to the ANS method's principle by the modification of the distribution of the deformation. Considering the ANS method, the sampling points have to be chosen for each type of element (form of the element and polynomial order of the ansatz function), which is not the case for the DSG method. The deformations are not computed directly using the interpolation of the displacement of the nodes, but the shear and bending parts are firstly decomposed. The differences between the actual displacements and the displacements related to a pure bending mode define the shear gaps, which are interpolated and used to compute the shear strains, resulting in an element free of locking, cf. [15, 13, 101].

The principle of the EAS (Enhanced Assumed Strain) method was firstly described by Simo & Rifai [173]. Its principle is to enable a linear deformation in thickness direction with the introduction of an extra degree of freedom, with the difference that the extra degree of freedom is not globally solved, but in the level of the element. Consequently, it is not considered in the global consistent tangent and the number of degrees of freedom is not increased, cf. [13]. The EAS method can be solely used in order to avoid the Poisson locking. In the present work, a similar principle as the EAS method is used in order to restraint the Poisson locking. An extra degree of freedom is introduced in the mesoscale, and is computed during a first iteration as the average value of the normal deformation in thickness direction. It is then transferred in the macroscale and used for the projection in the next iteration, which enables a consideration of the thickness change in the level of the plate and of the three-dimensional RVE.

In order to verify the implemented FE plate model, some tests can be made, like for instance the patch test, originally proposed by Bazeley et al. (1966), cf. [13]. Although the patch test is "neither essential nor sufficient"[2], cf. Bischoff [13], it will be adopted in our context for triangle elements, because it gives an indicator for convergence (but not for locking). The principle consists in the computation of a compression or a shear test

[2] "weder notwendig noch hinreichend", cf. Bischoff [13], translated by myself

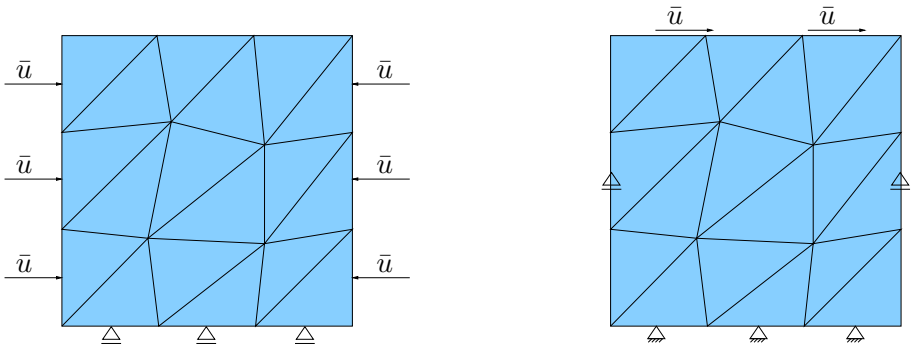

Figure 3.3: Boundary conditions for the patch test: compression test on the left, shear test on the right

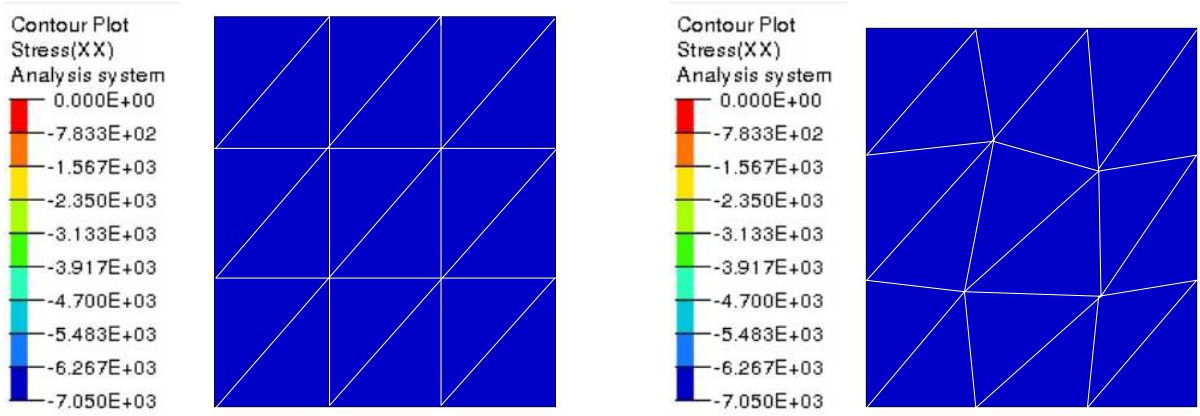

Figure 3.4: Result of the patch test for the compression (right: reference, left: patch test)

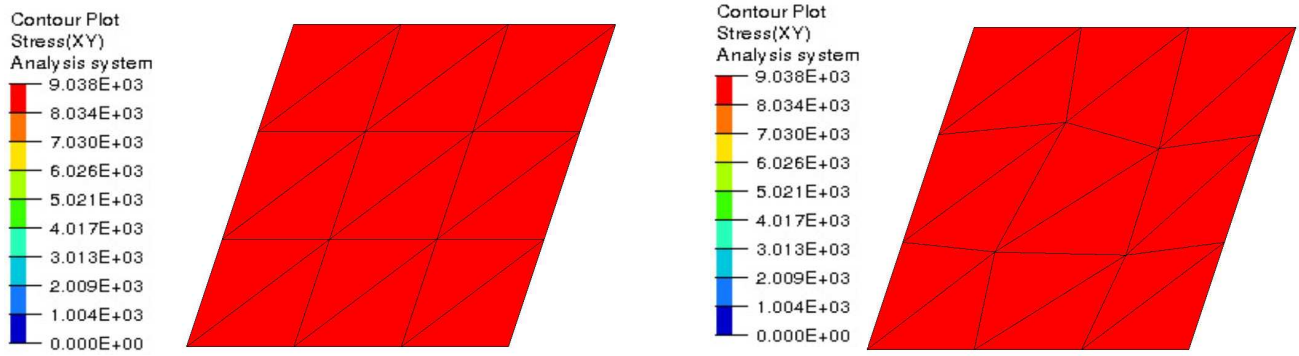

Figure 3.5: Result of the patch test for the shear test (right: reference, left: patch test)

on a square, where some nodes suffer a translation, as can be seen in Fig. 3.3.

The patch test is obviously validated in our context, because the stresses are homogeneous in the square, as can be seen in Fig. 3.4 for the compression test and in Fig. 3.5 for the shear test. In both cases, regular and slightly disturbed meshes are used for the computations. Both meshes lead to exactly the same results.

In the second example, a Cook's membrane is computed, cf. [165], as investigated by many authors since 1990. This problem -as shown in Fig. 3.6- is traditionally computed for a two-dimensional configuration in the plane stress state. However, a three-dimensional problem with a thin thickness is set as reference, in order to avoid any error obtained with the plane stress assumption. The resulting shear stress distribution is shown in Fig. 3.7. In the presented example only one material layer is considered, to enable an easier comparison with the three-dimensional modelling. The Cook's membrane enables to test the membrane behaviour of a plate with respect to shear locking. On the left side, the displacements are set to zero and on the right side, a vertical displacement is imposed, as represented in Fig. 3.6.

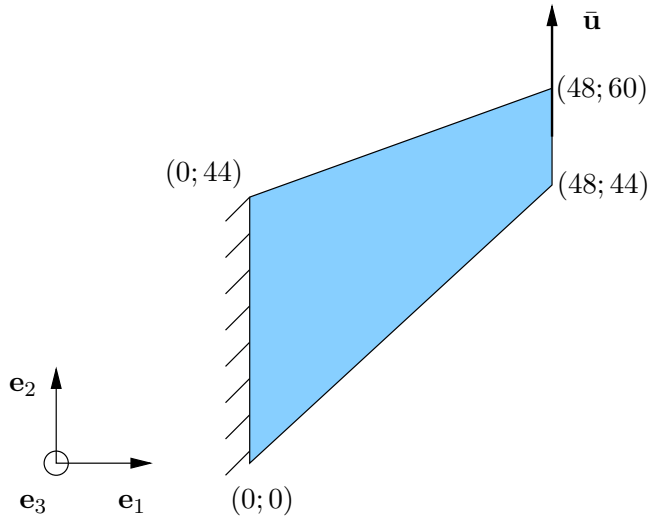

Figure 3.6: Boundary conditions for the Cook's membrane

The results obtained with the three-dimensional problem, computed by ABAQUS®, are represented in Fig. 3.7. They are considered as the reference. The elements are linear with reduced integration (C3D8R), and the discretisation is made with $32 \times 32 \times 1$ elements; because some authors [165] considered that a discretisation performed with at least 16×16 elements leads to accurate results. The results obtained by the plate theory following the Mindlin ansatz and the plate theory with thickness change are represented in Fig. 3.8. In order to obtain a discretisation, which can be accurately compared with the results given by the three-dimensional results, a "black jack" discretisation is considered. It can be observed that there are almost no differences between the stress computed for the plate theory with five and with seven degrees of freedom, due to the reduced thickness change in this test. In contrast, the difference in the shear stress is less than 1% between the shear stress given by the plate theories and the three-dimensional solution. It can be concluded that the considered plate theories gives accurate results for the Cook's test.

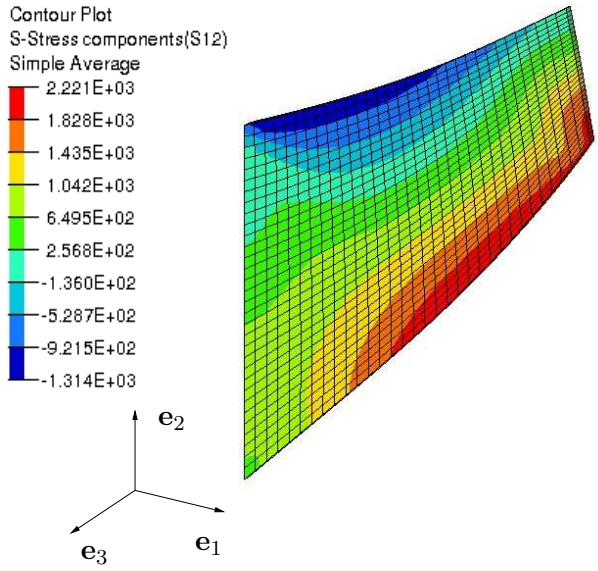

Figure 3.7: Shear stress for the Cook's membrane in a three-dimensional FE computation for ABAQUS®

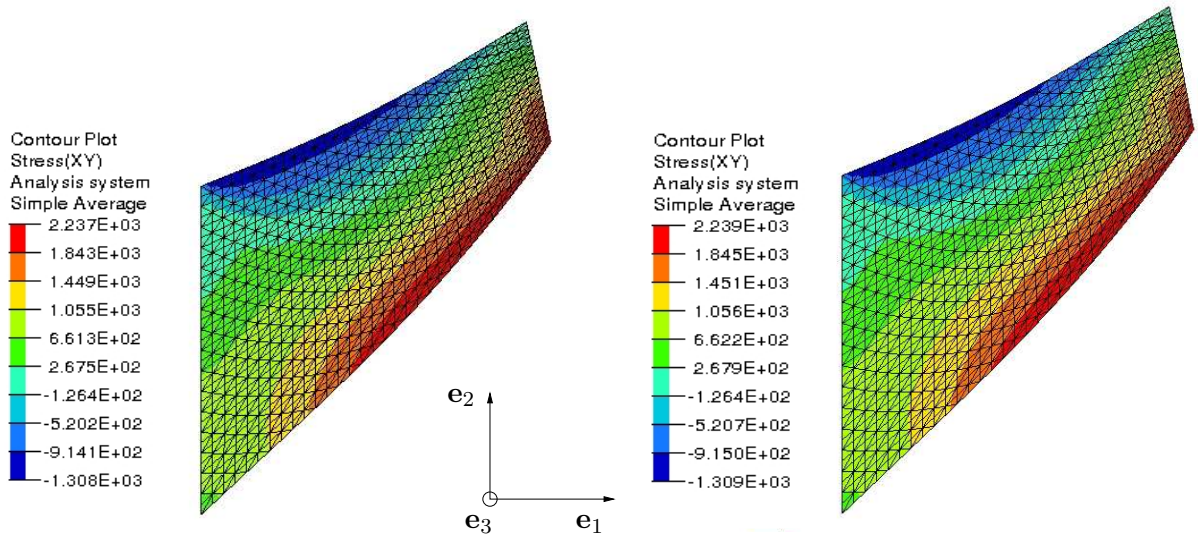

Figure 3.8: Shear stress for the Cook's membrane with for the plate theory (left: plate theory following the Mindlin ansatz, right: plate theory with thickness change)

3.5 Conclusions

In this part, the plate theories used in this work are presented. On the one hand, a plate theory following the Mindlin concept is employed in the framework of the FE^2 method for plates. This theory can be considered as a particular case of the plate theory with seven degrees of freedom, when the last two degrees of freedom vanishes. The plate theory with five degrees of freedom is consistent, cf. [96]. However, the constitutive laws are two-dimensional and the thickness change is not considered. Because of its stability, the plate theory following the Mindlin concept is further employed in the framework of the numerical homogenisation; nevertheless, a modified projection enables to consider the thickness change. On the other hand, the proposed FE^2 method is compared to the plate theory with seven degrees of freedom and with the three-dimensional solution, because the plate theory with seven degrees of freedom enables a consideration of the thickness change and of the three-dimensional constitutive material laws.

It is to mention that the presented work is restricted to composites plates; however, the same method can be used to model the behaviour of shells. For a description of the shell theories, it can be referred to [68, 140, 198], and further to the work of Matheas et al. [122] and Coda & Paccola [34] for the FE implementation of a finite shell model with thickness change.

In the next chapter, the theoretical context of the FE^2 method for plates will be described; the plate theory used for the macroscale computation is assumed to be the plate theory without thickness change, that means with only five degrees of freedom, described in this chapter as a particular case of the plate theory with thickness change.

Chapter 4

Numerical Homogenisation of Plates

In this part, the full description of the proposed numerical homogenisation method is explained. The numerical homogenisation or so-called FE^2 for plates consists in the separation of the problem in two scales: the macroscale, where a homogeneous layer is considered, and the mesoscale, consisting of a three-dimensional FE computation discretizing the layer organisation. The principle of the FE^2 method is summarized in Fig. 4.1 and consists of four steps, cf. [36, 65, 108].

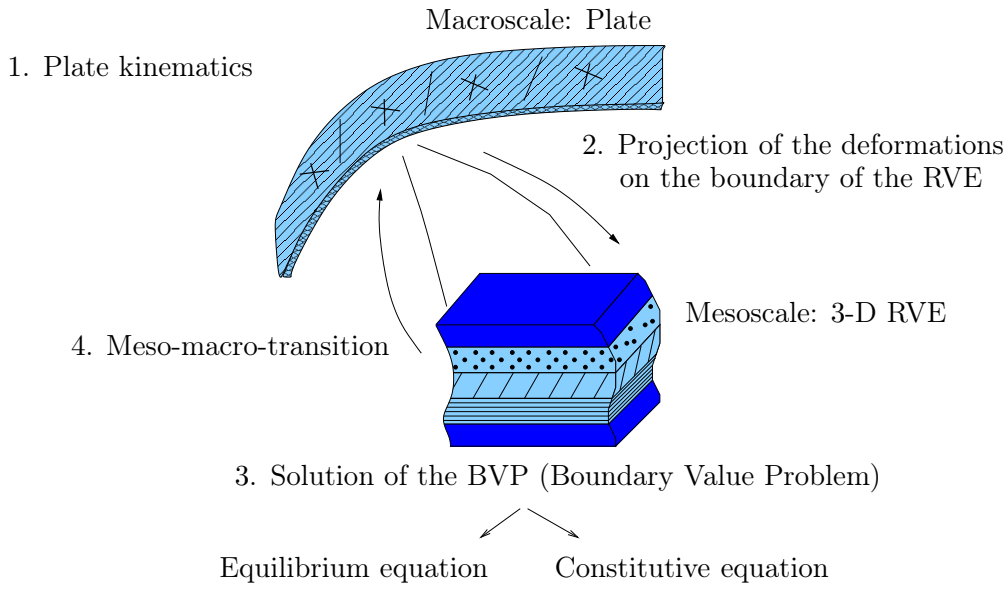

Figure 4.1: Schematic representation of the FE^2 method

1. Firstly, an accurate plate kinematic has to be defined. In the macroscale, a first FE computation of a plate is made, where the plate kinematics are considered. In the present work, the plate theory following the Mindlin concept is regarded.

2. Then, from each integration point of the macroscale discretisation, the deformations have to be projected in an accurate manner to the boundary of the RVE (Representative Volume Element). This defines a corresponding mesoscale boundary value problem with Dirichlet type conditions on the the boundaries. The so defined problems are solved by independent FE computations.

3. In a third step, the boundary value problem on the mesoscale is solved within the three-dimensional mesoscopic FE problem. As mentioned before, the RVE has to be large enough to be representative of the heterogeneities of the mesostructure, but not too large, in order to avoid extreme large computation time. Furthermore, gradients of the macroscale solution have to be resolved.

4. Finally, the stress resultants are determined using a meso-macro transition. Due to the high computational costs of the method, special attention is given towards the definition of an analytical tangent of the coupled multiscale computation.

The principle of this method can be found in [32]. Considering a homogenisation method, the principle of the scale separation has to be respected, as developed in [135]. In the framework of a numerical homogenisation of composite plates, a macro-, meso- and microscale can be defined. The macroscale defines the whole composite plate, as represented in Fig. 4.2 on the left, whereas the mesoscale takes into account the different layer organisation, as can be seen in Fig. 4.2 in the middle. As a following, the mesoscale can be

Figure 4.2: Representation of the three scales: a: picture of the whole composite structure (macroscale), b: picture of the layers organisation (mesoscale) and c: optical microscopy picture of the fibers surrounded by the matrix (microscale)

considered as a thin part of the macroscale. Consequently, the mesoscale is not a plate but a three-dimensional volume, because the typical length of the mesoscale is of the same order of magnitude as its width. The microscale defines the microstructure, that means for the considered composite plates the bounding between the different layers, or the bounding of the fibers surrounded by the matrix, as shown in Fig. 4.2 on the right. The composite plates represented in Fig. 4.2 a and 4.2 b are supplied by the DLR in Cologne (Prof. Dr.-Ing. Marion Bartsch, Dr.-Ing. Joachim Hausmann, Karola Schulze), and the structure represented in Fig. 4.2 c is given by the professorship lightweight structures and polymer engineering (Univ.-Prof. Dr.-Ing. habil. Lothar Kroll, Sebastian Nendel).

In the scope of a homogenisation, the principle of the scale separation [135] can be expressed as

$$\lambda_{\text{macro}} \gg \lambda_{\text{meso}}, \tag{4.1}$$

that means that the characteristic length scale λ_{macro} of the macroscale has to be much bigger than the characteristic length scale λ_{meso} of the mesoscale. In the case of a numerical homogenisation of plates, the assumption (4.1) is only true in the two directions parallel to the plate midsurface. It is namely not true for the direction normal to the plate's midplane, because the mesoscale can be considered as a thin part of the macroscale, which has for thickness the thickness of the whole composite. For this reason, the homogenisation is only applied in the two directions parallel to the midplane, and in the thickness direction a full resolution of the RVE occurs.

4.1 Plate Kinematics

In this part, the plate kinematics used for the FE^2 method are briefly described. A plate theory following the Mindlin concept with five degrees of freedom is considered [5, 6, 154] and the displacement can be written as

$$\begin{aligned} \bar{u}(\bar{x}_1, \bar{x}_2, x_3) &= \bar{u}_0(\bar{x}_1, \bar{x}_2) + x_3\, \bar{\varphi}_1(\bar{x}_1, \bar{x}_2), \\ \bar{v}(\bar{x}_1, \bar{x}_2, x_3) &= \bar{v}_0(\bar{x}_1, \bar{x}_2) + x_3\, \bar{\varphi}_2(\bar{x}_1, \bar{x}_2), \\ \bar{w}(\bar{x}_1, \bar{x}_2, x_3) &= \bar{w}_0(\bar{x}_1, \bar{x}_2). \end{aligned} \tag{4.2}$$

$\bar{u}, \bar{v}, \bar{w}$ are the three displacement degrees of freedom and $\bar{\varphi}_1, \bar{\varphi}_2$ are the two rotations. The coordinate in the macroscale are defined with bars, as $(\bar{x}_1, \bar{x}_2)$; it is to mention that the macroscopic thickness coordinate is equal to the mesoscopic thickness coordinate, with $\bar{x}_3 = x_3$. The two longitudinal coordinates are expressed with $\bar{x}_1, \bar{x}_2$ for the macroscale and x_1, x_2 for the three-dimensional mesoscale. The macroscopic displacements are written also with bars $\bar{\diamond}$, for clarity. The mesoscopic displacements are written by small letters without bars, e. g. $\diamond$. The reference and current configurations are defined for the macroscale and for the mesoscale in Fig. 4.3.

$\bar{\mathbf{X}}, \bar{\mathbf{x}}$ are defined as the position of a point in the macroscale in the reference and current configurations. The vector of displacement in the macroscale is defined as

$$\bar{\mathbf{u}} = \bar{\mathbf{x}} - \bar{\mathbf{X}} = \begin{bmatrix} \bar{u}_0 + x_3\, \bar{\varphi}_1 \\ \bar{v}_0 + x_3\, \bar{\varphi}_2 \\ \bar{w}_0 \end{bmatrix}. \tag{4.3}$$

The relative coordinates in the RVE are defined respectively to the center of the RVE in the reference and current configurations with $\mathbf{X}, \mathbf{x}$. In the mesoscale, the vector of displacement is described as

$$\mathbf{u} = \mathbf{x} - \mathbf{X}. \tag{4.4}$$

The surface of the mesoscale is defined as $\mathcal{A}_0$ and its volume as $\mathcal{V}_0$ in the reference configuration.

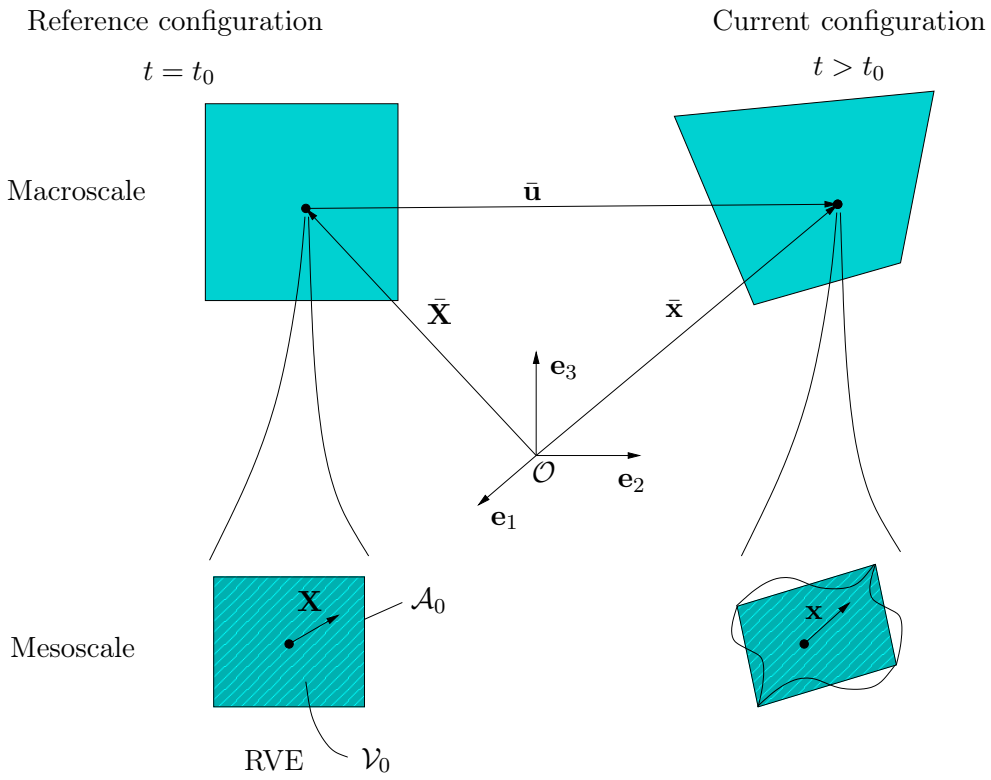

Figure 4.3: Reference and current configurations for the FE^2 problem: from each integration points of the macroscale discretisation, the deformations are projected to the boundary of the RVE (Representative Volume Element) in the mesoscale

The macroscopic deformations are defined using the Voigt notation as

$$
{}^1\bar{\boldsymbol{\varepsilon}} = \begin{pmatrix} \bar{u}_{0,1} \\ \bar{v}_{0,2} \\ 0 \\ \bar{u}_{0,2} + \bar{v}_{0,1} \\ \bar{w}_{0,1} + \bar{\varphi}_1 \\ \bar{w}_{0,2} + \bar{\varphi}_2 \end{pmatrix} + x_3 \begin{pmatrix} \bar{\varphi}_{1,1} \\ \bar{\varphi}_{2,2} \\ 0 \\ \bar{\varphi}_{1,2} + \bar{\varphi}_{2,1} \\ 0 \\ 0 \end{pmatrix}, \tag{4.5}
$$

with

$$
\begin{aligned}
{}^1\bar{\boldsymbol{\varepsilon}}_0 &= [\bar{u}_{0,1}, \bar{v}_{0,2}, 0, \bar{u}_{0,2} + \bar{v}_{0,1}]^T; \quad {}^1\bar{\boldsymbol{\kappa}} = [\bar{\varphi}_{1,1}, \bar{\varphi}_{2,2}, 0, \bar{\varphi}_{1,2} + \bar{\varphi}_{2,1}]^T; \\
{}^1\bar{\boldsymbol{\gamma}} &= [\bar{w}_{0,1} + \bar{\varphi}_1, \bar{w}_{0,2} + \bar{\varphi}_2]^T.
\end{aligned} \tag{4.6}
$$

Considering the plate theory following the Mindlin concept, the normal deformation in thickness direction ε_{033} is considered as insignificant in comparison to the normal deformations in longitudinal directions ε_{011} and ε_{022}. The mesoscopic volume of the reference and current configuration are defined as $\mathcal{V}_0$ and $\mathcal{V}$, respectively. The mesoscopic surfaces of the reference and current configuration are defined as $\mathcal{A}_0$ and $\mathcal{A}$, respectively. For a further description of the deformations and of the equilibrium equations, the reader is referred to Chapt. 3.

4.2 Projection

4.2.1 General aspects

In the presented work, it will be shown that the kind of projection has a critical influence on the results. There are several kinds of projection rules: the simplest one is the so-called Taylor or Voigt assumption, where a homogeneous deformation is projected to the RVE, cf. [102]. Its opposite is the Sachs or Reuss assumption, where a constant stress is projected to the mesoscale. However, the Taylor assumption leads to an overestimation of the results, whereas the Sachs assumption drives to an underestimation of the results. Furthermore, both Taylor and Sachs assumptions are inadequate for sandwich plates, due to the heterogeneities of the deformations or resultants. For theses reasons, a projection of the deformations is restricted to the boundaries of the RVE

$$\mathbf{u} \;=\; \mathrm{Grad}\,\bar{\mathbf{u}} + \widetilde{\mathbf{u}}, \tag{4.7}$$

where $\mathbf{u}$ represents the total displacement of the mesoscale and $\widetilde{\mathbf{u}}$ are the displacements which come from the fluctuation field. The fluctuations are also called by some authors $\mathbf{u}^f$ or $\mathbf{u}^S$ for subscale, cf. [110].

4.2.2 Taylor Development of the Macroscopic Field

The variation of the mesoscopic displacement can be written as

$$\Delta\mathbf{u} \;=\; \mathrm{Grad}\,\bar{\mathbf{u}} \cdot \Delta\mathbf{X} + \Delta\widetilde{\mathbf{u}}, \tag{4.8}$$

with $\Delta\mathbf{X}$ defined as the difference between the position of one point in the RVE and the center of the RVE

$$\Delta\mathbf{X} \;=\; \mathbf{X} - \mathbf{X}_0, \tag{4.9}$$

and $\mathbf{X}_0$ is the center of the RVE, as drawn in Fig. 4.4.

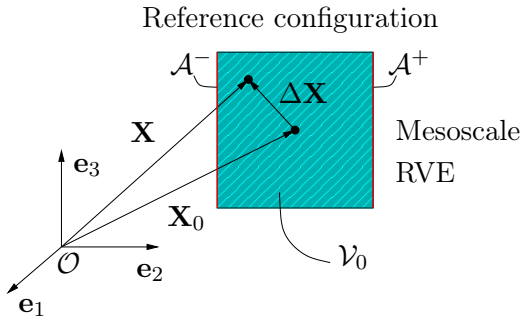

Figure 4.4: Definition of the mesoscopic RVE (Representative Volume Element) in the reference configuration

With insertion of the macroscopic displacement, defined in Eq. (4.2), the Taylor expansion of the macroscopic field becomes

$$\mathrm{Grad}\,\bar{\mathbf{u}}(\bar{x}_1, \bar{x}_2, x_3) \cdot \Delta\mathbf{X} \;=\; \begin{bmatrix} \bar{u}_{,\alpha}\,\Delta X_\alpha + x_3\,\bar{\varphi}_{1,\alpha}\,\Delta X_\alpha + \Delta\bar{\varphi}_1\,\Delta X_3 \\ \bar{v}_{,\alpha}\,\Delta X_\alpha + x_3\,\bar{\varphi}_{2,\alpha}\,\Delta X_\alpha + \Delta\bar{\varphi}_2\,\Delta X_3 \\ \bar{w}_{,\alpha}\,\Delta X_\alpha \end{bmatrix}. \tag{4.10}$$

The operator $\diamond_{,\alpha}$ is defined as the partial derivative $\dfrac{\partial \diamond}{\partial X_\alpha}$ of $\diamond$ with respect to X_α, $\alpha = 1, 2$.

4.2.3 Fluctuations

Due to the scale separation, it has to be assumed that the split $\mathbf{u} = \operatorname{Grad} \bar{\mathbf{u}} + \widetilde{\mathbf{u}}$ is unique, cf. [110]. In order to impose this condition, it is set that the average of the total mesoscopic field is equal to the average of the Taylor series

$$\langle \mathbf{u} \rangle \;=\; \langle \operatorname{Grad} \bar{\mathbf{u}} \rangle, \tag{4.11}$$

because the average of the fluctuation field is set to zero

$$\langle \widetilde{\mathbf{u}} \rangle \;=\; \mathbf{0}, \tag{4.12}$$

cf. [110]. $\langle \diamond \rangle$ is defined as the volume integral of $\diamond$ over the domain $\mathcal{V}_0$ of the RVE

$$\langle \diamond \rangle \;=\; \frac{1}{|\mathcal{V}_0|} \int_{\mathcal{V}_0} \diamond \, \mathrm{d}V. \tag{4.13}$$

Periodic boundary conditions are chosen, i. e. that the part of the displacement coming from the fluctuations from one side of RVE imposes the same fluctuation displacement on the other side of the RVE and it results

$$\mathbf{x}^+ - \mathbf{x}^- \;=\; \bar{\mathbf{F}} \cdot (\mathbf{X}^+ - \mathbf{X}^-) \;=\; (\mathbf{I} + \operatorname{Grad} \bar{\mathbf{u}}) \cdot (\mathbf{X}^+ - \mathbf{X}^-). \tag{4.14}$$

The index $\diamond^+$ accounts for one side of the RVE and the index $\diamond^-$ for the opposite side. The surfaces are defined as $\mathcal{A} = \mathcal{A}^+ \cup \mathcal{A}^-$. The principle of the periodicity of the fluctuation can be represented in Fig. 4.5, where the plain blue lines represent the mesoscopic displacement coming from the macroscopic displacement and the dotted black lines are the whole displacement. The difference between them, represented by the arrows, are the fluctuations (which are equal from one side to the other). It is to mention that the displacements are only applied to the surfaces of the RVE with a normal vector tangential to the midplane. The top and bottom surfaces (defined with a normal vector perpendicular to the midplane) are left free.

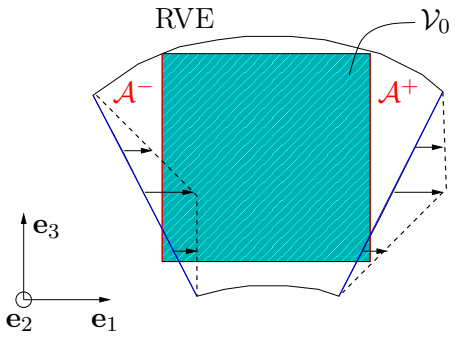

Figure 4.5: Schematic representation of the displacement fluctuation field

Firstly, the average of the fluctuations is per definition equal to zero with $\langle \widetilde{\mathbf{u}} \rangle = \mathbf{0}$, in order to guarantee an unique split, which leads to

$$\begin{aligned} \langle \widetilde{u} \rangle &= \frac{1}{|\mathcal{V}_0|} \int_{\mathcal{V}_0} \widetilde{u} \, \mathrm{d}V, \\ \langle \widetilde{v} \rangle &= \frac{1}{|\mathcal{V}_0|} \int_{\mathcal{V}_0} \widetilde{v} \, \mathrm{d}V, \\ \langle \widetilde{w} \rangle &= \frac{1}{|\mathcal{V}_0|} \int_{\mathcal{V}_0} \widetilde{w} \, \mathrm{d}V. \end{aligned} \tag{4.15}$$

Secondly, the average of the mesoscopic displacement coming from the Taylor series has to be equal to the macroscopic field, as written in Eq. (4.11). With the introduction of the Taylor development (Eq. 4.10), the volume average of $\operatorname{Grad} \bar{\mathbf{u}}$ becomes

$$\begin{aligned} \langle \mathbf{u} \rangle = \frac{1}{|\mathcal{V}_0|} \Bigg(& \int_{\mathcal{V}_0} \bar{u}_\alpha(\bar{x}_1, \bar{x}_2) \, \mathrm{d}V \, \mathbf{e}_\alpha + \underbrace{\int_{\mathcal{V}_0} \bar{u}_{\alpha,\beta}(\bar{x}_1, \bar{x}_2) \Delta X_\beta \, \mathrm{d}V}_{=0} \, \mathbf{e}_\alpha \\ & + \underbrace{\int_{\mathcal{V}_0} x_3 \, \bar{\varphi}_\alpha(\bar{x}_1, \bar{x}_2) \, \mathrm{d}V}_{=0} \, \mathbf{e}_\alpha + \underbrace{\int_{\mathcal{V}_0} \bar{\varphi}_\alpha(\bar{x}_1, \bar{x}_2) \Delta X_3 \, \mathrm{d}V}_{=0} \, \mathbf{e}_3 \\ & + \underbrace{\int_{\mathcal{V}_0} x_3 \, \bar{\varphi}_{\alpha,\beta}(\bar{x}_1, \bar{x}_2) \Delta X_\beta \, \mathrm{d}V}_{=0} \, \mathbf{e}_\alpha + \int_{\mathcal{V}_0} \bar{w}(\bar{x}_1, \bar{x}_2) \, \mathrm{d}V \, \mathbf{e}_3 \\ & + \underbrace{\int_{\mathcal{V}_0} \bar{w}_{,\beta}(\bar{x}_1, \bar{x}_2) \Delta X_\alpha \, \mathrm{d}V}_{=0} \, \mathbf{e}_3 \Bigg), \end{aligned}$$

with the indexes α and β equal to $1, 2$. Some terms are equal to zero, because the macroscopic displacements and their derivatives are not depending on the mesoscopic coordinates but on the macroscopic coordinates $(\bar{x}_1, \bar{x}_2, x_3)$. Furthermore, the integration of $\Delta \mathbf{X}$ and of the thickness coordinate x_3 over the volume is equal to zero. It leads to

$$\langle \mathbf{u} \rangle = \frac{1}{|\mathcal{V}_0|} \left[\left(\int_{\mathcal{V}_0} \mathrm{d}V \right) \bar{u}_\alpha(\bar{x}_1, \bar{x}_2) \, \mathbf{e}_\alpha + \left(\int_{\mathcal{V}_0} \mathrm{d}V \right) \bar{w}(\bar{x}_1, \bar{x}_2) \, \mathbf{e}_3 \right],$$

Consequently, it is then proved that

$$\begin{aligned} \langle u \rangle &= \bar{u}|_{\bar{\mathbf{X}}_0}, \\ \langle v \rangle &= \bar{v}|_{\bar{\mathbf{X}}_0}, \\ \langle w \rangle &= \bar{w}|_{\bar{\mathbf{X}}_0}, \end{aligned} \tag{4.16}$$

and $\bar{\mathbf{X}}_0$ is representing one point of the macroscale, which defines the center of the RVE.

4.2.4 Deformation Modes

Due to the absence of scale separation in the thickness direction, the projections are only applied to the in-plane faces with normals $\mathbf{e}_1, \mathbf{e}_2$, and the faces with normal $\mathbf{e}_3$ are left free. This can be seen with the projection modes in Fig. 4.6 and 4.7: due to the absence of projection on the faces of normal x_3, the free surfaces are not suffering a straight deformation (as observed in Fig. 4.6). In Figs 4.6 and 4.7, the undeformed configurations are represented with the red lines and the light turquoise colour, while the black lines and the dark turquoise represent the deformed RVEs.

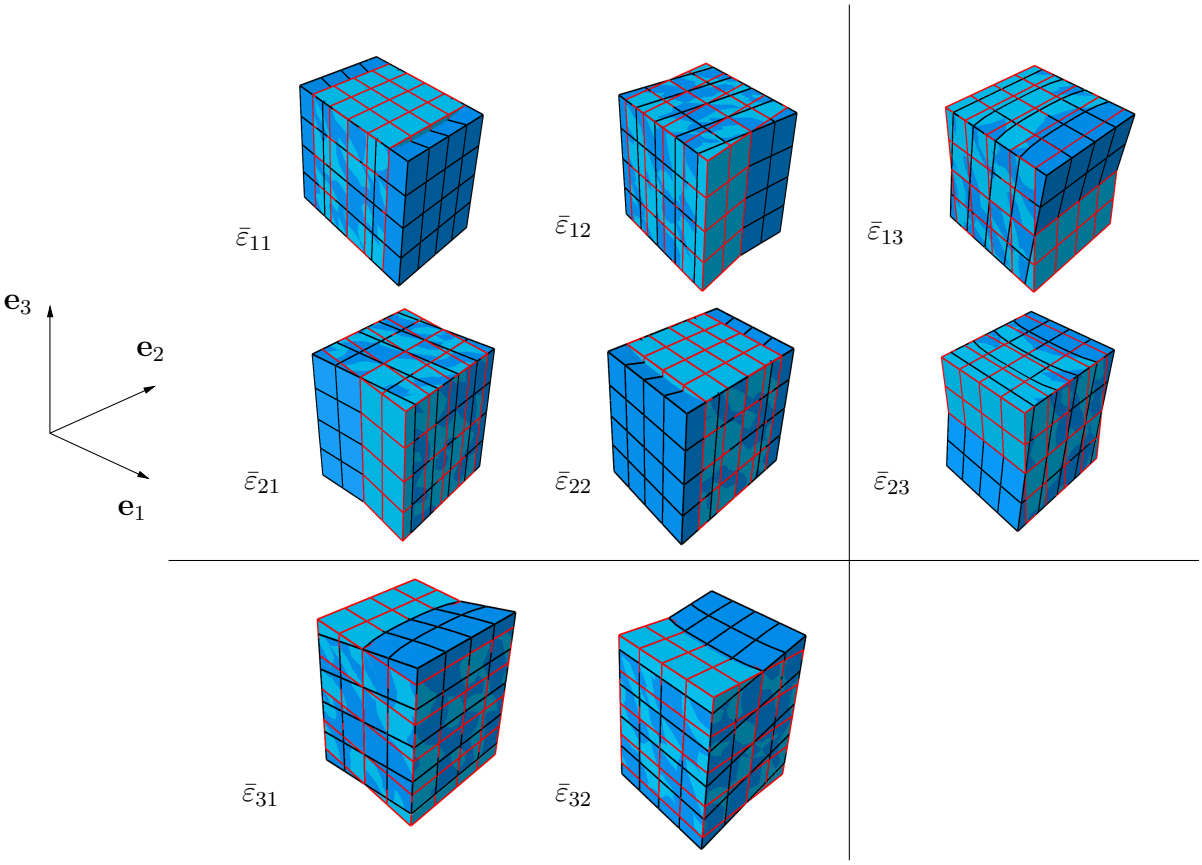

Figure 4.6: Zero order deformation modes $\bar{\boldsymbol{\varepsilon}}$ of the RVE

Moreover, in the framework of the Mindlin kinematics and with this kind of projection, no consideration of the thickness change is made

$$\Delta\mathbf{u} = \Delta\widetilde{\mathbf{u}} + \begin{bmatrix} \bar{u}_{,1} \cdot \Delta X_1 + X_3\, \bar{\varphi}_{1,1} \cdot \Delta X_1 + \bar{u}_{,2} \cdot \Delta X_2 + X_3\, \bar{\varphi}_{1,2} \cdot \Delta X_2 + \bar{\varphi}_1 \cdot \Delta X_3 \\ \bar{v}_{,1} \cdot \Delta X_1 + X_3\, \bar{\varphi}_{2,1} \cdot \Delta X_1 + \bar{v}_{,2} \cdot \Delta X_2 + X_3\, \bar{\varphi}_{2,2} \cdot \Delta X_2 + \bar{\varphi}_2 \cdot \Delta X_3 \\ \bar{w}_{,1} \cdot \Delta X_1 + \bar{w}_{,2} \cdot \Delta X_2 \end{bmatrix}. \tag{4.17}$$

Consequently for a plate theory with five degrees of freedom, a classical projection, as proposed by some authors, cf. [36, 65, 80], leads to an absence of thickness change for the

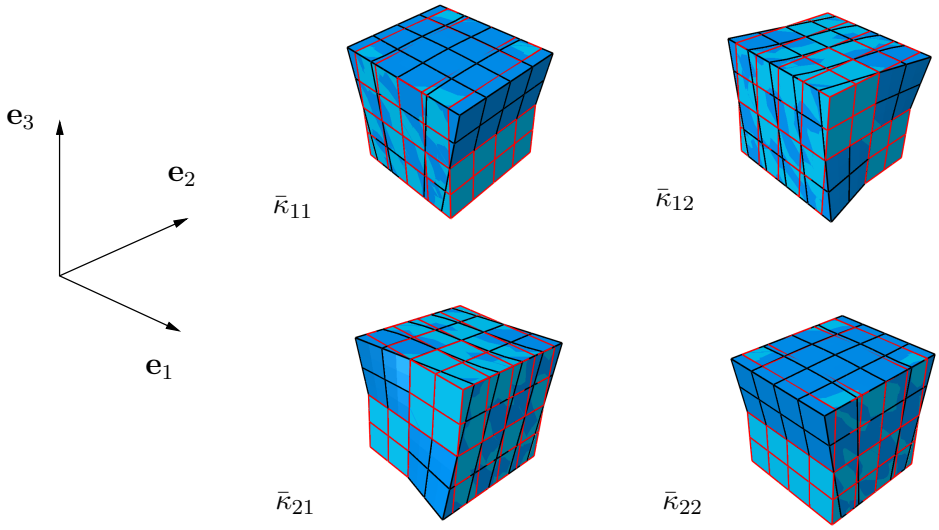

Figure 4.7: First order deformation modes $\bar{\boldsymbol{\kappa}}$ of the RVE

projections. To illustrate this, we consider the projections for an elastic isotropic material submitted to a tension test. The deformations and rotations of a three-dimensional element submitted to a tension test are defined as following

$$\begin{aligned} \varepsilon_{11} &= 0.1; \quad \varepsilon_{22} = -\nu\, 0.1; \quad \varepsilon_{33} = -\nu\, 0.1; \quad \varepsilon_{ij} = 0 \quad \text{for} \quad i \neq j, \\ \kappa_{ij} &= 0. \end{aligned} \tag{4.18}$$

Using the projection expressed in Eq. (4.17), the displacements applied to the mesoscale, in absence of fluctuations, can be written as

$$\Delta\mathbf{u} = \begin{bmatrix} \Delta u_1 \\ \Delta u_2 \\ \Delta u_3 \end{bmatrix} = \begin{bmatrix} 0.1\,\Delta X_1 \\ -\nu\, 0.1\,\Delta X_2 \\ 0 \end{bmatrix}. \tag{4.19}$$

As observed in Eq. (4.19), the information ε_{33} has not been transmitted from the macroscale to the mesoscale. It is to mention that if considering a plate theory following the Mindlin concept, the deformation ε_{33} vanishes anyway. In order to overcome this drawback, a first solution could be to consider a plate theory with thickness change for the macroscale, like for instance a plate theory with six or seven degrees of freedom, as proposed by [79, 108]. However, this solution is computationally more expensive, because of the two extra degrees of freedom. The FE^2 method based on the plate theory with seven degrees of freedom presents also some convergence problems, which can be related to the fact that the plate theory with seven degrees of freedom is not consistent, cf. [96]. Another solution is to use the plate theory following the Mindlin concept for the macroscale, and to introduce a new projection strategy.

Within the new projection strategy, the displacement is applied in a first iteration according to Eq. (4.17), and an additional internal variable is considered describing the thickness change. During the FE computation of the RVE, the average of the thickness change $\langle\varepsilon_{33}\rangle$ is computed, and this value is introduced in the projection for the next

iteration following

$$\operatorname{Grad}\bar{\mathbf{u}}\cdot\Delta\mathbf{X} = \begin{bmatrix} \bar{u}_{,\alpha}\,\Delta X_\alpha + X_3\,\bar{\varphi}_{1,\alpha}\,\Delta X_\alpha + \bar{\varphi}_1\,\Delta X_3 \\ \bar{v}_{,\alpha}\,\Delta X_\alpha + X_3\,\bar{\varphi}_{2,\alpha}\,\Delta X_\alpha + \bar{\varphi}_2\,\Delta X_3 \\ \bar{w}_{,\alpha}\,\Delta X_\alpha + \langle\varepsilon_{33}\rangle\,\Delta X_3 \end{bmatrix}. \tag{4.20}$$

This method can be regarded as similar as the EAS method for plates [13, 21, 165]. Indeed, an extra degree of freedom is applied locally, as proposed by the EAS method, and allows the consideration of the thickness change. This enables a consideration of a further deformation mode ε_{33}, as represented in Fig. 4.8. In Fig. 4.8, the undeformed configuration is drawn with the red lines, and the deformed RVE with the black lines and the turquoise colour. The result of the first iteration is represented, which explains the non-homogeneous deformation observed in Fig. 4.8. It is to mention that several iterations occur until $\langle P_{33}\rangle = 0$ and a homogeneous deformation state is reached.

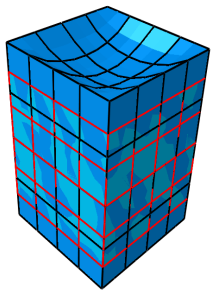

Figure 4.8: Extra deformation mode accounting for the thickness change ε_{33} of the RVE

For the zero order deformation modes, the symmetric shear modes are obtained for $\bar{\varepsilon}_{ij}+\bar{\varepsilon}_{ji}$ and a rigid body rotation is obtained for the skew symmetric shear mode with $\bar{\varepsilon}_{ij}-\bar{\varepsilon}_{ji}$. Similar results were observed for a numerical homogenisation for micromorphic media, cf. [88]. For the sum of the deformations $\bar{\varepsilon}_{12}+\bar{\varepsilon}_{21}$ for instance, the analytical calculation of the displacement leads to

$$\Delta\mathbf{u} = \begin{bmatrix} \Delta u_1 \\ \Delta u_2 \\ \Delta u_3 \end{bmatrix} = \begin{bmatrix} \bar{\varepsilon}_{12}\,\Delta X_2 \\ \bar{\varepsilon}_{21}\,\Delta X_1 \\ 0 \end{bmatrix}, \tag{4.21}$$

if no fluctuations are considered. In case of a difference $\bar{\varepsilon}_{12}-\bar{\varepsilon}_{21}$, the displacements are

$$\Delta\mathbf{u} = \begin{bmatrix} \Delta u_1 \\ \Delta u_2 \\ \Delta u_3 \end{bmatrix} = \begin{bmatrix} \bar{\varepsilon}_{12}\,\Delta X_2 \\ -\bar{\varepsilon}_{21}\,\Delta X_1 \\ 0 \end{bmatrix}. \tag{4.22}$$

Both analytical calculations of the deformation modes $\bar{\varepsilon}_{ij}-\bar{\varepsilon}_{ji}$ and $\bar{\varepsilon}_{ij}+\bar{\varepsilon}_{ji}$ can be drawn, as done in Fig. 4.9, where the plain black lines represent the undeformed configuration and the blue lines the deformed configuration. The symmetric shear mode and the skew symmetric deformation mode $\bar{\varepsilon}_{12}+\bar{\varepsilon}_{21}$ and $\bar{\varepsilon}_{12}-\bar{\varepsilon}_{21}$ are represented in Fig. 4.10, for the

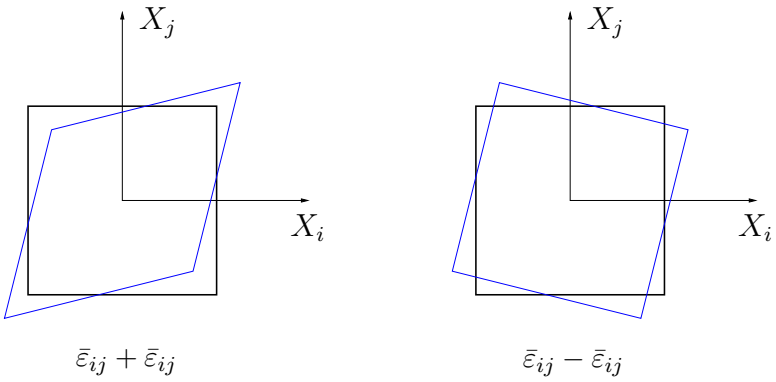

Figure 4.9: Analytical computation of the deformation modes $\bar{\varepsilon}_{ij} - \bar{\varepsilon}_{ij}$ and $\bar{\varepsilon}_{ij} + \bar{\varepsilon}_{ij}$ of the RVE

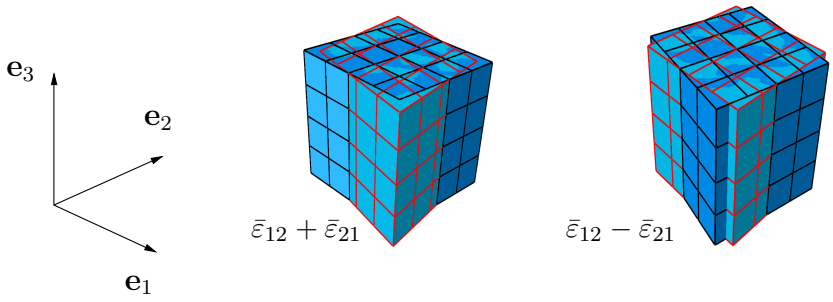

Figure 4.10: Symmetric and skew symmetric zero order deformation modes $\bar{\varepsilon}_{12} + \bar{\varepsilon}_{21}$ and $\bar{\varepsilon}_{12} - \bar{\varepsilon}_{21}$ of the RVE

in-plane deformations. The red lines and the light turquoise colour define the undeformed RVE and the blue lines with the dark turquoise define the deformed RVE.

For the first order deformation modes, the analytical calculation of the bending mode $\bar{\kappa}_{11}$ leads to the equation

$$\Delta\mathbf{u} = \begin{bmatrix} \Delta u_1 \\ \Delta u_2 \\ \Delta u_3 \end{bmatrix} = \begin{bmatrix} \bar{\kappa}_{11}\, X_3\, \Delta X_1 \\ 0 \\ 0 \end{bmatrix}, \tag{4.23}$$

with the representation in Fig. 4.11. It is to mention that the faces with normal $\mathbf{e}_3$ are left free.

For the first order deformation mode, the sum or difference of the shear deformation modes drive to a complex shear bending state, as represented in Fig. 4.12. The calculation of the deformation mode $\kappa_{12} + \kappa_{21}$ leads to

$$\Delta\mathbf{u} = \begin{bmatrix} \Delta u_1 \\ \Delta u_2 \\ \Delta u_3 \end{bmatrix} = \begin{bmatrix} \bar{\kappa}_{12}\, X_3\, \Delta X_2 \\ \bar{\kappa}_{21}\, X_3\, \Delta X_1 \\ 0 \end{bmatrix}, \tag{4.24}$$

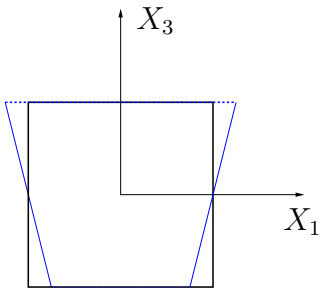

Figure 4.11: Analytical computation of the deformation modes κ_{11} of the RVE

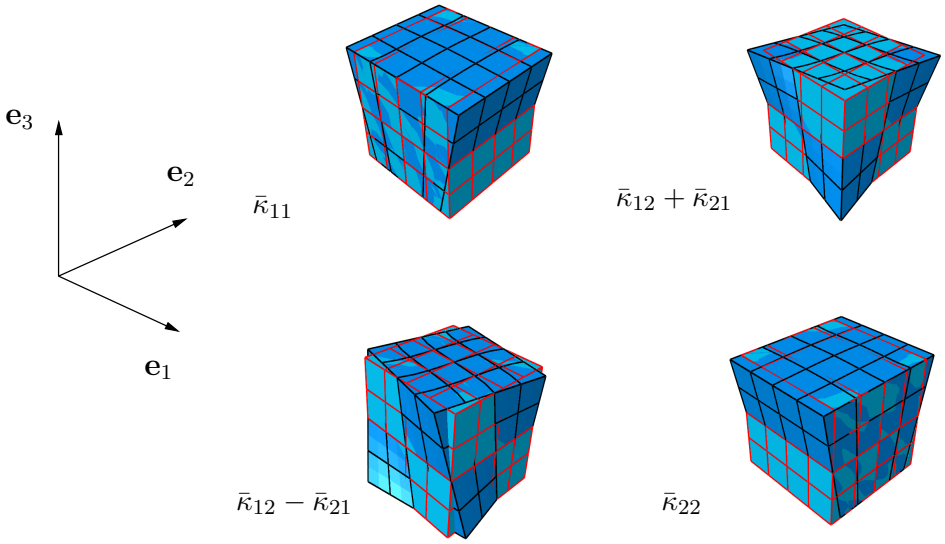

Figure 4.12: Symmetric and skew symmetric first order deformation mode of the RVE

and the difference $\bar{\kappa}_{12} - \bar{\kappa}_{21}$ is

$$\Delta\mathbf{u} = \begin{bmatrix} \Delta u_1 \\ \Delta u_2 \\ \Delta u_3 \end{bmatrix} = \begin{bmatrix} \bar{\kappa}_{12}\, X_3\, \Delta X_2 \\ -\bar{\kappa}_{21}\, X_3\, \Delta X_1 \\ 0 \end{bmatrix}. \tag{4.25}$$

For these deformation modes, the displacements are depending on both in-plane coordinates and out-of-plane coordinate, which explains the complex modes obtained in Fig. 4.12.

4.3 Boundary Value Problem of the Mesoscale

In the mesoscale, the balance equations and the constitutive equations are solved, cf. [36]. In the static case, the strong formulation of the balance equation can be written as

$$\operatorname{Div} \mathbf{P} = \mathbf{0} \tag{4.26}$$

It can be assumed that the boundary conditions are either of Neumann type or of Dirichlet type with $\mathcal{A}_0 = \mathcal{A}_n \bigcup \mathcal{A}_d$ and $\mathcal{A}_n \bigcap \mathcal{A}_d = 0$, where $\mathcal{A}_n$ is the Neumann boundary and $\mathcal{A}_d$

is the Dirichlet boundary. The constitutive equation on the mesoscale can be written for the different materials as

$$\mathbf{P} = \mathcal{F}(\mathbf{F}), \tag{4.27}$$

where $\mathbf{P}$ is the mesoscopic first Piola-Kirchhoff stress tensor, cf. Coenen et al. [36]. An important advantage of the FE^2 method is that any material behaviour, even non-linear ones, can be considered, cf. chapter 2.3.

4.4 Meso-Macro Transition

In the FE^2 method for plates, two types of information are passed from the mesoscale to the macroscale: firstly, the macroscopic stress resultants are computed from the mesoscopic stresses with the help of an accurate averaging rule. Secondly, an analytical tangent for the macroscale FE model has to be defined.

4.4.1 Hill-Mandel Condition

The Hill-Mandel condition is an energy condition which states that the macroscopic power is equal to the volume average of the mesoscopic power. For a numerical homogenisation of a three-dimensional material, the Hill-Mandel condition is given by

$$\frac{1}{\mathcal{V}_0} \int_{\mathcal{V}_0} \mathbf{P} : \operatorname{Grad} \Delta\mathbf{u} \, \mathrm{d}V = \bar{\mathbf{P}} : \operatorname{Grad} \Delta\bar{\mathbf{u}}, \tag{4.28}$$

cf. [56, 59, 88]. It has to be modified in order to consider the plate kinematics, cf. [35, 108]

$$\frac{1}{\mathcal{A}_0} \int_{\mathcal{V}_0} \mathbf{P} : \operatorname{Grad} \Delta\mathbf{u} \, \mathrm{d}V = \bar{\mathbf{N}} : \Delta\bar{\boldsymbol{\varepsilon}}_0 + \bar{\mathbf{M}} : \Delta\bar{\boldsymbol{\kappa}} + \bar{\mathbf{Q}} : \Delta\bar{\boldsymbol{\gamma}}, \tag{4.29}$$

where $\mathcal{A}_0$ represents the undeformed midplane of the plate with normal $\mathbf{e}_3$. With the split of the displacement according to Eq. (4.7), the left hand side of Eq. (4.29) becomes

$$\int_{\mathcal{V}_0} \mathbf{P} : \operatorname{Grad} \Delta\mathbf{u} \, \mathrm{d}V = \int_{\mathcal{V}_0} \mathbf{P} : \operatorname{Grad}(\operatorname{Grad} \bar{\mathbf{u}} \cdot \Delta\mathbf{X}) \, \mathrm{d}V + \int_{\mathcal{V}_0} \mathbf{P} : \operatorname{Grad} \Delta\widetilde{\mathbf{u}} \, \mathrm{d}V. \tag{4.30}$$

Firstly, it has to be guaranteed that the fluctuations are not leading to a new term in the balance equation, that means that the extension of the Hill-Mandel condition stays true also when fluctuations are considered. To do so, the last term of Eq. (4.30) is modified using the divergence theorem

$$\begin{aligned} \int_{\mathcal{V}_0} \mathbf{P} : \operatorname{Grad} \Delta\widetilde{\mathbf{u}} \, \mathrm{d}V &= \int_{\mathcal{V}_0} \operatorname{Div}(\mathbf{P}^T \cdot \Delta\widetilde{\mathbf{u}}) \, \mathrm{d}V, \\ &= \int_{\mathcal{A}_0} \mathbf{p} \cdot \Delta\widetilde{\mathbf{u}} \, \mathrm{d}A, \\ &= 0, \end{aligned} \tag{4.31}$$

with the traction vector $\mathbf{p}$ defined as the product of the first Piola-Kirchhoff stress by the outer unit vector $\mathbf{n}$, i. e. $\mathbf{p} = \mathbf{P} \cdot \mathbf{n}$. It is to mention that the projections of the

displacement are only applied to the surfaces of the RVE with a normal vector tangential to the midplane. The Eq. (4.31) carries on either $\mathbf{p} = \mathbf{0}$, or $\Delta\widetilde{\mathbf{u}} = \mathbf{0}$, or $\Delta\widetilde{\mathbf{u}}$ is periodic and $\mathbf{p}$ is antiperiodic -or vice versa. In this case, the anti-periodicity of the traction vector is assumed.

Secondly, it has to be proved that the new projection type does not disregard the extension of the Hill-Mandel condition. In order to prove this, similarly as for the Eq. (4.31), the use of the divergence theorem leads to

$$\begin{aligned}\frac{1}{\mathcal{A}_0}\int_{\mathcal{V}_0}\mathbf{P} : \operatorname{Grad}(\operatorname{Grad}\bar{\mathbf{u}}\cdot\Delta\mathbf{X})\,\mathrm{d}V &= \frac{1}{\mathcal{A}_0}\int_{\mathcal{V}_0}\operatorname{Div}(\mathbf{P}^T\cdot\operatorname{Grad}\bar{\mathbf{u}}\cdot\Delta\mathbf{X})\,\mathrm{d}V \\ &= \frac{1}{\mathcal{A}_0}\int_{\mathcal{A}_0}\mathbf{p}\cdot\operatorname{Grad}\bar{\mathbf{u}}\cdot\Delta\mathbf{X}\,\mathrm{d}A. \qquad (4.32)\end{aligned}$$

With the insertion of the new projection strategy given by Eq. (4.20), the average of the mesoscopic stress power results in

$$\begin{aligned}\int_{\mathcal{A}_0}\mathbf{p}\cdot\operatorname{Grad}\bar{\mathbf{u}}\cdot\Delta\mathbf{X}\,\mathrm{d}A &= \int_{\mathcal{A}_0}\mathbf{p}\cdot\bar{u}_{\alpha,\beta}\,\Delta X_\beta\,\mathbf{e}_\alpha\,\mathrm{d}A + \int_{\mathcal{A}_0}\mathbf{p}\cdot X_3\,\bar{\varphi}_{\alpha,\beta}\,\Delta X_\beta\,\mathbf{e}_\alpha\,\mathrm{d}A \\ &+ \int_{\mathcal{A}_0}\mathbf{p}\cdot\bar{\varphi}_\alpha\,\Delta X_3\,\mathbf{e}_\alpha\,\mathrm{d}A + \int_{\mathcal{A}_0}\mathbf{p}^T\cdot\bar{w}_{,\alpha}\,\Delta X_\alpha\,\mathbf{e}_3\,\mathrm{d}A \\ &+ \int_{\mathcal{A}_0}\mathbf{p}\cdot\langle\varepsilon_{33}\rangle\,\Delta X_3\,\mathbf{e}_3\,\mathrm{d}A. \qquad (4.33)\end{aligned}$$

Because the macroscopic deformations are not depending on the mesoscopic coordinates, the Eq. (4.33) leads to the relation between the mesoscopic stresses and the macroscopic engineering stress resultants

$$\begin{aligned}\bar{N}_{\alpha\beta} &= \frac{1}{\mathcal{A}_0}\int_h\left(\int_{\mathcal{A}_0}P_{\alpha\beta}\,\mathrm{d}A\right)\mathrm{d}x_3, \\ \bar{M}_{\alpha\beta} &= \frac{1}{\mathcal{A}_0}\int_h\left(\int_{\mathcal{A}_0}P_{\alpha\beta}\,X_3\,\mathrm{d}A\right)\mathrm{d}x_3, \\ \bar{Q}_\alpha &= \frac{1}{\mathcal{A}_0}\int_h\left(\int_{\mathcal{A}_0}P_{3\alpha}\,\mathrm{d}A\right)\mathrm{d}x_3, \qquad (4.34)\end{aligned}$$

and the modified Hill-Mandel condition (4.29) is verified for $\langle P_{33}\rangle \approx 0$ or $\langle\varepsilon_{33}\rangle \approx 0$. It is to mention that the mesoscopic stress P_{33} is converging to zero in our case, enabling a thickness change and in the general case $\langle\varepsilon_{33}\rangle \neq 0$.

4.4.2 Analytical Tangent: use of the MLNA

For both FE and FE^2 method, the tangent has a critical influence on the computing time. For the numerical homogenisation, most authors use a numerical tangent, which dramatically slows down the computations. In the framework of the numerical homogenisation for plates, a method to identify an analytical tangent is proposed: the basic idea is to use a Multi-Level Newton Algorithm (MLNA). As mentioned before, in the first instance, the MLNA was applied in order to define an accurate tangent for non-linear material behaviour like elasto-plasticity or viscoplasticity, cf. [70]. The principle of the MLNA is

to separate the problem into two levels: the macroscopic level, containing the equilibrium equation and having the displacements as variables and the local level, containing the evolution equations and considering the internal variables. A full description of the method in the scope of viscoplaticity was presented in Subsect. 2.3.3.

The MLNA method can also be applied for the FE^2, as firstly proposed by Helfen & Diebels, cf. [80]: in this case, it is not a question of a viscoplastic material behaviour with two systems of variables but of a two scales problem. The principle is to consider the macroscale as global level, containing the equilibrium equation of the plate

$$\mathbf{G} = \begin{bmatrix} N_{11,1} + N_{12,2} \\ N_{12,1} + N_{22,2} \\ Q_{1,1} + Q_{2,2} + \mathfrak{N}(w_0) + q \\ M_{11,1} + M_{12,2} - Q_1 \\ M_{12,1} + M_{22,2} - Q_2 \end{bmatrix} = \mathbf{0}, \tag{4.35}$$

and as the local level, the three-dimensional boundary value problem of the mesoscale attached to each integration point of the macro level. A discretisation of both global and local level has to be performed, i. e. both macroscopic FE plate and mesoscopic FE three-dimensional volume have to be discretized. In the local level, the variables have to be split in two types: the variables obtained by the projection of the displacements, on the boundary of the RVE and the variables inside the RVE, which result from the equilibrium equation, as represented in Fig. 4.13.

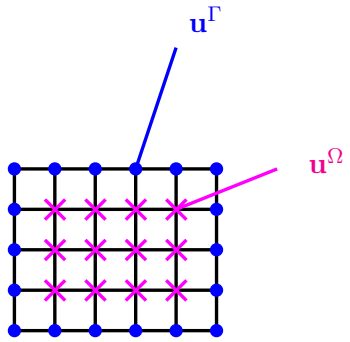

Figure 4.13: Schematic representation of the split of the variables for the local level

The local level contains the weak form of the boundary value problem for the RVE, i. e. the equilibrium equation for the mesocale and the constitutive equations for the different materials. It is sumed up as

$$\mathbf{l} = \mathbf{0}. \tag{4.36}$$

The displacements inside the element $\mathbf{u}^\Omega$ are defined with the equilibrium equation

$$\int_{\mathcal{V}_0} \mathbf{P} : \mathrm{Grad}\, \delta\mathbf{u}^\Omega \mathrm{d}V - \int_{\mathcal{A}_0} \delta\mathbf{u}^\Omega \cdot \mathbf{t}\, \mathrm{d}A = 0. \tag{4.37}$$

The displacements on the boundaries of the RVE $\mathbf{u}^\Gamma$ are described with the projection

$$\Delta\mathbf{u}^\Gamma = \mathrm{Grad}\, \bar{\mathbf{u}} \cdot \Delta\mathbf{X} + \langle \varepsilon_{33} \rangle \Delta X_3 + \Delta\widetilde{\mathbf{u}}, \tag{4.38}$$

which defines the coupling between the global and the local level. It is to mention that the modified projection strategy can be considered similar to the EAS method, because an extra degree of freedom is locally introduced, which enables the consideration of the thickness change.

In order to find an equilibrium, both systems of equations have to be solved simultaneously

$$\begin{cases} \mathbf{G} = \mathbf{0} \\ \mathbf{l} = \mathbf{0} \end{cases} \tag{4.39}$$

and the system is solved driving a Newton iteration, as explained in Subsect. 2.3.3

$$\left[\begin{array}{c|c} \dfrac{\partial \mathbf{G}}{\partial \bar{\mathbf{u}}} & \dfrac{\partial \mathbf{G}}{\partial \mathbf{u}} \\ \hline \dfrac{\partial \mathbf{l}}{\partial \bar{\mathbf{u}}} & \dfrac{\partial \mathbf{l}}{\partial \mathbf{u}} \end{array}\right] \cdot \left[\begin{array}{c} \mathrm{d}\bar{\mathbf{u}} \\ \hline \mathrm{d}\mathbf{u} \end{array}\right] = - \left[\begin{array}{c} \mathbf{R}_{\bar{\mathbf{u}}} \\ \hline \mathbf{R}_{\mathbf{u}} \end{array}\right]. \tag{4.40}$$

$\mathbf{R}_{\bar{\mathbf{u}}}$ is the residuum of the global level and $\mathbf{R}_{\mathbf{u}}$ the residuum of the local level. Because the global level is defined for the different macroscopic elements, there is a coupling between the different elements, and the matrix $\partial \mathbf{G}/\partial \bar{\mathbf{u}}$ is a sparse matrix. In contrast, each mesoscopic RVE is defined in relation to one integration point, that means that there is no coupling between the RVEs, and that the matrix $\partial \mathbf{l}/\partial \mathbf{u}$ is a block diagonal matrix. Consequently, it is convenient to use the Multi-Level Newton Algorithm for the solution of the system (4.40). The Multi-Level Newton Algorithm supposes the solution of the system in Eq. (4.40) by a decomposition in three steps.

1. Firstly, the local level is considered and this means that the global displacements are not varying with $\mathrm{d}\bar{\mathbf{u}} = \mathbf{0}$. Considering the second line of the system (4.40), it leads to

$$\frac{\partial \mathbf{l}}{\partial \mathbf{u}} \cdot \mathrm{d}\mathbf{u} = -\mathbf{R}_{\mathbf{u}}. \tag{4.41}$$

2. Secondly, the local displacement field is uploaded and the local level is examined again. A consideration of the second line of the system in Eq. (4.40) is

$$\frac{\partial \mathbf{l}}{\partial \bar{\mathbf{u}}} \cdot \mathrm{d}\bar{\mathbf{u}} + \frac{\partial \mathbf{l}}{\partial \mathbf{u}} \cdot \mathrm{d}\mathbf{u} = -\mathbf{R}_{\mathbf{u}}. \tag{4.42}$$

   If the equilibrium is found, the residuum vanishes $\mathbf{R}_{\mathbf{u}} = \mathbf{0}$ and the former equation can be written as

$$\mathrm{d}\mathbf{u} = \left(\frac{\partial \mathbf{l}}{\partial \mathbf{u}}\right)^{-1} \cdot \left(-\frac{\partial \mathbf{l}}{\partial \bar{\mathbf{u}}}\right) \cdot \mathrm{d}\bar{\mathbf{u}}, \tag{4.43}$$

   leading to a direct relation between the global and local displacement increments, or in other words between the macroscopic and mesoscopic displacement increments

$$\mathrm{d}\mathbf{u} = \mathrm{d}\mathbf{u}(\mathrm{d}\bar{\mathbf{u}}). \tag{4.44}$$

3. In a last step, the global level is considered again, and the first line of Eq. (4.40) can be written as

$$\frac{\partial \mathbf{G}}{\partial \bar{\mathbf{u}}} \cdot \mathrm{d}\bar{\mathbf{u}} + \frac{\partial \mathbf{G}}{\partial \mathbf{u}} \cdot \mathrm{d}\mathbf{u} \;=\; -\mathbf{R}_{\bar{\mathbf{u}}}, \tag{4.45}$$

which can be solved with the introduction of the direct relation between the global and local displacements (4.43) in

$$\left(\frac{\partial \mathbf{G}}{\partial \bar{\mathbf{u}}} + \frac{\partial \mathbf{G}}{\partial \mathbf{u}} \cdot \frac{\mathrm{d}\mathbf{u}}{\mathrm{d}\bar{\mathbf{u}}} \right) \cdot \mathrm{d}\bar{\mathbf{u}} \;=\; -\mathbf{R}_{\bar{\mathbf{u}}}. \tag{4.46}$$

In this case, the global equations are not directly depending on the global displacements but only indirectly

$$\frac{\partial \mathbf{G}}{\partial \bar{\mathbf{u}}} \;=\; \mathbf{0}. \tag{4.47}$$

Taking the problem by the end, the boundary value problem is solved, defining a direct relation between the mesoscopic stresses and the mesoscopic deformations or displacements. Due to the projection strategy, there is also a direct relation between the mesoscopic and macroscopic displacements. Then, the macroscopic force and moment are obtained from the Hill-Mandel condition, leading to a direct relation between the mesoscopic stresses and the macroscopic resultants by the homogenisation. These relations can be sumed up as

$$\frac{\partial \bar{\mathcal{N}}}{\partial \bar{\boldsymbol{\varepsilon}}} \;=\; \frac{\partial \bar{\mathcal{N}}}{\partial \boldsymbol{\sigma}} \frac{\partial \boldsymbol{\sigma}}{\partial \boldsymbol{\varepsilon}} \frac{\partial \boldsymbol{\varepsilon}}{\partial \bar{\boldsymbol{\varepsilon}}}, \tag{4.48}$$

with the stress resultants written as $\bar{\mathcal{N}} = (\bar{\mathbf{N}}, \bar{\mathbf{M}}, \bar{\mathbf{Q}})$. Eq. (4.48) means that the global resultants depend on the local stresses, which depend on the local variables. The local variables are obtained by the projection, in other words the local variables depend on the global variables. Consequently, it cannot be drawn some direct relations between the global resultants and the global variables and the partial derivative of the global resultants with respect to the global variables vanishes

$$\frac{\partial \mathbf{G}}{\partial \bar{\mathbf{u}}} \;=\; 0. \tag{4.49}$$

Because of the dependencies expressed in Eqs (4.48) and (4.49), the Eq. (4.46) can be simplified as

$$\left(\frac{\partial \mathbf{G}}{\partial \mathbf{u}} \cdot \frac{\mathrm{d}\mathbf{u}}{\mathrm{d}\bar{\mathbf{u}}} \right) \cdot \mathrm{d}\bar{\mathbf{u}} \;=\; -\mathbf{R}_{\bar{\mathbf{u}}}, \tag{4.50}$$

and the global stiffness matrix can be identified as

$$\mathbf{K} \;=\; \left(\frac{\partial \mathbf{G}}{\partial \mathbf{u}} \cdot \frac{\mathrm{d}\mathbf{u}}{\mathrm{d}\bar{\mathbf{u}}} \right) \;=\; \frac{\partial \mathbf{G}}{\partial \bar{\mathcal{N}}} \cdot \frac{\partial \bar{\mathcal{N}}}{\partial \mathbf{u}} \cdot \frac{\mathrm{d}\mathbf{u}}{\mathrm{d}\bar{\mathbf{u}}}. \tag{4.51}$$

In the scope of the multiscale problem, the relation between the mascroscopic and mesoscopic variables can be expressed as

$$\bar{\boldsymbol{\varepsilon}} \;=\; \frac{1}{\mathcal{V}_0} \int_{\mathcal{V}_0} \boldsymbol{\varepsilon} \, \mathrm{d}V, \tag{4.52}$$

which leads to the expression of the general stiffness coefficients $\mathbb{C}$ with

$$\bar{\mathcal{N}} = \mathbb{C} : \bar{\boldsymbol{\varepsilon}} \tag{4.53}$$

as

$$\mathbb{C} = \begin{bmatrix} \sum_p {}^2\mathbb{C}^p_{ijkl}\, h & \sum_p {}^2\mathbb{C}^p_{ijkl}\, h\, x_3 & \sum_p {}^2\mathbb{C}^p_{ij3l}\, h\, x_3^2 \\ \sum_p {}^2\mathbb{C}^p_{ijkl}\, h\, x_3 & \sum_p {}^2\mathbb{C}^p_{ijkl}\, h\, x_3^2 & \sum_p {}^2\mathbb{C}^p_{ij3l}\, h\, x_3^3 \\ \sum_p {}^2\mathbb{C}^p_{3jkl}\, h\, x_3^2 & \sum_p {}^2\mathbb{C}^p_{3jkl}\, h\, x_3^3 & \sum_p {}^2\mathbb{C}^p_{3j3l}\, h \end{bmatrix}. \tag{4.54}$$

It is to mention that in the case of composite plates -sandwich plates or hybrid laminates- with a symmetric layer stacking order, some of the stiffness coefficients vanish and the equation can be reduced to

$$\mathbb{C} = \begin{bmatrix} \sum_p {}^2\mathbb{C}^p_{ijkl}\, h & 0 & 0 \\ 0 & \sum_p {}^2\mathbb{C}^p_{ijkl}\, h\, x_3^2 & 0 \\ 0 & 0 & \sum_p {}^2\mathbb{C}^p_{3j3l}\, h \end{bmatrix}. \tag{4.55}$$

In the next chapter, some simulation results are presented in order to test the proposed method. In the presented work, the FE modelling of the macroscale is treated with a non-commercial software, using a plate theory following the Mindlin concept, while the FE computations of the mesoscale are achieved with ABAQUS® using an UMAT SUBROUTINE. The numerical results are compared with the plate theory with seven degrees of freedom, implemented in a non-commercial code, and with the three dimensional FE computations made with ABAQUS®.

Chapter 5

Applications

In this chapter, the proposed FE^2 method is tested in the framework of different examples, in order to define an estimation of the method. Whereas the FE computation of the macroscale is performed with a non-commercial code using a Pardiso solver, cf. [95, 163, 164], the FE computations of the mesoscale are done with ABAQUS® with an UMAT SUBROUTINE. The numerical concurrent homogenisation uses a plate theory with five degrees of freedom following the Mindlin concept for the macroscale, but with a modified projection, which enables a further consideration of the thickness change. In the following, the projection strategy, as defined in Eq. (4.17) is called the "classical" projection, in order to differentiate it from the innovative projection strategy proposed in this work and written in Eq. (4.20). A comparison of the two types of projections -the "classical" one, used by many authors, cf. [36, 65, 80] and the new projection strategy proposed in this work- is performed with a three-dimensional FE modelling computed with ABAQUS® and with a plate theory with seven degrees of freedom, implemented in the non-commercial code.

In a first instance, only elastic materials are considered and a validation of the method is proposed using the classical tension, shear and bending tests on a three-layers composite plate. Because the discretisation and size of the RVE have an influence on the results for some of the proposed tests; a study of these parameters is proposed in order to define an optimal RVE for the computations. Then, the numerical multi-scale homogenisation is also applied to a hybrid laminate containing ten layers showing linear elastic material behaviour. After the validation of the method for linear material behaviour, a three-layers composite, containing both linear and non-linear material behaviour, is tested under tension, shear and bending tests. Finally, the FE^2 method is applied to some of the classical problems for the plates, as the Cook's membrane, a plate with a hole and a Pagano problem.

5.1 Validation

In this part, the classical tests (tension, shear and bending) of a three-layers elastic composite plate are computed. In the performed tests, isotropic elastic and transverse isotropic elastic materials are considered, which may describe the material behaviour of the polymer -or of the metal- and of the fiber reinforced polymer, respectively. For clarity, a non-linear material behaviour is considered in Sect. 5.2.

5.1.1 Uniaxial Tension Test

Firstly, a tension test is computed with the boundary conditions expressed in Fig. 5.1. The plate has a dimension of $10 \times 10 \times 1$ mm^3, and the ratio of his thickness/length is of 1/10. In order to test the method, a sandwich plate consisting of three layers of thickness 0.25 mm, 0.5 mm and 0.25 mm, is computed. In this first example, the material behaviour of the top panels and of the core material are linear elastic isotropic. The top panels are supposed to be Aluminium material, whereas the core is a polymer. The Young's modulus and the Poisson's ratio of the top panels are $E = 70500$ MPa and $\nu = 0.3$; the material constants of the core material are $E = 55000$ MPa and $\nu = 0.4$.

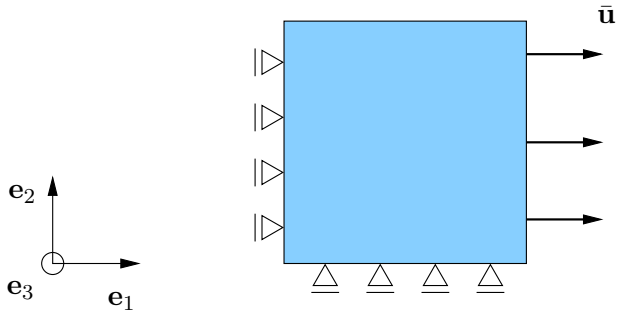

Figure 5.1: Schematic representation of the tension test

The results of the tension test of the elastic isotropic materials are represented in Fig. 5.2. On the left side of the Fig. 5.2, the normal force resultant is represented as a function of the deformation. In order to enable a comparison between the normal force obtained by both the FE^2 method and the FE plate with the normal stress resulting from the

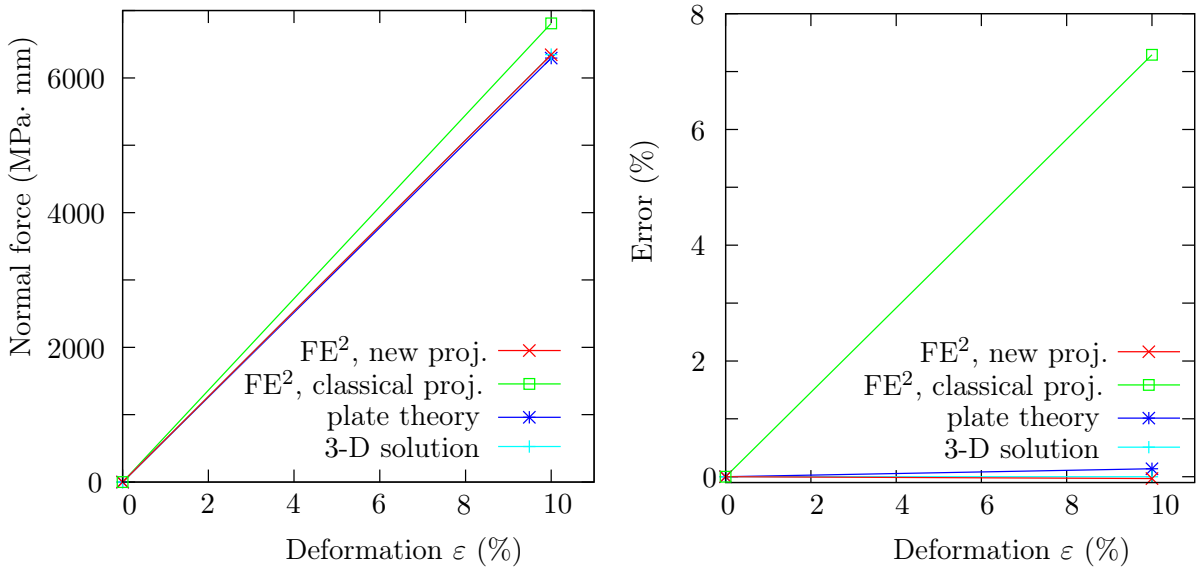

Figure 5.2: Normal force for a tension test of a three-layers sandwich plate containing isotropic elastic layers (relative error on the right)

three-dimensional computation, the forces obtained by the three-dimensional problem are computed as functions of the stresses using the Eq. (3.11) with

$$P_{ij}\, h \;=\; N_{ij}, \tag{5.1}$$

where h is the thickness of the plate before deformation, P_{ij} is here the first Piola-Kirchhoff stress, and the product between the first Piola-Kirchhoff stress and the thickness before deformation leads to the engineering stress resultant N_{ij}. This is applied to the whole chapter. On the right side in Fig. 5.2, the relative error is computed in percentage. A three-dimensional model, which is considered as the reference, is computed, as well as a plate theory with seven degrees of freedom and the FE^2 method.

One can observe that the result obtained with a numerical homogenisation using the Mindlin plate in combination with the "classical" projection (without thickness change), as proposed by many authors [36, 65, 80], leads to an error of 7%, compared with the three-dimensional result. This phenomenon can be explained by the neglect of the thickness change which induces the Poisson locking. On the contrary, a numerical homogenisation containing the new projection strategy as proposed in this work, solves the Poisson locking and the error decreases to 0.03% compared with the three-dimensional solution. The tension test can also be computed using a plate theory with seven degrees of freedom and it leads to 0.13% error. For the plate theory, the layers stacking order is taken into account as explained in Appendix 7.4. The average thickness change is of 3.4% for the FE^2 using the new projection strategy and of 1.7% for the FE^2 method without consideration of the thickness change, in this example, leading to the mentioned discrepancies. Both plate theory and FE^2 using the new projection strategy offer excellent results for this test.

Then the influence of the discretisation of the macroscale and of the mesoscale are considered, as represented in Fig. 5.3. Two different macro discretisations containing two and eight elements[1] for the macroscale and two different meso discretisations with 4^3 and 8^3 elements, are considered. The macro elements are triangle plate elements with a quadratic ansatz, while the three-dimensional elements are quadratic bricks elements (C3D20). It is to mention that the macro discretisation shows to have no influence in this example, because exactly the same results are obtained for a mesh on the macroscale containing two or eight elements, and for a fixed discretisation on the mesocale. In contrast, the meso discretisation has an influence, although this influence is small in this example (the error is decreasing from 0.03% to 0.008%), because the new projection strategy reduces the edge effects. The RVE for the different meso discretisations are represented in Fig. 5.4: on the left side, the meso discretisation with 4^3 elements is represented, and on the right side, the RVE contains 8^3 elements. It is to mention that in this case, there is no difference in the stress between the RVE obtained for the different macro discretisation. Consequently, a macro discretisation of two elements and a meso discretisation of 4^3 elements are used for the following examples of tension, shear and biaxial tension tests.

[1] el. is the abbreviation of elements in Fig. 5.3

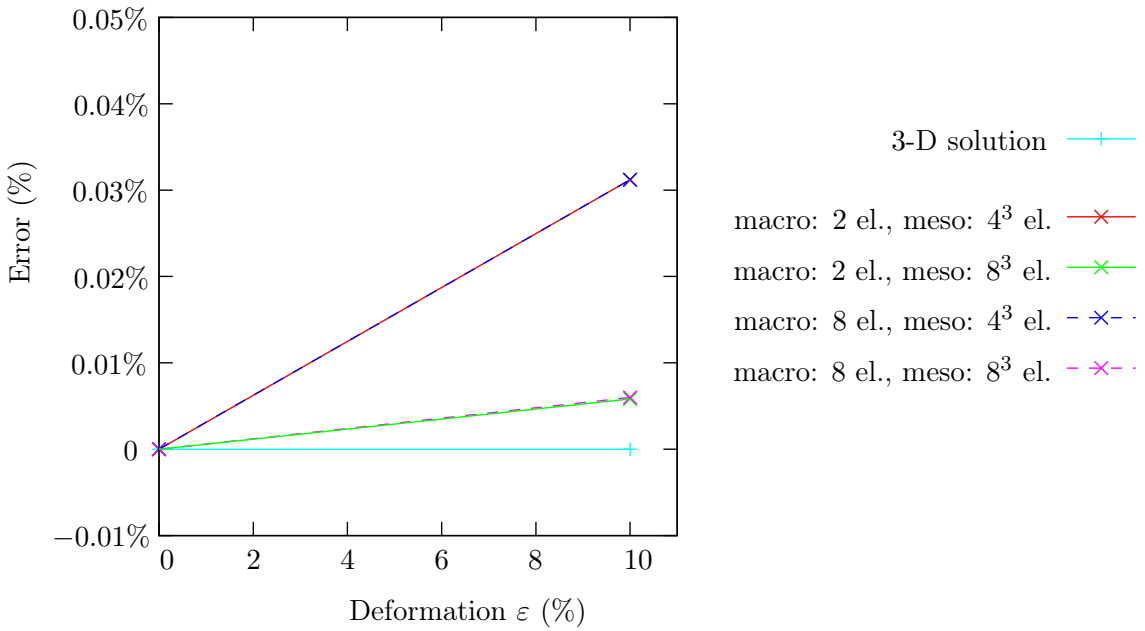

Figure 5.3: Influence of the macro and meso discretisations on the normal force for a tension test of a three-layers sandwich plate containing isotropic elastic layers

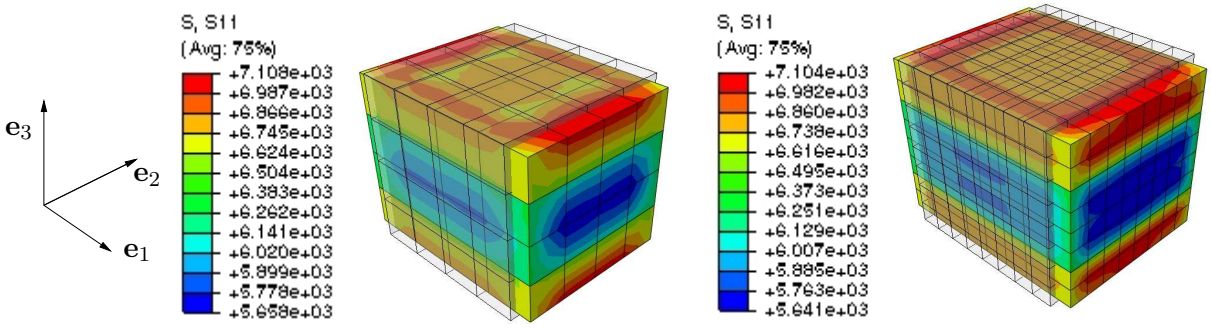

Figure 5.4: Normal stress in the RVE (Representative Volume Element) for the different meso discretisation for an uniaxial tension test

In a second numerical experiment, a sandwich plate containing an anisotropic core and elastic top panels, is submitted to a tension test. The top panels are elastic and have the Young's modulus $E = 70500$ MPa and the Poisson's ratio 0.3; the core consists of an elastic transverse isotropic material with the properties expressed in the Table 5.1.

In this example, the fibers are aligned with the tension direction. In the presented work, the hybrid laminate contains only layers with the fiber orientation of 0° and 90°. Therefore, only layers with these fiber directions are studied in this work.

$E_1 = 138$ GPa	$E_2 = 10.2$ GPa	$G_{23} = 5.7$ GPa	$\nu_{12} = 0.3$	$\nu_{23} = 0.275$

Table 5.1: Material constants for the transverse isotropic material

The normal stress resultants are represented as a function of the deformation on the left side in Fig. 5.5; on the right side, the relative error is given in percentage.

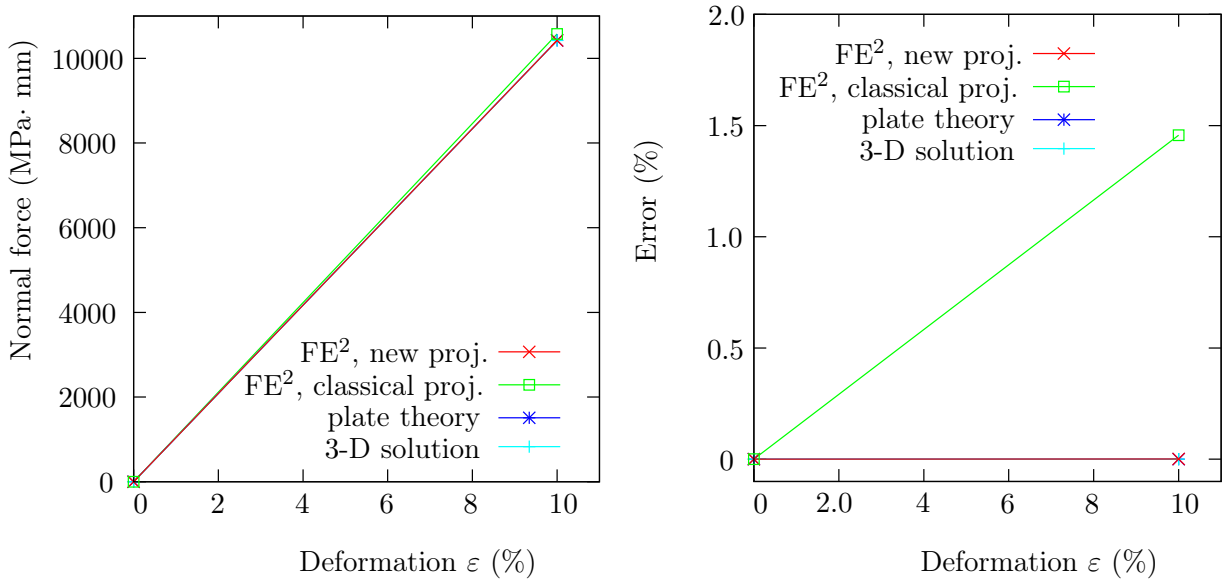

Figure 5.5: Normal force for a tension test of a three-layers sandwich plate containing isotropic and transverse isotropic (fiber orientation 0°) elastic layers (relative error on the right)

For the "classical" projection, the error reduces and is of 1.5%. For the FE^2 using the proposed projection strategy and the plate theory with thickness change, the errors are reduced and do not exceed 0.02%. In this case, we can assume that the fibers prevent a thickness change, tending to a better result, due to the reduction of the Poisson locking. The normal deformation in thickness direction reaches the average value of 3% for the FE^2 using the new projection strategy and is less than 1% for the FE^2 using the classical projection method.

The representation of the RVE for the two numerical homogenisations enables an understanding of the before mentioned results. In Figs 5.6 and 5.7 the RVE is represented for the proposed projection strategy on the left and for the "classical" projection without thickness change on the right. The grey cube represents the RVE before deformations; the stress distribution and the actual geometry are given in colours.

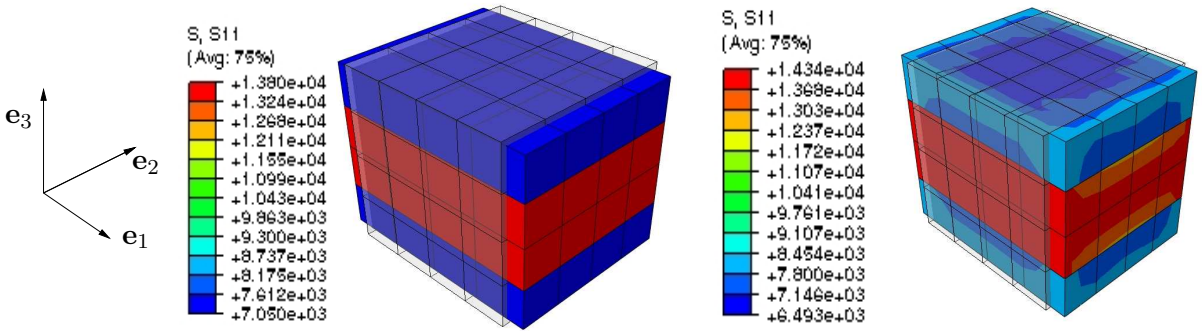

Figure 5.6: Normal stress in the RVE for the new projection on the left and the "classical" projection on the right, for an uniaxial tension test

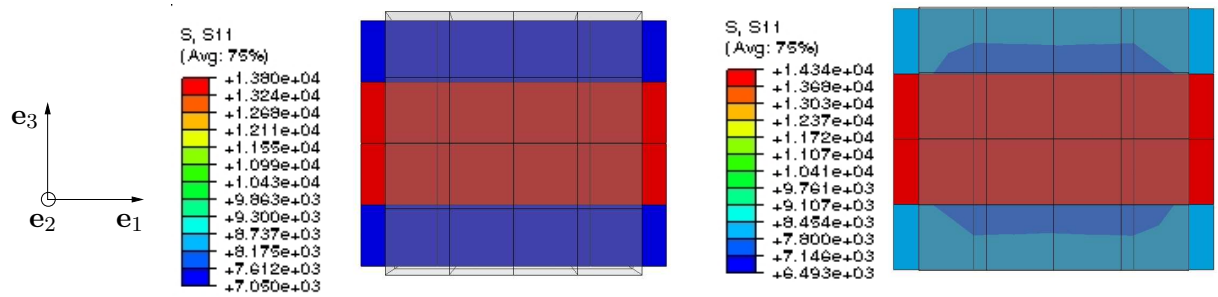

Figure 5.7: Normal stress in the RVE for the new projection on the left and the "classical" projection on the right, for an uniaxial tension test

In the framework of a numerical homogenisation of plates, the displacements are only projected in the surfaces of the RVE with a normal vector tangential to the midplane. Due to the free surfaces, it is to mention that the converged results are not obtained in one iteration but in more iterations, leading to one of the drawback on the method. Incidentally, even if considering a linear material behaviour submitted to linear deformations, some non-linearities are introduced to the linear problem, disturbing the convergence, i. e. the thickness change is obtained within the iterations of the MLNA. However, the method is stable enough to compute complicated issues like for instance a Cook's membrane or a plate with a hole, as seen further in this chapter. About the "classical" projection, a representation of the RVE shows that there is no consideration of the thickness change, as represented on the right side in Fig. 5.7 for a $(\mathbf{e}_1 - \mathbf{e}_3)$ plane.

On the opposite, the new projection strategy enables a thickness change, as observed in Figs 5.7 and 5.6 on the left side. The non-linear deformation state tends to disappear, as seen on the left side of Fig. 5.6, driving to the before mentioned better results.

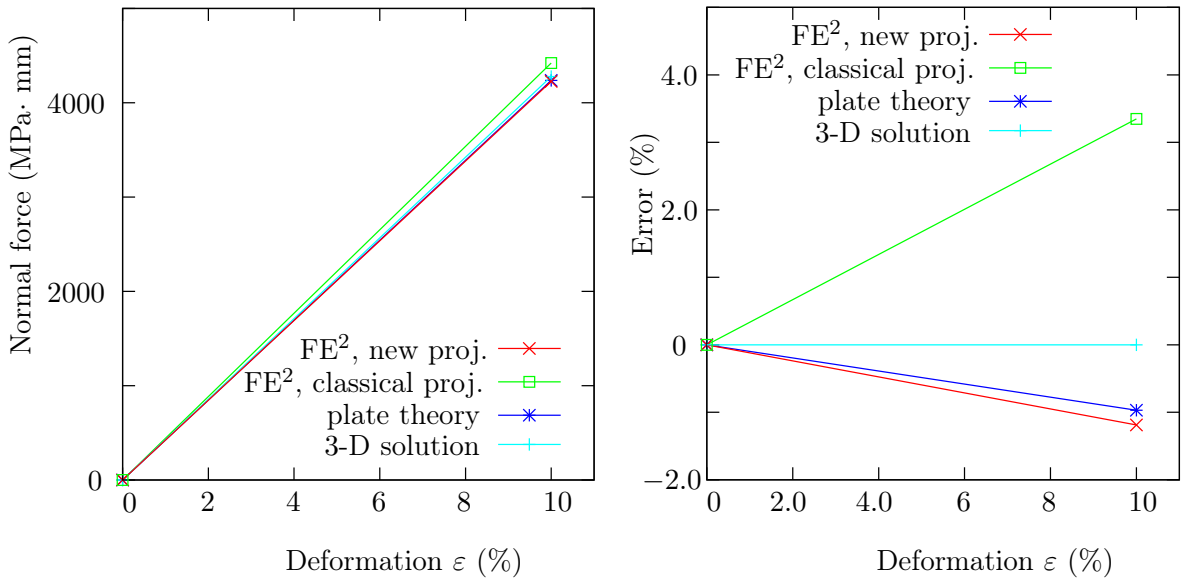

Figure 5.8: Normal force for a tension test of a three-layers sandwich plate containing isotropic and transverse isotropic (fiber orientation 90°) elastic layers (relative error on the right)

The hybrid laminate which has to be studied presents layers with the fiber orientation of only 0° and 90°. Consequently, a tension test of a three-layers plate containing a transverse isotropic core with these two fiber orientations is studied. The boundary conditions, the geometry and material properties are the same as for the precedent composite plate, only the fiber orientation of the core is changing and is of 90° -that means that the fibers are normal to the tension direction. The normal force is represented as a function of the normal strain on the left side in Fig. 5.8. The error are represented on the right side in Fig. 5.8.

A comparison of the results of the tension test of the sandwich structure with a transverse isotropic core with the two fiber orientations of 0° and 90° can be performed. In the case of the fiber orientation of 0°, the normal force reaches $N_{11} = 10425$ MPa.mm. If the fiber orientation is of 90°, i. e. that the fibers are normal to the tension direction, the value of the normal force is of $N_{11} = 4227$ MPa.mm, because the Young's modulus is much smaller in the direction normal to the fiber orientation. As previously, the errors are larger if the projection does not include any thickness change, as it is the case for the classical projection. The error given by the plate theory with seven degrees of freedom and by the FE^2 method following the new projection strategy shows a reduced error of around 1%, because both enables the consideration of the thickness change.

5.1.2 Shear Test

In a second part, a shear test is computed for the same three-layers plates as before, i. e. with the ratio thickness/length equal to 1/10. The boundary conditions are represented in Fig. 5.9.

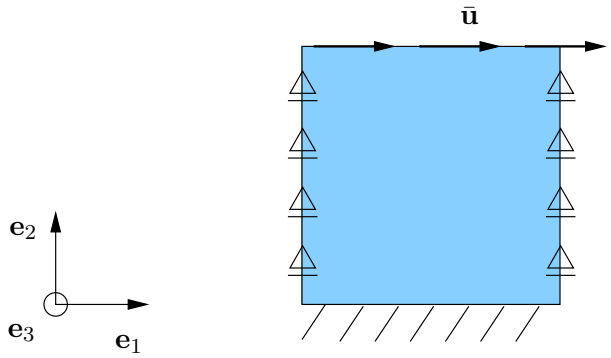

Figure 5.9: Schematic representation of the shear test

In a first numerical experiment, the three-layers composite is composed of elastic isotropic materials, with the material constants $E = 70500$ MPa, $\nu = 0.3$ for the top panels and $E = 55000$ MPa, $\nu = 0.4$ for the core material. We assume that a similar convergence as obtained for the tension test regarding the meso and macro discretisation can be observed for the shear test. For a three-layers sandwich composite containing only isotropic elastic layers, the results for the different methods -the FE^2 method using one or the other of the projection methods, the FE computation of the plate theory with seven degrees of freedom and the three-dimensional FE computation with ABAQUS®- give the same results. For clarity, only the result from one of the projection strategy is represented. Fig. 5.10 gives the shear force as a function of the shear deformation. Because a shear test is isochoric, there is no influence of the Poisson locking in this test. Therefore, the choice of the projection -the "classical" projection strategy or the projection proposed in this work- has no influence on the results for the shear test.

For a shear test of a sandwich plate made up of a transverse isotropic core and of elastic top panels, the results are represented in Fig. 5.11. In this example, the top panels have an elastic isotropic material behaviour with a Young's modulus of 70500 MPa and a Poisson's ratio of 0.3. The material constants of the transverse isotropic core are given in Table 5.1, and the fiber orientation is 0°. Similarly as for the shear test of the plate made up of elastic isotropic materials, very good results are observed for the different methods, due to the fact that the shear test is free of Poisson locking.

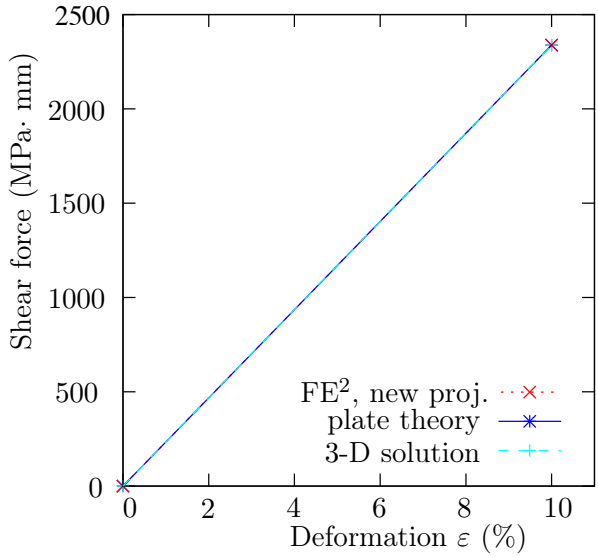

Figure 5.10: Shear force vs. deformation for a shear test of a three-layers sandwich plate containing isotropic elastic layers

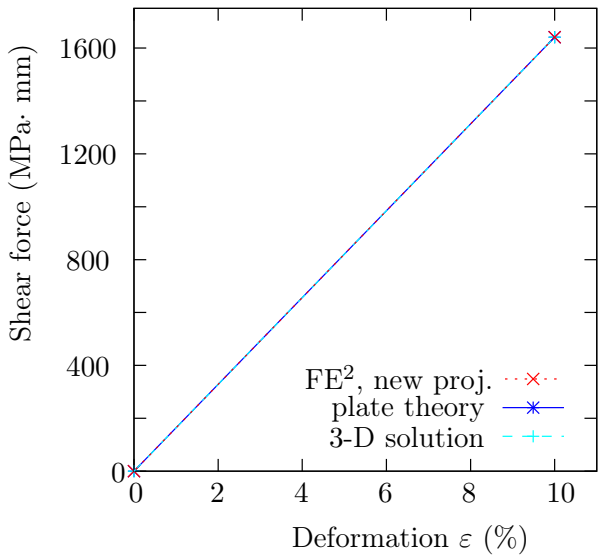

Figure 5.11: Shear force vs. deformation for a shear test of a three-layers sandwich plate containing isotropic and transverse isotropic (fiber orientation 0°) elastic layers

5.1.3 Equi-biaxial Tension Test

In the following, a biaxial tension test is computed and represented in Fig. 5.12. In order to reduce the computing time, only a quarter of the problem is computed.

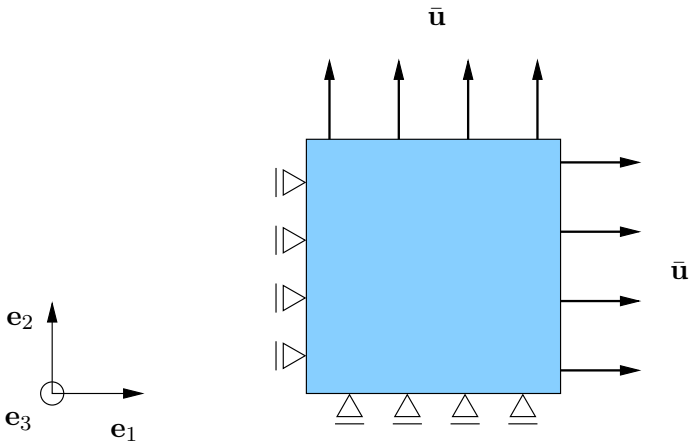

Figure 5.12: Schematic representation of the biaxial tension test

In a first numerical experiment, a biaxial tension test of a three-layers plate composed of elastic isotropic materials, is performed. The sandwich plate contains elastic isotropic materials, with the material constants $E = 70500$ MPa, $\nu = 0.3$ for the top panels and $E = 55000$ MPa, $\nu = 0.4$ for the core material. On this case, it is assumed that a similar convergence -regarding the macro and the meso discretisation- is obtained as for the uni-axial tension test. The normal force is represented as a function of the normal deformation in Fig. 5.13. Due to the neglect of the thickness change in the "classical" projection strategy, the error reaches 30% in comparison of the three-dimensional solution. In contrast, the projection strategy proposed in this work leads to an accurate result with an error of 2.5%. The plate theory with seven degrees of freedom gives an error of approximately 3%. This can be explained by the larger thickness change encounter in this problem: the average of the normal deformation in thickness direction reaches 10% for the FE^2 method with the new projection strategy enabling the consideration of the thickness change and 6% for the FE^2 method with the classical projection strategy. For the FE plate, only one integration point through the thickness is considered and the layers stacking order is taken into account as explained in Appendix 7.4, as a function of the relative thickness of the layers and of theirs material constants. It is to mention that a FE plate with several integration points may give a better result in this case.

A representation of the RVE enables to draw an explanation on the results observed with the different projections. As shown in Fig. 5.14 on the right side, the "classical" projection does not include any thickness change, but the surfaces normal to the thickness direction are let free. Because the materials are not infinitely compressible, the free surface encounters non-linear deformations in order to reduce the volume expansion. Consequently, the results are quite inaccurate for this method. On the contrary, the results given by the numerical multi-scale method with the new projection strategy proposed in this work (represented on the left side in Fig. 5.14) leads to better results, because the projection

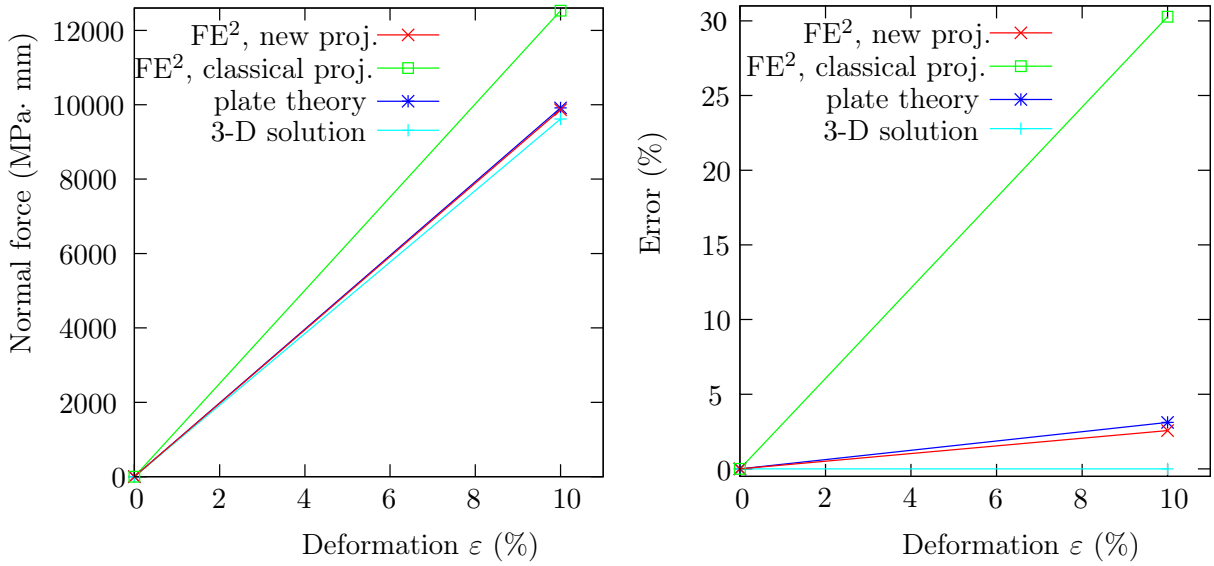

Figure 5.13: Normal force $N_{11} = N_{22}$ for a biaxial tension test of a three-layers sandwich plate containing isotropic elastic layers (relative error on the right)

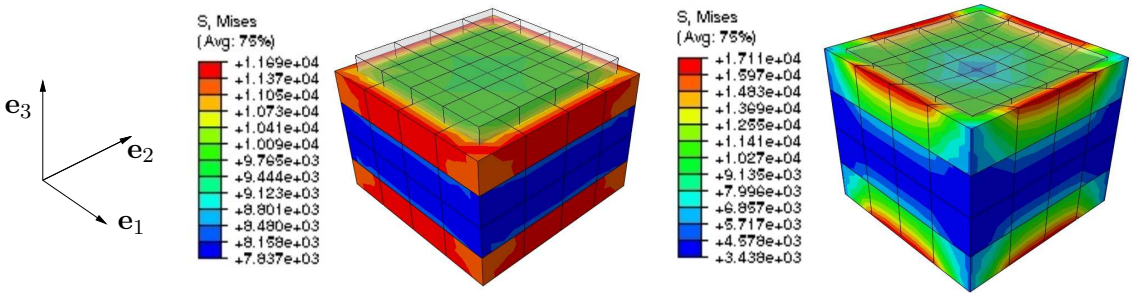

Figure 5.14: Von Mises stress in the RVE for the new projection on the left and the "classical" projection on the right, for a biaxial tension test

enables a thickness change.

Then, a biaxial tension test of a three-layers plate containing isotropic and transverse isotropic layers, is computed. In this example, the top panels have an elastic isotropic material behaviour with a Young's modulus of 55000 MPa and a Poisson's ratio of 0.4. The material behaviour of the core is given in the Table 5.1, and the fiber orientation is 0°. The results are drawn in Fig. 5.15 for the normal force in fiber direction N_{11} and in Fig. 5.16 for the normal force N_{22} normal to the fiber direction, represented as function of the deformation ε_{11} or ε_{22}, respectively.

The engineering stress resultant N_{11} in direction parallel to the fiber orientation leads to quite good results. Less than 1% error are obtained for the plate theory with seven degrees of freedom and with the FE^2 using the new projection strategy, compared with the three-dimensional solution. Even the "classical" projection strategy, which does not

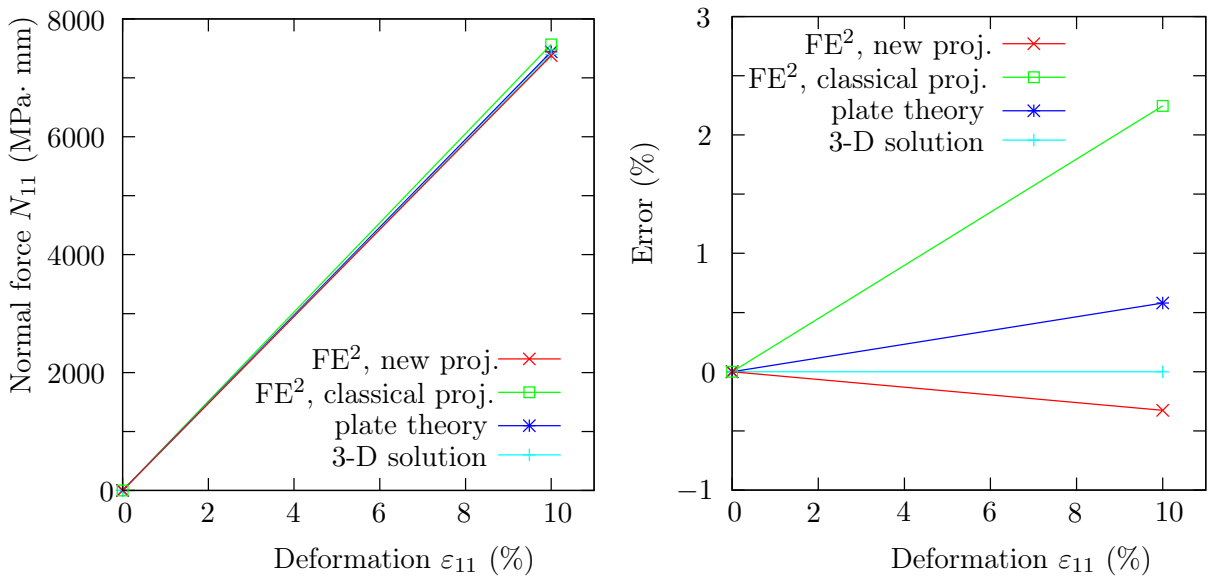

Figure 5.15: Normal force N_{11} for a biaxial tension test of a three-layers sandwich plate containing isotropic and transverse isotropic (fiber orientation 0°) elastic layers (relative error on the right)

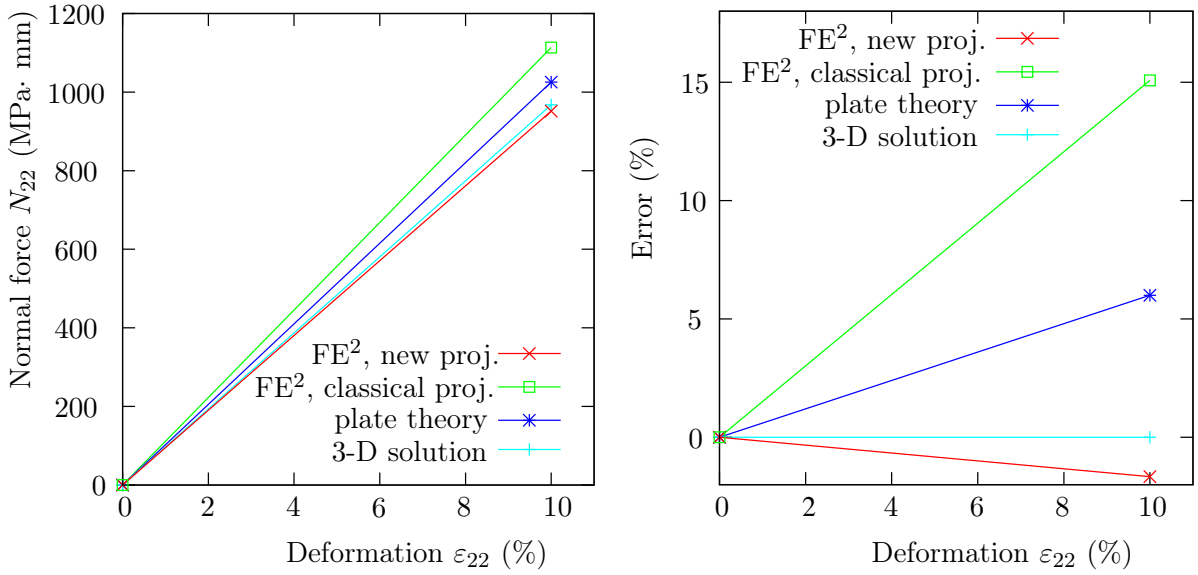

Figure 5.16: Normal force N_{22} for a biaxial tension test of a three-layers sandwich plate containing isotropic and transverse isotropic (fiber orientation 0°) elastic layers (relative error on the right)

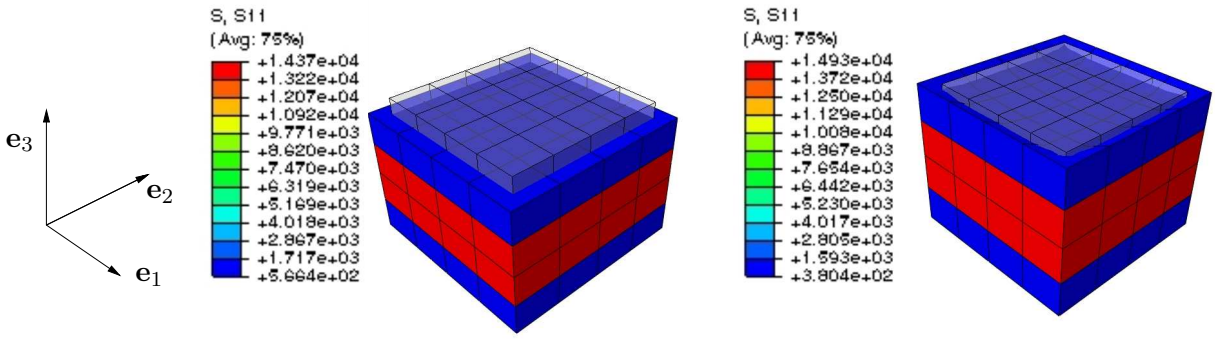

Figure 5.17: Von Mises stress in the RVE for the new projection on the left and the "classical" projection on the right, for a biaxial tension test

consider the thickness change, leads to 2% error. However, the normal force N_{22} in direction normal to the fiber orientation gives another tendency. As represented in Fig. 5.16, the error is larger for the normal force N_{22}, leading to 15% error for the "classical" projection and to 6% error for the plate theory. In contrast, the error obtained with the FE^2 method and with the projection strategy proposed in this work is less than 2%. As a consequence, it can be concluded that the FE plate, although taking the thickness change into account, can lead to incorrect results, if the plate is thick and the thickness change is large, or if only one integration point through the thickness is considered. In this case, the proposed solution, that means the numerical homogenisation, using a projection including the thickness change, shows to be better suited.

A consideration of the RVE leads to some explanations of the before mentioned results, as seen in Fig. 5.17. On the right hand side, the results of the "classical" projection are drawn. It can be seen that a non-linear deformation state occurs, as can be seen for the surfaces with normal $\mathbf{e}_3$. On the contrary for the new projection strategy, represented on the left side, a thickness change is introduced. Due to the presence of a transverse isotropic material law, which shows a high anisotropy and smaller Poisson's ratios, the Poisson locking may be somehow reduced, leading to better results as for isotropic elastic materials.

Under consideration of the presented examples, it can be observed that the Poisson locking is an important issue for the modelling of thick composite plates, therefore special attention is paid towards its resolution in the present work. However, the uniaxial and the biaxial tension tests, as well as the shear test, are membrane problems. What is about the out-of-plane deformation state, like it is the case for a bending problem? This question will be answered in the next part.

5.1.4 Bending Test

A bending problem of a three-layers sandwich plate is computed as represented in Fig. 5.18. A vertical displacement is applied to the composite plate on the one side, whereas the other side is clamped. The composite plate has the dimensions $10 \times 1 \times 1$ mm^3, and contains three elastic isotropic layers with the thickness 0.25 mm, 0.5 mm and 0.25 mm. The top panels have a Young's modulus of $E = 70500$ MPa and a Poisson's ratio of 0.3, while the core has the Young's modulus of $E = 55000$ MPa and the Poisson's ratio of 0.4.

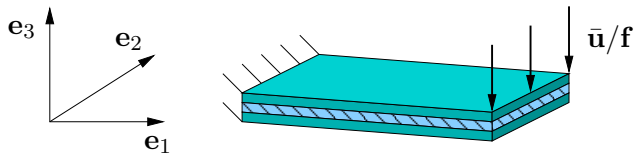

Figure 5.18: Schematic representation of the bending test

The influence of the discretisation is then considered in case of bending. In this part, three major influences are studied: firstly, the macro discretisation is studied. Secondly, the influence of the meso discretisation of the RVE is considered. Finally, the size of the RVE in the $\mathbf{e}_1$ direction is changed.

Influence of the Macro Discretisation

A bending test of the three-layers composite containing only elastic isotropic layers is performed. The macro discretisation is varying from 20 elements to 320 elements. The moment distribution is represented in Fig. 5.19, where the results given by the plate theory are drawn on the right side (d,e,f) and the results of the FE^2 method on the left side (a,b,c). It is to mention that 4^3 elements are considered for the mesoscale. Firstly, only the influence of the macro discretisation is considered, while the influence of the meso discretisation is studied thereafter. For clarity, the moment is represented as a function of the coordinate in the $\mathbf{e}_1$-direction in Fig. 5.20. In Fig. 5.20, the moment is represented for the three different macro discretisations containing 20, 70 and 320 elements, for the two methods, i. e. for the plate theory and the FE^2 method. It can be observed that the differences between the different macro discretisation are small.

The shear force distribution is represented as a function of the coordinate in $\mathbf{e}_1$-direction in Fig. 5.21, for a macro discretisation from 20 to 320 elements. Both results obtained by the plate theory and the FE^2 method are represented in Fig. 5.21. It can be observed that, in this case, the error between the value given by the plate theory for the finest mesh and the results given by the FE^2 method for the mesh with 20 elements is acceptable and shows a precision of approximately 4%. However, the FE^2 method is computationally very expensive, and for these reasons a macro discretisation of 20 elements is used in the next examples.

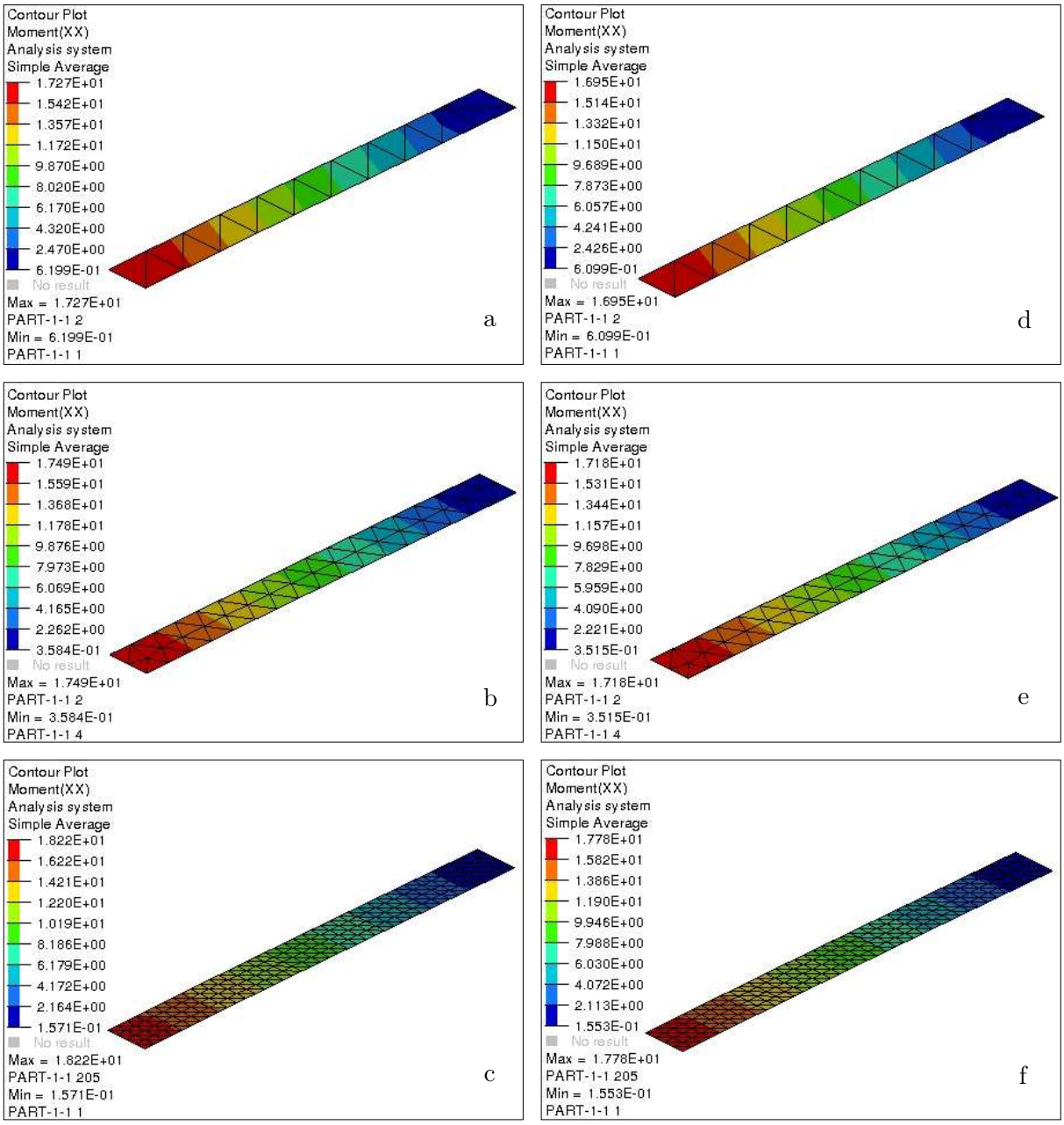

Figure 5.19: Moment distribution for the bending test of a three-layers sandwich plate containing isotropic elastic layers for the different macro discretisation; a,b,c: result of the FE^2 method; d,e,f: FE plate

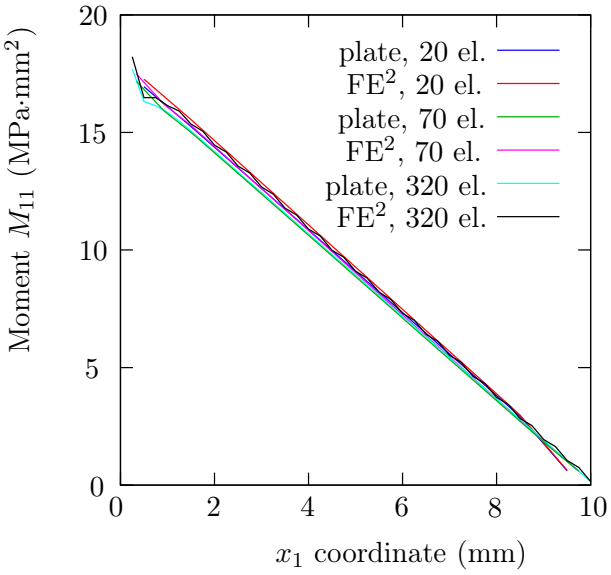

Figure 5.20: Influence of the macro discretisation on the moment distribution for the bending test of a three-layers sandwich plate containing isotropic elastic layers

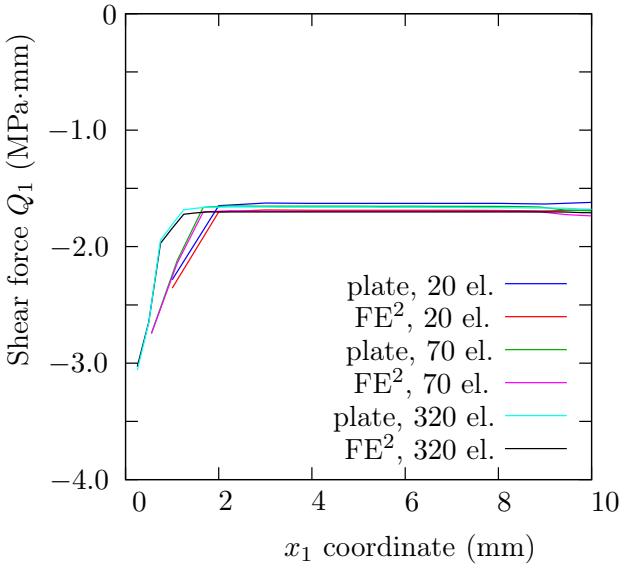

Figure 5.21: Influence of the macro discretisation on the shear force distribution for the bending test of a three-layers sandwich plate containing isotropic elastic layers

Influence of the Meso Discretisation

After the definition of the importance of the macro discretisation, the influence of the meso discretisation is studied. The same numerical experiment is considered, i. e. a vertical displacement is applied in one extremity of the plate, while the other extremity is

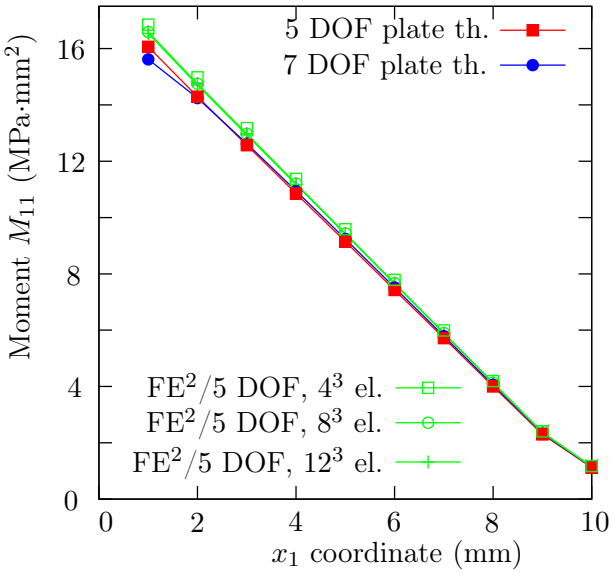

Figure 5.22: Moment distribution for the bending test of a three-layers sandwich plate containing isotropic elastic layers

clamped. The moment distribution is drawn in Fig. 5.22, for the different meso discretisations. Firstly, it can be observed that there is only a reduced difference between the results of the plate theories with five or seven degrees of freedom. Because the extra degrees of freedom describe a thickness change, the both plate theories give similar results for a bending test. Similar observations were made in the Ph.D. thesis by Bischoff [13]. Then, the RVE's discretisation is changed and the RVE contains 4^3, 8^3 and 12^3 elements. One could observe that for a finer discretisation, the accuracy of the results is better (from 4.8% to almost 3%). Nevertheless, for a finer RVE's discretisation, the computations slow down dramatically. However, it is to mention that a parallelisation could avoid this drawback.

A representation of the shear force resultant as a function of the horizontal position is then drawn in Fig. 5.23. It is to mention that similar results are also obtained for the shear force for the plate theory with five or with seven degrees of freedom, due to the absence of Poisson locking for this test. As a consequence, similar results are obtained for the FE^2 based on a plate theory with five or seven degrees of freedom. A relative error of approximately 5.3% to less than 4% is obtained for the shear force resultant, depending on the discretisation of the RVE. It is to mention that the projection including the thickness change leads to the same results as the so-called "classical" projection, without thickness change, due to the absence of thickness change in the bending test. The same results are obtained also for a numerical homogenisation based on a plate theory with seven degrees of freedom, as proposed in [79, 108]; however, the convergence is much quicker if using a plate theory with five degrees of freedom. It can be related to the work of Kienzler [96], where a consistent plate theory is defined if the plate formulation presents a polynomial order of the displacement in thickness direction smaller than the polynomial order of the

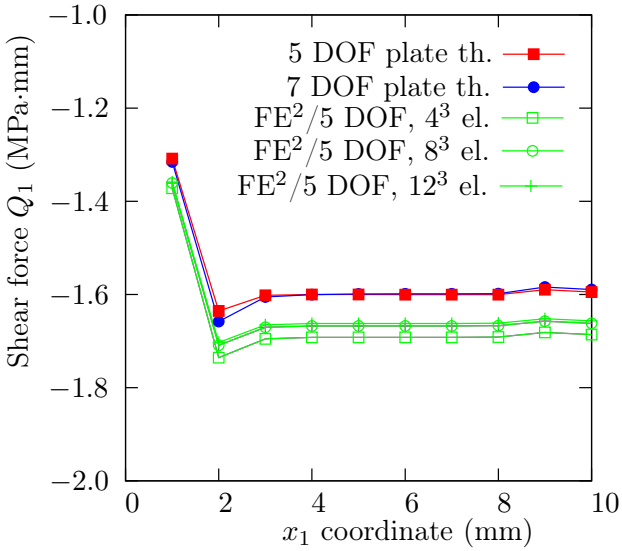

Figure 5.23: Shear force distribution for the bending test of a three-layers sandwich plate containing isotropic elastic layers

displacement in longitudinal direction.[2] A plate theory with seven degrees of freedom, that means with a polynomial order of the displacement in thickness direction larger than the one in longitudinal direction, shows to encounter some convergence problem in the case of a numerical homogenisation. It is to mention that no convergence problem were observed by the use of the FE plate with thickness change alone in the context of this work. Moreover, this plate theory has the advantage to consider the thickness change and presents a three-dimensional constitutive law. As a consequence, a plate theory following the Mindlin concept and a modified projection strategy, enabling the thickness change, are used for the numerical homogenisation, while the comparisons are performed with a three-dimensional problem or with the plate theory with seven degrees of freedom.

Influence of the Length of the RVE

Due to the high computational costs which result if using a finer mesh, another solution consisting by using a larger RVE is pointed out. The influence of the length of the RVE in $\mathbf{e}_1$-direction is studied in this part, as represented in the Fig. 5.24. The plate has a length of 10 mm, a width of $l = 1$ mm and a thickness of 1 mm. In the former case, the second RVE with the dimensions $1 \times 1 \times 1$ mm^3 was considered and only the discretisation was varying. However, this solution is computationally too expensive. Consequently, the influence of the length of the RVE is studied. In a first RVE, the RVE has a length which is the half of the thickness of the plate, and it has $2 \times 4 \times 4$ elements. The second RVE is cubic and contains $4 \times 4 \times 4$ elements. The third RVE has a length of $3/2\,l$ and contains $6 \times 4 \times 4$ elements. The length of the RVE varies from a length of $l/2$ to $3\,l$ with then $12 \times 4 \times 4$ elements. The moment distribution is represented in Fig. 5.25 and the shear

[2] If the displacement in thickness direction $\bar{w}$ is of polynomial order n, i. e. the polynomial function for $\bar{w}$ is of order n, the polynomial order of the longitudinal displacements $\bar{u}$ and $\bar{v}$ have to be of order $n+1$, with the displacement $\bar{\mathbf{u}} = [\bar{u}, \bar{v}, \bar{w}]^T$.

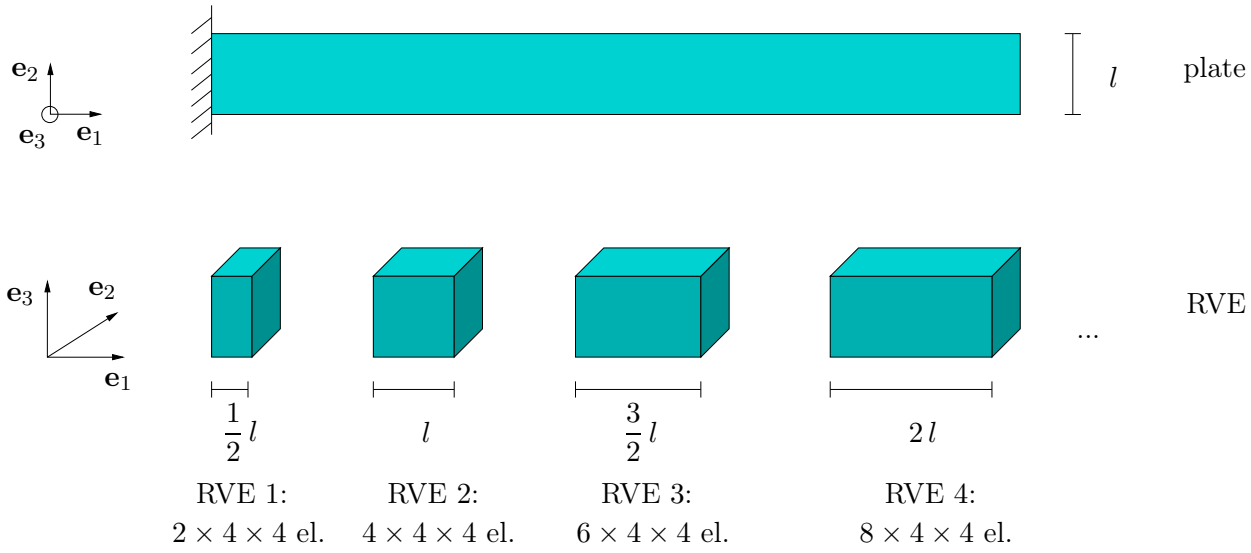

Figure 5.24: Schematic representation of the variation of length of the RVE for the bending test

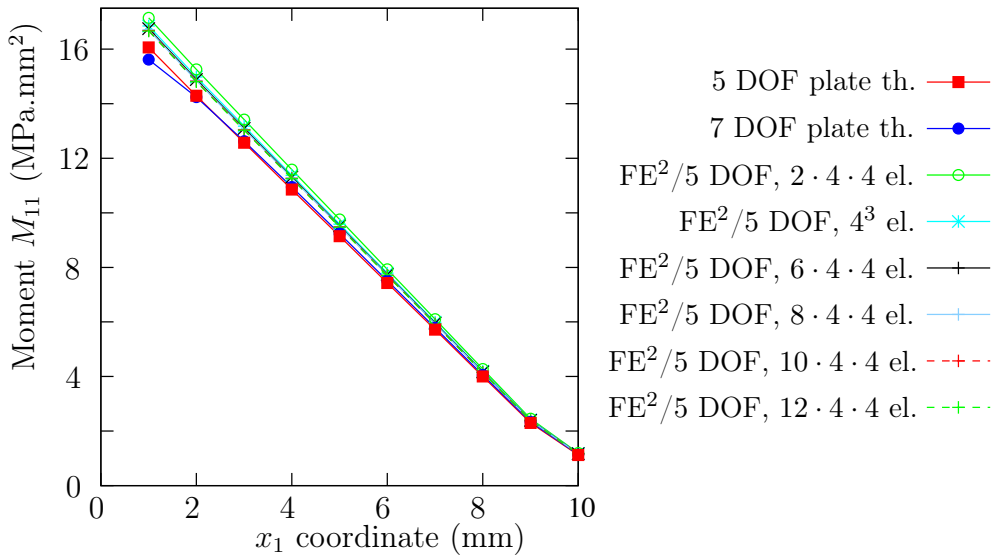

Figure 5.25: Moment distribution for the bending test of a three-layers sandwich plate containing isotropic elastic layers for different meso discretisation

force distribution in Fig. 5.26, for the different RVEs.

As observed in Fig. 5.25 and 5.26, the length of the RVE has only a reduced influence on the accuracy of the results. With a larger RVE, the error is smaller, but the improvement gained is minimal, from 7% for $2 \times 4 \times 4$ elements to 4.2% for the $6 \times 4 \times 4$ elements, for the moment resultants. The error reaches a value of 3.8% for a RVE with $12 \times 4 \times 4$ elements. For the considered composite materials, the RVE is homogeneous in the two

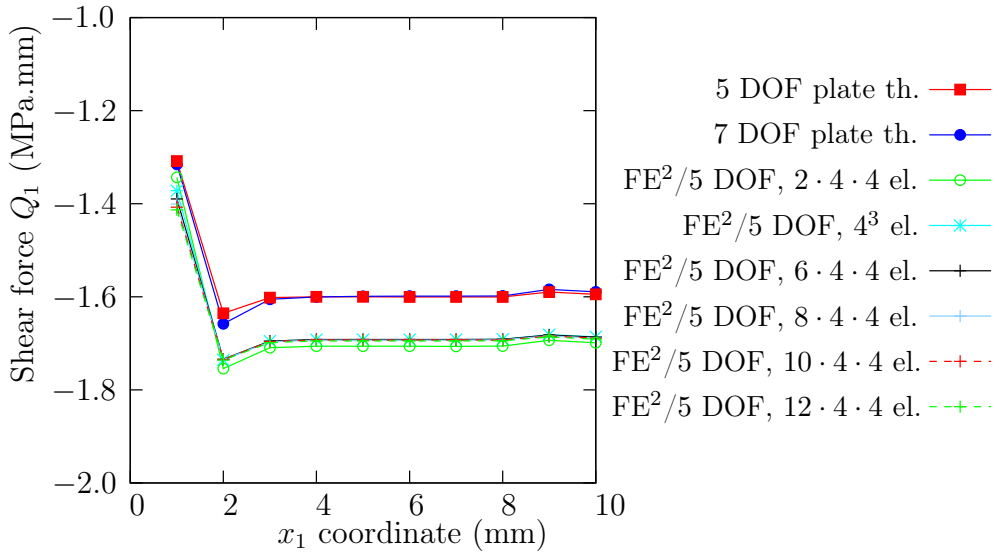

Figure 5.26: Shear force distribution for the bending test of a three-layers sandwich plate containing isotropic elastic layers for different meso discretisation

directions parallel to the midplane; as a consequence, the length of the RVE has only a reduced influence on the results. A much better improvement is obtained for a finer mesh; however, this represents too high computational costs.

Under the uniaxial or biaxial tension test and under the shear test, the size of the RVE has almost no influence on the accuracy of the results, because the tension and shear tests are homogeneous tests. On the contrary for the bending test, the size and the discretisation of the RVE have an influence on the results. Better results are obtained for a RVE with a discretisation of 8^3 or 12^3 elements; however, because of the high computing time, the optimal RVE size is set by 4^3 elements. Another possibility is to use a larger RVE in the direction parallel to the midplane, but the precision gained is very small, because the RVE is homogeneous in the two directions parallel to the midplane. However, the edge effects are reduced by a RVE with a larger length.

In order to test the method, a structure consisting of three-layers was submitted to an uniaxial and an equi-biaxial tension test, a shear test and a bending test. But can the numerical multi-scale method be accurately used for the computation of hybrid laminates? We will answer this question in the next subsection.

5.1.5 Hybrid Laminate

In the following, the mechanical behaviour of a hybrid laminate, made up of ten layers, is studied. The hybrid laminate is composed of ten layers, with the following organisation: $(\text{Al}/\text{CFRP}(0°/90°/0°)/\text{Al})_s$[3]. The layer's organisation is represented on Fig. 5.27. On the top and on the bottom, Aluminium layers are set (Al). An elastic isotropic material behaviour is assumed for the Aluminium layers. Then, three layers of CFRP (Carbon Fibers Reinforced Polymer) are set, with the fibers alignment (0°/90°/0°). The two layers in the middle are assumed to be elastic. The seventh, eighth and ninth layers are CFRP layers with the fibers alignment (0°/90°/0°). The last layer is an Aluminium layer. The Aluminium has a Young's modulus of 70500 MPa and a Poisson's ratio of 0.3. The Carbon Fibers Reinforced Polymer shows a transverse isotropic material behaviour, and the material constants are given in the Table 5.1.

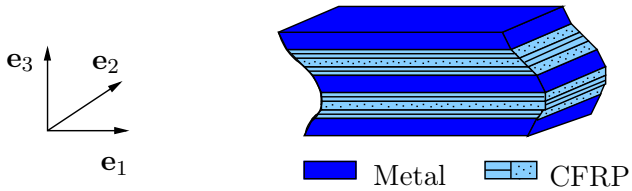

Figure 5.27: Structure of the hybrid laminate containing the layer organisation (metal/CFRP(0°/90°/0°)/metal/metal/CFRP(0°/90°/0°)/metal)

In a first instance, a tension test is computed, with the same boundary condition as used before and represented in Fig. 5.1. The plate has a length and a width of 10 mm, whereas its thickness is 1 mm. In the Subsect. 5.1.1, it was proved that the macro discretisation has a small influence on the accuracy of the results. The assumption is then set that the influence of the macro discretisation is also reduced in this example and two elements are considered for the macro discretisation. The RVE's discretisation has also to be defined. Because ten layers are considered, the smallest discretisation for a cubic RVE discretized with cubic elements is 10^3 elements, which shows to be computationally very expensive in the framework of a numerical homogenisation. Consequently, the discretisation of the RVE is not further refined.

In Fig. 5.28 on the left side, the normal forces are drawn. On the right side, the relative error is represented; the three-dimensional computation is considered as the reference solution. Again, several solutions are computed: the numerical homogenisation using the "classical" projection strategy -without consideration of the thickness change, cf. Eq. (4.17)-, the numerical homogenisation using the projection strategy developed in this work, cf. Eq. (4.20), the plate theory based on seven degrees of freedom and the three-dimensional modelling. It can be observed in Fig. 5.28 that the errors are globally very small. For the "classical" projection strategy, which does not include any thickness change, an error of almost 1.5% is obtained. The error is less than 0.04% for the FE^2 method using the new projection strategy and for the plate theory. The reduced error can be related to the reduction of the thickness change, due to the material behaviour of

[3]The $(\diamond)_s$ is set for a symmetric layer stacking order

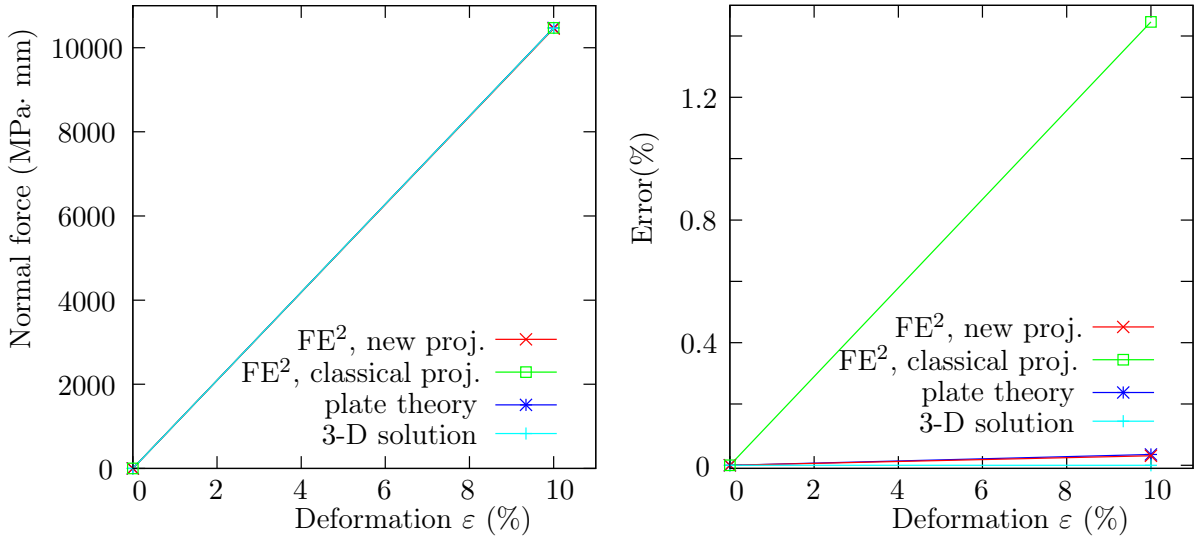

Figure 5.28: Normal force for a tension test of the ten-layers hybrid laminate represented in Fig. 5.27 (relative error on the right)

the different layers of the hybrid laminate.

The RVE is drawn in Figs 5.29 and 5.30. For both figures, the RVE resulting from the "new" projection strategy proposed in this work, including a thickness change due to consideration of an extra internal variable, is represented on the left side. The RVE resulting of the "classical" projection strategy is drawn on the left side. This projection is used by many authors [36, 65, 80] in the framework of a numerical homogenisation using a plate theory following the Mindlin ansatz, that means without consideration of any thickness change. As mentioned before, the "classical" projection does not consider any thickness change. On the contrary, the projection strategy proposed in this work includes a solution of the Poisson locking. However, the influence of the projection tends to be reduced for the hybrid laminate, in comparison with a three layers structure.

In a second instance, a shear test is computed, according to the boundary conditions expressed in Fig. 5.9. The material constants, the geometry of the plate and the discretisation for the macroscale and for the mesoscale are the same as for the tension test. The normal shear force is represented in Fig. 5.31 for the different methods.

It can be seen in Fig. 5.31, that, similarly as for the three layers structures, there are no major differences between the four methods for the shear test of a hybrid laminate. Due to the fact that a shear test is isochoric, the thickness change vanishes for this test. As a consequence, the Poisson locking does not take place, leading to no difference between the different projections. Due to the absence of the thickness changes, the plate theory of Mindlin type leads also to accurate results.

Then, a bending test of the hybrid laminate is computed, for the numerical homogenisation and for the plate theory. The moment resultant is represented in Fig. 5.32. It can

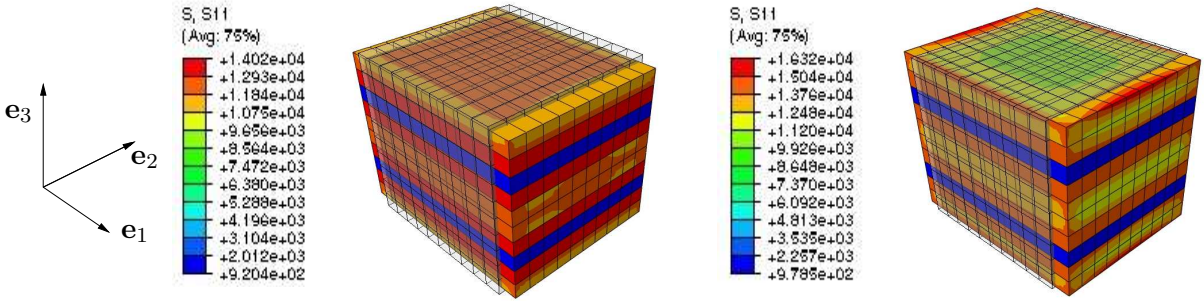

Figure 5.29: Normal stress in the RVE for the new projection on the left and the "classical" projection on the right, for an uniaxial tension test of a hybrid laminate

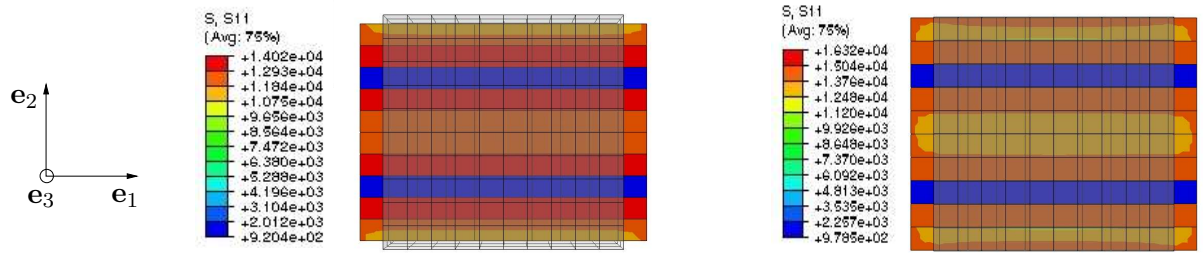

Figure 5.30: Normal stress in the RVE for the new projection on the left and the "classical" projection on the right, for an uniaxial tension test of a hybrid laminate

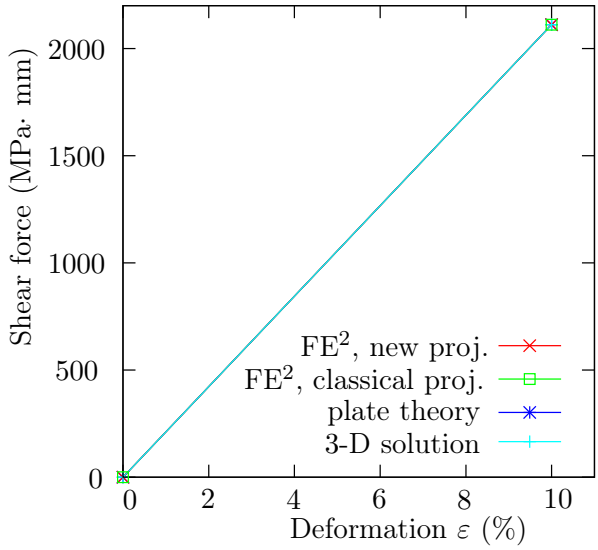

Figure 5.31: Shear force vs. deformation for a shear test of the ten-layers hybrid laminate represented in Fig. 5.27

be observed that there is less than 1% error between the moment distribution given by the plate theory or by the FE^2 method. As for the tension test, the error is reduced if a composite plate containing several layers is considered.

The shear force can also be represented as a function of the coordinate in $\mathbf{e}_1$-direction, as drawn in Fig. 5.33. There is approximately 2% error between the numerical homogenisation method and the three-dimensional solution. It is to mention that if a composite containing several layers is modelled, the error tends to be smaller. This can be explained in different ways: firstly, in order to model the different layers, a finer mesh is needed as for a three-layers structure, which leads to a reduction of the error. Secondly, a better result for the ten-layers laminate could be explained by the reduced thickness change resulting from the presence of fibers. The transverse isotropic layers shows a Poisson's ratio of 0.3 or 0.275 -depending on the direction- which is smaller than the Poisson's ratio of the matrix alone -around 0.4, as used for the tension test of the three-layers isotropic plate. It can be concluded that the numerical homogenisation is an useful method, enabling the computation of both the in-plane and the out-of-plane problem of sandwich plates and of hybrid laminates. However, the former examples consists of linear material behaviour; but what's about non-linear material behaviour? The question will be answered in the next section.

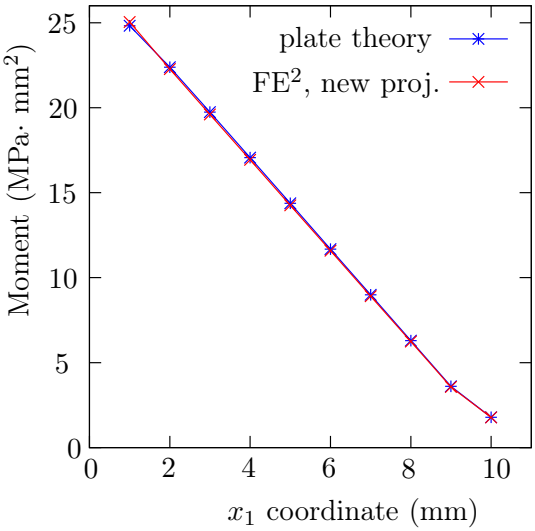

Figure 5.32: Moment distribution for a bending test of the ten-layers hybrid laminate represented in Fig. 5.27

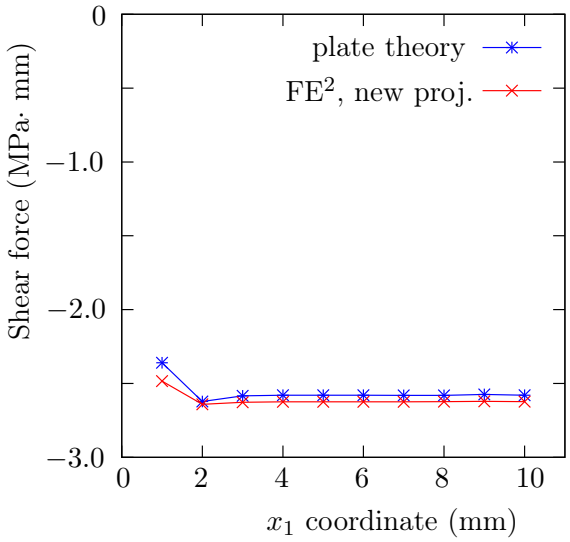

Figure 5.33: Shear force distribution for a bending test of the ten-layers hybrid laminate represented in Fig. 5.27

5.2 Non-Linear Material Behaviour

After the validation of the method for linear elastic material behaviour, it has to be tested for non-linear material behaviours. The plate has a length and a width of 10 mm, and a thickness of 1 mm. The macro and meso discretisation are the same as chosen before for the three-layers composite submitted to in-plane problems. Under this framework, an elasto-plastic material with isotropic hardening is considered. Two types of composite structures are studied in this part: in the first instance, a structure containing an elastic isotropic core and elasto-plastic top panels, is studied. The elastic isotropic core has a Young's modulus of 55000 MPa and a Poisson's ratio of 0.4. In the second instance, a composite plate containing an elastic transverse isotropic core material and elasto-plastic isotropic top panels is considered. The transverse isotropic elastic core has the properties expressed in the Table 5.1.

The elasto-plastic material presents an isotropic hardening. Its Young's modulus is 70500 MPa, with a Poisson's ratio of 0.3. The yield stress is 200 MPa. In a first instance, an unixial tension test and a shear test are computed for the elasto-plastic material only. The boundary conditions are represented in Figs 5.1 and 5.9 for the tension and shear test, respectively. The loading step is then followed by an unloading step. The displacement as a function of the time for the whole process can be represented in Fig. 5.34. In Fig. 5.35, the stress-strain curves of the RVE computed with the FE^2 method using the new projection strategy and of the reference solution, obtained with a FE computation of a three-dimensional model with the commercial software ABAQUS®, are represented.

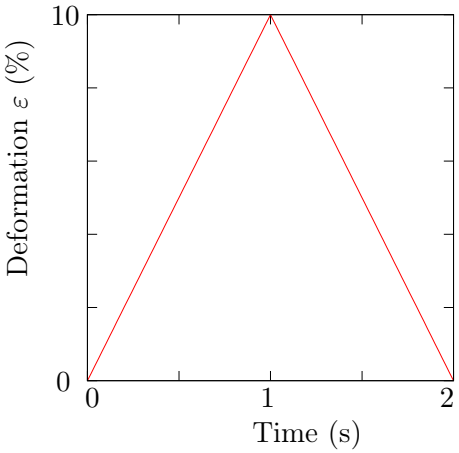

Figure 5.34: Schematic representation of the loading and unloading steps

Firstly, the results of the shear test are considered. The stress-strain curves obtained for the RVE and for the three-dimensional solution are drawn on the right side in Fig. 5.35. It can be observed that the stress-strain curves, given by the two methods, are similar but that a reduced discrepancy can be observed for the unloading step. This may be explained by the considered kinematics, which might be not sufficient for the description of the eigenstresses. We can assume that the consideration of the fluctuations could give better results for the description of the eigenstresses.

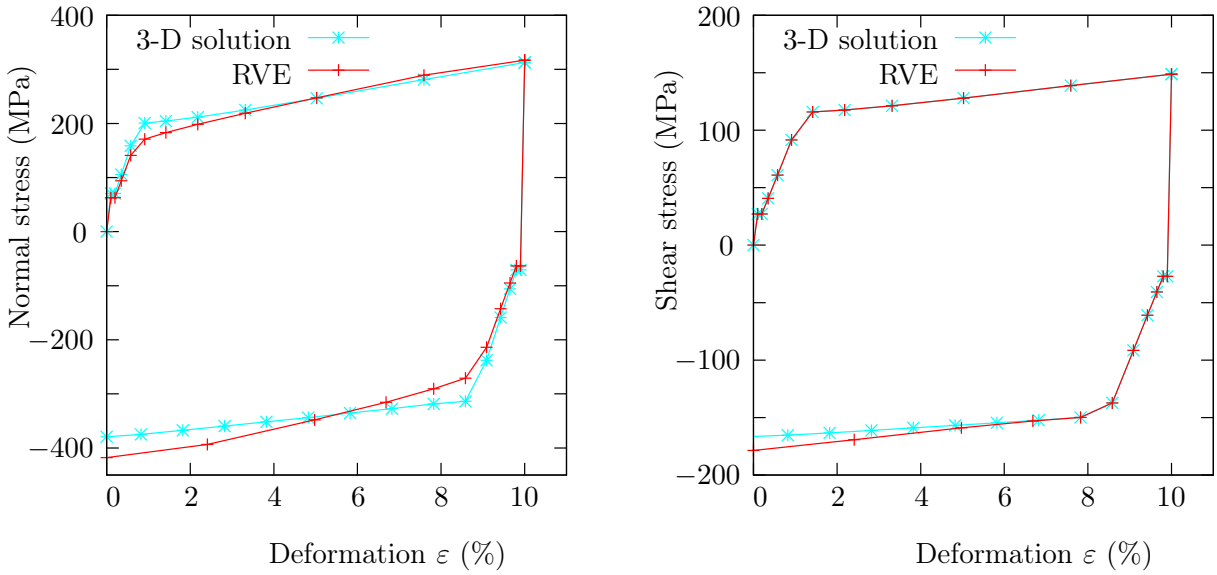

Figure 5.35: Stress-strain curve for the one elasto-plastic material for a tension test on the left and for the shear test on the right

Secondly, the stress-strain curves obtained for the tension test are considered, on the left side in Fig. 5.35. As observed in Fig. 5.35, the final state of the both results is similar for the loading; however, discrepancies arise in the transition between the elastic and the plastic domain. The plastic domain is reached for a larger stress σ_{11} for the three-dimensional composite computed with ABAQUS® as for the RVE[4]. It can be explained by the absence of boundary conditions applied to the surfaces with normal $\mathbf{e}_3$ for the RVE, leading to a parasitic stress in the third direction. As a consequence, the von Mises function reaches a value of zero, defining the begin of the plastic part, for a lower stress σ_{11}. It is also observed that this discrepancy vanishes at further deformations in the plastic part during the loading step, because the stress in thickness direction tends to vanish. Similar results have been observed by Altenbach et al. [7] for a creep-damage problem, where a discrepancy is observed for the results given by the shell elements and the volume elements. This discrepancy can be related to the plane stress assumption for the plate or shell elements and to the distribution of the stress through the thickness.

In a second instance, the composites are submitted to an uniaxial tension test, a shear test and a biaxial tension test. Finally, a bending test is computed.

5.2.1 Uniaxial Tension Test

In this part, unixial tension tests are considered, with the same boundary conditions as drawn in Fig. 5.1, which are then followed by an unloading, as represented in Fig. 5.34. A tension test of a three-layers composite plate containing elasto-plastic and isotropic elastic material behaviour is computed. The error obtained for the normal stress between the

[4]The Cauchy stress $\boldsymbol{\sigma}$ is considered in the following because the numerical experiments are performed in the small deformation domain.

FE^2 method using the new projection strategy and the three-dimensional computation is of maximal 1.6%. It is to mention that a maximal error of 6.9% is obtained using the classical projection strategy, which does not enable the consideration of the thickness change in the level of the plate. However, due to the non-linearity of one of the material laws, a representation of the stress -or normal force- as a function of the strain is needed. As a following, the average of the stress as function of the strain for both RVE and three-dimensional FE modelling of the composite, considered as the reference solution, are represented in Fig. 5.36. The three-dimensional computation and the FE^2 method using the new projection strategy lead to similar results for the stress-strain curves, but discrepancies arise for the stress-strain curve given by the FE^2 method using the classical projection.

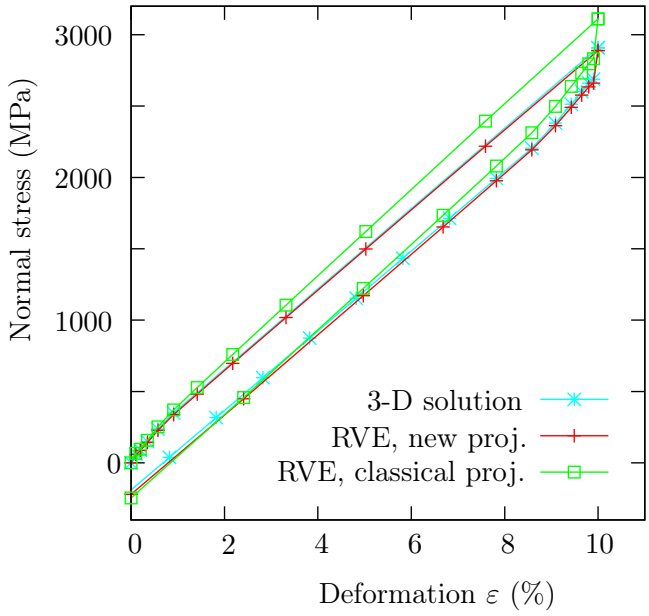

Figure 5.36: Stress-strain curve for a tension test for the three-layers sandwich plate containing an isotropic elastic core and elasto-plastic top panels

Then, a three-layers composite, made up of transverse isotropic elastic layers and elasto-plastic layers, is submitted to an uniaxial tension test. The fiber orientation is 0°, i. e. that the fibers are aligned with the tension direction. A representation of the average stress obtained for the RVE and the reference solution is given in Fig. 5.37.

In the presented example, the fibers are parallel to the direction of the tension test. Due to the anisotropy of the material, the response of the anisotropic layer is much stiffer than the response of the elasto-plastic layers, resulting in a quasi-linear progression of the stress, as can be seen in Fig. 5.37. As a consequence, the importance of the non-linear material behaviour is reduced, as well as the error, in comparison with the former example. In this case, almost no difference between the results obtained with the classical or with the new projection strategy can be observed.

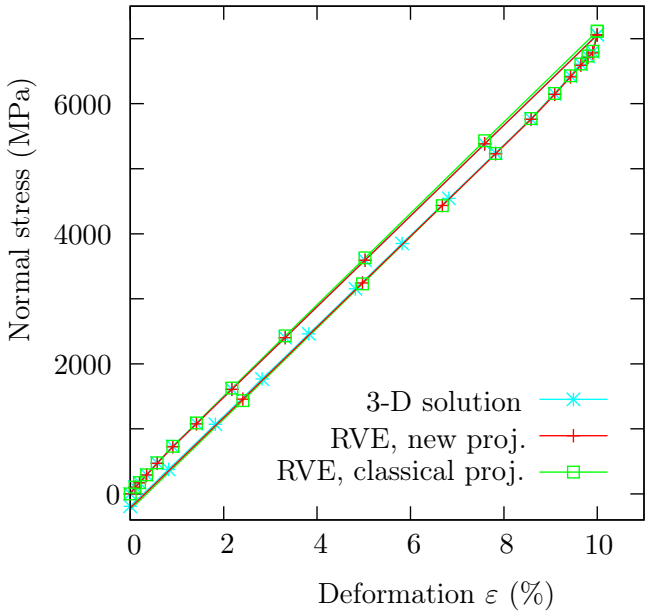

Figure 5.37: Stress-strain curve for a tension test for the three-layers sandwich plate containing a transverse isotropic elastic core (fiber orientation 0°) and elasto-plastic top panels

5.2.2 Shear Test

In this part, a shear test is computed, using the same boundary condition as before, (represented in Fig. 5.9). In a first instance, a shear test of a three-layers material, made up of an isotropic elastic core and elasto-plastic top panels, is computed. The error between the final shear reached for the FE^2 method and for the result of the three-dimensional modelling is smaller than 0.01% during the loading step. It is to mention that because the shear test is isochoric, the same results are observed using the classical or the new projection strategy. For a better comparison, the stress obtained in the RVE and with the reference solution are given as a function of the strain in Fig. 5.38. It can be seen that the stress obtained for the different methods are nearly the same, leading to an insignificant error.

In a second instance, a shear test of a three-layers composite containing both anisotropic elastic and elasto-plastic materials is computed. The core material has a transverse isotropic material behaviour with a fiber orientation of 0° -but a fiber orientation of 90° leads to the same results in this case. The stress resultant obtained for the FE^2 method, compared with the stress computed by the three-dimensional solution leads to a small error. However, due to the non-linearity of the elasto-plastic material law, more information are given by the stress-strain curve, as represented in Fig. 5.39.

The stress-strain curves obtained for an anisotropic/elasto-plastic composite are very similar for the two methods -namely, the FE^2 method and three-dimensional modelling. Because no volume changes occurs during a shear test, the classical projection and the new

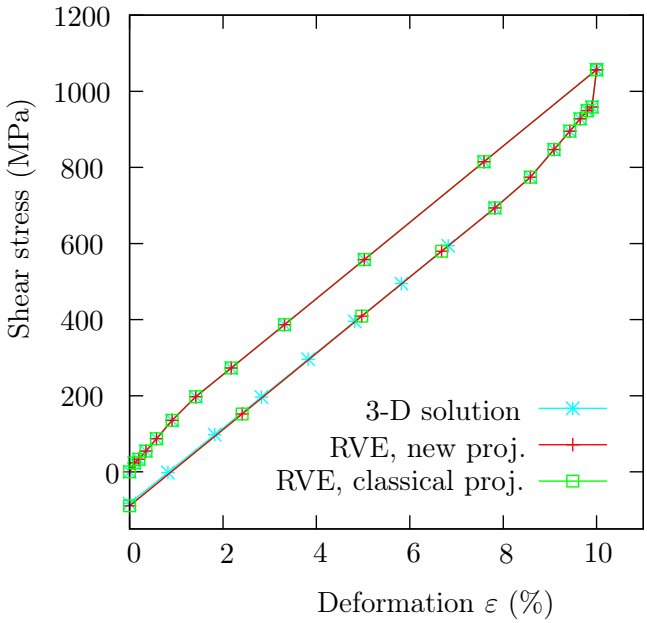

Figure 5.38: Stress-strain curve for a shear test for the three-layers sandwich plate containing an isotropic elastic core and elasto-plastic top panels

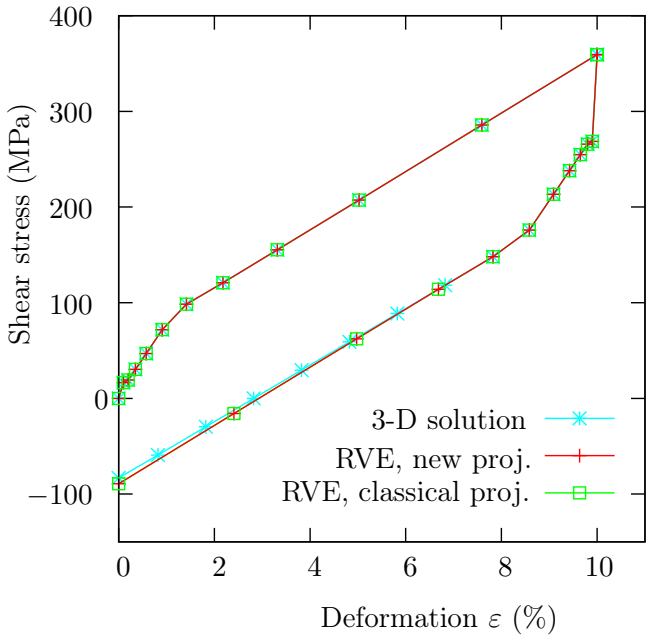

Figure 5.39: Stress-strain curve for a shear test for the three-layers sandwich plate containing a transverse isotropic elastic core (fiber orientation 0°) and elasto-plastic top panels

projection strategy lead to the same results. It enables to draw the conclusion that the FE^2 method gives accurate results, if no thickness change takes place. A further consider-

ation of a biaxial tension test brings further information about the validity of the method if a thickness change occurs.

5.2.3 Biaxial Tension Test

A three-layers material containing transverse isotropic elastic and elasto-plastic layers is computed under a biaxial tension test, with the boundary condition for the first step given in Fig. 5.12. A second step is applied, where an unloading takes place, as represented in Fig. 5.34. Two types of sandwich plates are considered: on the one hand, the core material presents an isotropic elastic material behaviour and elasto-plastic top panels. On the other hand, the core material presents a transverse isotropic material behaviour (with the fiber orientation of 0°) and elasto-plastic top panels.

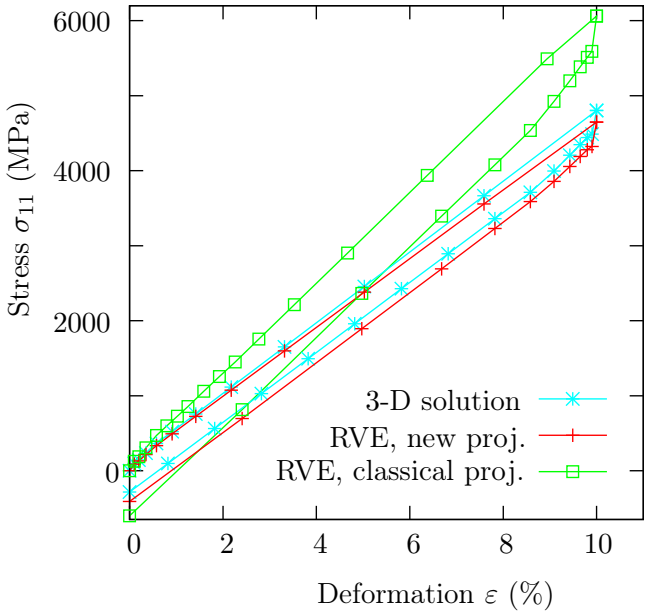

Figure 5.40: Stress-strain curve for a equi-biaxial tension test for the three-layers sandwich plate containing a isotropic elastic core and elasto-plastic top panels

Firstly, the composite plate containing an isotropic elastic core and elasto-plastic top panels is considered. The stress-strain curve obtained for the different methods -namely, the FE^2 method using the classical or the new projection strategy and three-dimensional modelling- are drawn in Fig. 5.40. The error in the stress between the numerical homogenisation method enabling the thickness change and the three-dimensional solution is around 3% in the loading step. The error obtained in the unloading step is larger, because the numerical homogenisation may not be enable to give an accurate description of the eigenstresses. It is to mention that a larger error is observed with the FE^2 method using the classical projection strategy than with the FE^2 method using the new projection strategy. Considering the stress-strain curve given by the numerical homogenisation with the classical projection strategy, the error reaches 26% during the loading step. We can conclude that the projection strategy proposed in this work, following a similar principle

as the EAS method, enable better results if incompressible material behaviours are considered and for the tests involving a large thickness change.

Secondly, the composite sandwich with a transverse isotropic core and elasto-plastic top panels is considered. The error obtained between the final stress resultant in the loading step using the FE^2 method with the projection strategy proposed in this work, compared with the three-dimensional solution, in direction parallel to the fibers and normal to the fibers are smaller than 1%. In contrast, the error observed in the stress resultant in the loading step using the numerical homogenisation with the classical projection, compared with the three-dimensional solution, are larger than the one obtained with the FE^2 method using the new projection strategy. The representation of the stress as a function of the strain, obtained for a RVE and for the reference solution are given in Fig. 5.41. On the right side, the stress in direction parallel to the fibers alignment is represented; on the left side, the stress in direction normal to the fibers is shown. It can be observed that, similarly as for the single material, the error is larger in the unloading step, especially for the FE^2 method using the classical projection strategy.

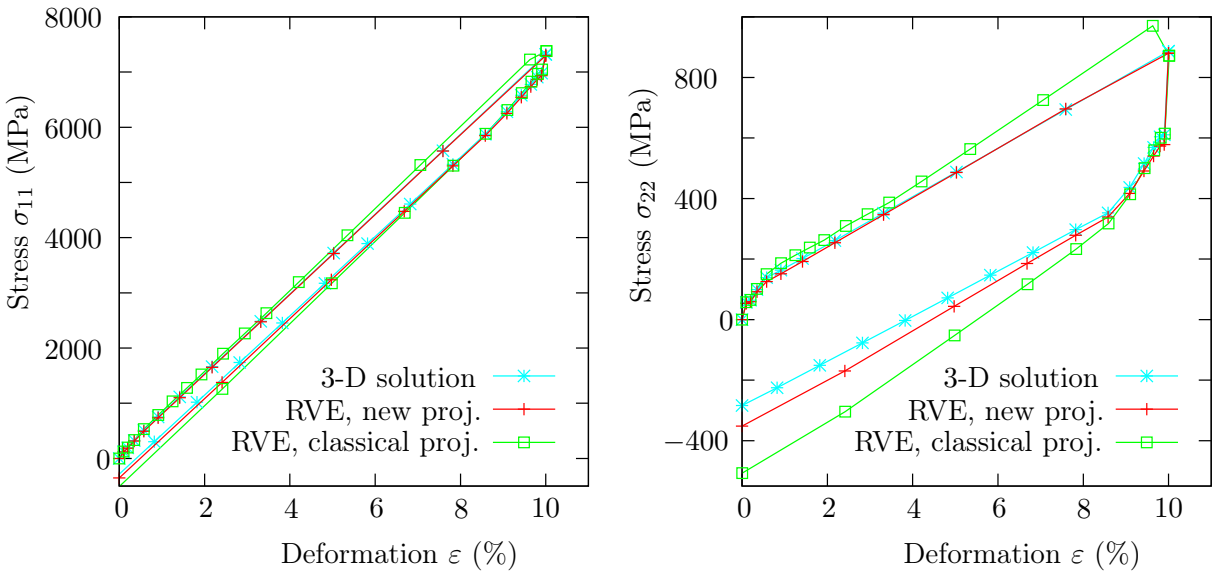

Figure 5.41: Stress-strain curve for a equi-biaxial tension test for the three-layers sandwich plate containing a transverse isotropic elastic core (fiber orientation 0°) and elasto-plastic top panels; in the direction parallel to the fibers alignment on the left and on the direction normal to the fibers alignment on the right

It can be seen that the influence of the elasto-plastic material law is much smaller in the stress response for the direction parallel to the fibers alignment. As a consequence, the error, due to the non-linear material law, is also much smaller for this direction. It can be observed a reduced difference in the stress using the FE^2 method and the new projection strategy and the global stress answer is considered as accurate. The conclusion can be drawn that the FE^2 method proposed in this work gives good results for membrane problems, for linear as well as for non-linear material behaviour. Furthermore, the FE^2 method using the projection strategy proposed in this work enables a consideration of the

thickness change and of any material behaviour without any further modification of the material law.

5.2.4 Bending Test

Finally, a bending test of two composite structures is computed, according to the boundary condition represented in Fig. 5.18. The composite plates consist of elasto-plastic top panels and of an isotropic or anisotropic elastic core, with the same material constants as before mentioned in this part. It is to mention that a force is applied to one extremity of the composite, whereas the other one is blocked. The plate has a length of 10 mm, whereas its width and thickness is of 1 mm. The same macro and meso discretisation are used as in Subsect. 5.1.4, that means that the mesh on the macroscale contains 20 plate elements with quadratic ansatz function. The RVE is meshed with 4^3 quadratic brick elements.

The vertical displacements obtained for the two structures are drawn in Fig. 5.42 as a function of the coordinate in $\mathbf{e}_1$-direction, for the result of the numerical homogenisation and for a three-dimensional computation. Because no thickness change occurs for the bending test, the results are the same considering the classical projection and the new projection strategy proposed in this work. It is to mention that for a mesoscopic mesh of 4^3 elements, an error approximately 1% is observed between the three-dimensional modelling and the FE^2 method, for the composite made up of isotropic linear and non-linear layers. Considering the sandwich structure composed of a transverse isotropic core and elasto-plastic top panels, the error in the displacements is of approximately 3%. Therefore, the numerical multi-scale method can be considered accurate for the modelling of linear and non-linear materials, under membrane problems but also under bending. Nevertheless, the FE^2 method shows particularly high computational costs, especially when dealing with non-linear material behaviour.

It can be concluded that the FE^2 method is able to describe membrane problems, as accurate as a plate theory for elastic material behaviour. However, the FE^2 method enables the consideration of any constitutive law without further transformations, as for instance for an elasto-plastic material behaviour. However, tension, shear and bending tests are classical problems; is the FE^2 method able to describe complicated issues like a Cook's membrane, a plate with a hole or a Pagano problem? This will be answered in the next sections.

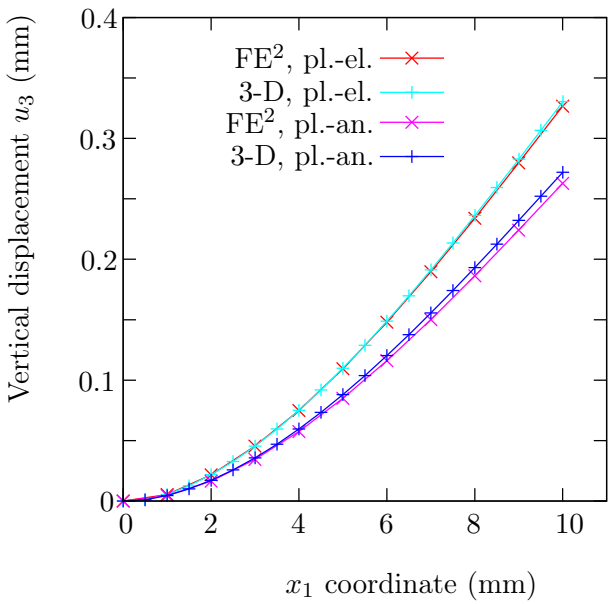

Figure 5.42: Vertical displacement distribution for the bending test of a three-layers sandwich plate containing an isotropic elastic core and elasto-plastic top panels (pl.-el.) and of a three-layers sandwich plate containing a transverse isotropic elastic core (fiber orientation 0°) and elasto-plastic top panels (pl.-an.)

5.3 Cook's Membrane

In this part, the computation of a Cook's membrane is performed. The applied boundary conditions are represented in Fig. 5.43. On the left side, the displacement and rotation degrees of freedom are set to zero, whereas on the right side, a force is applied in the $\mathbf{e}_2$ direction. The exact geometry of the Cook's membrane is given in Fig. 5.43. Its thickness is 1 mm.

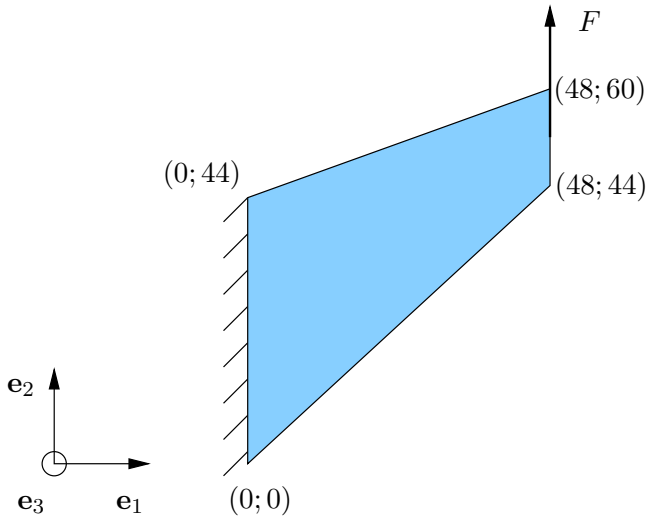

Figure 5.43: Schematic representation of the Cook's membrane

Firstly, a three-layers composite containing isotropic elastic layers is computed. The top panels have the following material properties: a Young's modulus of 70500 MPa and a Poisson's ratio of 0.3. The core material presents a Young's modulus of 55000 and a Poisson's ratio of 0.4. A force of 1000 N is applied to the right side of the Cook's membrane. The core has a thickness of 0.5 mm, and each of the top panels has a thickness of 0.25 mm. A discretisation of 4^3 quadratic brick elements is chosen for the RVE. About the macro discretisation, a computation with 8 and 32 elements using the FE^2 method is performed and the displacements in $\mathbf{e}_2$-direction are represented in Fig. 5.44 for the two macro discretisation. It it to mention that the mesh containing 8 and 32 elements gives an error of 6.8% and 3.5%, respectively, compared with the maximal displacement given by the three-dimensional computation. However, due to the high computing time which takes the FE^2 method, a macro discretisation with 32 elements is used thereafter.

In the following, a discretisation with 32 plate elements is used for the macro-discretisation under the FE^2 method and for the plate theory with thickness change, in order to enable a comparison of the method with the same mesh. The three-dimensional computation with ABAQUS® is performed with 1024 quadratic brick elements. Fig. 5.45 represents the displacement in $\mathbf{e}_2$-direction resulting from the numerical homogenisation on the left (a), the plate theory with thickness change in the middle (b) and the three-dimensional computation on the right (c). It can be observed that the difference between the three methods is very small and that the displacement distribution is similar. Considering the maximal displacement, the error obtained with the plate theory or with the numerical

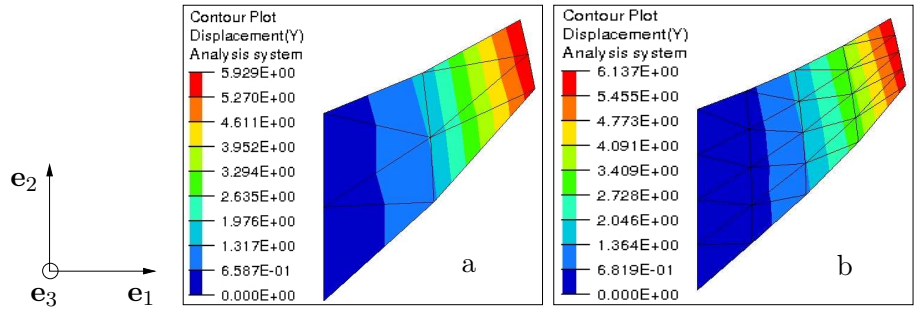

Figure 5.44: Displacement in $\mathbf{e}_2$-direction for the Cook's membrane on a three-layers sandwich plate containing isotropic elastic layers: results for the different discretisation (a: 8 elements and b: 16 elements)

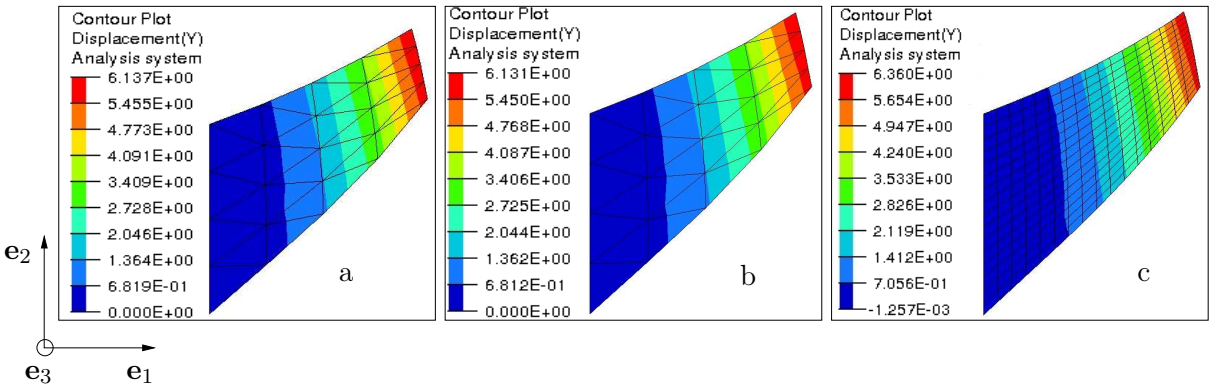

Figure 5.45: Displacement in $\mathbf{e}_2$-direction for the Cook's membrane of a three layers sandwich plate containing isotropic elastic layers: result of the FE^2 method on the left (a), of the plate theory in the middle (b) and of the three-dimensional computation with ABAQUS on the right(c)

homogenisation are around 3.5%, due to the coarse mesh. It is to mention that the plate theory with thickness change gives an error of 1.2% for a finer mesh with 512 plate elements.

Then, a non-linear material behaviour can be considered. In the following examples, two structures composed of an elasto-plastic material behaviour combined with either isotopic or transverse isotropic elastic core, are computed. The elasto-plastic material behaviour is the same as exposed in Sect. 5.2, the core material has either an isotropic elastic or a transverse isotropic elastic material behaviour. The elastic isotropic material presents a Young's modulus of 55000 MPa and a Poisson's ratio of 0.4, while the transverse isotropic material has the properties expressed in Table 5.1 and a fiber's orientation of 0°. A force of 200 N is applied for the two different sandwich structures containing elasto-plastic top panels and either an isotropic elastic or a transverse isotropic elastic core. Considering the composite plate with an isotropic elastic core, the displacements is $\mathbf{e}_2$-direction are drawn in Fig. 5.46 for the FE^2 method on the left (a) and for the three-dimensional computation on the right (b). It is to mention that an error of 5% is obtained for the maximal displacement. The results of the computation of the three-layers composite

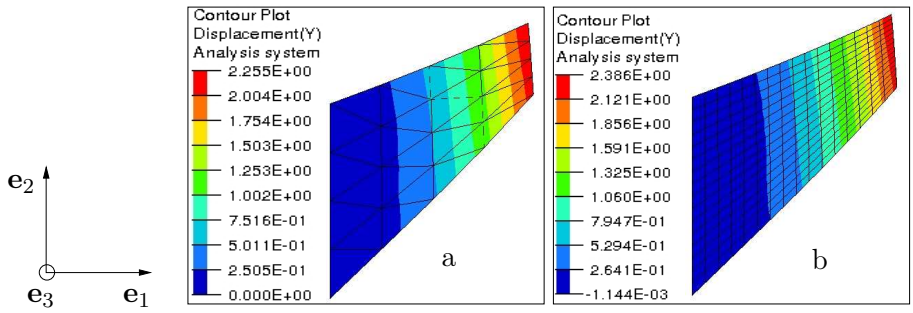

Figure 5.46: Displacement in $\mathbf{e}_2$-direction for the Cook's membrane of a three layers sandwich plate containing isotropic elastic and elasto-plastic layers: result of the FE^2 method on the left (a) and of the three-dimensional computation with ABAQUS on the right(b)

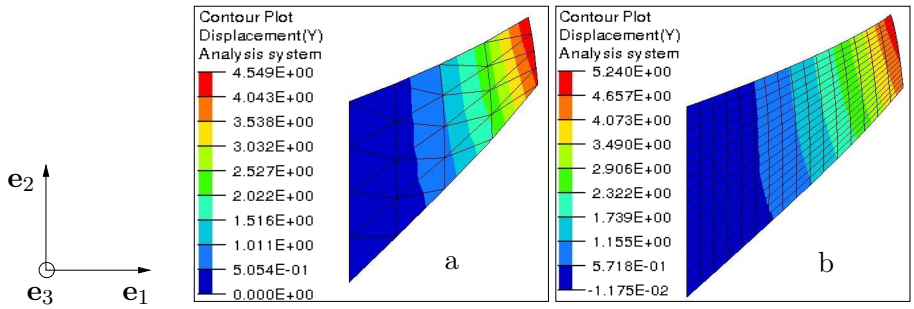

Figure 5.47: Displacement in $\mathbf{e}_2$-direction for the Cook's membrane of a three layers sandwich plate containing a transverse isotropic core and elasto-plastic top panels: result of the FE^2 method on the left (a) and of the three-dimensional computation with ABAQUS on the right(b)

plate containing a transverse isotropic core and elasto-plastic top panels are represented in Fig. 5.47. In Fig. 5.47, the displacements in $\mathbf{e}_2$-direction are represented for the FE^2 method on the left (a) and for the three-dimensional computation with ABAQUS on the right (b). It is to mention that an error of 10% is obtained for the FE^2 method, in comparison with the three-dimensional computation. This can be related to the coarse mesh used for the FE^2 method. In the next part, a plate with a hole is computed under a tension test.

5.4 Plate with Hole

In this part, a square plate containing a hole is computed under tension. In order to reduce the computing time, the quarter of the problem is considered. The boundary conditions are drawn in Fig. 5.48. The square plate has a length of 10 mm with an hole of diameter of 5 mm in its center. The displacement is applied on the right side of the plate on the $\mathbf{e}_1$-direction and has the amplitude of 1 mm.

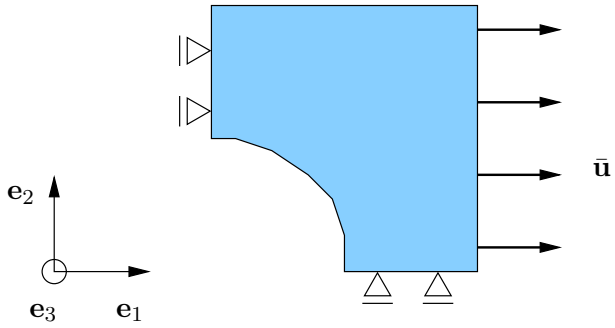

Figure 5.48: Schematic representation of the plate with an hole

In a first instance, a composite plate containing three layers consisting of isotropic elastic materials are tested under tension. The top panels present a Young's modulus of 70500 MPa and a Poisson's ratio of 0.3, while the core has a Young's modulus of 55000 MPa and a Poisson's ratio of 0.4. The RVEs are meshed with 4^3 quadratic brick elements and the macro discretisation is performed with 94 elements. The macro discretisation is defined as a optimum between the computing time and the precision: two other FE^2 problems with a macro discretisation with 21 and 176 elements are computed and the results are drawn in Fig. 5.49. In Fig. 5.49, the normal force is drawn for the three different discretisations of the macroscale: for the coarse mesh with 21 elements (a), for the mesh containing 94 elements (b) and for the finer mesh with 174 elements (c). It can be observed that the results are converging to the values given by the finer mesh; but that the error between the mesh with 94 elements and the finer mesh is around 7% for the maximal value. This error is not negligible, but the computing time needed for the FE^2 value does not enable to consider a larger mesh, especially if non-linear material behaviour is considered. Consequently, a macro discretisation with 94 elements is considered further for the different composite plates.

In Fig. 5.50, the normal force is drawn for the FE^2 method proposed in the presented work on the left and for the plate theory with thickness change on the right. The same discretisation is applied for the plate for the two methods, in order to enable a comparison of them. There is a very reduced error of 0.4% between the two results for the maximum normal force and of 0.6% for the minimal normal force. Moreover, the normal force distribution is extremely similar for the two methods.

Then, a three-layers composite plate with a hole, containing a transverse isotropic elastic core and isotropic elastic top panels, is computed under tension. The core material consists in the transverse isotropic material with the constants expressed in Table 5.1. The elastic

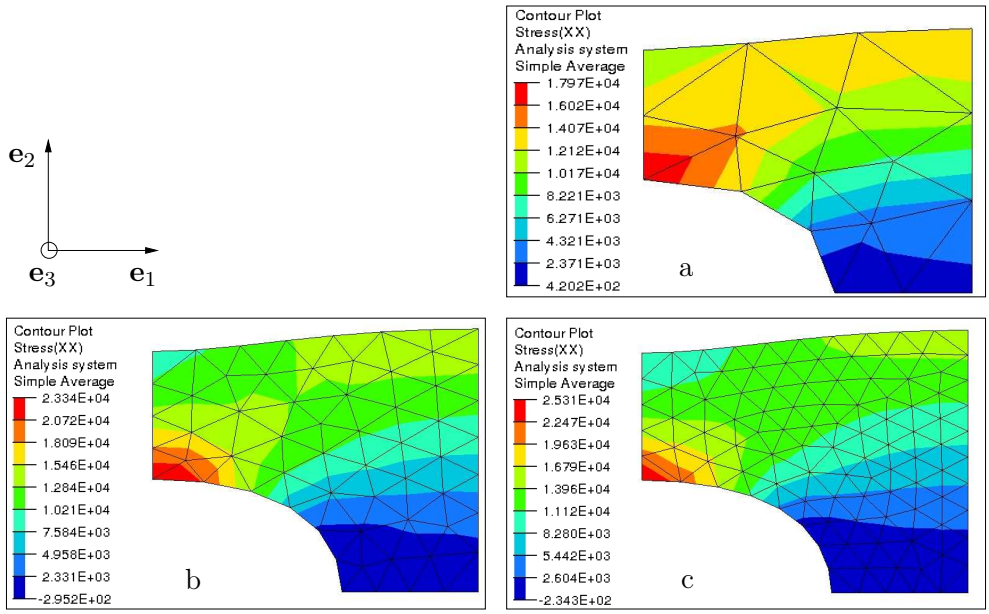

Figure 5.49: Normal force for a tension test on a plate with a hole of a three-layers sandwich plate containing isotropic elastic layers: results for the different discretisation (a: 21 elements, b: 94 elements and c: 174 elements)

top panels have the Young's modulus of 55000 MPa and a Poisson's ratio of 0.4. The distribution of the normal force can be drawn in Fig. 5.51. It can be seen that the stress repartition is extremely similar for the numerical method and for the plate theory. Moreover, the error between the two methods is around 0.2% for the maximal and minimal values of the force.

Then, a non-linear material behaviour is considered. Two composite plates containing elasto-plastic top panels and an isotropic elastic or a transverse isotropic elastic core are submitted to the tension test. The elasto-plastic material behaviour is the same as studied in Sect. 5.2. The core material shows either an isotropic elastic or a transverse isotropic elastic material behaviour; the elastic isotropic material has a Young's modulus of 55000 MPa and a Poisson's ratio of 0.4, while the transverse isotropic material presents the properties expressed in Table 5.1.

The distribution of the normal force is represented in Fig. 5.52 for the composite composed of elastic isotropic and elasto-plastic material behaviours. In Fig. 5.53, the tension test of the three-layers composite plate containing anisotropic elastic and elasto-plastic material behaviours is represented. It can be observed that the numerical homogenisation enables a computation of complicated problems, also with non-linear material behaviour like elasto-plasticity. It is to mention that the advantage of this method leads to the possibility to include any material behaviour into account, also no linear ones, and without any further transformations of the material laws.

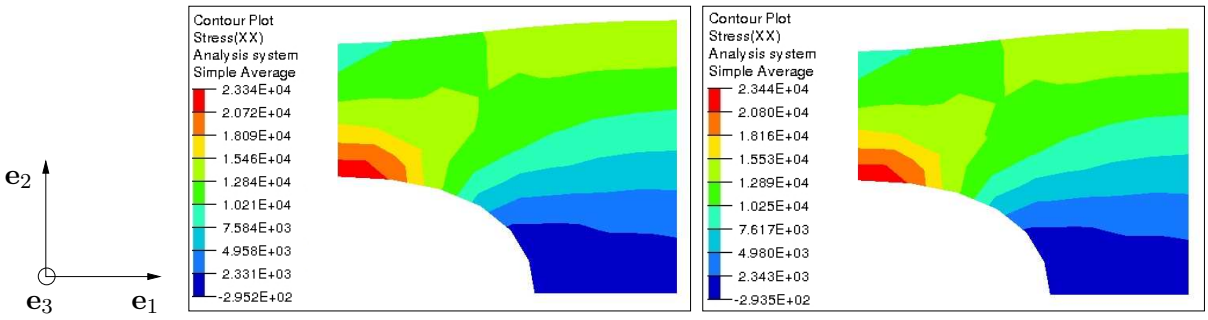

Figure 5.50: Normal force for a tension test on a plate with a hole of a three-layers sandwich plate containing isotropic elastic layers: result of the FE^2 method on the left and plate theory on the right

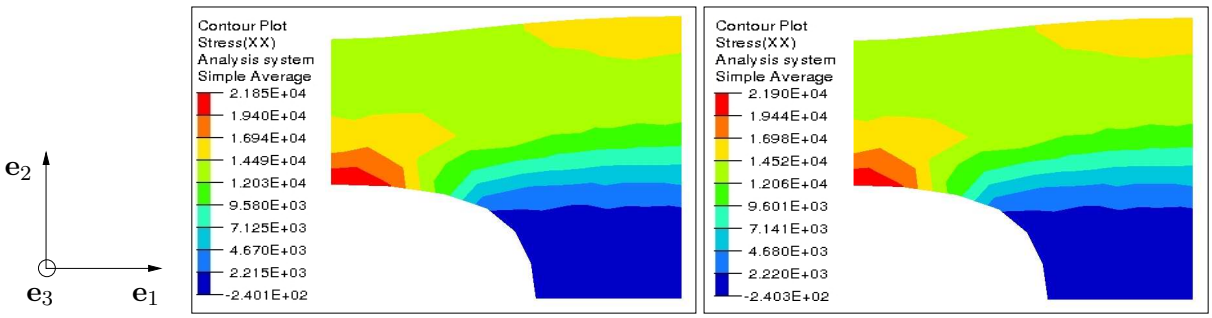

Figure 5.51: Normal force for a tension test on a plate with a hole of a three-layers sandwich plate containing isotropic and transverse isotropic (fiber orientation 0°) elastic layers: result of the FE^2 method on the left and plate theory on the right

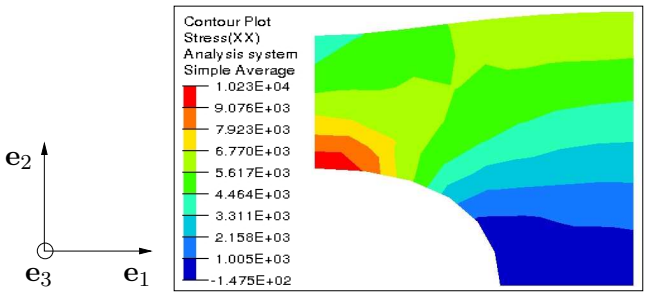

Figure 5.52: Normal force for a tension test on a plate with a hole of a three-layers sandwich plate containing isotropic elastic and elasto-plastic layers

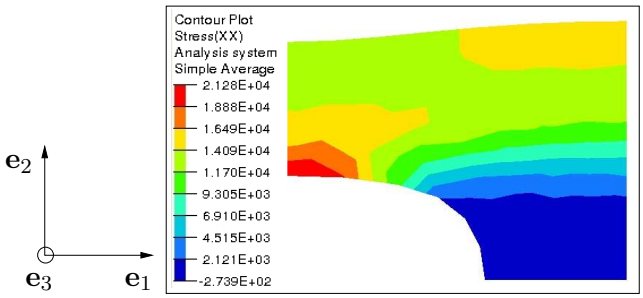

Figure 5.53: Normal force for a tension test on a plate with a hole of a three-layers sandwich plate containing transverse isotropic elastic (fiber orientation 0°) and elasto-plastic layers

5.5 Pagano Problem

In the following part, a Pagano problem is computed, as illustrated in Fig. 5.54. The principle consists on the application of a sinusoidal load on the bottom of a plate of a length of $L = 20$ mm and of a width and thickness of 1 mm. The two extremities are blocked. In order to reduce the computation time, half of the problem is computed in the framework of the FE^2 method. 20 elements are used for the plate. The RVEs are meshed with 4^3 quadratic brick elements for the single layers and for the three-layers structures. For the hybrid laminates, the RVEs are meshed with 6^3 and 10^3 quadratic brick elements for the six-layers structure and the ten-layers structure, respectively. The results are compared with the solution of the three-dimensional problem computed with ABAQUS®. The three-dimensional FE composites computed with ABAQUS® are meshed with 640 quadratic brick elements for the one-layer structure and the composite sandwich, and with 2152 and 10^4 elements for the six-layers hybrid laminate and the ten-layers hybrid laminate. The vertical displacement is represented as a function of the coordinate in $\mathbf{e}_1$-direction in Fig. 5.55 for the different elastic material behaviour and the composite containing elastic material behaviour.

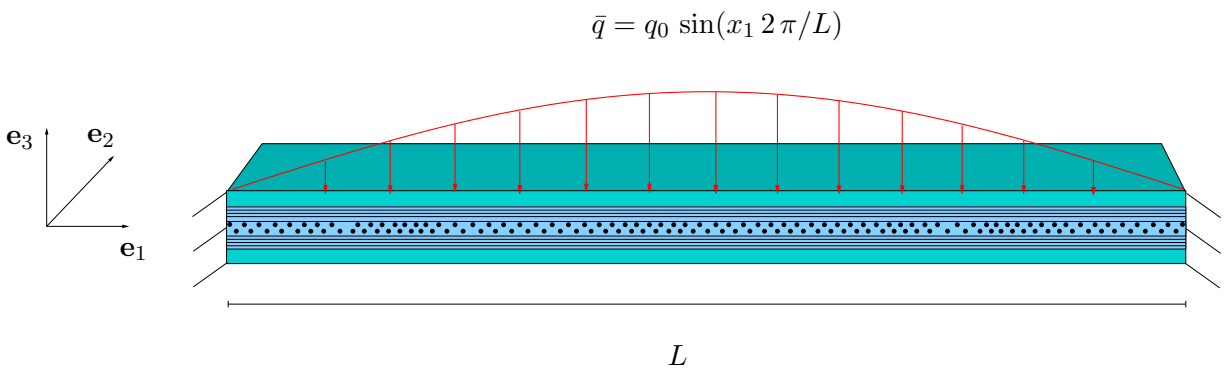

Figure 5.54: Schematic representation of the Pagano problem

As represented in Fig. 5.55, the vertical displacement is represented for different composite plates submitted to a sinusoidal loading. In a first instance, we can consider the case of composite plates containing one linear layer, which presents an isotropic or an anisotropic elastic material behaviour, drawn in red and in dark blue. The elastic isotropic material is Aluminium and has a Young's modulus of $E = 70500$ MPa and a Poisson's ratio of 0.3. The anisotropic layer is used to simulate the behaviour of a Carbon Fiber Reinforced Polymer layer, which shows a transverse isotropic material behaviour with the material constants expressed in Table 5.1. The fiber orientation is 0°, that means that the fibers are aligned with the plate length L. In this case, the error obtained between the FE^2 method and the three-dimensional solution is of 1.6% to 2.7% for the different material behaviours, which is considered as accurate. Indeed, the mesoscopic discretisation is performed with 4^3 elements, and a finer mesh would produce a better precision, but would also increase the computing time.

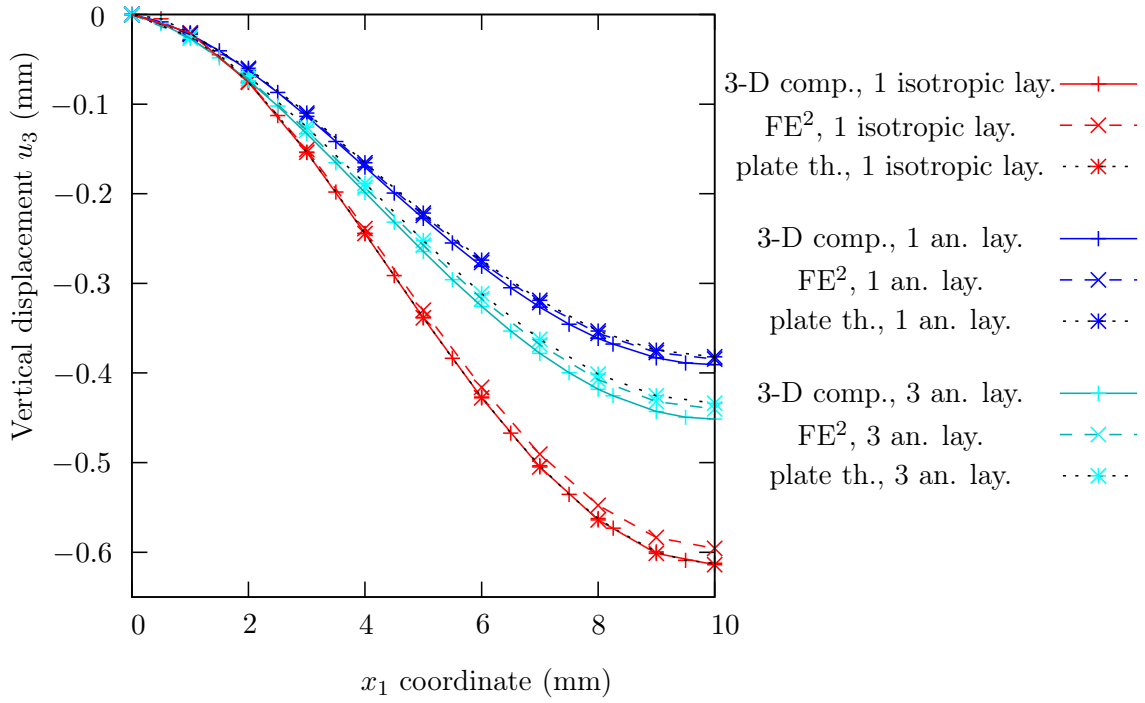

Figure 5.55: Vertical displacement for the composite plates containing linear materials: computation for one isotropic layer (1 isotropic lay.) in red, computation for one anisotropic layer (1 an. lay.) in dark blue and computation for three anisotropic layers (3 an. lay.) in cyan

In a second instance, the computation of a sandwich plate composed of transverse isotropic layers, with the fiber orientation $(0° - 90°)_S$ is performed and the results are represented in cyan. In this case, an error of 2.5% between the vertical displacement given by the FE^2 method and the three-dimensional solution is obtained. The black dot curve with colored points gives the solution given by the plate theories for the different structures. It is to mention that the plate theory with thickness change gives a comparable result to the one given by the FE^2 method in this case.

In the following numerical experiments, some composite plates containing linear and non-linear materials are computed under a sinusoidal loading. The vertical displacements obtained by the FE^2 method and the three-dimensional computation with ABAQUS® are drawn in Fig. 5.56. Firstly, a sandwich plate containing elasto-plastic top panels with the elasto-plastic behaviour described in Subsect. 5.2 and either an isotropic or an anisotropic elastic core is considered. The elastic isotropic and anisotropic materials have the same properties as the single materials. The displacements obtained for the two sandwich plates are drawn in red and in blue in the Fig. 5.56. With regard to the composite structure containing an elastic isotropic core and non-linear top panels, the error between the FE^2 method and the three-dimensional computation is around 2.5%. It can be observed that a larger error is obtained for the structure containing a transverse isotropic elastic core.

Secondly, some hybrid laminates are submitted to the sinusoidal loading. In a first instance, a hybrid laminate with six layers is considered. It contains Aluminium top panels, a transverse isotropic core, and between the transverse isotropic and the elasto-plastic top panels some elastic isotropic layers. The Aluminium layers present an elasto-plastic material behaviour described in Subsect. 5.2. The transverse isotropic layers has the properties expressed in Table 5.1 and the fiber orientation of 0°. The isotropic elastic material presents a Young's modulus of 55000 MPa and a Poisson's ratio of 0.4. The vertical displacement is represented in cyan in Fig. 5.56, and it can be observed that an error of less than 2% is reached. A hybrid laminate containing ten layers and with an elasto-plastic metal layer in the middle of the composite is also considered and drawn in green. The ten-layers hybrid laminate presents the layers organisation $(\mathrm{Al/CFRP(0°/90°/0°)/Al})_s$[5]. The Aluminium has the same elasto-plastic behaviour as the single elasto-plastic layer and the CFRP layers show a transverse isotropic elastic behaviour with the material constants expressed in Table 5.1. It is to mention that the relative error is reduced for a hybrid laminate and reached 2.6% and it can be concluded that the FE^2 method presents accurate results, for linear and non-linear material behaviours, in the case of the Pagano problem.

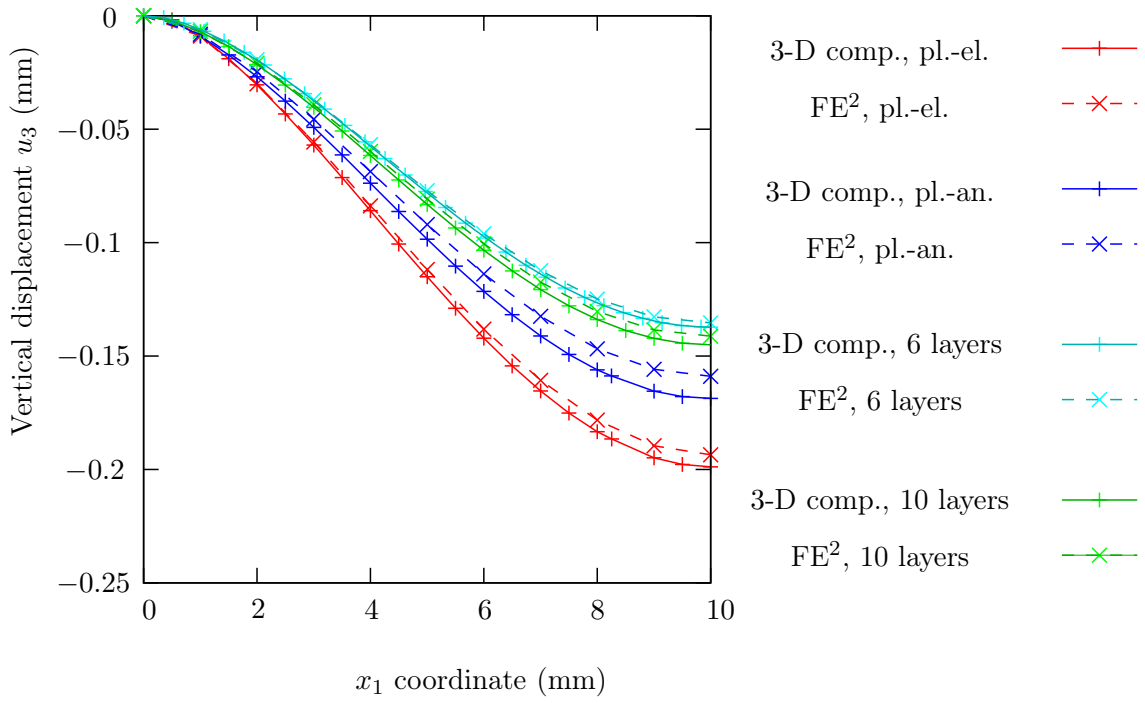

Figure 5.56: Vertical displacement for the composite plates containing linear and non-linear materials: computation for the sandwich plate containing elasto-plastic and isotropic elastic layers (pl.-el.) in red, computation for the sandwich plate containing elasto-plastic and anisotropic elastic layers (pl.-an.) in dark blue, computation for the hybrid laminate containing six layers (6 layers) in cyan and computation for the hybrid laminate containing ten layers (10 layers) in green

[5]The $(\diamond)_s$ is set for a symmetric layer stacking order

Chapter 6

Conclusions

In the present work, an innovative solution for the modelling of the mechanical behaviour of composite plates is proposed. The chosen method is a numerical multi-scale modelling for plates. Its principle is that a first FE computation of the macroscale, containing the plate kinematics, is performed. But instead of using one of the linear constitutive laws proposed by most of the plate theories, the deformations are transferred to the RVE on the mesoscale. Because the scale separation is only true in the two directions parallel to the midplane, i. e. there is no scale separation in the thickness direction between the macroscale and the mesoscale, the homogenisation is only applied in the two directions parallel to the midplane. In the thickness direction, a full resolution takes place. Therefore, the displacements are only projected in the surfaces of the RVE normal to the midplane. In the mesoscale, a three-dimensional FE computation of the boundary value problem is solved. The macroscopic force and moment resultants are obtained from the mesoscopic stresses by using a modified Hill-Mandel condition.

In this work, special attention is given to the resolution of the Poisson locking phenomenon, which occurs for a plate theory following the Mindlin concept. The Poisson locking appears if the plate theory is not considering any thickness change. Actually, the Poisson locking is solved by using an innovative projection strategy. In the macroscale, a plate theory with five degrees of freedom is taken into account, i. e. no thickness change is considered in the macroscale. However, the thickness change is incorporated within the projection strategy: during the computation, the displacements are projected to the RVE. In the RVE, the average value of the thickness change is computed and transferred back to the macroscale, where it is projected to the RVE in the next iteration. With this method, the free surfaces (the surfaces normal to the thickness direction, where the scale separation does not occur) enable the thickness change and a solution of the Poisson locking is then defined. It is to mention that the plate theory following the Mindlin concept encounters the problem of Poisson locking; but this plate theory under the framework of the FE^2 method and used with the innovative projection strategy, proposes a solution to the Poisson locking.

Maybe the critical drawback of the method results from the high computational costs. Two major solutions can be applied to reduce them: the first one is the parallelisation. Due to the use of the commercial software ABAQUS® for the mesoscale, a parallelisation is not possible, due to the available licence. The second solution is to define the analytical tangent, which enables an important decrease of the computational costs. Following this way, the present work considers the Multi-Level Newton Algorithm (MLNA), a method

which enables the definition of the analytical tangent for a non-linear material behaviour. For viscoelastic, viscoplastic or elasto-plastic material behaviours, the analytical tangent can be defined by splitting the problem in two levels: on the global level, the equilibrium equations are solved, and the local level contains the evolution equations. In contrast, the FE^2 method does not focus on the resolution of a mechanical problem with primary and internal variables, but on the resolution of a problem split in two scales. Therefore, the MLNA can be successfully applied: the global level contains the macroscale, that means the kinematics of the plate and its equilibrium equations. The local level consists of the mesocale, i.e. the three-dimensional boundary value problem. Consequently, this innovative method enables the definition of an accurate analytical tangent.

The present work proposes the modelling of the composite plates, considering linear, but also non-linear material behaviour, like for instance elasto-plasticity. Although some plate theories enable the treatment of non-linear material behaviour, cf. [161], most of them are limited to linear material behaviour. Moreover, the plate theories considering elasto-plastic material behaviour suffer limitations, too. One of them is related to geometrical linearity, due to the additive split of the deformations. As can be read in the paper of Roehl et al. from 1996 [161], the "additive form does not satisfy patch incremental test". Therefore, for a non-linear material behaviour for plates, there is the necessity to consider a multiplicative split, as done for a non-linear material behaviour for finite deformations. Concerning linear material behaviour, the computing time for the FE^2 method is much larger than for the FE plates. However, the FE^2 method offers more possibilities than a plate theory, due to the possibility to consider any material behaviour easily, which does not need to be changed in order to fit into the plate kinematics, as it is the case for plates. Nevertheless, the numerical multi-scale modelling could enable the consideration of the fluctuations, resulting in a correct treatment of the different layers, as can be seen in figure 6.1.

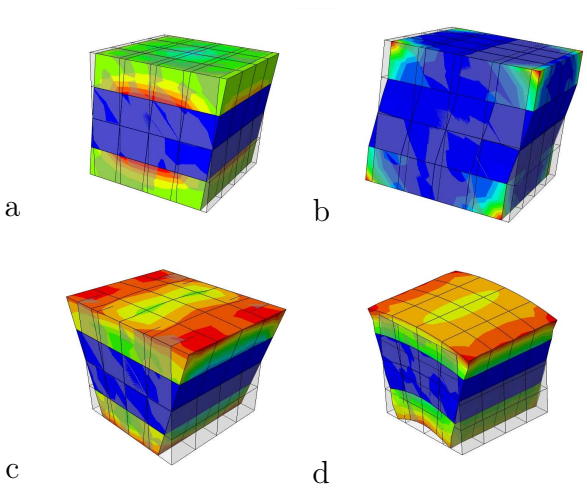

Figure 6.1: Schematic representation of the RVE submitted to a transverse shear deformation without fluctuations (a), with fluctuation (b); schematic representation of the RVE submitted to a bending without fluctuations (c), with fluctuation (d)

In figure 6.1, a RVE is submitted to a shear deformation and to a bending test, without fluctuations on the left and with fluctuations on the right. It can be observed that the fluctuations enable a better treatment of the composite layup, due to their capability to take the rigidity of the different layers into account. To the knowledge of the author, there is no possibility to incorporate the fluctuations in the plate theory, although there are some extensions which enable similar behaviour, as for instance the zig-zag theories or the layerwise theories. But again, both are limited to linear material behaviour. As a consequence, an interesting future work could be related to the incorporation of the fluctuations in the present numerical multi-scale method, which may also enable a better treatment of the eigenstresses.

Then, it may be of interest to develop a FE^2 method for plates, where the plate kinematics present higher order displacements for the two in-plane directions. For example, a plate theory with a cubic approximation for the two in-plane displacements may be considered, leading to a cubic distribution of the deformation for the RVE. Alternatively, a consideration of the same plate theory with five degrees of freedom, but with an extended projection, enabling for instance a displacement of cubic order for the projection, could be drawn.

The present work is limited to plates; similarly as for plates, an introduction of the shell kinematics in the macroscale could be proposed. Then, another improvement consists in the possibility to consider more integration points through the thickness for the macroscale, although this could lead to an important increase of the computational costs.

In contrast to the plate theories, the numerical homogenisation is not restricted to hybrid laminates, but enables the consideration of any composite plates, like for instance a sandwich plate containing a foam core or even more complicated structures. Another improvement of the current method could be to use the constitutive law proposed by the plate theory, if the material is elastic, but to apply the FE^2 method only for the parts of the composite which present non-linear material behaviours or complex structures.

The numerical multi-scale method for plates could be extended to the treatment of contact, enabling the modelling of a forming process. One of the advantages of the numerical homogenisation -towards the plate theories- is the possibility to model the interface between the different layers. This would be possible by the simple introduction of the interpose in the three-dimensional RVE. It is to mention that dynamic analysis could also be possible, or the treatment of damage. Because the delamination are important issues for composite materials, the modelling of the damage for fiber reinforced materials, as proposed by Schröder et al. [167] and by Nguyen [137] for a FE^2 method, could be also imagined for composite plates. Recently, the modelling of cohesive laws in the framework of the numerical homogenisation has been studied, cf. [183]; and a transposition to the numerical multi-scale modelling of plates could also be an interesting issue.

Chapter 7

Appendix

7.1 Voigt Notation

The Voigt notation is defined as a representation of the stress tensor as vector, that means as tensor first order, and not as tensor of second order, like it it the case for the classical continuum mechanics. In classical continuum mechanics, the elasticity relation can be expressed as

$$^2\mathbf{T} = {}^4\mathbb{C} : {}^2\mathbf{E}, \tag{7.1}$$

with the stress and strains defined as second order tensors. Because the stress tensor can be assumed to be symmetric, the stress can be expressed as a tensor

$$^1\mathbf{T} = [T_{11}, T_{22}, T_{33}, T_{23} = T_4, T_{13} = T_5, T_{12} = T_6]^T, \tag{7.2}$$

as well as the strains

$$^1\mathbf{E} = [E_{11}, E_{22}, E_{33}, 2\,E_{23} = E_4, 2\,E_{13} = E_5, 2\,E_{12} = E_6]^T. \tag{7.3}$$

Considering the Voigt notation, the relation between the stress and the strains becomes

$$^1\mathbf{T} = {}^2\mathbb{C} \cdot {}^1\mathbf{E}, \tag{7.4}$$

with $^2\mathbb{C}$ the elasticity tensor, which becomes a tensor of second order containing $6 \cdot 6 = 36$ entries. However, some simplifications are needed, because the elasticity tensor is normally a tensor of fourth order containing $3^4 = 81$ entries. One of the simplification is related to the major symmetries, which means that there is some redundancies in the elasticity tensor, cf. [84]

$$^4\mathbb{C}_{ijkl} = {}^4\mathbb{C}_{klij}. \tag{7.5}$$

The minor symmetries are defined as

$$^4\mathbb{C}_{ijkl} = {}^4\mathbb{C}_{jikl} = {}^4\mathbb{C}_{ijlk}. \tag{7.6}$$

Consequently, the elasticity tensor can be reduced to a tensor of second order.

7.2 Elasto-Plasticity for Finite Strains

In this part, an elasto-plastic model for finite strains is explicitly given for the intermediate or stress free configuration, cf. [73]. Firstly, the elastic function, which defines the behaviour of the material in the elastic domain is written

$$\hat{\mathbf{S}} = \mathbf{g}_1(\hat{\mathbf{\Gamma}}_\mathrm{e}), \tag{7.7}$$

where $\mathbf{g}_1$ is an isotropic tensor function.

The yield function has to be defined, following the definition

$$F = F(\hat{\mathbf{S}}, \hat{\mathbf{X}}, k) = f(\hat{\mathbf{S}} - \hat{\mathbf{X}}, k). \tag{7.8}$$

It gives the the border between the elastic and elasto-plastic domain.

The associated flow rule defines how the material behaves in the plastic part and is written as

$$\hat{\mathbf{D}}_\mathrm{p} = \overset{\triangle}{\hat{\mathbf{\Gamma}}}_\mathrm{p} = \begin{cases} \lambda \dfrac{\partial}{\partial \hat{\mathbf{S}}} F(\hat{\mathbf{S}}, \hat{\mathbf{X}}, k), & \text{for } F = 0 \text{ and } B > 0, \\ 0, & \text{otherwise,} \end{cases} \tag{7.9}$$

Then, the evolution equation has to be given

$$\overset{\triangledown}{\hat{\mathbf{X}}} = c\,\hat{\mathbf{D}}_\mathrm{p} - b\,\dot{s}_\mathrm{p}(t)\,\hat{\mathbf{X}} \tag{7.10}$$

In the case of an isotropic hardening we get

$$k = k(s_\mathrm{p}), \tag{7.11}$$

with the plastic arc length defined as

$$\dot{s}_\mathrm{p}(t) = ||\hat{\mathbf{D}}_\mathrm{p}||. \tag{7.12}$$

Then, the consistency condition has to be given.

$$\frac{\mathrm{d}}{\mathrm{d}t} F(\hat{\mathbf{S}}(t), \hat{\mathbf{X}}(t), k(t)) = 0 \tag{7.13}$$

Its resolution leads to the value of the parameter λ.

7.3 Pegasus Method

The Pegasus method is used to find the root of an equation, following the method explained in [44, 50].

$$f(\zeta) = 0, \qquad \zeta \in [a, b]. \tag{7.14}$$

1. The intersection point of the secant and the x-axis is called ζ_3 and it can be compute as

$$\zeta_3 = \zeta_2 - f(\zeta_2)\,\frac{\zeta_2 - \zeta_1}{f(\zeta_2) - f(\zeta_1)}. \tag{7.15}$$

2. The function of the intersection point $f(\zeta_3)$ is then computed. If the function $f(\zeta_3)$ is equal to zero, the computation ended and ζ_3 is the root of the function f.

3. If $f(\zeta_3)\,f(\zeta_2) > 0$, it means that f reaches a zero between ζ_2 and ζ_3 and the new values for the next iteration are

$$\zeta_1 := \zeta_2; \qquad f(\zeta_1) := f(\zeta_2); \zeta_2 := \zeta_3; \qquad f(\zeta_2) := f(\zeta_3).$$

   On the opposite, if $f(\zeta_3)\,f(\zeta_2) < 0$, it means that f reaches a zero between ζ_1 and ζ_3 and the new values for the next iteration are

$$\zeta_1 := \zeta_1; \qquad f(\zeta_1) := \frac{f(\zeta_1)\,f(\zeta_2)}{f(\zeta_2) + f(\zeta_3)}; \zeta_2 := \zeta_3; \qquad f(\zeta_2) := f(\zeta_3).$$

4. If $|\zeta_2 - \zeta_1| < \epsilon$ and ϵ defining the tolerance, the root is found. For $f|(\zeta_2)| \leq 0$, the root equals ζ_2, otherwise, the root equals ζ_1. For $|\zeta_2 - \zeta_1| > \epsilon$, we return to the step 1.

The advantage of this method is that it does not need the derivative of the function, that is of great interest for plasticity.

7.4 Constitutive Law for the Plate Theory

For a composite plate containing several layers, the constitutive law, as proposed by the First order Shear Deformation Theory, cf. [5, 154], can be developed. The composite contains n layers, and their thickness coordinates are defined as shown in figure 7.1. As mentioned before, the plate theory with thickness change is involving a three-dimensional constitutive law. In contrast, for the plate theory from Love, Kirchhoff, Reissner or Mindlin, the constitutive law are two-dimensional ones and can be written for instance for a one-layer elastic isotropic material as

$$\begin{bmatrix} N_{11} \\ N_{22} \\ N_{12} \\ M_{11} \\ M_{22} \\ M_{12} \end{bmatrix} = \begin{bmatrix} \frac{E}{1-\nu^2}\,h & \frac{E\,\nu}{1-\nu^2}\,h & 0 & 0 & 0 & 0 \\ \frac{E}{1-\nu^2}\,h & \frac{E\,\nu}{1-\nu^2}\,h & 0 & 0 & 0 & 0 \\ 0 & 0 & G\,h & 0 & 0 & 0 \\ 0 & 0 & 0 & \frac{E}{1-\nu^2}\,\frac{h^3}{12} & \frac{E\,\nu}{1-\nu^2}\,\frac{h^3}{12} & 0 \\ 0 & 0 & 0 & \frac{E\,\nu}{1-\nu^2}\,\frac{h^3}{12} & \frac{E}{1-\nu^2}\,\frac{h^3}{12} & 0 \\ 0 & 0 & 0 & 0 & 0 & G\,\frac{h^3}{12} \end{bmatrix} \cdot \begin{bmatrix} \varepsilon_{11} \\ \varepsilon_{22} \\ \varepsilon_{12} \\ \kappa_{11} \\ \kappa_{22} \\ \kappa_{12} \end{bmatrix}, \tag{7.16}$$

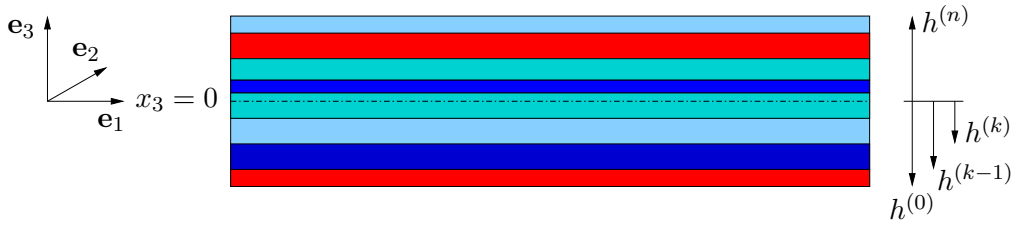

Figure 7.1: Definition of a composite plate with n layers, adapted from Altenbach, Altenbach and Rikards, Einführung in die Mechanik der Laminat- und Sandwichtragwerke: Modellierung und Berechnung von Balken und Platten aus Verbundwerkstoffen, Deutscher Verlag für Grundstoffindustrie, 1996 [5]

for the force and moment resultants. For the shear forces, the constitutive law is defined as

$$\begin{bmatrix} Q_1 \\ Q_2 \end{bmatrix} = \begin{bmatrix} K\,G\,h & 0 \\ 0 & K\,G\,h \end{bmatrix}, \tag{7.17}$$

for the extension of the plate following Mindlin concept for laminates. K is the correction factor; it is equal to 5/6 for the Reissner assumption, or to $\pi^2/12$ following Mindlin. The correction factor is obtained for the Reissner assumption if a parabolic function is assumed for the shear forces, for an isotropic single layer, cf. [5]. For anisotropic plates, the correction factor may be different in every direction, as explained by [142]. Another solution consists in the comparison of the strain energy of the average shear stress with the strain energy obtained by the equilibrium, cf. [67], leading to a dependency on the Poisson's ratio.

For a plate theory with thickness change, the constitutive laws for the force and moment are three-dimensional and can be written as

$$\begin{bmatrix} \sum_{k=1}^{n} \frac{E^{(k)}}{1-(\nu^{(k)})^2} & \sum_{k=1}^{n} \frac{E^{(k)}\,\nu^{(h)}}{1-(\nu^{(k)})^2} & \sum_{k=1}^{n} \frac{E^{(k)}\,\nu^{(h)}}{1-(\nu^{(k)})^2} & 0 & 0 & 0 \\ \sum_{k=1}^{n} \frac{E^{(k)}\,\nu^{(h)}}{1-(\nu^{(k)})^2} & \sum_{k=1}^{n} \frac{E^{(k)}}{1-(\nu^{(k)})^2} & \sum_{k=1}^{n} \frac{E^{(k)}\,\nu^{(h)}}{1-(\nu^{(k)})^2} & 0 & 0 & 0 \\ \sum_{k=1}^{n} \frac{E^{(k)}\,\nu^{(h)}}{1-(\nu^{(k)})^2} & \sum_{k=1}^{n} \frac{E^{(k)}\,\nu^{(h)}}{1-(\nu^{(k)})^2} & \sum_{k=1}^{n} \frac{E^{(k)}}{1-(\nu^{(k)})^2} & 0 & 0 & 0 \\ 0 & 0 & 0 & \sum_{k=1}^{n} G^{(h)} & 0 & 0 \\ 0 & 0 & 0 & 0 & \sum_{k=1}^{n} G^{(h)} & 0 \\ 0 & 0 & 0 & 0 & 0 & \sum_{k=1}^{n} G^{(h)} \end{bmatrix} \mathcal{H}, \tag{7.18}$$

where $\mathcal{H}$ is defined as

$$\mathcal{H} = h^{(h)} - h^{(k-1)} \tag{7.19}$$

for the force resultants and as

$$\mathcal{H} = \frac{(h^{(h)})^3 - (h^{(k-1)})^3}{3} \tag{7.20}$$

for the moment resultants. The hyperstresses are defined as

$$\mathbb{C}^4 = \begin{bmatrix} \sum_{k=1}^{n} G & 0 \\ 0 & \sum_{k=1}^{n} G \end{bmatrix} \frac{(h^{(h)})^5 - (h^{(k-1)})^5}{5}. \tag{7.21}$$

7.5 Symmetric Stiffness for the Plate Theory with Thickness Change

The symmetric stiffness is written in equation (7.22) for the considered plate theory with thickness change. In this case the plates (laminates or sandwich or hybrid laminates) are symmetric. The letter α and β are used for the index $1, 2$.

$$
\mathbf{K} = \begin{bmatrix}
D_{0_{1\alpha}} \dfrac{\partial N_{1\alpha}}{\partial \varepsilon_{1\beta}} D_{0_{1\beta}} & D_{0_{1\alpha}} \dfrac{\partial N_{1\alpha}}{\partial \varepsilon_{2\beta}} D_{0_{2\beta}} & 0 & 0 & 0 & D_{0_{11}} \dfrac{\partial N_{11}}{\partial \varepsilon_{33}} \psi_{1_3} & 0 \\
D_{0_{2\alpha}} \dfrac{\partial N_{2\alpha}}{\partial \varepsilon_{1\beta}} D_{0_{1\beta}} & D_{0_{2\alpha}} \dfrac{\partial N_{2\alpha}}{\partial \varepsilon_{2\beta}} D_{0_{2\beta}} & 0 & 0 & 0 & D_{0_{22}} \dfrac{\partial N_{22}}{\partial \varepsilon_{33}} \psi_{1_3} & 0 \\
0 & 0 & D_{0_{3\alpha}} \dfrac{\partial N_{3\alpha}}{\partial \varepsilon_{3\beta}} D_{0_{3\beta}} & D_{0_{3\alpha}} \dfrac{\partial N_{3\alpha}}{\partial \varepsilon_{31}} \psi_{1_1} & D_{0_{3\alpha}} \dfrac{\partial N_{3\alpha}}{\partial \varepsilon_{32}} \psi_{1_2} & 0 & 0 \\
0 & 0 & \psi_{1_1} \dfrac{\partial N_{31}}{\partial \varepsilon_{3\alpha}} D_{0_{3\alpha}} & D_{1_{1\alpha}} \dfrac{\partial M_{1\alpha}}{\partial \kappa_{1\beta}} D_{1_{1\beta}} + \psi_{1_1} \dfrac{\partial N_{31}}{\partial \varepsilon_{31}} \psi_{1_1} & D_{1_{1\alpha}} \dfrac{\partial M_{1\alpha}}{\partial \kappa_{2\beta}} D_{1_{2\beta}} + \psi_{1_1} \dfrac{\partial N_{31}}{\partial \varepsilon_{32}} \psi_{1_2} & 0 & D_{1_{11}} \dfrac{\partial M_{11}}{\partial \kappa_{33}} 2\,\psi_2 \\
0 & 0 & \psi_{1_2} \dfrac{\partial N_{32}}{\partial \varepsilon_{3\alpha}} D_{0_{3\alpha}} & D_{1_{2\alpha}} \dfrac{\partial M_{2\alpha}}{\partial \kappa_{1\beta}} D_{1_{1\beta}} + \psi_{1_2} \dfrac{\partial N_{32}}{\partial \varepsilon_{31}} \psi_{1_1} & D_{1_{2\alpha}} \dfrac{\partial M_{2\alpha}}{\partial \kappa_{2\beta}} D_{1_{2\beta}} + \psi_{1_2} \dfrac{\partial N_{32}}{\partial \varepsilon_{32}} \psi_{1_2} & 0 & D_{1_{22}} \dfrac{\partial M_{22}}{\partial \kappa_{33}} 2\,\psi_2 \\
\psi_{1_3} \dfrac{\partial N_{33}}{\partial \varepsilon_{11}} D_{0_{11}} & \psi_{1_3} \dfrac{\partial N_{33}}{\partial \varepsilon_{22}} D_{0_{22}} & 0 & 0 & 0 & D_{1_{3\alpha}} \dfrac{\partial M_{1\alpha}}{\partial \kappa_{3\beta}} D_{1_{3\beta}} + \psi_{1_3} \dfrac{\partial N_{33}}{\partial \varepsilon_{33}} \psi_{1_3} & 0 \\
0 & 0 & 0 & 2\,\psi_2 \dfrac{\partial M_{33}}{\partial \kappa_{11}} D_{1_{11}} & 2\,\psi_2 \dfrac{\partial M_{33}}{\partial \kappa_{22}} D_{1_{22}} & 0 & D_{2_\alpha} \dfrac{\partial H_\alpha}{\partial \theta_\beta} D_{2_\beta} + 2\,\psi_2 \dfrac{\partial M_{33}}{\partial \kappa_{33}} 2\,\psi_2
\end{bmatrix} \tag{7.22}
$$

Bibliography

[1] B. Abbès and Y. Q. Guo. Analytic homogenization for torsion of orthotropic sandwich plates: Application to corrugated cardboard. *Composite Structures*, 92:699–705, 2010.

[2] S. Ahmad, B. M. Irons, and O. C. Zienkiewicz. Curved thick shell and membrane elements with particular reference to axi-symmetric problems. In *Proceedings of the 2nd. Conference on Matrix Methods in Structural Mechanics*. L. Berke et al. eds., 1968.

[3] H. Altenbach. Eine direkt formulierte lineare Theorie für viskoelastische Platten und Schalen. *Ingenieur-Archiv*, 58:215–228, 1988.

[4] H. Altenbach. *Kontinuumsmechanik: Einführung in die materialunabhängigen und materialabhängigen Gleichungen*. Springer Verlag, 2. Auflage, Berlin Heidelberg, 2012.

[5] H. Altenbach, H. Altenbach, and W. Kissing. *Mechanics of Composite Structural Elements*. Springer Verlag, Berlin Heidelberg New York, 2004.

[6] H. Altenbach, J. Altenbach, and R. Rikards. *Einführung in die Mechanik der Laminat- und Sandwichtragwerke: Modellierung und Berechnung von Balken und Platten aus Verbundwerkstoffen*. Deutscher Verlag für Grundstoffindustrie, Stuttgart, 1996.

[7] H. Altenbach, V. Kushnevsky, and K. Naumenko. On the use of solid- and shell-type finite elements in creep-damage predictions of thinwalled structures. *Arch. Appl. Mech.*, 71:164–181, 2001.

[8] H. Altenbach and J. Meenen. Single layer modelling and effective stiffness estimations of laminated plates. In *Modern trends in composite laminates mechanics*. Springer Verlag, Wien New York, 2003.

[9] J. Altenbach, H. Altenbach, and V. A. Eremeyev. On generalized Cosserat-type theories of plates and shells: a short review and bibliography. *Arch. Appl. Mech.*, 80:73–92, 2010.

[10] J. Altenbach and V. A. Eremeyev. On the linear theory of micropolar plates. *Z. Angew. Math. Mech.*, 89 (4):242–256, 2009.

[11] D. Balzani, P. Neff, J. Schröder, and G. A. Holzapfel. A polyconvex framework for soft biological tissues. Adjustment to experimental data. *Int. J. Solids Structures*, 43:6052–6070, 2006.

[12] A. Bertram. *Elasticity and Plasticity of Large Deformations*. Springer Verlag, 3rd ed., Berlin Heidelberg, 2012.

[13] M. Bischoff. *Theorie und Numerik einer dreidimensionalen Schalenformulierung*. Ph.D.-thesis, Bericht Nr. 30 (1999) Institut für Baustatik, Univerität Stuttgart, 1999.

[14] M. Bischoff, W. A. Wall, K.-U. Bletzinger, and E. Ramm. Models and Finite Elements for Thin-walled Structures. In *Encyclopedia of Computational Mechanics*, volume 2 of *Solids and Structures*. John Wiley & Sons, 2004.

[15] K. U. Bletzinger, M. Bischoff, and E. Ramm. A unified approach for shear-locking-free triangular and rectangular shell finite elements. *Computers and Structures*, 75:321–334, 2000.

[16] J. P. Boehler. *Representations for isotropic and anisotropic non-polynomial tensor functions*. Springer Verlag, Wien, 1987.

[17] D. Braess. *Finite Elemente*. Springer-Verlag, Berlin, 1997.

[18] A. Brandmair, W. Müller, M. Savenkova, and S. Sheshenin. A multi-scale homogenization technique applied to the elastic properties of solders. *Technische Mechanik*, 31 (2):156–170, 2011.

[19] M. Brun, O. Lopez-Pamies, and P. Ponte Castaneda. Homogenization estimates for fiber-reinforced elastomers with periodic microstructures. *Int. J. Solids Structures*, 44:5953–5979, 2007.

[20] N. Buechter and E. Ramm. Shell Theory versus degeneration- a comparison in large rotation finite element analysis. *Int. J. Numer. Meth. Eng.*, 34:39–59, 1992.

[21] N. Buechter, E. Ramm, and D. Roehl. Three-dimensional extension of non-linear shell formulation based on the enhanced assumed strain concept. *Int. J. Numer. Meth. Eng.*, 34:2551–2568, 1994.

[22] I. A. Burchitz and T. Meinders. Adaptive through-thickness integration for accurate springback prediction. *Int. J. Numer. Meth. Eng.*, 75:533–554, 2008.

[23] B. Carleer. *Finite element analysis of deep drawing*. Ph.D.-thesis, University of Twente, The Netherlands, 1997.

[24] E. Carrera. Theories and Finite Elements for Multilayered Anisotropic, Composite Plates and Shells. *Arch. Comput. Meth. Engng.*, 9(2):87–140, 2002.

[25] E. Carrera and F. Miglioretti. Selection of appropriate multilayered plate theories by using a genetic like algorithm. *Composite Structures*, 94:1175–1186, 2012.

[26] P. Ponte Castaneda. Second-order homogenization estimates for nonlinear composites incorporating field fluctuations: I–theory. *J. Mech. Phys. Solids*, 50:737–757, 2002.

[27] P. Ponte Castaneda. Second-order homogenization estimates for nonlinear composites incorporating field fluctuations: II–applications. *J. Mech. Phys. Solids*, 50:759–782, 2002.

[28] A. Cecchi and K. Sab. Out of plane model for heterogeneous periodic materials: the case of masonry. *Eur. J. Mech., A/Solids*, 21 (5):715–746, 2002.

[29] A. Cecchi and K. Sab. A homogenized Love-Kirchhoff model for out-of-plane loaded random 2D lattices: Application to "quasi-periodic" brickwork panels. *Int. J. Solids Structures*, 46:2907–2919, 2009.

[30] J. L. Chaboche. A review of some plasticity and viscoplasticity constitutive theories. *Int. J. Plast.*, 24:1642–1693, 2008.

[31] H. D. Chalak, A. Chakrabarti, M. A. Iqbal, and A. H. Sheikh. An improved C^0 FE model for the analysis of laminated sandwich plate with soft core. *Finite Element in Analysis and Design*, 56:20–31, 2012.

[32] C. Chambon and S. Diebels. FE^2 modelling of hybrid sandwich composites. *Proc. Appl. Math. Mech.*, 11(1):505–506, 2011.

[33] P. G. Ciarlet and P. Destuynder. Justification of the 2-dimensional linear plate model. *J. Mecanique*, 18 (2):315–344, 1979.

[34] H. B. Coda and R. R. Paccola. An alternative positional FEM formulation for geometrically non-linear analysis of shells: curved triangular isoparametric elements. *Comp. Mech.*, 40:185–200, 2007.

[35] E. W. C. Coenen, V. G. Kouznetsova, and M. G. D. Geers. A multi-scale computational strategy for structured thin sheets. *Int J Mater Form*, Suppl. 1:61–64, 2008.

[36] E. W. C. Coenen, V. G. Kouznetsova, and M. G. D. Geers. Computational homogenization for heterogeneous thin sheets. *Int. J. Numer. Meth. Eng.*, 83(8-9):1180–1205, 2010.

[37] B. D. Coleman and W. Noll. Foundations of Linear Viscoelasticity. *Reviews of Modern Physics*, 33(2):239–249, 1961.

[38] B. D. Coleman and W. Noll. The thermodynamics of elastic materials with heat conduction and viscosity. *Arch. Rat. Mech. Anal.*, 13:167–178, 1963.

[39] E. Cosserat and F. Cosserat. *Théorie des Corps Déformables*. A. Hermann et Fils, Paris, 1909.

[40] M. A. Crisfield. *Non-linear Finite Element Analysis of Solids and Structures, Volume 1: Essentials*. John Wiley & Sons, Chichester, 2000.

[41] S. Diebels. *Kontinuumsmechanik*. Vorlesungskript, Höhere Mechanik I. Universität des Saarlandes, 2008.

[42] S. Diebels. *Technische Mechanik IV*. Vorlesungskript, Höhere Mechanik I. Universität des Saarlandes, 2010.

[43] S. Diebels and B. Svendsen. *Einführung in die Kontinuumsmechanik/Introduction to Continuum Mechanics*. lectures notes. Universität des Saarlandes/Technische Universität Dortmund, 2008.

[44] M. Dowell and P. Jaratt. The "Pegasus" method for computing the root of an equation. *BIT Numerical Mathematics*, 12:503–508, 1972.

[45] V. Ebbing, D. Balzani, J. Schröder, P. Neff, and F. Gruttmann. Construction of anisotropic polyconvex energies and applications to thin shells. *Computational Materials Science*, 46:639–641, 2009.

[46] V. Ebbing, J. Schröder, and P. Neff. Approximation of anisotropic elasticity tensors at the reference state with polyconvex energies. *Arch. Appl. Mech.*, 79:651–657, 2009.

[47] P. Ellsiepen. *Zeit- und ortsadaptive Verfahren angewandt auf Mehrphasenprobleme poröser Medien*. Dissertation, Institut für Mechanik (Bauwesen), Lehrstuhl II, Universität Stuttgart, 1999.

[48] P. Ellsiepen and S. Diebels. Error-controlled Runge-Kutta time integration in elastoplasticity and viscoplasticity. In S. Diebels, editor, *Zur Beschreibung komplexen Materialverhaltens: Beiträge anläßlich des 50. Geburtstags von Herrn Prof. Dr.-Ing. Wolfgang Ehlers*, pages 189–206. Institut für Mechanik (Bauwesen) Nr. 01-II-7, Universität Stuttgart, 2001.

[49] P. Ellsiepen and S. Hartmann. Remarks on the interpretation of current non-linear finite element analysis as differential-algebraic equations. *Int. J. Numer. Meth. Eng.*, 51:679–707, 2001.

[50] G. Engeln-Müllges and F. Reutter. *Numerik-Algorithmen: Entscheidungshilfe zur Auswahl und Nutzung*. VDI Verlag, 8. Auflage, Düsseldorf, 1996.

[51] J. L. Ericksen. Exact theory of stress and strain in rods and shells. *Arch. Rat. Mech. Anal.*, 1:295–322, 1958.

[52] A. C. Eringen. Linear theory of micropolar elasticity. *Math. Mech.*, 15(6):909–923, 1966.

[53] R. Fan, Z. Yuan, and J. Fish. Adaptive Two-Scale Nonlinear Homogenization. *International Journal Computational Methods in Engineering Science and Mechanics*, 11:27–36, 2010.

[54] A. J. M. Ferreira, C. M. C. Roque, E. Carrera, M. Cinefra, and O. Polit. Two higher order zig-zag theories for the accurate analysis of bending, vibration and buckling response of laminated plates by radial basis functions collocation and a unified formulation. *Journal of Composite Materials*, 45 (24):2523–2536, 2011.

[55] F. Feyel. A multilevel finite element method (FE^2) to describe the response of highly non-linear structures using generalized continua. *Comp. Meth. Appl. Mech. Eng.*, 192:3233–3244, 2003.

[56] F. Feyel and J. L. Chaboche. FE^2 multiscale approach for modelling the elastovis-coplastic behaviour of long fiber SiC/Ti composite materials. *Comp. Meth. Appl. Mech. Eng.*, 183:309–330, 2000.

[57] J. Fish and A. Wagiman. Multiscale finite element method for a locally nonperiodic heterogeneous medium. *Comp. Mech.*, 12:164–180, 1993.

[58] S. Forest. Mechanics of generalized continua: construction by homogenization. *J. Phys. IV*, 8:39–48, 1998.

[59] S. Forest. Homogenization methods and the mechanics of generalized continua - Part 2. *Theoretical and Applied Mechanics*, 28–29:113–143, 2002.

[60] S. Forest and K. Sab. Cosserat overall modeling of heterogeneous materials. *Mech. Res. Commun.*, 25(4):449–454, 1998.

[61] S. Forest and D. Trinh. Generalized continua and non-homogeneous boundary conditions in homogenisation methods. *Z. Angew. Math. Mech.*, 91:90–109, 2010.

[62] M. Frantz, C. Lauter, and T. Tröster. Schadensdetektion in hybriden Metalle-Faserverbundkunststoff-Konstruktionen. *Konstruktion, Springer, VDI Verlag*, 10:iw8–iw10, 2011.

[63] T. C. Gasser and G. A. Holzapfel. A rate-independant elastoplastic constitutive model for biological fiber-reinforced composites at finite strains: continuum basis, algorithmic formulation and finite element implementation. *Comp. Mech.*, 29:340–360, 2002.

[64] T. C. Gasser, R. W. Ogden, and G. A. Holzapfel. Hyperelastic modelling of arterial layers with distributed collagen fibre orientations. *J. R. Soc. Interface*, 3:15–35, 2006.

[65] M. G. D. Geers, E. W. C. Coenen, and V. G. Kouznetsova. Multi-scale computational homogenization of structured thin sheets. *Modelling Simul. Mater. Sci. Eng.*, 15:393–404, 2007.

[66] A. E. Green and P. M. Naghdi. A note on the cosserat surface. *Quarterly J. Mech. Appl. Math.*, 21(2):135–139, 1968.

[67] F. Gruttmann and W. Wagner. Shear correction factors in Timoshenko's beam theory for arbitrary shaped cross-sections, Mitteilung (6), Universität Karlsruhe, Institut für Baustatik, 2001.

[68] R. Grytz and G. Meschke. Consistent micro-macro transitions at large objective strains in curvilinear convective coordinates. *Int. J. Numer. Meth. Eng.*, 73:805–824, 2008.

[69] Y. Guan and L. Tang. A geometrically non-linear quadrilateral degenerated solid shell element. *Int. J. Numer. Meth. Eng.*, 38:927–942, 1995.

[70] S. Hartmann, G. Lührs, and P. Haupt. An efficient stress algorithm with applications in viscoplasticity and plasticity. *Int. J. Numer. Meth. Eng.*, 40:991–1013, 1997.

[71] S. Hartmann, K. J. Quint, and A. W. Hamkar. Displacement control in time-adaptive non-linear finite-element analysis. *Z. Angew. Math. Mech.*, 88(5):342–364, 2008.

[72] S. H. Hashemi, S. R. Atashipour, and M. Fadaee. An exact analytical approach for in-plane and out-of-plane free vibration analysis of thick laminated transversely isotropic plates. *Arch. Appl. Mech.*, 82:667–698, 2012.

[73] P. Haupt. *Continuum Mechanics and Theory of Materials.* Springer-Verlag, Berlin, 2000.

[74] P. Haupt and A. Lion. Experimental identification and mathematical modeling of viscoplastic material behavior. *Continuum Mech. Therm.*, 7:73–96, 1995.

[75] P. Haupt and A. Lion. A generalisation of the Mooney-Rivlin model to finite linear viscoelasticity. In D. Besdo, R. H. Schuster, and J. Ihlemann, editors, *Constitutive Models for Rubber*, pages 57–64. Swets & Zeitlinger, London, 2001.

[76] P. Haupt and Ch. Tsakmakis. On the application of dual variables in continuum mechanics. *Continuum Mech. Therm.*, 1:165–196, 1989.

[77] R. Hautpmann, S. Doll, M. Harnau, and K. Schweizerhof. 'Solid-shell' elements with linear and quadratic shape functions at large deformations with nearly incompressible materials. *Composite Structures*, 79:1671–1685, 2001.

[78] R. Hautpmann and K. Schweizerhof. A systematic development of 'solid-shell' element formulations for linear and non-linear analyses employing only displacement degrees of freedom. *Int. J. Numer. Meth. Eng.*, 42:49–69, 1998.

[79] C. Helfen and S. Diebels. A numerical homogenisation method for sandwich plates based on a plate theory with thickness change. *Z. Angew. Math. Mech.*, accepted for publication:1–13, 2012.

[80] C. Helfen and S. Diebels. Numerical multiscale modelling of laminated plates. *Technische Mechanik*, 32 (2–5):251–264, 2012.

[81] F. B Hildebrand, E. Reissner, and G. B. Thomas. Notes on the Foundations of the Theory of Small Displacements of Orthotropic Shells. *NACA (National Advisory Comittee for Aeronautics)*, Technical Note No. 1833:1–60, 1949.

[82] J. Hohe. A direct homogeneisation approach for determination of the stiffness matrix for microheterogeneous plates with application to sandwich panels. *Composites: Part B*, 34:615–626, 2003.

[83] G. A. Holzapfel. On large strain viscoelasticity: continuum formulation and finite element applications to elastomeric structures. *Int. J. Numer. Meth. Eng.*, 39:3903–3926, 1996.

[84] G. A. Holzapfel. *Nonlinear Solid Mechanics*. John Wiley & Sons, Chichester, 2000.

[85] G. A. Holzapfel, T. C. Gasser, and R. W. Ogden. A new constitutive framework for arterial wall mechanics and a cmparative study of material model. *J. Elasticity*, 61:1–48, 2000.

[86] T. J. R. Hughes. *The Finite Element Method*. Prentice-Hall, Englewood Cliffs, New York, 1987.

[87] M. Janghorban. Two different types of differential quadrature methods for static analysis of microbeams based on nonlocal thermal elasticity theory in thermal environment. *Arch. Appl. Mech.*, 82:669–675, 2012.

[88] R. Jänicke. *Micromorphic media: Interpretation by homogenisation*. Saarbrücker Reihe, Band 12, Materialwissenschaft und Werkstofftechnik. Shaker Verlag, Aachen, 2010.

[89] R. Jänicke and S. Diebels. Numerical homogenisation of micromorphic media. *Technische Mechanik*, 30 (4):364–373, 2010.

[90] R. Jänicke and S. Diebels. Requirements on periodic micromorphic media. In G. A. Maugin and A. Metrikine, editors, *Mechanics of Generalized Continua*, pages 99–108. Springer-Verlag, Berlin, 2010.

[91] R. Jänicke, S. Diebels, H. G. Sehlhorst, and A. Düster. Two-scale modelling of micromorphic continua. *Continuum Mech. Therm.*, 21 (4):297–315, 2009.

[92] M. Johlitz. *Materialmodellierung*. lectures notes. Universität des Saarlandes, 2009.

[93] T. Kanit, S. Forest, I. Galliet, V. Mounoury, and D. Jeulin. Determination of the size of the representative volume element for random composites: statistical and numerical approach. *Int. J. Solids Structures*, 40(13-14):3647–3679, 2003.

[94] P. Kanouté, D. P. Boso, J. L. Chaboche, and B. A. Schrefler. Multiscale Methods for Composites: A Review. *Arch. Comput. Methods Eng.*, 16:31–75, 2008.

[95] G. Karypis and V. Kumar. A fast and high quality multilevel scheme for partitioning irregular graphs. *SIAM Journal on Scientific Computing*, 20 (1):359–392, 1999.

[96] R. Kienzler. On consistent plate theories. *ARAM*, 72:229–247, 2002.

[97] F. Kikuchi. On a Finite Element scheme based on the Discrete Kirchhoff Assumption. *Numer. Math.*, 24:211–231, 1975.

[98] W. Kim and J. N. Reddy. Novel mixed finite element models for nonlinear analysis of plates. *Latin American Journal of Solids and Structures*, 7:201–226, 2010.

[99] G. Kirchhoff. Über das Gleichgewicht und die Bewegung einer elastischen Scheibe. *J. Reine Angew. Math.*, 40:51–88, 1850.

[100] E. Klingbeil. *Tensorrechnung für Ingenieure*. Institut für praktische Mathematik der technischen Hochschule Darmstadt, 1966.

[101] F. Koschnick. *Geometrische Locking-Effekte bei Finiten Elementen und ein allgemeines Konzept zu ihrer Vermeidung*. Ph.D.-thesis, Technische Universität München, Germany, 2004.

[102] V. G. Kouznetsova. *Computational homogenization for the multi-scale analysis of multi-phase m aterial*. Ph.D.-thesis, Technische Universiteit Eindhoven, The Netherlands, 2002.

[103] V. G. Kouznetsova, M. G. D. Geers, and W. A. M. Brekelmans. Multi-scale constitutive modelling of heterogeneous materials with a gradient-enhanced computational homogenization scheme. *Int. J. Numer. Meth. Eng.*, 54:1235–1260, 2002.

[104] V. G. Kouznetsova, M. G. D. Geers, and W. A. M. Brekelmans. Multi-scale second-order computational homogenization of multi-phase materials: a nested finite element solution strategy. *Comp. Meth. Appl. Mech. Eng.*, 193:5525–5550, 2004.

[105] W. B. Krätzig. Bestmögliche innere Schalengleichungen für schubweiche Werkstoffe unter Berücksichtigung von Dickenänderungen. *Arch. Appl. Mech.*, 64:1–19, 1993.

[106] W. B. Krätzig and D. Jun. On best shell models - From classical shells, degenerated and multi-layered concepts to 3D. *Arch. Appl. Mech.*, 73:1–25, 2003.

[107] E. Kröner. Allgemeine Kontinuumstheorie der Versetzungen und Eigenspannungen. *Arch. Rat. Mech. Anal.*, 4:273–334, 1960.

[108] M. Landervik and R. Larsson. A higher-order stress-resultant shell formulation based on multiscale homogenization. In M. Landervik, editor, *Modeling of foams for impact simulation, Ph.D.-thesis*, page Paper D. Chalmers University of Technology, Göteborg, 2008.

[109] M. Landervik and R. Larsson. Multiscale homogenization and shell theory for modeling thin porous layers. In M. Landervik, editor, *Modeling of foams for impact simulation, Ph.D.-thesis*, page Paper D. Chalmers University of Technology, Göteborg, 2008.

[110] F. Larsson and K. Runesson. On two-scale adaptive FE analysis of micro-heterogeneous media with seamless scale-bridging. *Comp. Meth. Appl. Mech. Eng.*, 200 (37-38):2662–2674, 2010.

[111] R. Larsson and S. Diebels. A second-order homogenization procedure for multi-scale analysis based on micropolar kinematics. *Int. J. Numer. Meth. Eng.*, 69:2485–2512, 2007.

[112] G. Laschet, J. P. Jeusette, and P. Beckers. Homogenization and pre-integration techniques for multilayer composite and sandwich finite element models. *Int. J. Numer. Meth. Eng.*, 27:257–269, 1989.

[113] E. H. Lee. Elastic-plastic deformation at finite strain. *J. Appl. Mech.*, 36:1–6, 1969.

[114] S. Lejeunes. *Modélisation de structures lamifiées élastomère-métal à l'aide d'une méthode de réduction de modèles*. Ph.D.-thesis, Université de la Mediterranée (Aix-Marseille II), 2006.

[115] M. Lévesque. *Modélisation du comportement mécanique de matériaux composites viscoélastiques non linéaires par une approche d'homogénéisation*. Dissertation, ENSAM, Centre de Paris, 2004.

[116] R. Lillbacka, F. Larsson, and K. Runesson. On the implementation of plane stress in computational multiscale modeling. *Int. J. of Multiscale Computational Engineering*, 4 (5-6):771–790, 2006.

[117] A. Lion. Constitutive modelling in finite thermoviscoplasticity: a physical approach based on nonlinear rheological models. *Int. J. Plast.*, 16:469–494, 2000.

[118] J. LLorca, C. González, J. M. Molina-Aldareguía, J. Segurado, R. Seltzer, F. Sket, M. Rodríguez, S. Sádaba, R. Munoz, and L. P. Canal. Multiscale modeling of composite materials : a roadmap towards virtual testing. *Advanced Materials*, 23:5130–5147, 2011.

[119] S. Loehnert and P. Wriggers. Effective behaviour of elastic heterogeneous thin structures at finite deformations. *Comp. Mech.*, 41:595–606, 2008.

[120] A. E. H. Love. On the small vibrations and deformations of thin elastic shells. *Philosophical Transactions of the Royal Society*, 179:491ff, 1888.

[121] S. Maleki, M. Tahani, and A. Andakhshideh. Transcient response of laminated plates with arbitrary laminations and boundary conditions under general dynamic loadings. *Arch. Appl. Mech.*, 82:615–630, 2012.

[122] J. Matheas, R. Schlebusch, and B. W. Zastrau. *Zur Herleitung einer oberflächenorientierten Schalentheorie und deren Umsetzung im Rahmen der Finite-Element-Methode*. Hegger, J.: Textilbeton - 1. Fachkolloquium der Sonderforschungsbereiche 528 und 532, 1. Auflage Aachen, 2001.

[123] K. Matous, M. G. Kulkarni, and P. H. Geubelle. Multiscale cohesive failure modeling of heterogeneous adhesives. *J. Mech. Phys. Solids*, 56:1511–1533, 2008.

[124] M. Matthes. *Berechnung der Verformungs- und Schnittgrößen am TIMOSHENKO-Balken mit viskoplastischem Materialverhalten unter stoßartiger Belastung*. Verlag Shaker, Aachen. Ph.D.-thesis, Technische Universität Darmstadt, 1994.

[125] A. Menzel and P. Steinmann. On the comparaison of two strategies to formulate orthotropic hyperelasticity. *J. Elasticity*, 62:171–201, 2001.

[126] C. Miehe. Numerical computation of algorithmic (consistent) tangent moduli in large-strain computational inelasticity. *Comp. Meth. Appl. Mech. Eng.*, 134:223–240, 1996.

[127] C. Miehe and C. G. Bayreuther. On multiscale FE analyses of heterogeneous structures: From homogenization to multigrid solvers. *Int. J. Numer. Meth. Eng.*, 71:1135–1180, 2007.

[128] C. Miehe and J. Keck. Superimposed finite elastic-viscoelastic-plastoelastic stress response with damage in filled rubbery polymers. Experiments, modelling and algorithmic implementation. *J. Mech. Phys. Solids*, 48:323–365, 2000.

[129] C. Miehe and A. Koch. Computational micro-to-macro transitions of discretized microstructures undergoing small strains. *Arch. Appl. Mech.*, 72:300–317, 2002.

[130] C. Miehe, J. Schröder, and C. Bayreuther. On the homogenization analysis of composite materials based on discretized fluctuations on the micro-structure. *Acta Mater.*, 155:1–16, 2001.

[131] R. D. Mindlin. Influence of rotatory inertia and shear on flexural motions of isotropic, elastic plates. *J. Appl. Mech.*, 18:31–38, 1951.

[132] P. M. Naghdi. The Theory of Shells. In Hrsg. S. Flügge, editor, *Handbuch der Physik, Vol. VI/2,*. Springer, Berlin, 1972.

[133] P. Neff. A geometrically exact Cosserat shell-model including size effects, avoiding degeneracy in the thin shell limit. Part I: Formal dimensional reduction for elastic plates and existence of minimizers for positive Cosserat couple modulus. *Continuum Mech. Therm.*, 16:577–628, 2004.

[134] P. Neff and S. Forest. A geometrically exact micromorphic model for elastic metallic foams accounting for affine microstructure. modelling, existence of minimizers, identification of moduli and computational results. *J. Elasticity*, 87(2-3):239–276, 2007.

[135] S. Nemat-Nasser and M. Hori. *Micromechanics: overall properties of heterogeneous materials*. North-Holland, Amsterdam, 1999.

[136] N. H. Nguyen. *Development of solid-shell elements for large deformation simulation and springback prediction*. Ph.D.-thesis, Université de Liège, Liège, 2009.

[137] V. P. Nguyen. *Multiscale failure modelling of quasi-brittle materials*. Ph.D.-thesis, Technische Universiteit Delft, The Netherlands, 2011.

[138] W. Noll. A new mathematical theory of simple materials. *Arch. Rat. Mech. Anal.*, 48:1–50, 1973.

[139] C. Oskay and G. Pal. A multiscale failure model for analysis of thin heterogeneous plates. *Int. J. of Damage Mechanics*, 19 (5):575–610, 2010.

[140] H. Parisch. A continuum-based shell theory for non-linear applications. *Int. J. Numer. Meth. Eng.*, 38:1855–1883, 1995.

[141] E. Pena, B. Calvo, M. A. Martínez, and M. Doblaré. An anisotropic visco-hyperelastic model for ligaments at finite strains. Formulation and computational aspects. *Int. J. Solids Structures*, 44:760–778, 2007.

[142] F. P. Perngjin. A new look at shear correction factors and warping functions of anisotropic laminates. *Int. J. Solids Structures*, 32 (16):2295–2313, 1995.

[143] P. Perzyna. The constitutive equations for rate sensitive plastic materials. *Quarterly Applied Mathematics*, 20:321–332, 1963.

[144] P. Perzyna. Fundamental problems in viscoplasticity. *Advances in Applied Mathematics*, 9:243–377, 1966.

[145] P. Perzyna. *Thermodynamic Theory of Viscoplasticity*. Advances in Applied Mechanics. Academic Press, Boston-New York, 1971.

[146] M. Petrov, S. Tipalin, J. Bast, P. Petrov, N. Kosatschjov, and S. Guk. Umformen eines Verbundwerkstoffs aus Stahlblechen. *Konstruktion, Springer, VDI Verlag*, 7/8:iw5–iw7, 2012.

[147] F. Peyrault, C. Renaud, N. Labed, and Z.-Q. Feng. Modélisation de tissus biologiques en hyperélasticité anisotrope - étude théorique et approche éléments finis. *C. R. Mécanique*, 337:101–106, 2009.

[148] O. Polit, P. Vidal, and M. D'Ottavio. Robust C^0 high-order plate finite element for thin to very thick structures: mechanical and thermo-mechanical analysis. *Int. J. Numer. Meth. Eng.*, 90:429–451, 2012.

[149] V. Prot, B. Skallerud, and G. A. Holzapfel. Transversely isotropic membrane shells with application to mitral valve mechanics. Constitutive modelling and finite element implementation. *Int. J. Numer. Meth. Eng.*, 71:987–1008, 2007.

[150] N. B. Guy Rabbat, A. L. Sangiovanni-Vincentelli, and H. Y. Hsieh. A multilevel newton algorithm with macromodeling and latency with analysis of large-scale nonlinear circuits in the time domain. *IEEE Transactions on circuits and systems*, 26(9):733–741, 1979.

[151] E. Rank, A. Düster, V. Nübel, K. Preusch, and O. T. Bruhns. High order finite elements for shells. *Comp. Meth. Appl. Mech. Eng.*, 194:2494–2512, 2005.

[152] J. N. Reddy. A general non-linear third-order theory of plates with moderate thickness. *Int. J. Non-Linear Mech.*, 25(6):677–686, 1990.

[153] J. N. Reddy. On refined theories of composite laminates. *Meccanica*, 25:230–238, 1990.

[154] J. N. Reddy. *Mechanics of Laminated Composite Plates, Theory and Analysis*. CRC Press, Inc., 1997.

[155] S. Reese and S. Govindjee. A theory of finite viscoelasticity and numerical aspects. *Int. J. Solids Structures*, 35:3455–3482, 1998.

[156] E. Reissner. On the theory of bending of elastic plates. *J. Math. Phys.*, 23:184–191, 1944.

[157] S. Rieger. *Temperaturabhängige Beschreibung visko-elasto-plastischer Deformationen kurzglasfaserverstärker Thermoplaste: Modellbildung, Numerik und Experimente*. Dissertation, Institut fur Mechanik (Bauwesen), Lehrstuhl I, Stuttgart, 2004.

[158] R. S. Rivlin. Large elastic deformation of isotropic materials IV:Further developments of the general theory. *Phil. Trans. Roy. Soc. Lond A*, A241:379–397, 1948.

[159] R. S. Rivlin. Large elastic deformation of isotropic materials V:The problem of flexure. *Phil. Trans. Roy. Soc. Lond A*, A195:463–473, 1948.

[160] R. S. Rivlin. Large elastic deformation of isotropic materials VI:further results in the theory of torsion, shear and flexure. *Phil. Trans. Roy. Soc. Lond A*, 242:173–195, 1949.

[161] D. Roehl and E. Ramm. Large elasto-plastic finite element analysis of solids and shells with the enhanced assumed strain concept. *Int. J. Solids Structures*, 33:3215–3237, 1996.

[162] C. Sansour. A theory and finite element formulation of shells at finite deformations involving thickness change: Circumventing the use of a rotation tensor. *Arch. Appl. Mech.*, 65:194–216, 1995.

[163] O. Schenk and K. Gärtner. Solving unsymmetric sparse systems of linear equations with pardiso. *Journal of Future Generation Computer Systems*, 20 (3):475–487, 2004.

[164] O. Schenk and K. Gärtner. On fast factorization pivoting methods for symmetric indefinite systems. *Elec. Trans. Numer. Anal.*, 23:158–179, 2006.

[165] R. Schlebusch. *Theorie und Numerik einer oberflächenorientierten Schalenformulierung*. Ph.D.-thesis, Berichte des Instituts für Mechanik und Flächentragwerke, Heft 3, Technische Universität Dresden, 2005.

[166] J. Schröder. *Theoretische und algorithmische Konzepte zur phänomenologischen Beschreibung anisotropen Materialverhaltens*. Ph.D.-thesis, Stuttgart, 1996.

[167] J. Schröder, D. Balzani, and D. Gross. Aspects of modeling and computer simulation of soft tissues: applications to arterial walls. *Mat.-wiss. u. Werkstofftech.*, 36(12):795–801, 2005.

[168] J. Schröder, F. Gruttmann, and J. Löblein. A simple orthotropic finite elastoplasticity model based on generalized stress-strain measures. *Comp. Mech.*, 30:48–60, 2002.

[169] J. Schröder and P. Neff. Construction of polyconvex, anisotropic free-energy functions. *Proc. Appl. Math. Mech.*, 2:172–173, 2003.

[170] J. Schröder and P. Neff. Invariant formulation of hyperelastic transverse isotropy based on polyconvex free energy functions. *Int. J. Solids Structures*, 40:401–445, 2003.

[171] K. Sedlan. *Viskoelastisches Materialverhalten von Elastomerwerkstoffen, Experimentelle Untersuchung und Modellbildung*. Dissertation, Berichte des Instituts für Mechanik (2/2001), Universität Gesamthochschule Kassel, 2001.

[172] J. Segurado, R. A. Lebensohn, J. Llorca, and C. N. Tomé. Mutliscale modeling of plasticity based on embedding the viscoplastic self-consistent formulation in implicit finite elements. *Int. J. Plast.*, 28:124–140, 2012.

[173] J. C. Simo and M. S. Rifai. A class of mixed assumed strain methods and the method of incompatible modes. *Int. J. Numer. Meth. Eng.*, 29:1595–1638, 1990.

[174] G. F. Smith. On a fundamental error in two papers of C.-C. Wang "On representations for isotropic functions, Part I and II". *Arch. Rat. Mech. Anal.*, 36:161–165, 1969.

[175] E. Stein and G. Sagar. Convergence behavior of 3D finite elements for Neo-Hookean material. *Engineering Computations: Int. J. Comput. Aided Eng. Software*, 25(3):220–232, 2008.

[176] G. Strang and G. J. Fix. *An Analysis of the Finite Element Method*. Prentice-Hall, Englewood Cliffs, New York, 1973.

[177] P. Suquet. Local and global aspects in the mathematical theory of plasticity. In *Plasticity Today: Modelling, Methods and Applications*, pages 279–310. Elsevier, London, 1985.

[178] I. Szabó. *Geschichte der mechanischen Prinzipien*. Birkhäuser Verlag, Basel, 1977.

[179] M. Talbot and G. Dhatt. Three discrete Kirchhoff elements for shell analysis with large geometrical non-linearities and bifurcations. *Eng. Comp.*, 4:15–22, 1987.

[180] A. Tessler. An improved plate theory of {1,2}-order for thick composite laminates. *Int. J. Solids Structures*, 30 (7):981–1000, 1993.

[181] A. Tessler, M. S. Annett, and G. Gendron. A {1,2}-order plate theory accounting for three-dimensional thermoelastic deformations in thick composite and sandwich laminates. *Composite Structures*, 52:67–84, 2001.

[182] C. Truesdell and W. Noll. The non-linear field theories of mechanics. In S. Flügge, editor, *Handbuch der Physik*, volume III/3. Springer-Verlag, Berlin, 1965.

[183] F. P. van der Meer. *Computational modeling of failure in composite laminates*. Ph.D.-thesis, Technische Universiteit Delft, The Netherlands, 2010.

[184] O. van der Sluis, P. J. G. Schreurs, W. A. M. Brekelmans, and H. E. H. Meijer. Overall behaviour of heterogeneous elastoviscoplastic materials: effect of microstructural modelling. *Mech. Mater.*, 32:449–462, 2000.

[185] P. Vannucci and G. Verchery. Anisotropy of plane complex elastic bodies. *Int. J. Solids Structures*, 47(9):1154–1166, 2010.

[186] T. P. Vo and J. Lee. Geometrical nonlinear analysis of thin-walled composite beams using finite element method based on first order shear deformation theory. *Arch. Appl. Mech.*, 81:419–435, 2011.

[187] C. C. Wang. On representations for isotropic functions. Part I. Isotropic functions of symmetric tensor and vectors. *Arch. Rat. Mech. Anal.*, 33:249–267, 1969.

[188] C. C. Wang. On representations for isotropic functions. Part II. Isotropic functions of skew-symmetric tensors, symmetric tensors, and vectors. *Arch. Rat. Mech. Anal.*, 33:268–287, 1969.

[189] C. C. Wang. A new representation theorem for isotropic functions: An answer to Professor G. F. Smith criticism of my paper on representation for isotropic functions. Part I. Scalar-valued isotropic functions. *Arch. Rat. Mech. Anal.*, 36:166–197, 1970.

[190] C. C. Wang. A new representation theorem for isotropic functions: An answer to Professor G. F. Smith criticism of my paper on representation for isotropic functions. Part II. Vector-valued isotropic functions, symmetric tensor-valued functions, and skew-symmetric tensor-valued functions. *Arch. Rat. Mech. Anal.*, 36:198–223, 1970.

[191] E. J. Weinberg and P. Neff. A geometrically exact thin membrane model-investigation of large deformations and wrinkling. *Int. J. Numer. Meth. Eng.*, 74:871–893, 2008.

[192] J. A. Weiss, B. N. Maker, and S. Govindjee. Finite element implementation of incompressible, transversely isotropic hyperelasticity. *Comp. Meth. Appl. Mech. Eng.*, 135:107–128, 1996.

[193] T. O. Williams. A new theoretical framework for the formulation of general, nonlinear, multiscale plate theories. *Int. J. Solids Structures*, 45:2534–2560, 2008.

[194] P. Wriggers. *Nichtlineare Finite-Elemente-Methoden*. Springer-Verlag, Berlin, 2001.

[195] R. Xiaohui, C. Wanji, and W. Zhen. A new zig-zag theory and C^0 plate bending element for composite and sandwich plates. *Arch. Appl. Mech.*, 81:185–197, 2011.

[196] Z. Yuan and J. Fish. Toward realization of computational homogenization in practice. *Int. J. Numer. Meth. Eng.*, 73:361–380, 2008.

[197] Z. Yuan and J. Fish. Multiple scale eigendeformation-based reduced order homogenization. *Comp. Meth. Appl. Mech. Eng.*, 198:2016–2038, 2009.

[198] W. Zerna. Mathematisch strenge Theorie elastischer Schalen. *Z. Angew. Math. Mech.*, 42:333–341, 1962.

[199] P. A. Zhilin. Mechanics of deformable directed surfaces. *Int. J. Solids Structures*, 12:635–648, 1976.

[200] T. I. Zohdi and P. Wriggers. Computational micro-macro material testing. *Arch. Computational Methods in Engineering*, 8(2):131–228, 2001.